RIKAGAKU KENKYUSHO

*the Institute of Physical and Chemical Research*

Wako-shi, Saitama Pref., JAPAN

'78

*IPCR* cyclotron
Progress Report 1978

Vol. 12

# *IPCR* Cyclotron Progress Report

# Vol. 12

# Editors

This volume contains recent information of the IPCR Cyclotron, informal reports and abstracts of papers which will be published at scientific meetings or in publications by staff members, guests, and visitors.

# CONTENTS

# 1. INTRODUCTION

During the past one year the IPCR cyclotron was operated in good condition as before. Several improvements have been made in the machine itself and its accessory facilities which resulted in more stable and efficient operation.

In the fields of research using the cyclotron a majority of research works have been carried out with heavy ions. Extensive studies on pre equilibrium emmission of light particles and energy relaxation phenomena were performed in nuclear reactions induced by heavy ions. Nuclear structure studies were also continued. Multiple ionization phenomena in the collision of heavy ions on gaseous and solid materials were extensively studied to get information on the excitation mechanism as well as the effects of chemical environment on X-ray spectra. Channeling experiments were continued to study the location of impurity atoms and radiation damage in solids. Positron annihilation studies were made on transition metals. Activation analysis by charged particles were applied for the study of the surface of semiconductors. Studies of radiation chemistry and radiation biology were continued by using heavy ions as well as alpha particles.

All the resonators of the new heavy ion linac were installed and the oscillator system for the first resonator was built. The beam transport system and the beam handling devices were designed. Model study of the separated sector cyclotron was also continued.

Hiromichi Kamitsubo
Editor

# 2. MACHINE OPERATION

T. Kageyama, H. Nakajima, K. Ogiwara,
S. Fujita, K. Ikegami, S. Kohara,
H. Takebe, and I. Kohno

The cyclotron was operated on the 24 h a day basis during the period from Oct. 23, 1977 to Oct. 22, 1978.

Statistics of machine operation time is shown in Table 1. The total beam time of 4535.3 h is slightly, i.e. 2.2% (188.4 h), longer than that of the last year. This increase in beam time is due to the decrease in the overhaul time.

Table 2 shows the machine time allotted to various activities in this period. In this period, 3427 h (59.6 %) of the 5748 h scheduled for use in experimental programs, were used by nuclear physics groups and 2321 h (40.4 %) by groups of fields other than nuclear physics and also by outside users. Requests for heavy ion beam continued to increase and the cyclotron was operated with heavy ion for 4459 h which was 77.6 % of the total scheduled beam time.

Table 3 shows the distribution of the beam time among particles accelerated. $N^{5+}$, $O^{5+}$, and $Ne^{6+}$ ions were accelerated using pulsed operation of the heavy ion source and the scheduled beam time for these ions were 1795 h (31.2 %).

Table 1. Machine operation.

|  | Oscillator | Ion-source | Beam |
|---|---|---|---|
| Reading of time meter on Oct. 23, 1977 | 51750.8 (h) | 55308.8 (h) | 23821.8 (h) |
| Reading of time meter on Oct. 22, 1978 | 56752.7 | 60594.1 | 28357.1 |
| Difference | 5001.9 | 5285.3 | 4535.3 |
| Percentage of 365 days | 57.1 % | 60.3 % | 51.8 % |
| Schedule in this period |  |  |  |
|     Beam time |  | 243 (days) |  |
|     Overhaul and installation work |  | 54 |  |
|     Periodical inspection and repair |  | 25 |  |
|     Vacation and holidays |  | 43 |  |

Table 2.  Scheduled beam time and subjects of activity in the period XIII.

| Subject | | Heavy ion | Light particles | Total |
|---|---|---|---|---|
| Nucl. Phys. | Nuclear reaction | 2673 (h) | 141 (h) | 2814 (h) |
| | In-beam spectroscopy | 515 | 24 | 539 |
| | RI production | 40 | 34 | 74 |
| Fields others than Nucl. Phys. | Nuclear chemistry | 0 | 203 | 203 |
| | Radiation chemistry | 292 | 26 | 318 |
| | Radiation biology | 205 | 90 | 295 |
| | Solid state physics | 0 | 440 | 440 |
| | Inner atomic shell excitation study | 683 | 48 | 731 |
| | Stopping power study | 27 | 39 | 66 |
| Outside users | Nuclear medicine | 0 | 14 | 14 |
| | Nuclear fuel study | 24 | 217 | 241 |
| | RI production | 0 | 13 | 13 |
| Total | | 4459 | 1289 | 5748 |
| Percent in total | | 77.6 % | 22.4 % | 100 % |

| Maintenance, operation and engineering | |
|---|---|
| Exchange of ion sources | 66 (h) |
| Machine inspection and repair | 600 |
| Total | 666 |

Table 3.  Distribution of beam time among particles accelerated.

| Particle | (h) | (%) |
|---|---|---|
| P | 431 | 7.5 |
| d | 70 | 1.2 |
| $^3\mathrm{He}^{++}$ | 240 | 4.2 |
| $^4\mathrm{He}^{++}$ | 548 | 9.5 |
| $\mathrm{C}^{4+}$ | 348 | 6.1 |
| $\mathrm{N}^{4+}$ | 2316 | 40.3 |
| $\mathrm{N}^{5+}$ | 1168 | 20.2 |
| $\mathrm{O}^{5+}$ | 83 | 1.5 |
| $^{20}\mathrm{Ne}^{6+}$ | 549 | 9.6 |
| Total | 5748 | 100.0 |

# 3. MACHINE DEVELOPMENT AND ACCELERATOR PHYSICS

## 3-1. A Proposed Multi-Purpose Separated Sector Cyclotron

H. Kamitsubo, S. Motonaga, N. Kumagai, T. Nomura, N. Nakanishi,

T. Wada, I. Kohno, J. Fujita, H. Nakajima,

K. Ogiwara, H. Takebe, and F. Yoshida

A 160 cm ordinary cyclotron constructed in 1967 has been used as a multi-purpose facility providing heavy ions (B, C, N, O, and Ne) as well as light particles to researchers in various fields. In course of time, demands for heavier ions with higher energies have grown up among many users as clearly seen from recent statistics which shows that about two thirds of the total beam time has been devoted to heavy ion experiments at nearly maximum energies (around 9 MeV/u). Although much effort has been made to improve the existing cyclotron, it became apparent even in the early 70's that the present machine could not meet the future demands satisfactorily. Therefore, extensive discussion to upgrade the facility and a design study of a new heavy ion accelerator were initiated at that time.[1] In 1972, a separated sector cyclotron combined with a variable-frequency linac of Wideröe type was proposed.[2]

The main beam requirements for this facility are as follows: It should be able to accelerate beam of all elements up to uranium. The beam energy should be high enough to overcome the Coulomb barrier in the whole range of the accelerating ions, desirably over 100 MeV/u for fully stripped light ions and over 10 MeV/u for very heavy ions such as uranium. High intensity beam of protons, deuterons and α-particles are also required for studies of nuclear chemistry and radiation biology as well as nuclear physics.

Among various types of accelerator complex to satisfy the above requirements, a separated sector cyclotron (SSC) with an appropriate injector has been selected to be the most suitable machine from various points of view. The main advantages of the SSC can be considered to be a large value of flutter in the magnetic fields to enable acceleration of energetic particles with high intensity over a wide range of ion masses and relative easiness for the beam injection and extraction. The simpleness in the design and construction of SSC is considered also important to facilitate attaining the level of the scheduled operation and thus to ascertain preparatory works in many research fields expected at the proposed multi-purpose facility.

The proposed facility consists of a SSC with four $50°$ sector magnets, a variable frequency linac[3] and an AVF cyclotron. Figure 1 shows the energy-mass capability of the proposed facility. Table 1 shows the characteristics of the proposed accelerators and injectors. The maximum beam energies of the SSC are about 120 MeV/u for light ions and about 15 MeV/u for very heavy ions. The accelerating abilities of this SSC for various ions are shown in Fig. 2. The four non-spiral sector magnets yield the required isochronous field of 17.7 kG at maximum. From the matching conditions with the injectors under consideration, ions can be accelerated, in principle, with harmonic number h = 4, 6, 8, 10, and 12.

The focusing properties of the SSC were calculated with the modified SPYRING code[4] including the soft-edge effect on the magnetic field. Two sector magnets (approximately 1/4 scale model) have been constructed to obtain detailed information on the properties of the sector magnets such as their excitation characteristics and field distribution including the interference by adjacent magnets. Whole magnetic motive force, maximum coil power and magnet weight are estimated to be $2 \times 10^5$ A T, 960 kW and 1900 t, respectively. The field distributions have been measured in the range of 8 − 17.5 kG by using a NMR calibrated Hall probe (SBV-595) and an on-line computer. Detailed calculation of the beam dynamics is now in progress using the measured magnetic fields of the model magnets.

Ions are accelerated by $22.5°$, delta-shaped two dees located at opposite valley spaces between the sector magnets. The frequency range of the RF system is chosen to be 17 − 45 MHz to realize the synchronous

## Table 1.  Characteristics of accelerators.

### SSC

| | |
|---|---|
| Maximum energy for $U^{37+}$, $(U^{40+})$ | 15 MeV/u |
| Maximum energy for $C^{6+}$, $Ne^{10+}$ | 120 MeV/u |
| Number of sectors | 4 |
| Sector angle | 50° |
| Magnet fraction | 0.555 |
| Magnet gap | 8 cm |
| Maximum magnetic field | 18.0 kG |
| Main coil power | 950 kW |
| Number of trimming coils | >40 |
| Magnet weight | 1900 ton |
| Injection mean radius | 79 cm |
| Extraction mean radius | 338 cm |
| $E_f/E_i$ | 18 − 21 |
| Number of dees | 2 |
| Dee angle | 22.5° |
| Peak voltage | 250 kV |
| RF power | 300 kW × 2 |
| RF frequency range | 17(22) − 45 MHz |
| Number of harmonic acceleration | 4, 6, 8, 12 |

### LINAC

| | |
|---|---|
| Number of tanks | 6 |
| Number of drift tubes per tank | 19 − 11 |
| Gap length | 4 − 9 cm |
| Peak voltage of gaps | 180 − 300 kV |
| Maximum total voltage gain | 16(20) MV |
| RF frequency range | 17 − 45 MHz |
| Q-value of cavity | 12000 − 17000 |
| Accelerating mode | $\pi/3\pi$, $\pi/\pi$ |
| Duty factor (macroscopic) | 100 % |
| Mass to charge ratio | 4 − 24 |
| Emittance at exit | 7.8 cm mrad |
| Energy resolution | 0.3 % |

### AVF cyclotron

| | |
|---|---|
| Energy constant, K | 90 MeV |
| Number of sectors | 4 |
| Magnet gap at hill | ∼ 20 cm |
| Maximum mean magnetic field | 17 kG |
| Extraction mean radius | 79 cm |
| Main coil power | ∼ 250 kW |
| Number of dees | 2 |
| Dee angle | 90° |
| RF frequency range | 9 − 20 MHz |
| Maximum RF voltage | 50 kV |
| RF power | 150 kW |
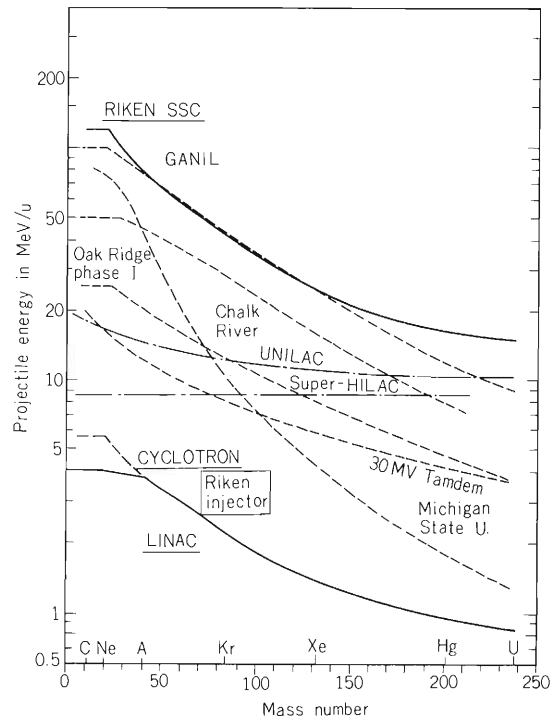


Fig. 1.   Maximum beam energy per nuclear vs. mass number of the proposed facility together with those of heavy ion accelerators in operation or under construction in some other laboratories.
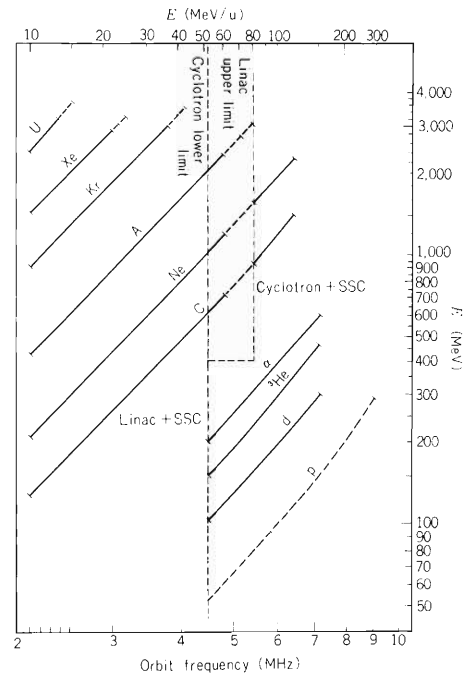


Fig. 2.   Energies and orbit frequencies for various ions obtained from the proposed accelerator complex.   Two vertical dashed lines indicate the lower and upper energy limits of the cyclotron- and linac-injected SSC, respectively.   Solid and dashed lines for heavy ions correspond to the scheduled operation of the linac in the early stage and its expected energy increase afterwards.

operation with the linac, the optimum harmonic number in acceleration being h = 8, while h = 4 in the case of injection from the AVF cyclotron.   For this purpose, a half-wave cavity resonator having coaxial structure with delta-shaped cross section has been designed.   This structure of the cavity was chosen to realize reasonable values of current density at the shorting end and power loss in the case of maximum dee voltage (250 kV) over the whole range of frequency.   The resonating frequencies, electric potential distributions and Q-values for the designed resonator have been tested by a half-scale model cavity.

The operating pressure of $1 \times 10^{-7}$ torr is desirable in the median plane of the SSC to limit beam losses due to charge-exchange to less than about 10 % in the case of very heavy ions.   Based on the estimated surface area of vacuum chambers, the degassing rate has been estimated to be around 5 lus.   Two cryopumps of 25000 $\ell$/sec and two titanium-sublimation pumps of 5000 $\ell$/sec, for example, will be needed to get the above mentioned vacuum. More detailed design of vacuum chamber and pumping system is currently in progress.

This facility will be used for researchers in various fields such as nuclear and atomic physics, solid-state study, material science, radiation chemistry and biology and RI production.   The use for the radiotherapy is also being considered.   Figure 3 shows the proposed layout of beam lines in various experimental areas.
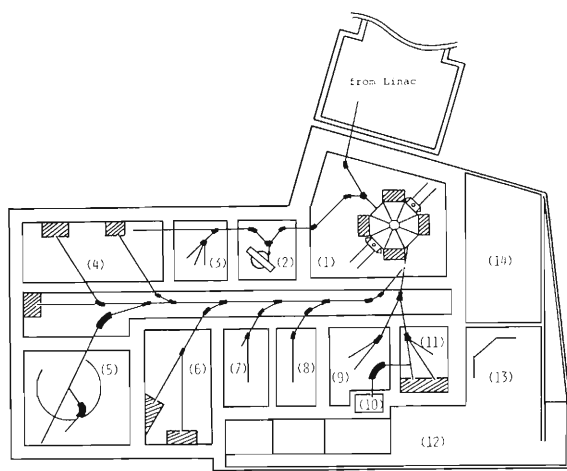


Fig. 3.   Proposed layout of beam lines.

References

1)   K. Matsuda: Sci. Papers I. P. C. R., 66, 33 (1972).

2)   M. Odera and T. Tonuma: 283, AIP 9, Cyclotrons-1972; M. Odera, I. Kohno, and H. Kamitsubo: Intern. Conf. Reactions between Complex Nuclei, Held at Vanderbolt University, Nashville, Tennessee, p. 63 (1974).

3)   M. Odera: Proc. of the 1976 Proton Linear Accelerator Conf; T. Tonuma, F. Yoshida, and M. Odera: IEEE Trans. Nucl. Sci., NS-23, 1031 (1976).

4)   I. Miura: Private communication.

# 3-2. Design of Full Scale Magnet of Separated Sector Cyclotron

N. Kumagai, S. Motonaga, H. Kamitsubo,

T. Wada, F. Yoshida, K. Ogiwara,

I. Yokoyama, J. Fujita, and H. Takebe

The separated sector cyclotron(SSC) proposed[1] at IPCR is intended to accelerate ions of all elements up to 120 MeV/u for light ions(B, C, N, O, and Ne) and 15 MeV/u for heavy ions (Pb, U, etc.). This SSC consists of four non-spiral sector magnets with sector angle of 50°, gap distance of 8 cm and maximum magnetic field of 17.7 kG. The geometrical shape and maximum magnetomotive force of this SSC magnet were evaluated from the measurement of magnetic flux along the return path of approximately 1/4 scale model of this magnet. The measurement of this flux was carried out by using nine flux measuring coils and a flux meter of integrated type. Their positions and the ratio of cross-sectional area of each coil to that of coil(1) are shown in Fig. 1(a) and (b), respectively. From the measured relative flux and the ratio of the cross-sectional area, the flux density at each position relative to that of pole surface was calculated along the return path of model magnet. The results at $B_c$ = 6.6 and 18 kG are shown in Fig. 1(c). The flux density was found to be 5 – 10 % higher at the position of coil(3), 5 – 10 % lower at the position of coil(5) and 5 – 15 % higher at the side yoke. On the basis of these density profiles, the full scale SSC was designed to have approximately uniform flux density along the return path. The
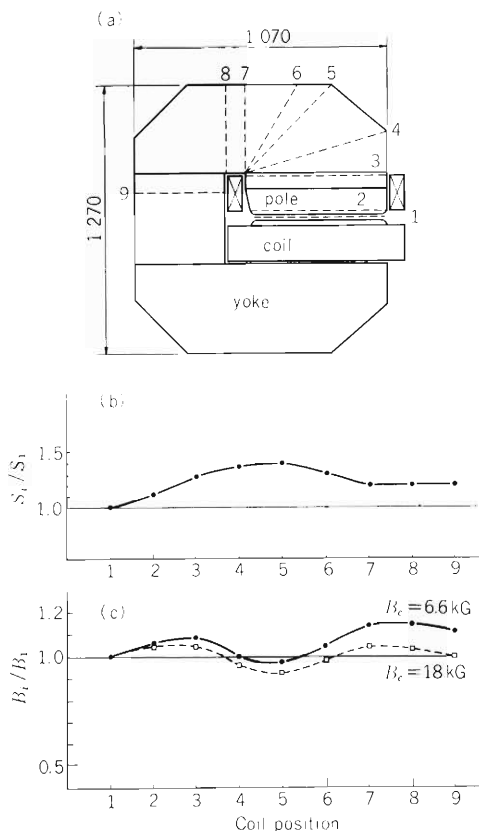


Fig. 1. (a) Side view of model magnet of 1/4 scale and positions of measuring coils. Their positions are shown by a dashed line. (b) The ratio of cross-sectional area of each coil to that of coil (1). (c) The relative flux density $(B_i/B_1)$ measured at $B_c$ = 6.6 and 18 kG.

result is shown in Fig. 2. The ratio of cross-sectional area of pole base to that of pole surface is taken to be the same (1.28) as that of the model magnet but that of the pole base to side yoke is modified from 1.15 of the model magnet to 1.10. The shape of pole edge is approximated by that of the Rogowski profile. The total weight of this four magnet system was estimated to be about 2000 tons.

The maximum magnetomotive force of this full scale magnet was estimated for the field of $B_c = 18$ kG from following equation

$$NI = \sum_i B_1 \times (B_i/B_1) \times \Delta\ell_i / (\mu_0 \cdot \mu_{ri}),$$

where $\mu_0$ and $\mu_{ri}$ are free-space permeability and relative permability of iron, respectively and $\Delta\ell_i$ length of flux path between adjacent flux coils. The value obtained was $2.07 \times 10^5$ Ampere turn for $B_c = 18$ kG. For this estimation, the relative flux density measured for 1/4 scale model and approximate $\mu_{ri}$-values of iron along the return path at $B_c = 18$ kG were used. The maximum coil power was calculated to be about 1000 kW for copper conductor with maximum current density of 6 A/mm$^2$. The size of the main coil was designed to be 5 cm in thickness and 50 cm in height to accept the RF cavities in the narrow space between magnets. This coil is also shown in Fig. 2.
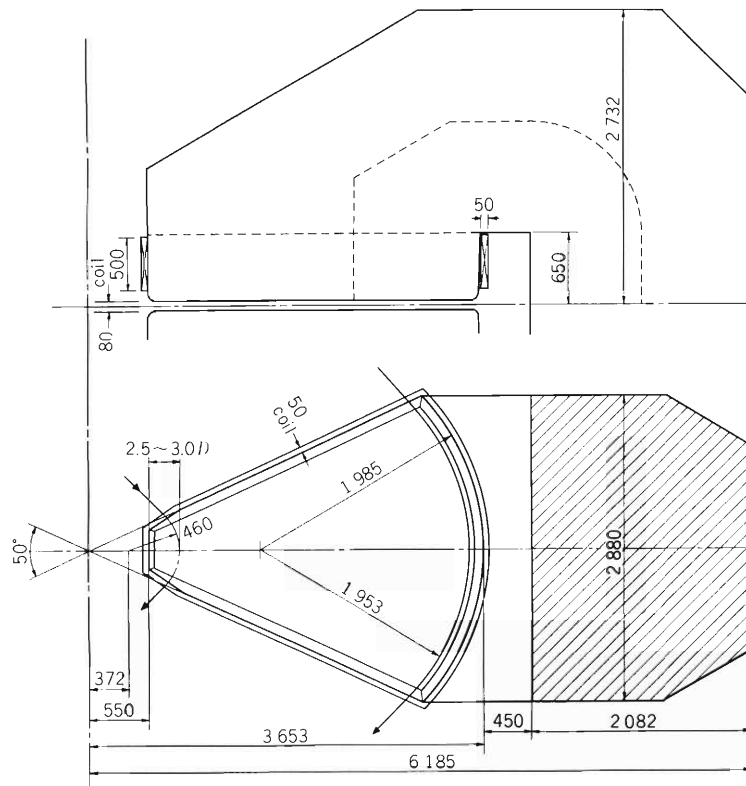


Fig. 2.   Profile and dimension of the full scale SSC magnet.

Magnetomotive force evaluated for various fields was compared with the theoretical one calculated by computer program TRIM.[2] It is shown in Fig. 3. Agreement between the two is very well at low field but poor at high field. This is supposed to be due to the saturation effect of iron, since cross-sectional area of the yoke is taken much larger for TRIM calculation in order to make the program coding easier.
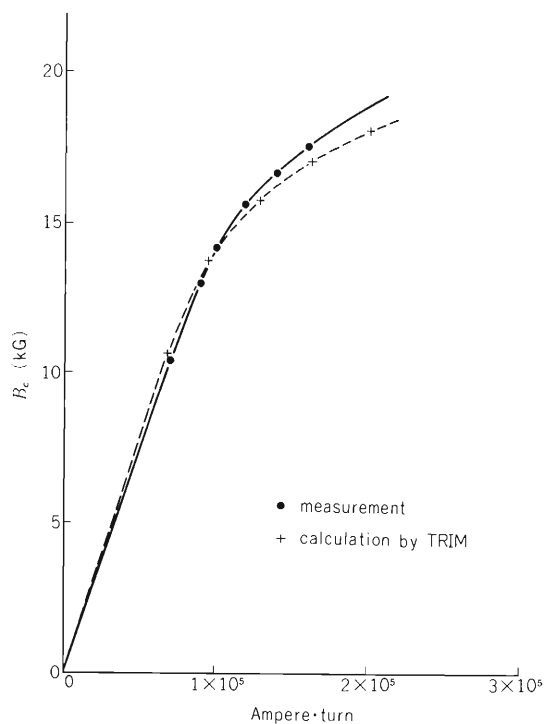
Fig. 3. Comparison of the measured magnetomotive force with the theoretical one calculated by computer code TRIM.

References

1) H. Kamitsubo et al.: IPCR Internal Report SSC-1; Presented at 2nd Symposium on Accelerator Science and Technology, at INS Tokyo, Tokyo, March (1978).

2) J. S. Colonias and J. H. Dorst: Magnet Design Applications of the Magnetostatic Program Called TRIM, UCRL-16382 (1965).

# 3-3.  Magnetic Field Profile of 1/4 Scale SSC Model Magnet

N. Kumagai, S. Motonaga, H. Kamitsubo, T. Wada,

F. Yoshida, K. Ogiwara, N. Nakanishi,

J. Fujita, I. Yokoyama, and H. Takebe

The magnetic field profile of a 1/4 scale model magnet of the proposed K = 620 MeV separated sector cyclotron (SSC)[1] was investigated in order to evaluate the injection and extraction radii, focusing properties, beam dynamics and injection system of this SSC.   The area between the center line of the sector magnet ($\theta$ = 0°) and that of the free space between the magnets ($\theta$ = 45°) was mapped out with polar grids which consisted of 59 points in radial direction and 90 points in azimuthal one.   The scan of field in radial direction was limited within 235 to 735 mm of the model due to the geometry of the magnetic detection system.   This mapping measurement was carried out by using a NMR calibrated Hall element (FC-33) with its temperature and control current stabilized.   The Hall probe was mounted on an aluminum arm, which was rotated at the step of 0.5° by a pulse motor controlled with a computer.   The uncertainty of magnetic field due to reproducibility of probe position was 1.5 % in the region of large field gradient and less than 0.01 % in the region of uniform field, and the variation of output Hall voltage during a period of one week was less than $4 \times 10^{-5}$.

The field profile was obtained at the step of 1 kG over the excitation range from 8 to 17.5 kG.   The results are presented in the following.   Figure 1 shows the profile of magnetic field along the center line of the sector magnet at $B_C$ = 10, 15, 16, and 17.5 kG.   At higher field, the magnetic field begins to sag appreciably at both inner and outer radii of this model magnet.   This field decrease at 17.5 kG is about 2 % near the injection radius and about 0.5 % at the extraction radius.   This is supposed to be due to the saturation of iron near the pole tip and the leakage of magnetic flux from the pole edge.   Also, radial magnetic profile at various azimuthal angles at $B_C$ = 17.5 kG are shown in Fig. 2.   In this diagram, profiles for intermediate radii are not included in order to emphasize the field gradient features at small and large radii.   These results are implying that the 2.5 — 3 times of the gap distance from the pole edge must be taken as the
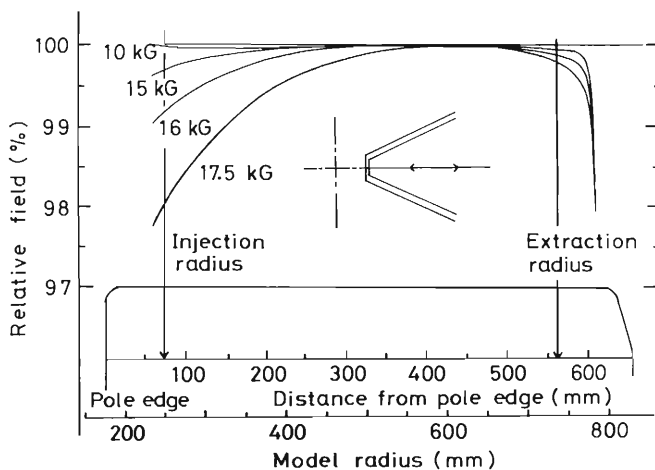


Fig. 1.   Relative profiles of magnetic field along the center line of the model magnet for $B_C$ = 10, 15, 16, and 17.5 kG.
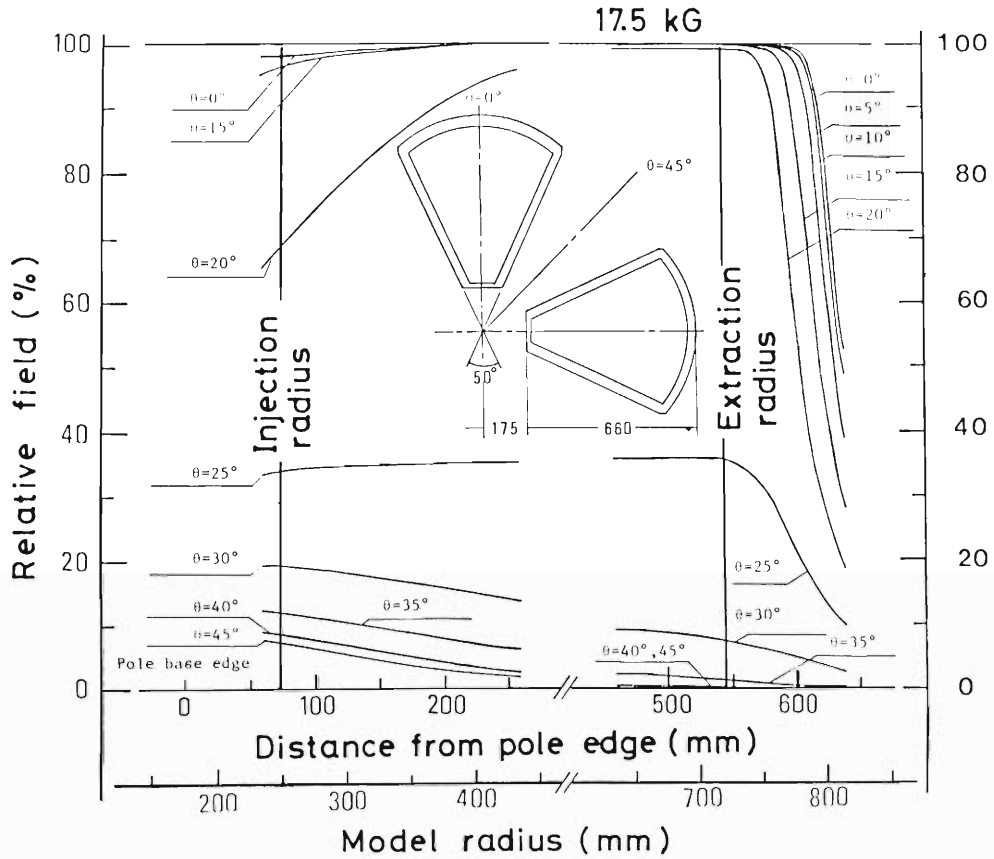
Fig. 2.    Relative profiles of magnetic field for various azimuthal angles at $B_c$ = 17.5 kG.

position of injection and extraction orbits.    The region of the rapid decrease of magnetic field are not favorable for purpose of injection or extraction of the beam.    It should be noted in the 45° curve that the fringing field becomes about 10 % of maximum field at small radius, since along this valley line the beam is transfered to the injection system of SSC.

The azimuthal profiles of the 17.5 kG field at 4 different radii are shown in Fig. 3, in which
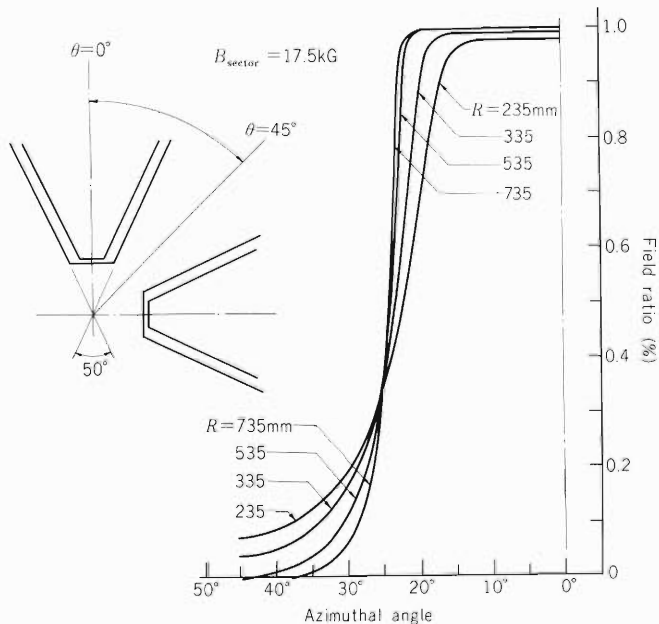


Fig. 3.    Azimuthal profiles of magnetic field at 4 different radii in $B_c$ = 17.5 kG.

large leakage is observed at small radius. The effective sector angles at the four radii were calculated from the measured profiles. The results are shown in Table 1 together with those results at $B_c$ = 8 kG. These calculated values agree with the designed value of 50° within 0.5°. The agreement between the angles at low and high field is also very well. This demonstrates that the desired shape of the pole edge is well approximated by the Rogowski profile.

Table 1.   Effective sector angle calculated from the measured azimuthal magnetic profiles.

| R (model radius) | Effective sector angle (degree) | |
|---|---|---|
| (mm) | $B_c$ = 8 kG | $B_c$ = 17.5 kG |
| 235 | 25.41 | 24.95 |
| 335 | 25.84 | 25.38 |
| 535 | 25.75 | 25.33 |
| 735 | 25.53 | 25.22 |

In Fig. 4, the flutter without trim coils as a function of model radius is presented for three different magnetic fields (10, 15, and 17.5 kG). The flutter shapes are very similar among them, and change smoothly from 0.45 near injection radius to 0.7 at extraction radius. This change is due to the azimuthal leakage of magnetic flux as shown in Fig. 3. The detailed calculation of beam dynamics using these results are in progress.
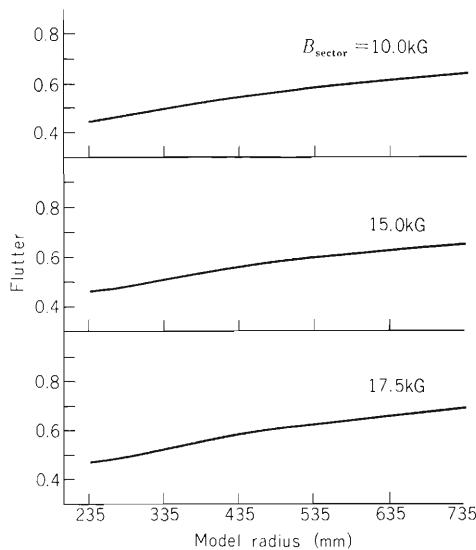


Fig. 4.   Flutter as a function of model radius at three magnetic fields (10, 15, and 17.5 kG).

Reference

1)   H. Kamitsubo et al.:  IPCR Internal Report SSC-1; Presented at 2nd Symposium on Accelerator Science and Technology, at INS Tokyo, Tokyo, March (1978).

## 3-4. Beam Transfer Line between Linac and Separated Sector Cyclotron

N. Kumagai, T. Wada, H. Takebe, and H. Kamitsubo

We have designed a beam transfer line to be used between the proposed separated sector cyclotron (SSC)[1] and the IPCR variable frequency heavy-ion linac.[2]   This transfer line was designed under the following conditions:

1) to guide the beam as shown in Table 1 without intensity loss from the linac to SSC;
2) to match the beam qualities to the acceptance of SSC in six dimensional phase space.

Table 1.   Characteristics of transfer beam.

| | |
|---|---|
| Maximum energy per nucleon | 4 MeV for $^{12}C^{6+}$, 0.84 MeV for $^{238}U^{40+}$ |
| M/q | 2 for $^{12}C$, 24 for $^{238}U$ |
| Beam emittance | $25\pi$ mm mrad in both x and y directions |
| Energy spreading | 0.3% |
| Bunch width | $\pm33°$ |

Figure 1 is the layout of the transfer line.   The horizontal distance between the linac and SSC is about 40 m and about 7 m vertically.   This transfer line consists of a charge stripper, beam bunchers, conventional bending magnets and quadrupoles.   Thirteen quadrupole units (Q1 to Q13) and six dipoles (D1 to D6) were used for the transfer system in the horizontal and vertical directions.   The magnetic properties of these elements are calculated by using the computer code TRANSPORT.[3]   In carrying out this calculation, we regarded the position of slit S1 to be the starting point of this transfer line.   The result is shown in Fig. 2.   In order to make these transfer elements to be compact and economical in size and to accelerate ions efficiently in SSC, M/q of the ions is increased by a charge stripper.
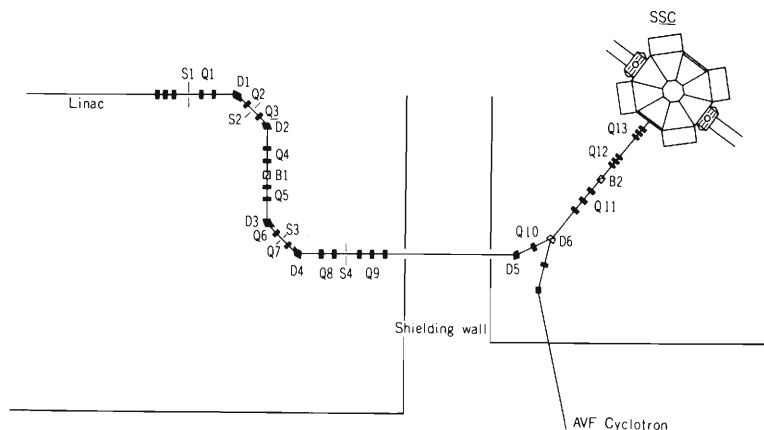


Fig. 1.   Layout of the beam transfer line between linac and SSC.   The S, Q, D, and B refer to slit, quadrupole magnet, dipole magnet and buncher, respectively.
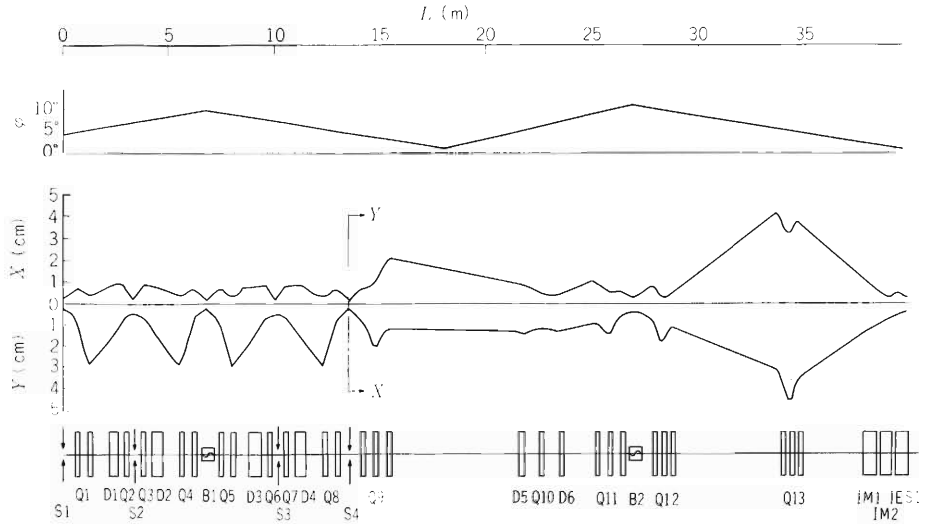
Fig. 2.    Beam envelopes in the longitudinal ($\varphi$), vertical (x) and
horizontal (y) directions along the transfer line from the linac to SSC.
The beam moves from left to right.

This charge stripper is placed at the position of double waist of slit S1 in order to avoid the
deterioration of beam quality.    The beam is vertically transfered from the beam line of linac to
that of SSC by using two achromatic systems (D1-Q2-Q3-D2 and D3-Q6-Q7-D4) between S1 and
S4.    Ions of desired charge is selected at slit S2, at which the resolving power is chosen to be
about 250 for the slit S1 of 4 mm in width.    This value is enough to separate ions with adjacent
charge state in uranium region.    A dispersion matching element (D5-Q10-D6) and two quadrupole
triplets, Q12 and Q13, match the beam qualities to the requirement of SSC.    The beam is injected
via a dee-free valley into injection element in SSC.    The layout of injection system is shown in
Fig. 3.    Elements IM1 and IM2 bend the beam into the entrance of a 39 cm long electrostatic
inflector (LES-1), which brings the beam into the first orbit of SSC.    The characteristics of these
elements are presented in Fig. 3.



| | IM-1 | IM-2 | IES-1 |
|---|---|---|---|
| Angle | 7° | 79° | 70° |
| $B, E_{max}$ | 2kG | 17kG | 110kV/cm |
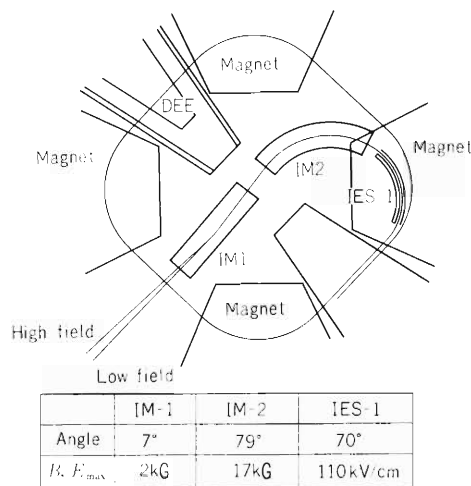
Fig. 3.    Layout of injection elements at the central region of SSC.

Two beam bunchers are provided in order to match the bunch width to the RF acceptance of SSC. The first buncher B1 is placed at the double waist point between two achromatic systems and focuses the bunch width ($\varphi$) at the middle point of "a burst phase shifter (BPS)". The second buncher B2 is used to match the bunch width to the longitudinal acceptance of SSC. A sinusoidal buncher can be approximated as a thin lens if the beam width ($\varphi$) at the buncher is not large compared with the linear part of a sinusoidal wave. The magnification, then, is given by the ratio of an image distance to an object one. The result is shown in Fig. 2.

If the lowest frequency of the RF system of SSC is limited to 20 MHz, very heavy elements, such as Pb, U, can not be accelerated using the same frequency with the linac. In this case, not all the beam bunch from the linac is accelerated by the phase mismatch as shown in Fig. 4 (a). This can be avoided if the time interval between the beam bunches is transformed to the phase interval of accelerating frequency of SSC as shown in Fig. 4 (b). For this purpose, a burst phase shifter which consists of two beam bunchers is being investigated. Extensive computation of transfer and injection system are in progress.
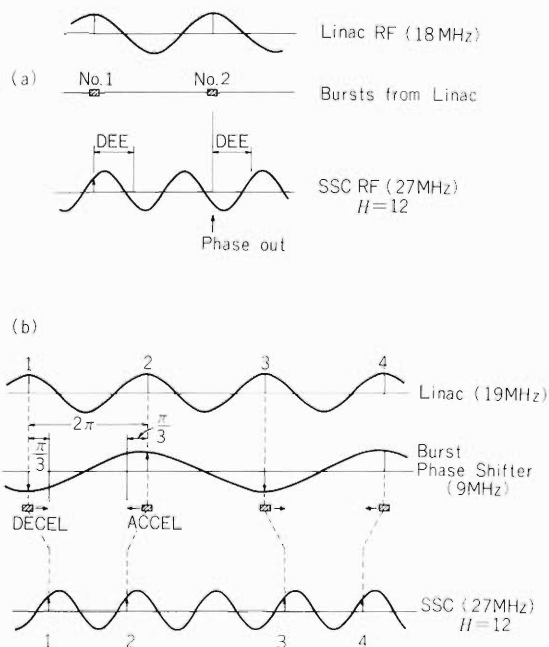


Fig. 4. Operational scheme of the proposed burst phase shifter.

References

1)   H. Kamitsubo et al.: IPCR Internal Report SSC-1; Presented at 2nd Symposium on Accelerator Science and Technology, at INS Tokyo, Tokyo, March (1978).
2)   M. Odera: Proc. Proton Linear Accelerator Conference, Chalk River, p. 62 (1976).
3)   K. L. Brown and S. K. Howry: SLAC Report, No. 91, Stanford (1974).

### 3-5. Design of RF Resonators and RF Characteristics of a Half-scale Model Cavity for Proposed Separated Sector Cyclotron

H. Nakajima, K. Ogiwara, F. Yoshida, and J. Fujita

1. Design of RF resonators

We designed the RF resonators according to the following conditions:

(1) 22.5° delta-shaped two dees locate at opposite valley spaces between the sector magnets.

(2) The RF frequency range is 17–45 MHz.

(3) The minimum clearance of acceleration gap is 10 cm.

(4) The power loss in cavity is as little as possible.

(5) The current density at the short end is less than or equal to 40 peak A/cm.

(6) The characteristic impedance of the coaxial part of the half-wave resonator is greater than or equal to 30 Ω.

(7) The stem is as short as possible when used for the low frequency and is as long as possible when used for the high frequency.

Regarding the cavity as a series combination of distributed constant circuits, we calculated characteristics of cavities of various shapes. The result is shown in Fig. 1, which approximately meets above conditions.
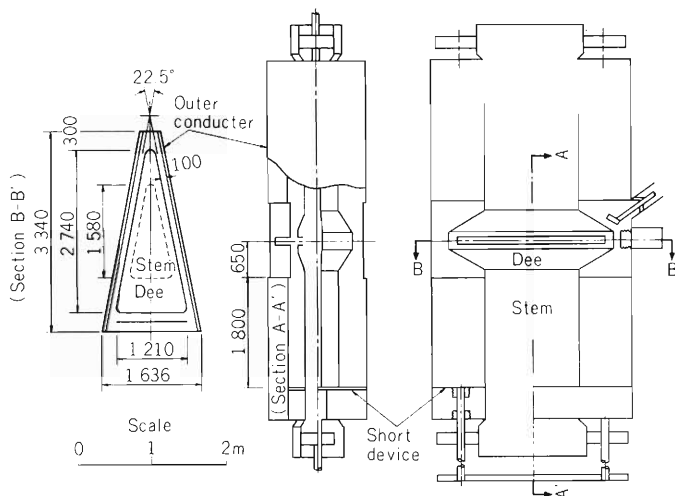


Fig. 1. Cross-sectional top and side view of the proposed resonator for the Separated Sector Cyclotron, giving the main dimensions.

2. A half-scale model cavity

A half-scale model cavity was constructed to investigate the radio-frequency characteristics. Figure 2 shows this model cavity. Figure 3 shows the Q values and position of shorting panel as function of the resonant frequency. Resonant frequency is satisfactorily compared with the calculated one. The Q values obtained were about 10000 in all frequency range. Relatively poor agreement between the measured and calculated Q values is probably due to dirty surface and

Fig. 2. Photograph of a half-scale model cavity.
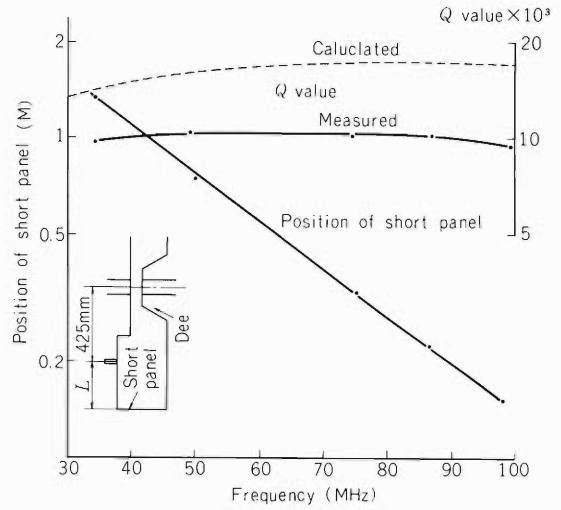


Fig. 3. Q value and position of shorting panel.
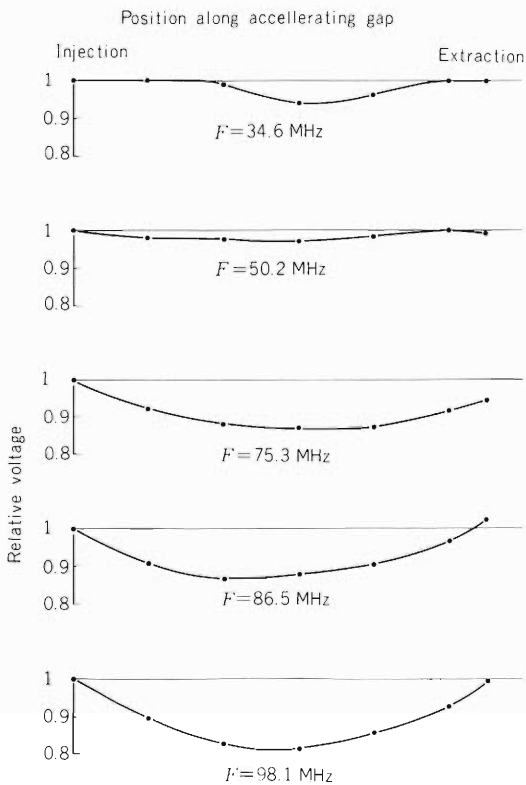


Fig. 4. Relative distribution of electrical field intensity along the dee edge of the half-scale model cavity obtained by the perturbation method.

poor contact at the shorting end of the model cavity. Figure 4 shows relative voltage distribution along the accelerating gap at the half-scale model cavity measured by the perturbation method. The distribution which was normalized at injection radius showed about 20 % decrease at the intermediate radius at maximum frequency.

## 3-6. Computer Code for the Equilibrium Orbit in a Separated Sector Cyclotron

N. Nakanishi and S. Motonaga

A 1/4-scale model magnet system was constructed for basic studies on a separated-sector cyclotron (SSC), and the magnetic field distribution in the median plane have been measured both in radial and azimuthal directions at different excitation conditions.[1] This has been done in order to calculate various beam dynamical properties in the cyclotron using the field shape measured, and to deduce basic parameters which will allow design of the full scale magnet system. For this purpose, a computer code has been developed for the calculation of some properties of the equilibrium orbit.

Output voltage from a Hall probe is amplified and digitized to be stored in an online computer OKITAC 4500, and is transferred to a magnetic tape. The subsequent treatments are made with a computer FACOM 230-75.

The measured data, which are the digital voltmeter readings (mV unit), are converted to magnetic induction values (Gauss unit) using a polynomial expression which reproduces calibration data, and Fourier analysis is done. Fourier coefficients obtained are stored in a disk. Since the SSC is of a 4-sector type and the angular range measured is 45 degrees, the following expression is used:

$$B(r, \theta) = 2\overline{B(r)} + \sum_k a_{4k} \cos(4k\theta),$$

where $\overline{B(r)}$ is the azimuthally averaged magnetic field at radius r. The maximum k is determined to satisfy the least square condition

$$\sum_i \{B_a(\theta_i) - B(\theta_i)\}^2 \approx \text{minimum},$$

where $B$ and $B_a$ are, respectively, measured value and abridged one, the latter being truncated at the index 4k. Points including accidental errors are difficult to be reproduced by the analysis. Therefore the data points which show disagreement larger than a certain amount between observed and calculated values are able to replaced by the calculated values by specifying the limit.

Generally, the number of measured data is much less than that required for exact integration. Moreover, measured data will contain experimental error and show a certain fluctuation. The Fourier analysis of data a priori has effect of giving the averaged tendency of the measured values azimuthally. Interpolation and extrapolation in the radial direction are made for the Fourier coefficients using the Lagrange six-point method. In integrating differential equations, interpolation is done further using the previously calculated field.

Since the measured magnetic field is not of isochronous profile, it is necessary that the isochronous field is formed in advance of the calculation of the equilibrium orbit. The fractional change $\sigma = \Delta L / 2\pi r_0$ in the length of the equilibrium orbit from that of the equilibrium circle is

given by [2)]

$$\sigma(r_0) = -\frac{1}{4(1+\mu')} \sum_k \frac{1}{(4k)^2-(1+\mu')} \left\{ \frac{(4k)^2(2-\mu')+\mu''-2}{(4k)^2-(1+\mu')} a_{4k}^2 +2a_{4k}a_{4k}' \right\},$$

where $\mu$ and $a_{4k}$ are the magnetic field strength and Fourier coefficient respectively, and primes

denote $\frac{r_0}{B} \frac{d}{dr} \Big]_{r=r_0}$ and $\frac{r_0^2}{B} \frac{d^2}{dr^2} \Big]_{r=r_0}$. Thus the isochronous field $B_s(r)$ is [3)]

$$B_s(r) = \frac{1+\sigma(r)}{\sqrt{1-r^2\{1+\sigma(r)\}^2}} \quad .$$

The calculation of the equilibrium orbit is repeated changing the initial condition until we get

$$|r(0°)-r(90°)| + |P_r(0°)-P_r(90°)| < \varepsilon,$$

in which r and $P_r$ are the radius and the radial component of momentum respectively, and $\varepsilon$ is a given small value. Thirteen differential equations, which specify the beam motion in the field, are integrated through one sector by the Runge-Kutta-Gill method, after the equilibrium orbit is found.[4)] However, these equilibrium orbits have been found not to satisfy the condition of isochronism. Therefore above calculations are iterated until both the conditions of the equilibrium
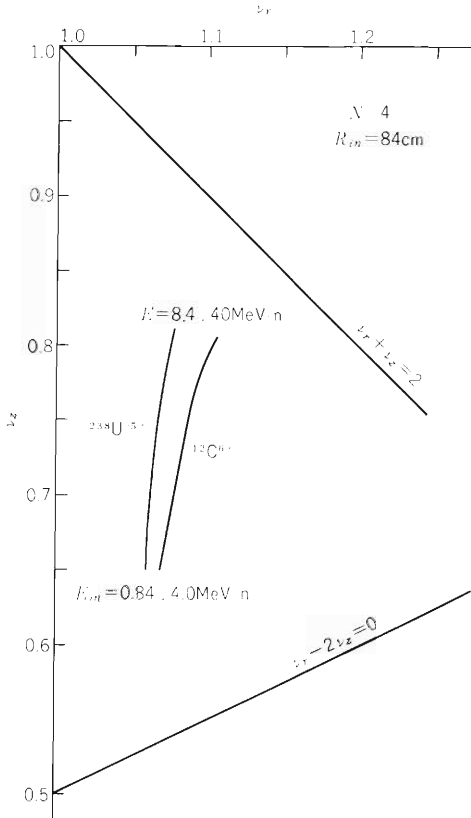


Fig. 1.   Focusing frequencies calculated for $^{12}C^{6+}$ and $^{238}U^{37+}$. These nuclei are assumed to be injected at the radius of 84 cm with energies of 4.0 and 0.84 MeV/n, respectively.
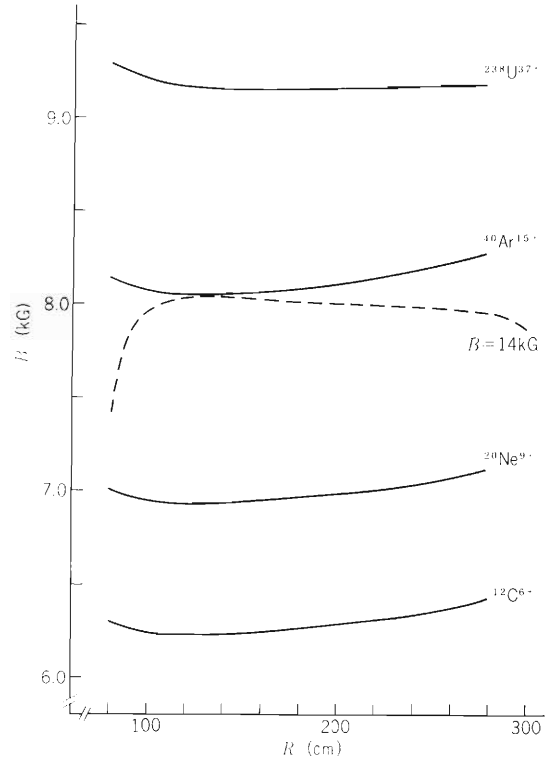
Fig. 2.   Isochronous fields averaged azimuthally. The broken line shows the averaged field which has been measured at 14 kG.

orbit and isochronism are fulfilled simultaneously.

Energy E, betatron frequencies $\nu_r$, $\nu_z$, mean radius $<r>$, amplitude of the beam, period and so on are printed out. The isochronous field, also, is written down.

The innermost orbit in the SSC is restricted in its parameter value because it has to fulfill the matching condition determined by the injector linac. The condition is that the length of the innermost orbit should be the integral multiple of the length of the last drift tube section. This condition, however, is not taken in the calculation because of the lack of data in the inner region. Result of preliminary calculation on the behavior of focusing frequency is shown in Fig. 1 for two nuclei. The calculation was done using the field shape measured at 14 kG. The radial range of the magnet is limited by the data which is available at present. Figure 2 shows a comparison between measured and isochronous fields which are averaged azimuthally.

Work is now in progress to check the accuracy of the calculation and to proceed further in the calculation using the data expanded in the radial direction.

References

1) N. Kumagai, S. Motonaga, H. Kamitsubo, T. Wada, F. Yoshida, K. Ogiwara, N. Nakanishi, I. Yokoyama, and H. Takebe: IPCR Cyclotron Progr. Rep., 12, 10 (1978).
2) L. Smith and A. A. Garren: UCRL-8598.
3) A. A. Garren: Nucl. Inst. and Meth., 18·19, 309 (1962).
4) M. M. Gordon, T. A. Welton, T. I. Arnette, and H. C. Owens: ORNL 59-11-2.

## 3-7. Measurement of the Turn-Separation, the Effective Acceleration Voltage and the Focusing Frequency $\nu_z$ of the Ion Beams in the Cyclotron

H. Takebe, K. Ogiwara, and I. Kohno

In order to study the motion of various ions in the cyclotron, a four-finger beam probe (Fig. 1), which has three differential electrodes and an integrating electrode, was installed to the cyclotron.[1,2]   Radial distribution of the beam intensity measured by these electrodes is shown in Fig. 2.   As shown in Fig. 3, the turn-separation, $\Delta r$, the voltage gain per turn, $4V_p\cos\theta$, and the phase of the ion with respect to the RF, $\theta$, are deduced from these data by following equations:

$$\Delta E = 4qV_p \cdot \cos\theta = \frac{E_R}{R^2} 2r \cdot \Delta r ,$$

where $\Delta E$ is the energy gain per turn, R the extraction radius, $E_R$ the maximum energy, q the charge of the ion and r the radius of the ion orbit.   $V_p$ is estimated from the maximum value of $4V_p\cos\theta$ obtained when $\theta = 0$, and is plotted in Fig. 4, against the nominal dee-voltage, $V_d$, at the control desk.   This $V_d$ was calibrated by the dividing condenser method in 1977.   The estimated points are well on a straight line given by $V_p = \sqrt{2}\,V_d$.

The difference in the current between the upper and the lower electrodes is shown in Fig. 5, in which turn-number, t, of the beam in half period of the betatron oscillation in the z-direction is also indicated.   This t gives the n-value by $2t = \omega_0/\omega_z = \nu^{-1} = n^{-1/2}$,   Further, n can be written as $n = n_1 + n_2 + n_3$, where $n_1$ is the focusing index of the main magnet, $n_2$ is a term originating from phase change of the accelerating voltage and $n_3$ is a term which comes from velocity change while the ions cross the dee gap.   In Fig. 6, n-values are plotted and compared with $n_1$ derived
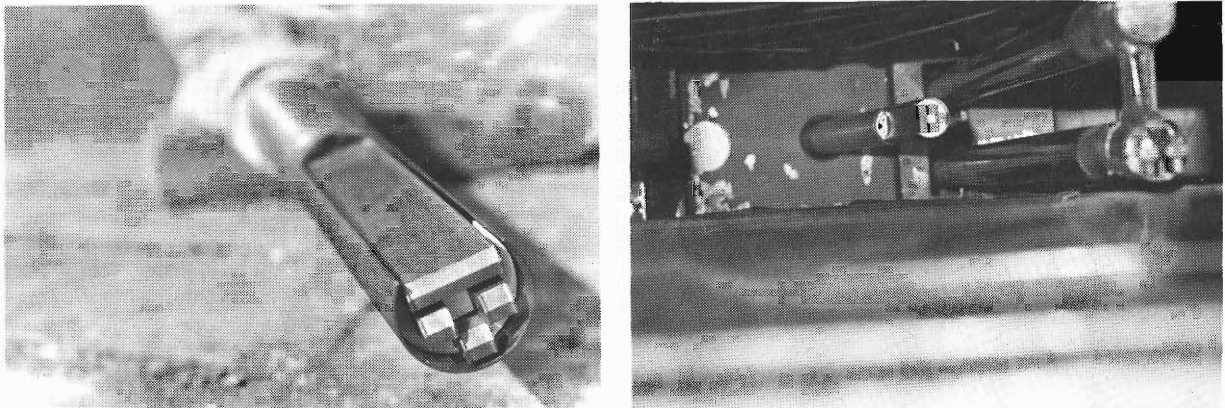


Fig. 1.   Photographs of the four-finger beam probe head (left figure) and the probe inserted in the port of the acceleration chamber besides the heavy ion source.
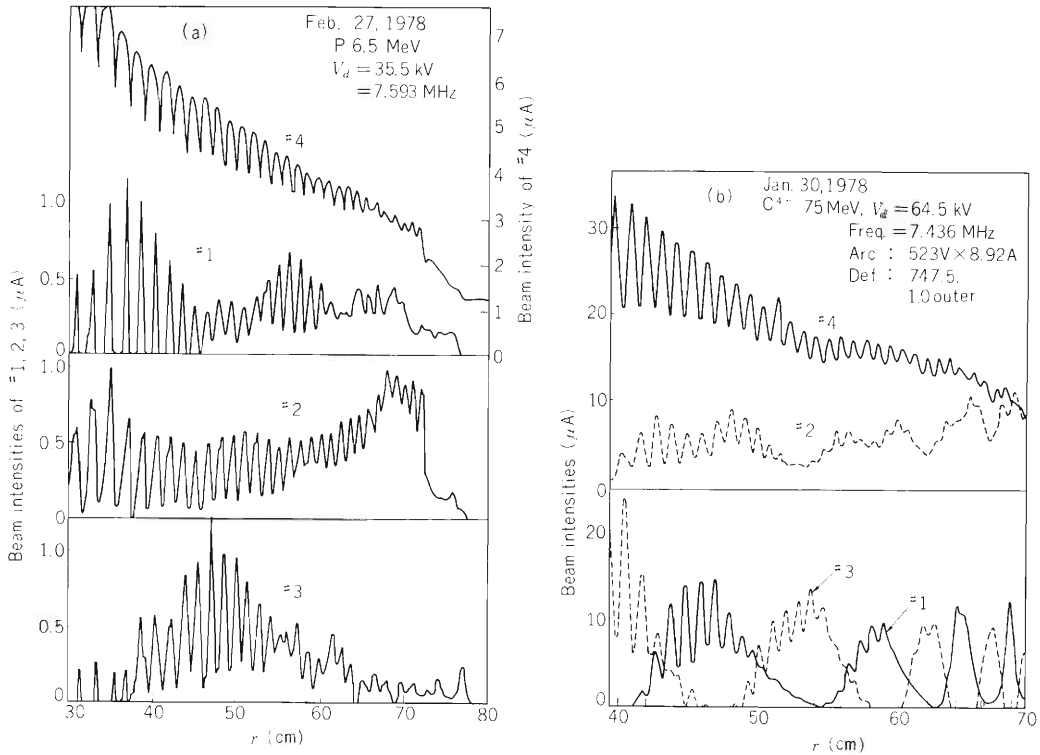
Fig. 2. Beam intensity distributions: 6.5 MeV protons, and 75 MeV $C^{4+}$. #1, #2, and #3 correspond to the beam intensities of upper, middle and lower electrodes respectively.
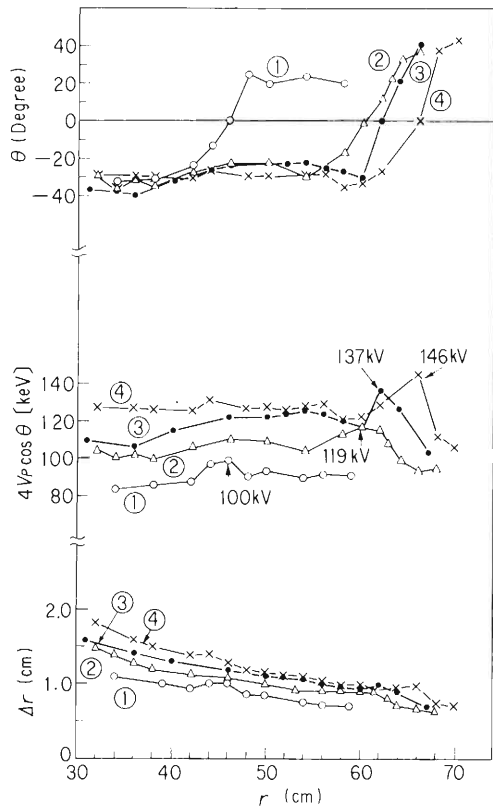


Fig. 3. $\Delta r$, $4V_p \cos\theta$ and $\theta$ distributions along the radial direction at following acceleration voltages $V_d$: (1) 17.1 kV, (2) 20.2 kV, (3) 22.3 kV, (4) 24.0 kV.
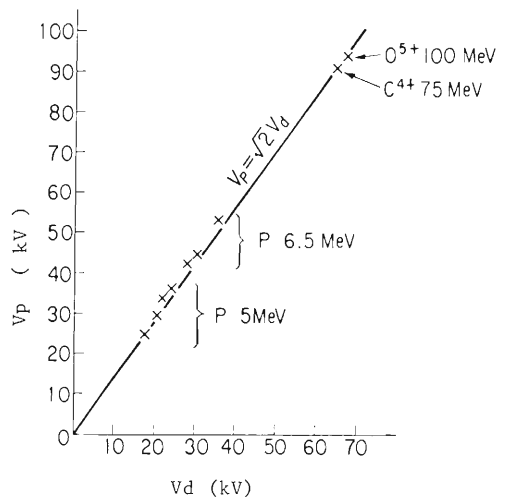
Fig. 4. The calculated peak voltage (X) against the dee-voltage indicated at the control desk.
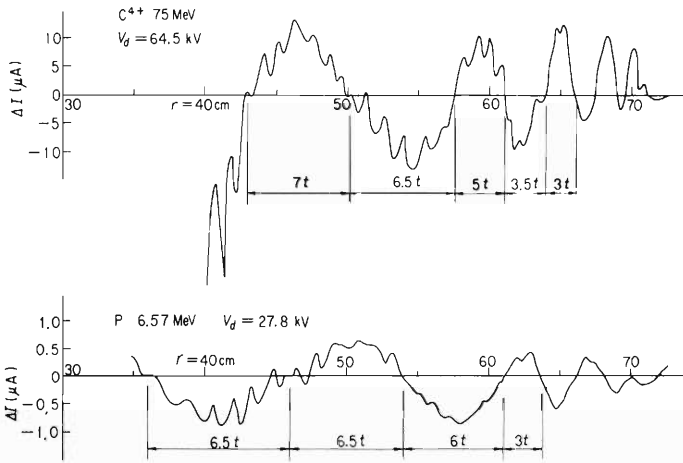
Fig. 5. Vertical oscillation of the beam given by $\Delta I = I_{upper} - I_{lower}$ along the radial direction and the turn-number in half period of the betatron oscillation in z-direction.
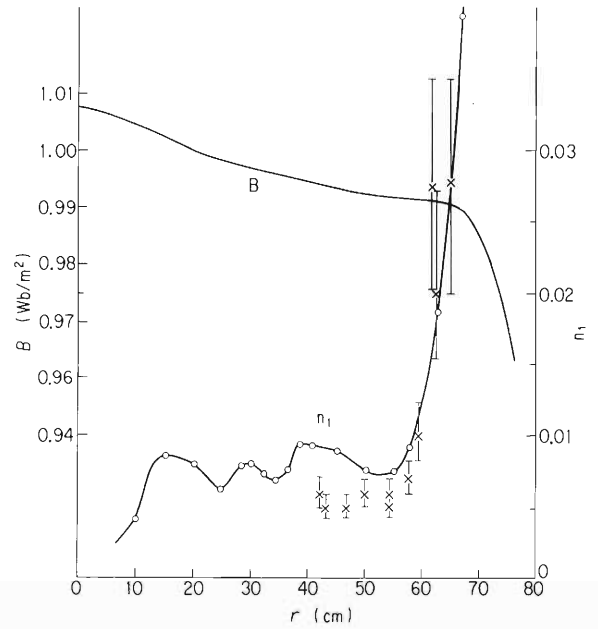
Fig. 6. The n-value (X) calculated from the experimentally obtained $\nu_z$, radial distributions of the main magnet B and the focusing index $n_1$ derived from the B distribution.

from the radial distribution of the magnetic field B of the cyclotron measured in 1966.[3] These measurements give good evidence that behavior of the beam in our cyclotron is in good agreement with the theory of the weak focusing cyclotron, by which the machine was designed.

References

1) K. Ogiwara and H. Takebe: IPCR Cyclotron Progr. Rep., 11, 4 (1977).
2) H. Takebe, K. Ogiwara, and I. Kohno: Reports I.P.C.R., (in Japanese), 54, 77 (1978).
3) S. Motonaga: Private communication.

## 3-8. Acceleration of Lithium Ion in the Cyclotron

K. Ikegami and I. Kohno

For the production of $Li^{2+}$ or $Li^{3+}$ ions we prepared two kinds of hot cathode PIG sources: one has a sputtering electrode and the other a sputtering anode. We accelerated $Li^{2+}$ and $Li^{3+}$ in the cyclotron using the source which has a sputtering anode. $Li^{2+}$ and $Li^{3+}$ ions are produced in this source by a process that involves ions which are unable to cross the first acceleration gap between the ion source and the dee. These ions are accelerated back into the ion source where they sputter Li atoms into the arc. The Li atom is ionized and extracted from the source. Figure 1 is a photograph of the source having a sputtering anode. A rectangular block of LiF of dimension $8 \times 8.5 \times 16$ mm$^3$ is installed in the anode chamber facing the slit. Figure 2 shows the m/q spectrum measured with a beam probe fixed at the radius of 55 cm in the cyclotron by varying the magnetic field strength under the conditions of constant oscillator frequency and dee voltage when the source was operated at arc voltage of 350 V and current of 5.5 A using Xe as the supporting gas. This spectrum shows clearly that $^6Li^{2+}$, $^7Li^{2+}$, $^6Li^{3+}$, and $^7Li^{3+}$ ions were produced and accelerated. The intensity of $^7Li^{2+}$ ion extracted from the cyclotron was 0.3 e$\mu$A. The ion source was operated stably for about 6 h.

In order to increase the intensity of Li ion beam, we are preparing another sputtering ion source. Figures 3 and 4 show a cross sectional view and a photograph of this ion source. This ion source is of a hot cathode PIG type source and has a sputtering electrode inserted into the
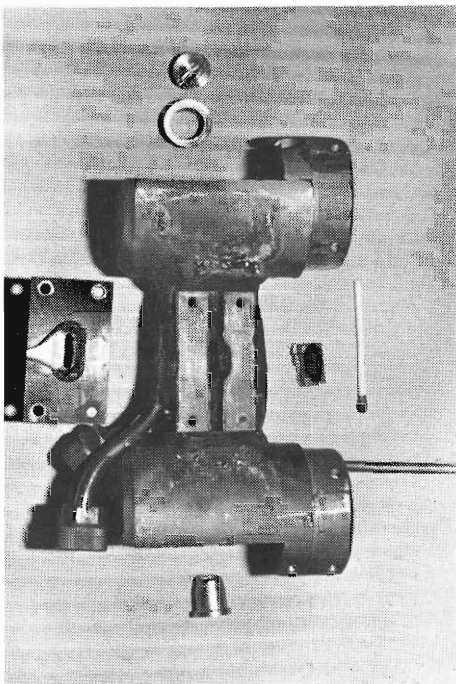


Fig. 1. A photograph of the beam sputtering source.
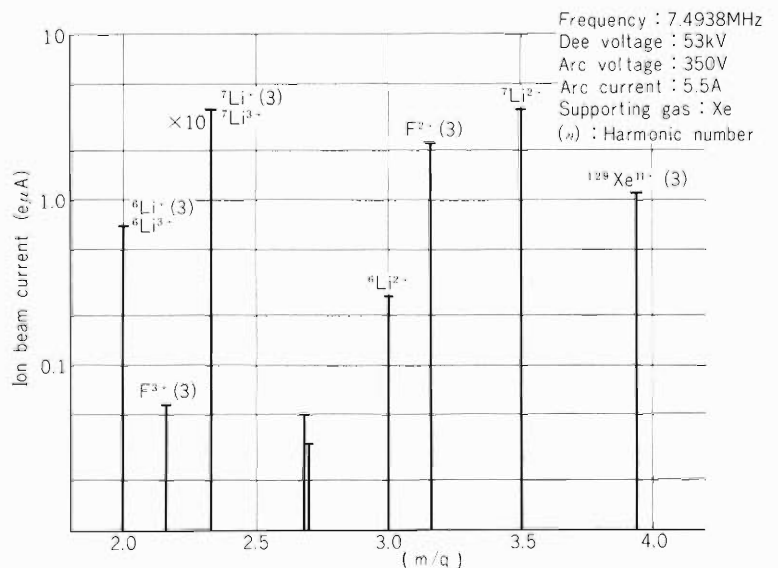


Fig. 2. The m/q spectrum measured in the cyclotron at the radius of 55 cm.

0      50mm
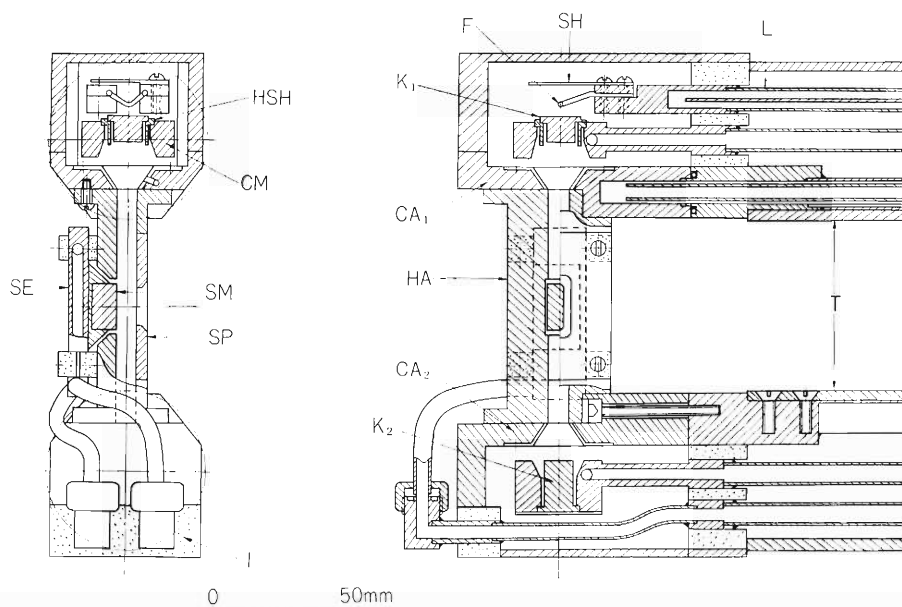
Fig. 3.   Cross-sectional view of the ion source with a sputtering electrode.

$K_1$   : hot cathode (W)

$K_2$   : reflector cathode (W)

CM   : cathode mount (copper, water-cooled)

HSH : cathode heat shield (W)

SH   : electron shield

F    : filament (W)

SP   : slit plate (Mo)

SM   : charge material to be sputtered

SE   : charge material mount (copper, water-cooled)

I    : insulator (ceramic)

L    : leading tube

$CA_1$ : upper cold anode (copper, water cooled)

$CA_2$ : lower cold anode (copper, water cooled)

HA   : hot anode (stainless steel)

T    : supporting tube (stainless steel)
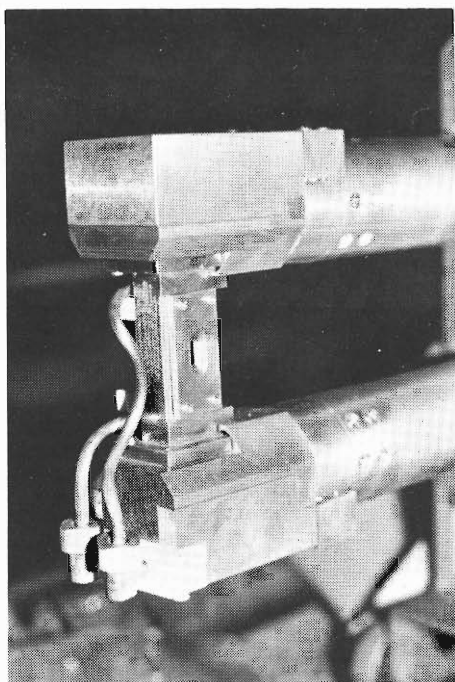


Fig. 4.   A photograph of the ion source with sputtering electrode.

anode chamber at the opposite position of the slit and insulated from the anode.   A voltage of 500 − 1000 V is applied between the sputtering electrode and the anode, and the electrode material is sputtered by bombardment with the ions in the arc plasma.   We intend to try the acceleration of Li ions in the cyclotron using this source in the future.

Reference

1)   Y. Miyazawa, I. Kohno, T. Inoue, T. Tonuma, A. Shimamura, and S. Nakajima:   IPCR Cyclotron Technical Report, No. 2 (1972).

3-9. Beam Study on the Baby Cyclotron

T. Karasawa

(1) Phase history of deuterons

The phases of deuterons accelerated in the 4th harmonic mode with two 45 degree dees have been determined by the same method described in a previous paper.[1]   The phase, $\theta$, crossing the acceleration gap at the radius r, is given by the following equation,

$$\sin\theta - \sin\theta_0 = \frac{2\pi E}{V_0}\left[\frac{\omega e/4 - \omega_0}{\omega_0} + \frac{1}{r^2}\int_0^r \frac{B_0 - B(r)}{B_0}d(r^2) + \frac{E}{m_0 c^2}\right].$$

Here, notations are the same as those in Ref. 1.

We measured the beam intensities and calculated the phase of deuterons as a function of the radius r for various magnetic field distributions in the central region of the magnet, (r = 0 $\sim$ 80mm). Two experimental results are shown in Fig. 1 and Fig. 2.   In the case of Fig. 1, the relative magnetic field at the center of the magnet, B(r = 0 mm) / B(r = 150 mm), is 2.6 % higher than that in the case of Fig. 2.   It is known that in the case of Fig. 1, the phase itself and the width of variation of the phase as the function of r are suitable for large energy gain per turn, except for near the maximum radius, and therefore higher relative magnetic field distribution near the center of the magnet is necessary for actual operation.
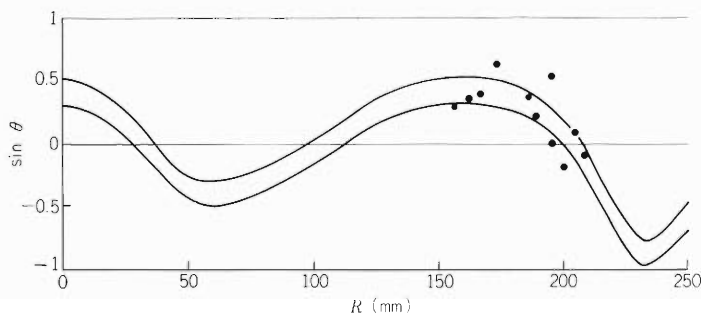


Fig. 1.   Phase history of 4.7 MeV deuterons in case of high magnetic field near the center. The full circles are deduced from the beam intensity vs the radius.
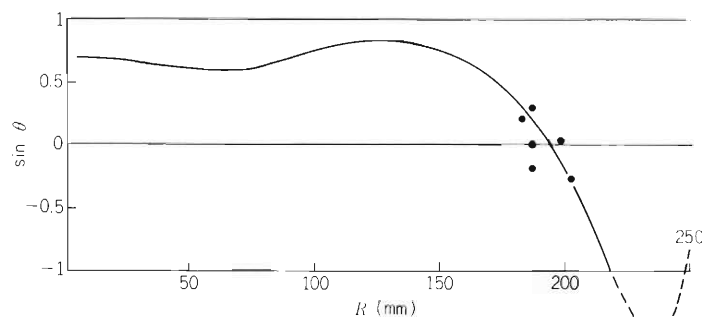


Fig. 2.   Phase history of 4.7 MeV deuterons in case of low magnetic field near the center.

(2)  Displacement of the center of the ion orbit

In the high harmonic mode acceleration, displacement of the center of the ion orbit from the magnetic center is induced by asymmetries of both the magnetic field and the electric accelerating field.   Even though the geometrical configuration of the accelerating electrodes is symmetrical, asymmetry of the accelerating field is generated by the phase difference of the ion arriving at the accelerating gaps.   We express the displacement of the center by polar coordinates, $(\rho, \varphi)$, and variation of $\rho$ and $\varphi$ per revolution by $\Delta\rho$ and $\Delta\varphi$, respectively.   For the displacement caused by the asymmetry of the electric acceleration field in addition to the magnetic field, the following equations hold for the fourth harmonic mode acceleration,

$$\Delta\rho = 2\sqrt{2} \; V/E \; \rho \; \sin\theta \; \sin 2\varphi + \pi r \, c_1 \sin(\varphi - \psi_1)$$

$$\Delta\varphi = -4V/E \sin\theta \; (1 - 1/\sqrt{2} \cos 2\varphi) + \pi r/\rho \; c_1 \cos(\varphi - \psi_1) + 2\pi (\nu r - 1) \; .$$

Here, notations are the same as those in Ref. 1.

It is known from the equation that the smaller the value of $\sin\theta$ is, the smaller the displacement is.   As described in section (1), reduction of the value of $\sin\theta$ can be achieved by the high relative magnetic field near the center of the magnet.   In order to reduce the displacement of the center of the ion orbit further, we are now preparing to install two pairs of harmonic coils at proper positions on the pole faces of the magnet.

The harmonic coils will generate the first harmonics of the magnetic field at arbitrary azimuth. The first harmonics generated by the coils can reduce the displacement caused by the asymmetries of both the electric acceleration field and the magnetic field.

Reference

1)    T. Karasawa: IPCR Cyclotron Progr. Rep., 11, 15 (1977).

# 4. NUCLEAR PHYSICS

## Scattering and Reactions

### 4-1. Spin Flip Asymmetry in the Inelastic Scattering of Protons on $^{12}$C at 28 MeV

T. Fujisawa, M. Nakamura,* M. Yasue,** N. Ueda,** T. Hasegawa,**
H. Kamitsubo, K. Hatanaka,* T. Tanaka,*** M. Sekiguchi,**
T. Wada, Y. Toba,**** and F. Soga**

We have measured the difference between the analyzing power and the polarization (A-P) in order to investigate the spin dependence of the effective two-nucleon interaction and the reaction mechanism.[1]-[4] Direct measurement of the polarization, however, is very difficult because it requires a double scattering. So the (A-P) was deduced by measuring the spin-flip probability of polarized protons.[5]

The spin flip probability was measured by the (p, p'$\gamma$) method, i.e., by measuring the angular correlation between protons scattered inelastically from the $2^+$ excited state and the E2($2^+$→$0^+$ ground) de-excitation $\gamma$-rays emitted perpendicularly to the scattering plane.[6],[7]

If the z-axis is chosen along the normal to the scattering plane the inelastic observables for a proton are expressed as follows:

$$\sigma_0 = (\sigma_{++} + \sigma_{+-} + \sigma_{-+} + \sigma_{--})/2, \qquad A = (\sigma_{++} + \sigma_{+-} - \sigma_{-+} - \sigma_{--})/2\sigma_0,$$

$$P = (\sigma_{++} - \sigma_{+-} + \sigma_{-+} - \sigma_{--})/2\sigma_0, \qquad SF = (\sigma_{+-} + \sigma_{-+})/2\sigma_0,$$

$$SFA = (\sigma_{+-} - \sigma_{-+})/(\sigma_{+-} + \sigma_{-+}) = (A-P)/(2 \cdot SF),$$

where $\sigma_{+-}$ is the partial differential cross section for scattering from an incoming spin-up state (+) to a final spin-down state (−). In the experiment with proton counters at symmetric angles relative to the beam direction we obtained the $\sigma_0$, A, SF, and SFA simultaneously.

The scattered protons were detected by four pairs of SSDs. The fixed pair at 62.5° was used simultaneously as a monitor of the beam polarization.[8] Asymmetries caused by the detector system were compensated by flipping the beam polarization about every one minute.

Figure 1 shows the differential cross section and the analyzing power of the elastic scattering. The curves
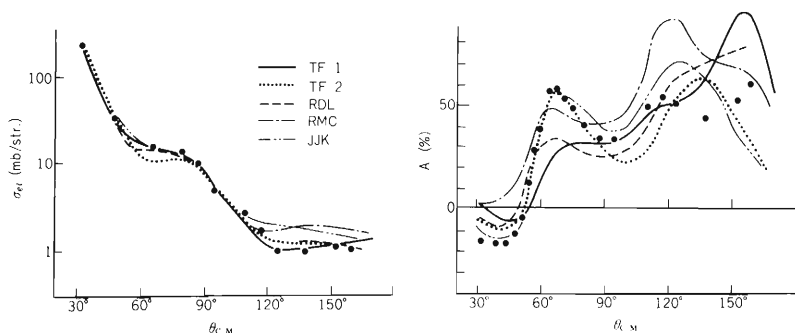


Fig. 1. The differential cross section and the analyzing power of the elastic scattering of protons from $^{12}$C at 28 MeV. The optical parameters used for the calculation are in Table 1.

* Department of Physics, Kyoto University.

** Institute of Nuclear Study, University of Tokyo.

*** Department of Engineering, Kyushu University.

**** Department of Physics, Tsukuba University.

show the results of the optical model calculations. The sets of the optical parameters are listed in Table 1. The sets TF-1, and 2 were obtained by $\chi^2$-fitting for A and $\sigma_0$ of the elastic scattering with SEARCH code developed by Wada.[9] All of the sets give good fits to the cross section but the predicted analyzing power is different from each other.

Table 1. The optical parameters.

| Potential name | $V_0$ (MeV) | $r_0$ (fm) | $a_0$ (fm) | $W_D$ (MeV) | $W_1$ (MeV) | $r_D$ (fm) | $a_D$ (fm) | $V_{SO}$ (MeV) | $r_{SO}$ (fm) | $a_{SO}$ (fm) |
|---|---|---|---|---|---|---|---|---|---|---|
| TF-1 | 60.9 | 1. | 0.665 | 8.26 | 0. | 0.954 | 0.578 | 6.38 | 1. | 0.697 |
| TF-2 | 50. | 1.08 | 0.593 | 6. | 0. | 1.214 | 0.51 | 6. | 1.09 | 0.388 |
| RDL[10] | 61.2 | 1.0 | 0.65 | 6.24 | 0. | 1.055 | 0.68 | 6.01 | 1.05 | 0.51 |
| RMC[8] | 37. | 1.25 | 0.65 | 0.6 | 7. | 1.25 | 0.47 | 6. | 1.25 | 0.54 |
| JJK[11] | 48.48 | 1.07 | 0.634 | 3.33 | 0. | 1.34 | 0.682 | 7.34 | 1.01 | 0.485 |

Figure 2 shows the differential cross section and the analyzing power of the inelastic scattering together with the results of the macroscopic DWBA calculation. The code is developed by H. Sherif. The interaction potential is obtained by deforming the optical potential. The deformed spin dependent term is of the full Thomas form or the Oak Ridge form. It was shown that the full Thomas form gave better fits to inelastic asymmetries and spin flip probabilities than the Oak Ridge form.[12],[13] Two forms give similar differential cross sections but different analyzing powers in the present analyses. It seems that the full Thomas form is more suitable for the analyzing power at small angles than the Oak Ridge form. All of the sets of the optical parameters give fairly good fits to the cross section but any set does not give a good fit to the analyzing power. As well-known, the spin-orbit part should have a greater deformation than the central part.[10] The results of DWBA calculations for the different ratios of the deformation parameters ($\beta_{SO}/\beta_0$) are shown in Fig. 2. Dependence of the cross section on the ratios is small so it is not shown.
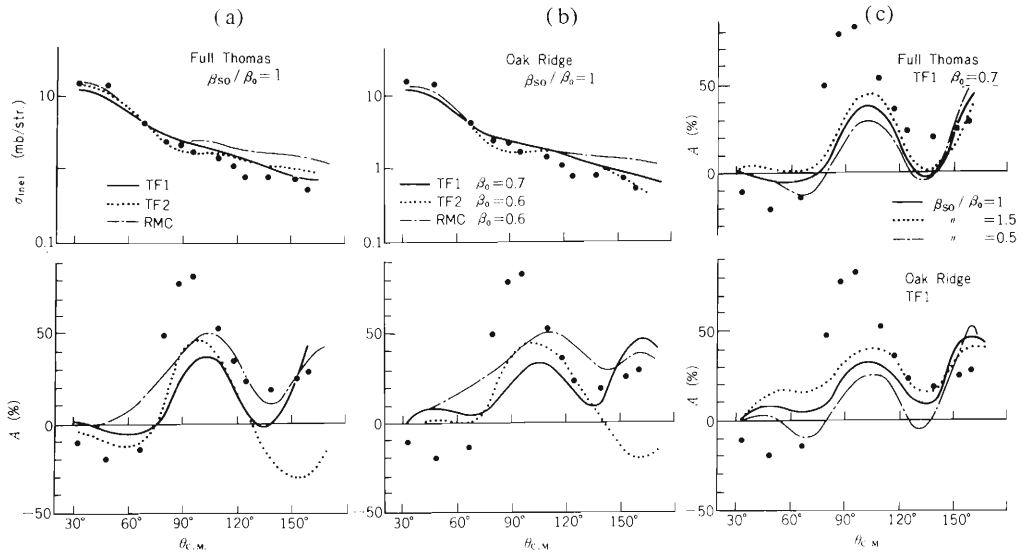


Fig. 2. The differential cross section and the analyzing power of the inelastic scattering of protons from $^{12}C$ at 28 MeV. The curves show the prediction with macroscopic DWBA theory. (a) The full Thomas form deformation.( b) The Oak Ridge form deformation. (c) Changes of the Analyzing power to the ratio $\beta_{SO}/\beta_0$.

Figure 3 shows the SF, SFA, and (A-P). The value of SF have been corrected for non-spin-flip contributions due to the off-z axis-$\gamma$-ray. The solid bar shows the statistical error and the dotted bar indicates the uncertainty caused by the lack of measurements of the other substate populations (m = ±2 and m = 0) and the finite solid angle of the $\gamma$-ray detector. However, we can see the pronounced peak of the SFA at 100°. The curves are the
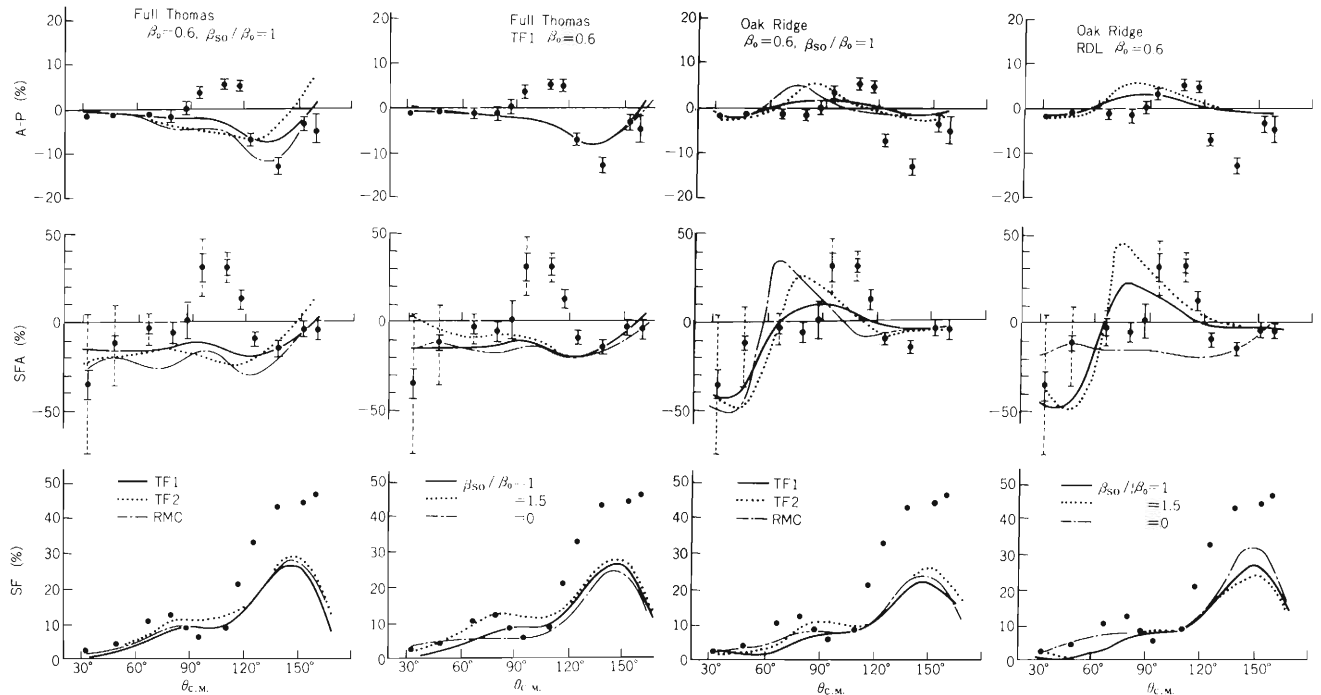
Fig. 3.  The spin-flip probability, the spin-flip asymmetry and the (A-P) in the inelastic scattering
of proton on $^{12}C$ at 28 MeV.  The curves are the calculated values with macroscopic DWBA theory.

value calculated with Sherif's code.  The interaction including the full Thomas form deformation is invariant under
the projectile time reversal operator but one including the Oak Ridge form is not.  Therefore the finite value of
the calculated SFA with the full Thomas form spin-orbit deformation, is due to non-adiabaticity but the SFA
predicted with the Oak Ridge form has a finite value in the adiabatic process ($E_{in} = E_{out}$).  Any parameter set
cannot reproduce the SFA or the (A-P).  It was reported that the large values of the SF around $150°$ are the
effect of the E2 quadrupole giant resonance.[8]  The macroscopic DWBA calculations cannot reproduce such large
SF.  If the effect of the resonance is small for the SFA, the interference between S = 1 and S = 0 components
of the effective two nucleon interaction arises in the reaction or the interaction potential of the macroscopic DWBA
needs some other spin-dependent force which gives an account of the SFA.  The effect of such resonance on the
SFA, however, is not known.  So it is interesting to see the energy dependence of the SFA.

References

1)  G. R. Satchler:  Phys. Lett., 19, 312 (1965).

2)  H. Sherif:  Canadian J. Phys., 49, 983 (1971).

3)  M. Thumm, G. Mertens, H. Lesiecki, G. Mack, and K. Schmidt:  Proc. of the 4th Intern. Symp. on Pol. Phen.
    in Nucl. React., Zurich, p. 799 (1975).

4)  T. Hasegawa et al.:  Proc. Intern. Conf. on Nucl. Phys., München, p. 409 (1973).

5)  R. Boyd, S. Davis, C. Glashauser, and C. F. Haynes:  Phys. Rev. Lett., 27, 1590 (1971);  ibid., 29, 955 (1972).

6)  F. H. Schmidt, Ronald E. Brown, J. B. Gerhart, and W. A. Kolasinski:  Nucl. Phys., 52, 253 (1964).

7)  T. Fujisawa, S. Motonaga, F. Soga, M. Yasue, N. Ueda, T. Hasegawa, M. Nakamura, T. Wada, H. Toba, and
    H. Kamitsubo:  IPCR Cyclotron Progr. Rep., 11, 18 (1977).

8)  R. M. Craig, J. C. Dore, G. W. Greenlees, J. Lowe, and D. L. Watson:  Nucl. Phys., 83, 493 (1966).

9)  T. Wada:  IPCR Cyclotron Progr. Rep., 2, 87 (1968).

10)  R. De Leo, G. D'erasmo, F. Ferrero, A. Pantaleo, and M. Pignanelli:  Nucl. Phys., A254, 159 (1975).

11)  J. J. Kolata and A. Galonsky:  Phys. Rev., 182, 1073 (1969).

12)  G. R. Satchler:  Proc. of the 3rd Intern. Symp. on Pol. Phen. in Nucl. React., Madison, p. 155 (1970).

13)  H. Sherif and J. S. Blair:  Phys. Lett., 26B, 489 (1968).

## 4-2.  The  (p, d)  Reaction  on  p  and  s - d  Shell  Nuclei

T. Noro, K. Hosono,* M. Kondo,* T. Saito,*
S. Nagamachi,* N. Matsuoka,* S. Kato,** K. Okada,**
K. Ogino,*** and Y. Kadota***

Differential cross sections $\sigma$ $(\theta)$ and vector analyzing powers $A_y$ $(\theta)$ have been measured for (p, d) reactions on $^{12}C$, $^{13}C$, $^{24}Mg$, $^{28}Si$, $^{29}Si$, and $^{40}Ca$ using 65 MeV polarized proton beam accerelated by RCNP AVF Cyclotron.   Outgoing deuterons were detected by a pair of counter telescopes positioned at the symmetric angles to the beam axis.   Each telescope consisted of a 500 $\mu$m thick transmission-type Si-detector and a 15 mm thick high-purity Ge-detector cooled by liquid nitrogen.   The overall energy resolution was about 250 keV in FWHM.

The angular distributions of $\sigma$ $(\theta)$ and $A_y$ $(\theta)$ obtained in this experiment are summarized in Fig. 1.   The $A_y$ $(\theta)$ for $p_{3/2}$ and $d_{5/2}$ (j = $\ell$ + 1/2) neutron pick up reactions are very similar to each other.   These $A_y$ $(\theta)$ show a dip at about 30° and increase with angles in wavy pattern.   The $A_y$ $(\theta)$ for $p_{1/2}$ and $d_{3/2}$ (j = $\ell$ − 1/2) neutron pick up reactions are different from these for j = $\ell$ + 1/2.   The DWBA calculations have been carried out with TWOSTP code using FACOM230-75 at IPCR, and the results are also presented in Fig. 1 with the solid line.   For the deuteron channel, the adiabatic deuteron potentials proposed by Johnson and Soper were used and the parameters of these potentials and proton channel optical potentials are listed in Table 1.   In these calculation, qualitatively good fits were obtained for the angular distributions of $\sigma$ $(\theta)$ and $A_y$ $(\theta)$ when the transferred $\ell_j$ are $s_{1/2}$ and $p_{3/2}$, but for the other cases, the fits are not so good.   A more detailed analysis is in progress.

Table 1.   Optical potential sets.

| Channel | $V_0$ | $r_0$ | $a_0$ | $W_v$ | $W_s$ | $r_i$ | $a_i$ | $V_{so}$ | $r_{so}$ | $a_{so}$ | |
|---|---|---|---|---|---|---|---|---|---|---|---|
| p + $^{12}C$ | 25.39 | 1.244 | 0.712 | 2.84 | 2.32 | 1.469 | 0.390 | 6.79 | 1.041 | 0.532 | a) |
| d + $^{12}C$ | 102.0 | 1.15 | 0.62 | 0.0 | 11.6 | 1.15 | 0.62 | 5.0 | 1.15 | 0.62 | Ref. 3 |
| p + $^{24}Mg$ | 40.26 | 1.112 | 0.747 | 8.40 | 2.00 | 1.358 | 0.557 | 6.127 | 1.041 | 0.532 | a) |
| d + $^{24}Mg$ | 89.6 | 1.21 | 0.64 | 0.0 | 16.9 | 1.14 | 0.55 | 5.15 | 0.97 | 0.32 | Ref. 4 |
| p + $^{28}Si$ | 38.63 | 1.116 | 0.739 | 7.18 | 3.46 | 1.288 | 0.507 | 5.79 | 1.021 | 0.587 | a) |
| d + $^{28}Si$ | 91.47 | 1.17 | 0.68 | 2.71 | 10.51 | 1.33 | 0.61 | 6.58 | 0.94 | 0.60 | Ref. 5 |
| p + $^{40}Ca$ | 38.03 | 1.16 | 0.75 | 1.41 | 4.48 | 1.37 | 0.63 | 6.04 | 1.064 | 0.738 | Ref. 6 |
| d + $^{40}Ca$ | 98.98 | 1.152 | 0.718 | 0.0 | 16.45[b] | 1.309 | 1.166 | 6.23 | 1.014 | 0.526 | Ref. 7 |

a)  Present set.

b)  Gauss type.

*  Research Center for Nuclear Physics, Osaka University.

**  Laboratory of Nuclear Studies, Osaka University.

***  Department of Nuclear Engineering, Kyoto University.
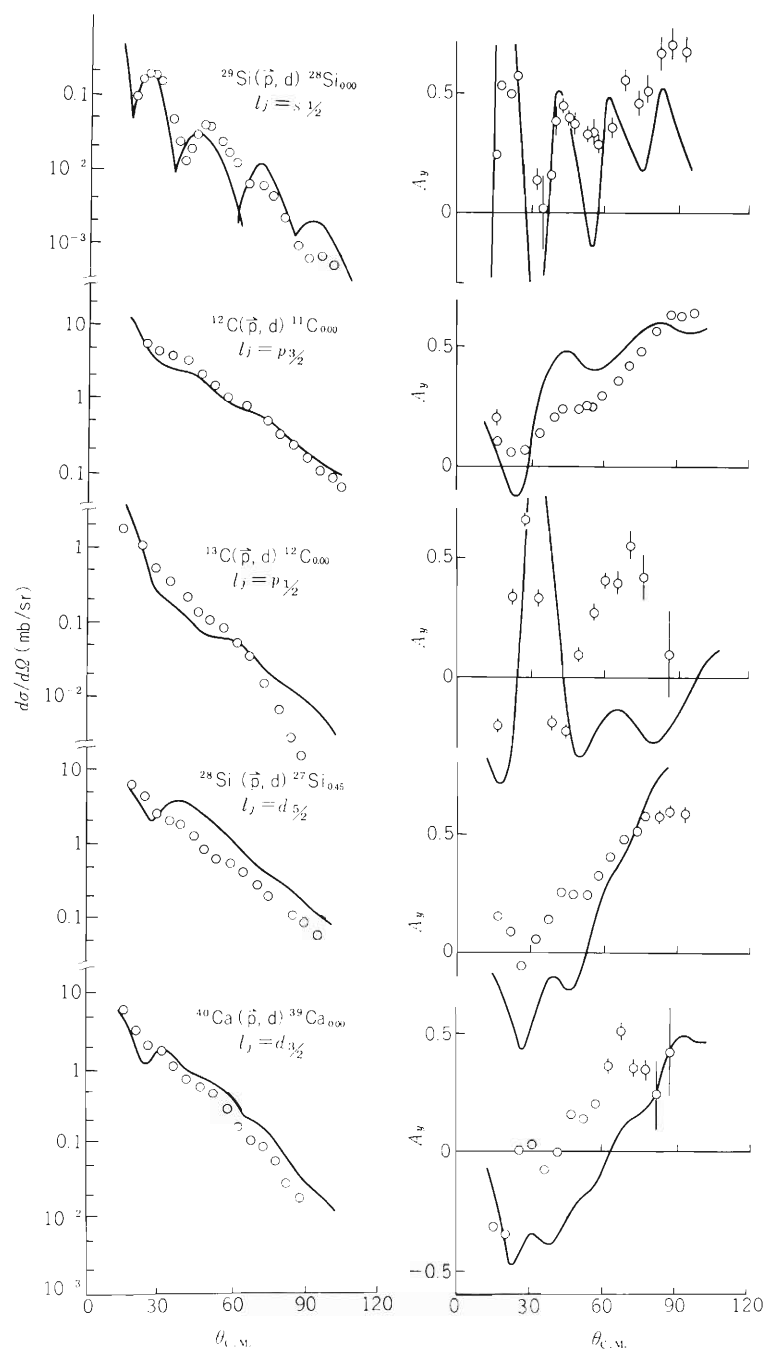
Fig. 1. Differential cross sections and analyzing powers of (p, d) reaction at 65 MeV. The solid lines show the results of DWBA calculations.

References

1) M. Toyama and M. Igarashi: unpublished.

2) R. C. Johnson and P. J. R. Soper: Phys. Rev., C1, 976 (1970).

3) P. G. Roos, et al.: Nucl. Phys., A255, 187 (1975).

4) A. G. Blair, et al.: Phys. Rev., C1, 444 (1970).

5) C. R. Lamontage, et al.: Phys. Lett., 45B, 465 (1973).

6) C. B. Fulmer, et al.: Phys. Rev., 181, 1566 (1969).

7) K. H. Bray, et al.: Nucl. Phys., A167, 57 (1971).

## 4-3. Exact Finite-range DWBA Calculations Including the Deuteron D-state for the $^{58}$Ni(p, d)$^{57}$Ni Reaction at 52 MeV

N. Kishida and H. Ohnuma

At lower energies D-state of the deuteron ground state has small effects on cross sections and on vector analyzing powers, but is very important to describe tensor analyzing powers. At high energy ($\simeq 700$ MeV) the D-state is known to give primary contributions to (p, d) differential cross sections. However, the D-state effects have not been investigated well at intermediate energy region. In this report data from INS for the (p, d) reaction on $^{58}$Ni at 52 MeV[1] are compared with calculations based on the exact finite-range DWBA, in which the D-state is included.

The method of Delic and Robson[2] is used for all exact finite-range calculations (EFR) using the computer code TWOFNR.[3] The n-p interaction, which is used to describe the transfer reaction as well as to generate the deuteron internal wave function, is taken to be the soft core interaction of Reid. Distorting potentials are the set 1P-1D of Ref. 1 and non-locality corrections (NL) are included with $\beta_p = 0.85$ fm and $\beta_p = 0.54$ fm. Form factors are generated by usual separation-energy method.

Results of EFR DWBA calculations are shown in Figs. 1 $-$ 3 together with the experimental angular distributions. Solid and dashed curves are the predictions of EFRNL calculations with and without the D-state contributions, respectively. None of the calculations reproduce the
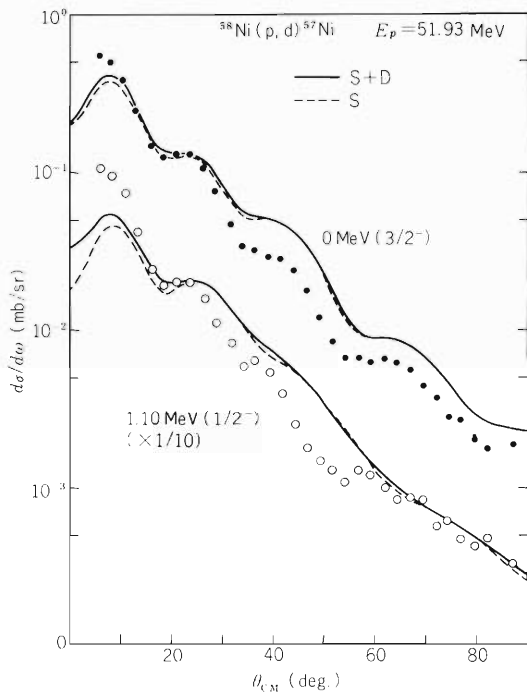


Fig. 1. EFR DWBA calculations with and without the D-state compared with the experimental angular distributions for the ground state (3/2$^-$) and the 1.10 MeV state (1/2$^-$).
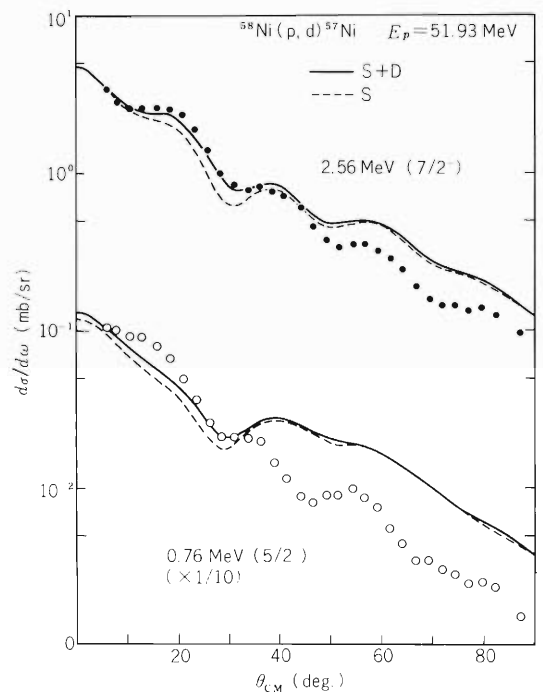
Fig. 2. EFR DWBA calculations for the 2.56 MeV state (7/2$^-$) and for the 0.76 MeV state (5/2$^-$) compared with the experiment.
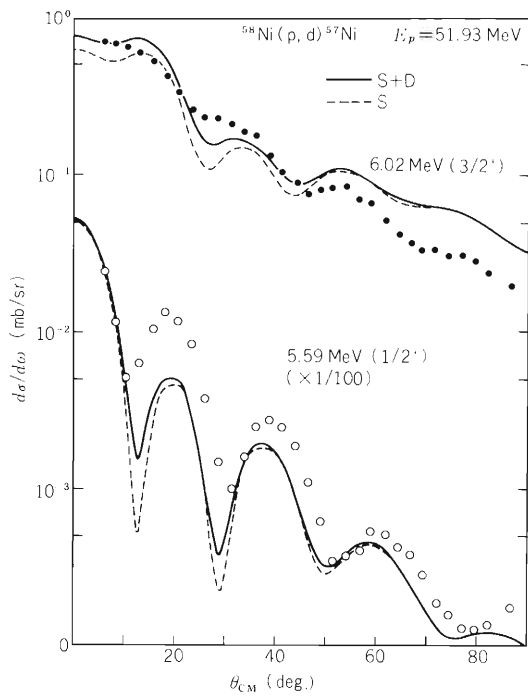
Fig. 3. EFR DWBA calculations for the 6.02 MeV state (3/2⁺) and for the 5.59 MeV state (1/2⁺) compared with the experiment.

experimental angular distributions well. It seems that the inclusion of the D-state slightly improves the quality of fits for most transitions. However, the effects on the differential cross sections are surprisingly small in spite of relatively large momentum transfer in the present (p, d) reaction (See Ref. 4).

References

1) H. Ohnuma, T. Suehiro, M. Sekiguchi, and S. Yamada: J. Phys. Soc. Japan, 36, 1236 (1974); ibid., p. 1245.

2) G. Delic and B. A. Robson: Nucl. Phys., A156, 97 (1970).

3) M. Igarashi: unpublished.

4) E. Rost and J. R. Shepard: Phys. Lett., 59B, 413 (1975).

# 4-4. Analyzing Power of the $(\vec{p}, t)$ Reaction Leading to the Unnatural Parity State

H. Amakawa and K. I. Kubo*

The conventional zero-range DWBA forbids the excitation of the unnatural parity states by (p. t) reactions. A great deal of calculations concerning this type of transitions have been performed with higher-order treatments and considerable successes of reproducing the differential cross sections have been reported. [1], [2] The present authors have also reported successful results of two-step excitation calculation for the $^{18}O(p, t)^{16}O(2^-, 8.88$ MeV) transition. [1], [2] A particular interest is the energy dependence of the differential cross section; it decreases by a factor of about one-thirtieth as the incident energy changes from 20 to 45 MeV. The calculation by the two-step approach has been reported to be able to reproduce this strong energy dependence fairly well as well as the angular distributions of the cross sections. [2]

So far those studies have been performed only for the differential cross sections. Other important experimental informations, e. g., analyzing power and/or polarization were not concerned, which might clarify the reaction mechanism more sensitively. Therefore, we calculate the analyzing power of the $^{18}O(\vec{p}, t)^{16}O(2^-, 8.88$ MeV) transition at 24.4 MeV for testing the two-step approach. The experimental data have been reported by Pignanelli et al. [3] only at this incident energy. We use the same methods as employed in the previous papers. [1], [2] They are summarized as follows. Three types of processes are included: the (p, p', t) process via $^{18}O(2^+)$ state, the (p, t, t') processes via $^{16}O(1^-$ and $3^-)$ states and the (p, d, t) processes via $^{17}O(5/2^+, 1/2^-, 3/2^-,$ and $3/2^+)$ states. The wave functions of $^{18}O$ and $^{16}O$ are taken from Refs. 4 and 5. The values of $D_0^2(p, d)$, $D_0^2(d, t)$, and $D_0^2(p, t)$ used are 1.58, 3.37, and 145 in units of $10^4$ MeV$^2$ fm$^3$, respectively, which are the same as those used in Ref. 2. The parameters of the distorting potentials are listed in Table 1.

Table 1. Distorting potential parameters used in the calculations.

| | V | $r_0$ | a | $W_V$ | $W_D$ | $r_0'$ | a' | $V_{so}$ | $r_{so}$ | $a_{so}$ |
|---|---|---|---|---|---|---|---|---|---|---|
| $^{18}O + p$[6] | 56.0 | 1.17 | 0.75 | 2.667 | 7.03 | 1.32 | 0.588 | 6.2 | 1.01 | 0.75 |
| $^{17}O + d$[3] | 115.6 | 1.07 | 0.717 | − | 9.18 | 1.39 | 0.67 | 5.0 | 1.03 | 0.59 |
| $^{16}O + t$[6] | 146.8 | 1.4 | 0.44 | 12.51 | − | 1.4 | 0.551 | − | 1.4 | 0.44 |

Figure 1 shows the differential cross sections (at the upper portion) and the analyzing powers (at the lower portion). The differential cross section illustrated by the solid line is the same as that reported previously in Ref. 2 obtained by using the standard distorting potential parameters

* Department of Physics, Faculty of Science, Tokyo Metropolitan University.

given in Table 1. The corresponding analyzing power (solid line) gives a good fit to the observed value except for the forward angle region less than $30°$ where the calculated differential cross section has previously been pointed out to deviate from the experimental data.[1], [2] The calculated value decreases with the decrease of the scattering angle from $30°$ but the observed value shows an increasing trend.
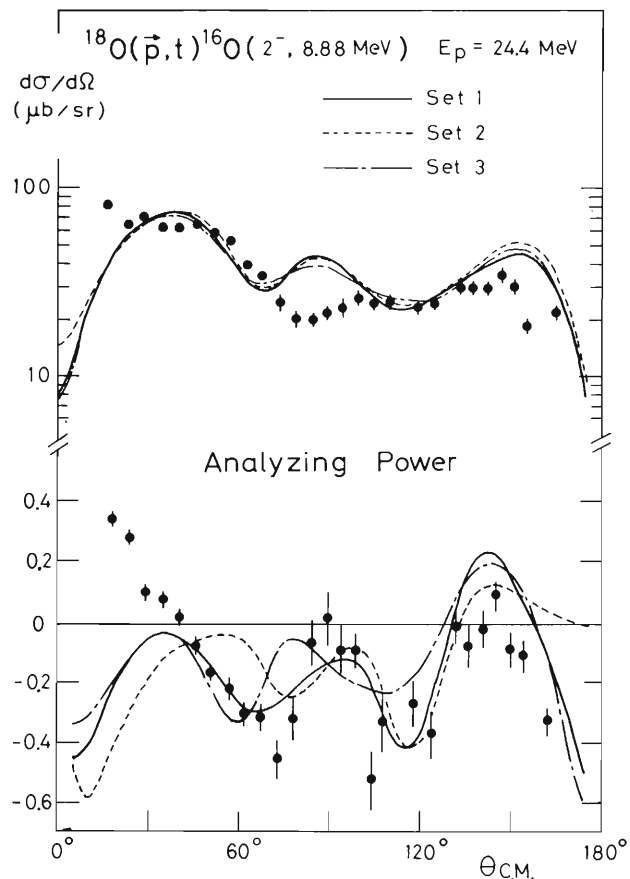


Fig. 1. Angular distributions of the differential cross sections and analyzing powers for the $^{18}O$ ($\vec{p}$, t) $^{16}O$ ($2^-$, 8.88 MeV) reaction at 24.4 MeV. Parameters of the distorting potentials are given in Table 1 and those of the spin-orbit part are listed in Table 2.

Arbitral changes of the distorting potential parameters have been tested. The parameters of the spin-orbit potential tested here are given in Table 2 where set 1 is an original parameter set. The parameters of the central part are fixed to those given in Table 1. The cross sections calculated with set 2 and 3 are illustrated by the dashed and dash-dotted curves, respectively. While the differential cross section is scarcely changed by the change of the spin-orbit potentials, the change of the spin-orbit potentials gives rather large effects on the analyzing power. A gross structure of the analyzing power, however, is preserved. It can be concluded that the analyzing power is determined mainly by the reaction mechanism.

Table 2. Spin-orbit potential parameters.

|       | $V_{so}(p)$ | $V_{so}(d)$ | $V_{so}(t)$ |
|-------|-------------|-------------|-------------|
| Set 1 | 6.2         | 5.0         | 0           |
| Set 2 | 0           | 5.0         | 0           |
| Set 3 | 6.2         | 5.0         | 2.5         |

38

In summary, the observed analyzing power for the $^{18}O(\vec{p}, t)^{16}O(2^-, 8.88\,\text{MeV})$ transition at 24.4 MeV can be reproduced reasonably well by the two-step approach except for the forward angle region. This fact supports the two-step approach to the unnatural parity state transitions. However, Nagarajan and his coworkers have found that this type of transitions can also be well reproduced even by the first-order calculation at one incident energy when the realistic triton wave function is used together with the finite-range interaction.[7] Their calculation casts a doubt on the pure two-step approaches for the unnatural parity state excitations. It is not quite sure that the DWBA amplitude for the present reaction calculated by their method has a comparable magnitude with the two-step amplitude. If it is so, the study for the reaction mechanism must be finalized by performing the coherent sum of such a sophisticated DWBA amplitude and the two-step amplitude.

The numerical calculations of this work were performed using the FACOM 230-75 computer at IPCR.

References

1) H. Segawa, K. I. Kubo, and A. Arima: Phys. Rev. Lett., 35, 357 (1975).

2) K. I. Kubo and H. Amakawa: Phys. Rev., C17, 1271 (1978); other references therein.

3) M. Pignanelli, J. Gosset, F. Resmini, B. Mayer, and J. L. Escudié: ibid., C8, 2120 (1973).

4) T. Inoue, T. Sebe, H. Hagiwara, and A. Arima: Nucl. Phys., 59, 1 (1964).

5) J. P. Elliot and B. H. Flowers: Proc. Roy. Soc., A242, 57 (1957).

6) M. Pignanelli, S. Micheletti, I. Iori, P. Guazzoni, F. G. Resmini, and J. L. Escudié: Phys. Rev., C10, 445 (1974).

7) M. A. Nagarajan, M. R. Strayer, and M. F. Werby: Phys. Lett., 68B, 421 (1977).

# 4-5. Adiabatic Treatment of Elastic Deuteron-Nucleus Scattering

H. Amakawa, S. Yamaji, A. Mori,* and K. Yazaki**

We calculate the contributions of the d-wave and g-wave breakup channels to the elastic deuteron-$^{58}$Ni scattering as well as the s-wave breakup channel in the framework of the three-body model using the adiabatic approximation.[1]   In the three-body model, a deuteron-nucleus scattering system is assumed to consist of a proton, a neutron and an inert target nucleus.   The three-body wave function $\Psi(\vec{r}, \vec{R})$ satisfies the Schrödinger equation

$$( T_R + H_{pn} + V(\vec{r}, \vec{R}) - E)\, \Psi(\vec{r}, \vec{R}) = 0, \tag{1}$$

where $\vec{r}$ and $\vec{R}$ are the relative and the center of mass coordinates of the p-n system with respect to the target, $H_{pn} = T_r + V_{pn}$ is the Hamiltonian of the p-n relative motion, $T_R$ is the kinetic energy operator of the center of mass motion and $V(\vec{r}, \vec{R})$ is given by the sum of the proton-target and the neutron-target potentials evaluated at half of the incident energy of the deuteron.   We neglect the Coulomb breakup, since its effect is expected to be small for high energy deuteron.   The spin-orbit potential is also neglected to simplify the calculation, and this effect will be briefly discussed later.   If the deuteron incident energy is sufficiently high, we can use the adiabatic approximation in which the excitation energy of the p-n relative motion is neglected.   Then, Eqn. (1) becomes

$$( T_R + V(\vec{r}, \vec{R}) + \varepsilon_d - E)\, \Psi(\vec{r}, \vec{R}) = 0, \tag{2}$$

where $H_{pn}$ has been replaced by a constant $\varepsilon_d$, which is the binding energy of the deuteron.   The total wave function $\Psi(\vec{r}, \vec{R})$ is written as

$$\Psi(\vec{r}, \vec{R}) = \sum_{\ell L J} \chi_{\ell L J}(r, R)[Y_\ell(\hat{r}), Y_L(\hat{R})]_J . \tag{3}$$

We solve the coupled equations for $\chi_{\ell L J}$ keeping r and J fixed, and obtain the r-dependent t-matrix $T^J_{\ell' L': \ell L}(r)$. The deuteron wave function contains intrinsic d-state as well as s-state.   In the absence of the spin-orbit potential, however, the additional effects due to the intrinsic d-state contribute only incoherently and are expected to give a minor correction.   We therefore consider the intrinsic s-state only.   Then the elastic t-matrix T which includes the breakup effect in the intermediate stage is given by,[1]

$$T = \int T(r)\,|\phi_d(r)|^2 r^2 dr,$$
$$T(r) = \sum_L (2L+1) T^L_{0L:0L}(r) P_L(\cos\theta), \tag{4}$$

where $\phi_d$ is the deuteron wave function.   The numerical calculation can easily be performed by using the conventional coupled-channel program with slight modification.

We calculate the elastic deuteron scattering from $^{58}$Ni target.   Optical potential parameters of nucleon-$^{58}$Ni are taken from Refs. 2 and 3 which were obtained by the systematic search.   The interaction $V(\vec{r}, \vec{R})$ is expanded as

$$V(\vec{r}, \vec{R}) = 4\pi \sum_\lambda V_\lambda(r, R)(Y_\lambda(\hat{r}) \cdot Y_\lambda(\hat{R})), \tag{5}$$

* Numazu Technical College.

** Department of Physics, University of Tokyo.

40
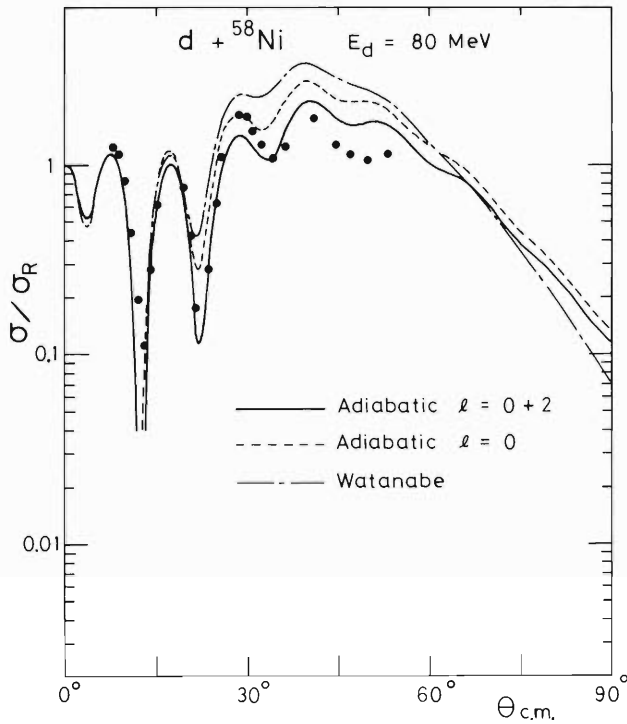


Fig. 1. Elastic cross sections of deuteron-$^{58}$Ni scattering at 80 MeV. Solid and dashed lines show, respectively, the cross sections obtained by the adiabatic method with s-wave and d-wave breakup channels and with s-wave channel only. Dashed-dot line illustrates the cross section for the Watanabe potential. The experimental data are taken from Ref. 6.
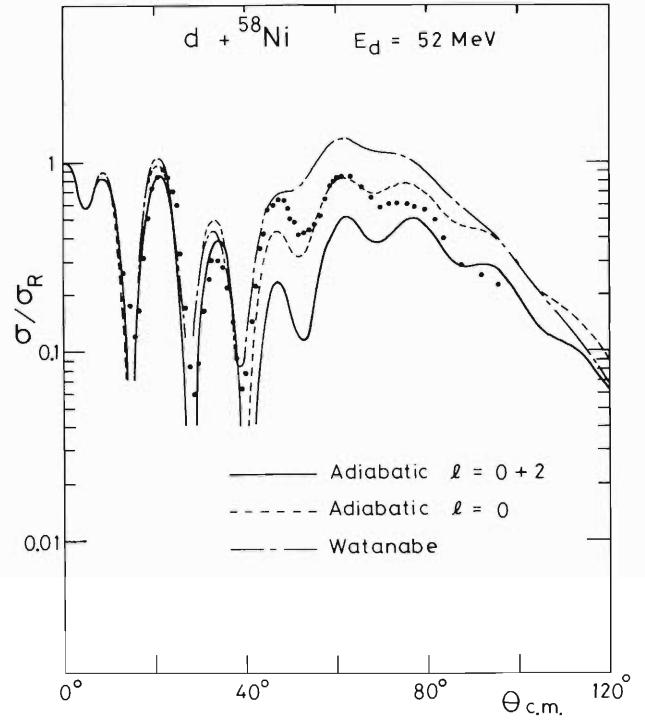


Fig. 2. Elastic cross sections of deuteron-$^{58}$Ni scattering at 52 MeV. The experimental data are taken from Ref. 7. See caption to Fig. 1.
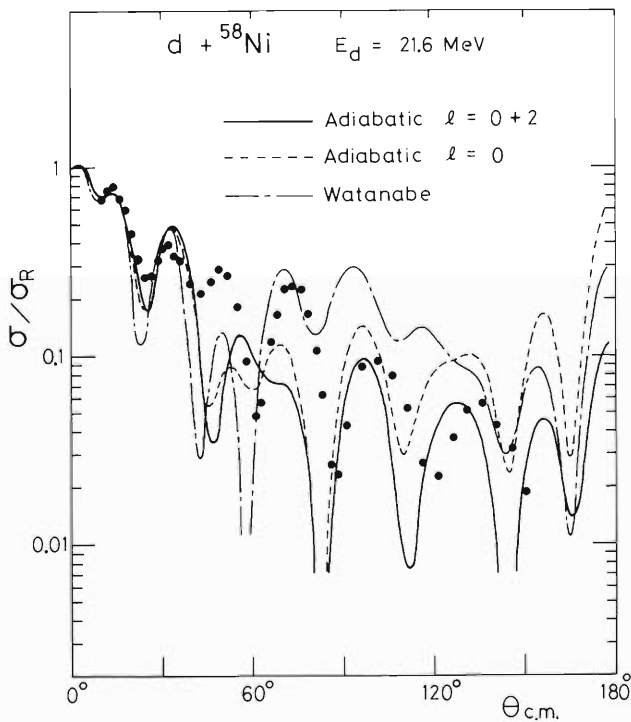


Fig. 3. Elastic cross sections of deuteron-$^{58}$Ni scattering at 21.6 MeV. The experimental data are taken from Ref. 8. See caption to Fig. 1.

and $V_0$ (r, R), $V_2$ (r, R), and $V_4$ (r, R) are included in the actual calculation. The coupled equations are solved with d-wave ($\ell = 2$) and g-wave ($\ell = 4$) breakup channels as well as s-wave ($\ell = 0$) breakup channel by using the coupled-channel code CCSEARCH[4] with minor modification. The t-matrix is calculated using Eqn. (4). In this calculation, Hulthén wave function is used for $\phi_d$ (r).

Figures 1, 2, and 3 show the calculated and observed elastic cross sections for deuteron scattering from $^{58}$Ni at 80 MeV, 52 MeV, and 21.6 MeV, respectively. In all cases, it is found that the cross sections obtained by the present adiabatic method are appreciably different from those for the Watanabe potential[5] (folding potential) which does not contain the effect of deuteron breakup. The effect of the d-wave breakup channel is found to be fairly large. On the other hand, the effect of the g-wave breakup channel, which is not illustrated in the figures, is very small. In the case of $E_d$ = 80 MeV, the cross section calculated by the adiabatic method with s-wave and d-wave breakup channels (solid line) is found to be in good agreement with the experimental data.[6] The cross section obtained by the Watanabe potential (dashed-dot line) is too large except in the forward angle region. Adding the breakup channels changes the cross section towards the experimental data very nicely.

In the case of $E_d$ = 52 MeV, the cross section obtained by the adiabatic method with s-wave and d-wave breakup channels gives better agreement with the experimental data[7] than that by the Watanabe potential in the forward angle region, but gives poorer agreement in the large angle region. The cross section obtained by the adiabatic method with the s-wave breakup channel only well reproduces the experimental data in the large angle region, while the inclusion of the d-wave breakup channel gives too much reduction of the cross section in the neighbourhood of $\theta = 60°$.

The cross section at 21.6 MeV obtained by the adiabatic method gives fairly good account of the experimental data[8] in the forward ($10° < \theta < 40°$) and backward ($90° < \theta < 140°$) angle regions but gives too small cross section in the region $40° < \theta < 90°$. This bombarding energy might be too low to apply the adiabatic approximation and to neglect the Coulomb breakup.

All of the above results are obtained by neglecting the spin-orbit potential. We include the spin-orbit potential into Watanabe potential to examine its effect. The inclusion of the spin-orbit potential at 80 MeV is found to change the cross section slightly in the forward angle region, while the effect seems to become important at large angles. We therefore expect that the effect of the spin-orbit potential will not be important in the forward angle region in the present adiabatic treatment.

The numerical calculations of this work were carried out using the FACOM 230-75 computer at IPCR.

References

1)   Yu. A. Berezhnoi and E. V. Inopin: Yadern. Fiz., 6, 1197 (1967); [English Transl., Soviet J. Nucl. Phys., 6, 872 (1968)]; N. Austern, C. M. Vincent, and J. P. Farrell, Jr.: Ann. Phys., N. Y., 114, 93 (1978).

2)   F. D. Becchetti, Jr. and G. W. Greenlees: Phys. Rev., 182, 1190 (1969).

3)   F. G. Perey: ibid., 131, 745 (1963); D. Wilmore and P. E. Hodgson: Nucl. Phys., 55, 673 (1964).

4)   T. Wada and S. Yamaji: Sci. Papers I. P. C. R., 68, 65 (1974).

5)   S. Watanabe: Nucl. Phys., 8, 484 (1958).

6)   G. Duhamel, L. Marcus, H. Langevin-Joliot, J. P. Didelez, P. Narboni, and C. Stephan: ibid., A174, 485 (1971).

7)   F. Hinterberger, G. Mairle, U. Schmidt-Rohr, G. J. Wagner, and P. Turek: ibid., A111, 265 (1968).

8)   J. L. Yntema: Phys. Rev., 113, 261 (1959).

## 4-6. Study on (d, p) Reactions

### Number of Steps Which Should be Taken into Account

M. Ichimura, B. Imanishi, and M. Kawai*

Rearrangement collisions are usually analysed by the distorted wave Born approximation (DWBA). Recently, analyses which take account of two step rearrangement processes have also been carried out for some specific processes such as $(^3He, t)$, $(p, t)$, etc. However, few analyses which take more steps into account have been performed except that of the infinite steps, namely, the coupled channel (CC) calculations.

A study was made here as to how many steps should be taken into account in the analyses. As examples, we analysed (d, p) reactions together with the associated (d, d) and (p, p) scatterings. The analysis is based on the coupled integro-differential equations derived before[1] for the wave functions, $\chi_\alpha(r_\alpha)$, $(\alpha = d, p)$, of the relative motion of the deuteron- and the proton-channel:

$$(T_\alpha + U_\alpha - E_\alpha)\chi_\alpha(r_\alpha) = \lambda \int K_{\alpha\beta}(r_\alpha, r_\beta)\chi_\beta(r_\beta)d^3r_\beta,$$

$$(\alpha, \beta = d, p, \quad \alpha \neq \beta),$$

where the kernel $K_{\alpha\beta}$ includes the so-called non-orthogonality term as well as the interaction kernel. A constant $\lambda$ is intentionally introduced to investigate the question. The physical case corresponds to the case of $\lambda = 1$.

In order to estimate the number of steps, we solved the coupled equations for several values of $\lambda$ ( = 0.01, 0.1, 0.5, 0.7, 0.9, and 1.0). Then, the obtained S-matrices, $S_{\alpha\beta}^J(\lambda)$, are simulated by a polynomial of $\lambda$ as

$$S_{\alpha\beta}^J(\lambda) = \sum_{n=0} \lambda^n S_{\alpha\beta}^{J,n}.$$

If $\left| S_{\alpha\beta}^{J,n} \right|$ decreases rapidly with increasing n, the power n of $\lambda$ may be interpreted as the number of steps. In particular, n = 0 and 1 correspond to the optical potential scatterings and one-step processes ($\simeq$DWBA), respectively. Actual calculations show that the rapid decrease occurs in most partial waves except for very low ones, for which the concept of steps becomes questionable.

We define the up-to-N-step cross sections $\sigma_{\alpha\beta}^{(N)}$ as those calculated by the up-to-N-step S matrices

$$S_{\alpha\beta}^{J,(N)} = \sum_n^N S_{\alpha\beta}^{J,n},$$

and see how they reproduce the results of the full coupled channel calculations, $\sigma_{\alpha\beta}^{(CC)}$.

Numerical analyses have been carried out for reactions (1) $^{16}O(d, p)^{17}O(2s)$ with Q-value (Q)

of 1.046 MeV and the incident energy ($E_{c.m.}$) of 10.49 MeV and (2) $^{40}$Ca(d, p)$^{41}$Ca(2p) with Q = 4.19 MeV and $E_{c.m.}$ = 10.48 MeV, together with the (d, d) and (p, p) scatterings associated with the above reactions through the coupling between the deuteron- and the proton-channels.

In Figs. 1 to 6, $\sigma_{\alpha\beta}^{(N)}$ are compared with $\sigma_{\alpha\beta}^{(CC)}$. When the optical model results or the DWBA results are, from the beginning, close to the coupled channel results (such as (d, p) in Ca and (d, d) in O), rapid convergence has been found as is expected. Even when that is not the case (such as (d, d) and (p, p) in Ca and (d, p) in O), the results of the CC calculations are satisfactorily reproduced by at most up-to-4 or 5-step cross sections, except for the (p, p) scattering in the oxygen. For this case, the convergence could not be obtained and thus the coupled channel effects cannot be treated by perturbation series.

It must be noticed that the satisfactory convergence in the cross sections does not necessarily mean the convergence of all the S-matrix elements. In most case, the S-matrices in J = 0 partial waves do not converge, but their fluctuations due to non-convergence do not manifest themselves clearly in the cross sections.
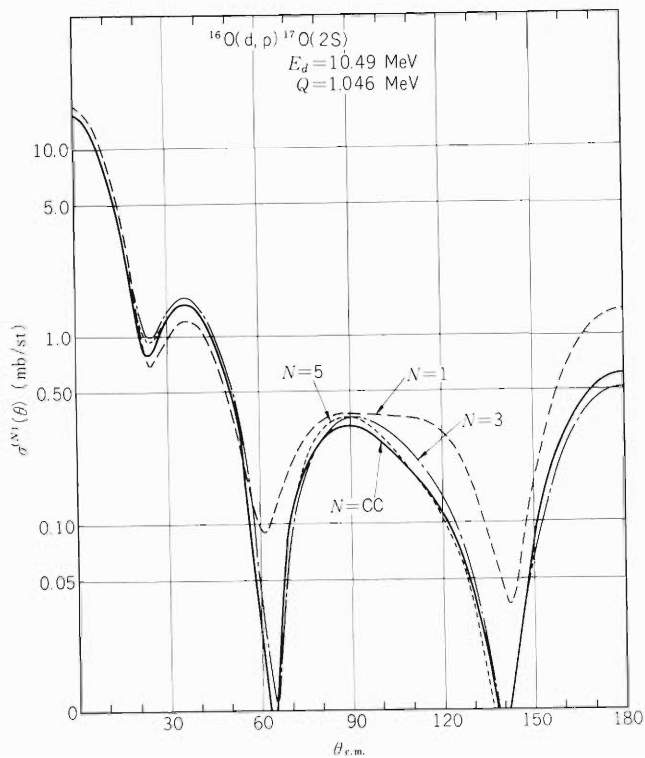


Fig. 1. Differential cross sections of the reaction $^{16}$O(d, p)$^{17}$O (2s). The full line represents the cross section obtained by the full coupled channel calculation (which is denoted by N = CC). The dash line (N = 1) corresponds to the one-step cross section (DWBA), while the dash-dot line (N = 3) and the dot line (N = 5) correspond to the up-to-3 and up-to-5 step cross sections, respectively.
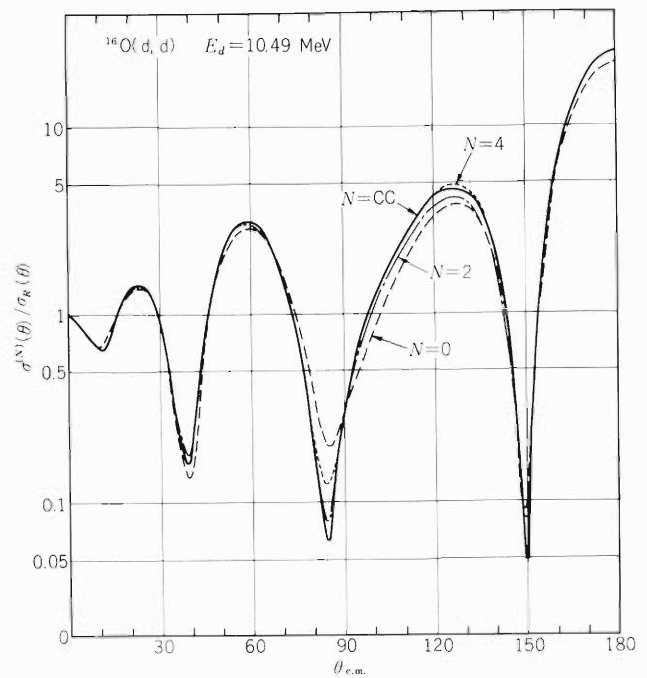
Fig. 2. Rutherford ratios of the scattering $^{16}$O(d, d). The full line represents the Rutherford ratio obtained by the full coupled channel calculation (which is denoted by N = CC). The dash line (N = 0) corresponds to the results obtained by the pure distorting potential, while the dash-dot line (N = 2) and the dot line (N = 4) correspond to the up-to-2 and up-to-4 step results, respectively.

44
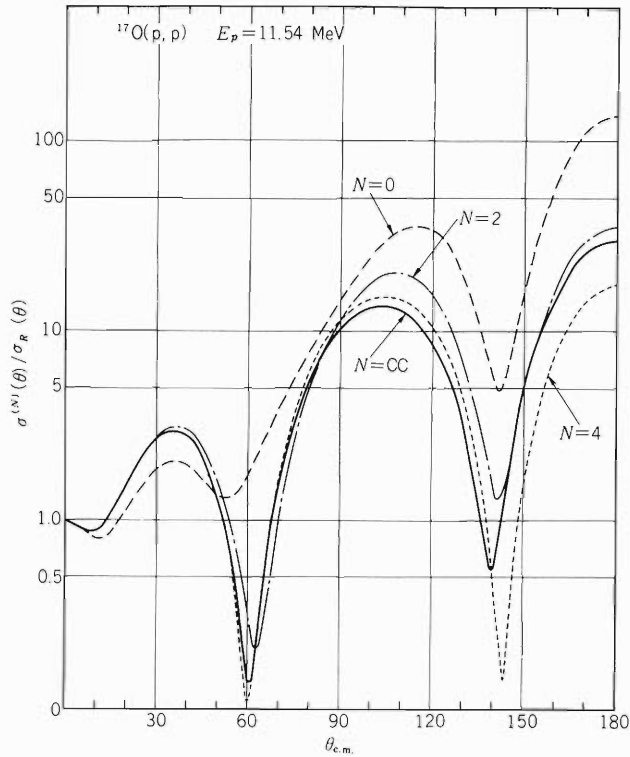


Fig. 3. Rutherford ratios of the scattering $^{17}O(p, p)$. For details, see the caption of Fig. 2.
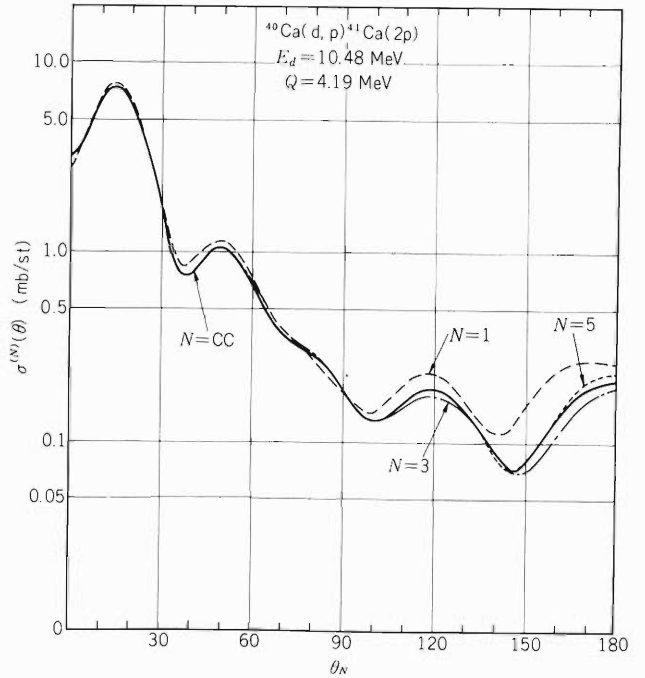


Fig. 4. Cross sections of the reaction $^{40}Ca$ $(d, p)^{41}Ca$ (2p). For details, see the caption of Fig. 1.
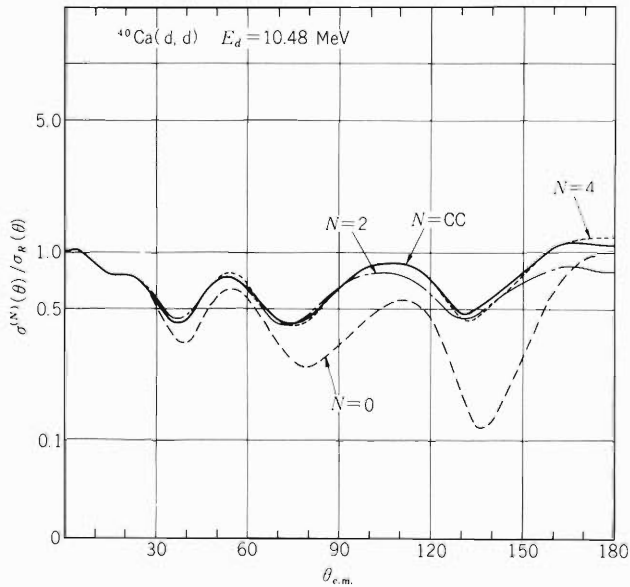


Fig. 5. Rutherford ratios of the scattering $^{40}Ca$ (d, d). For details, see the caption of Fig. 2.
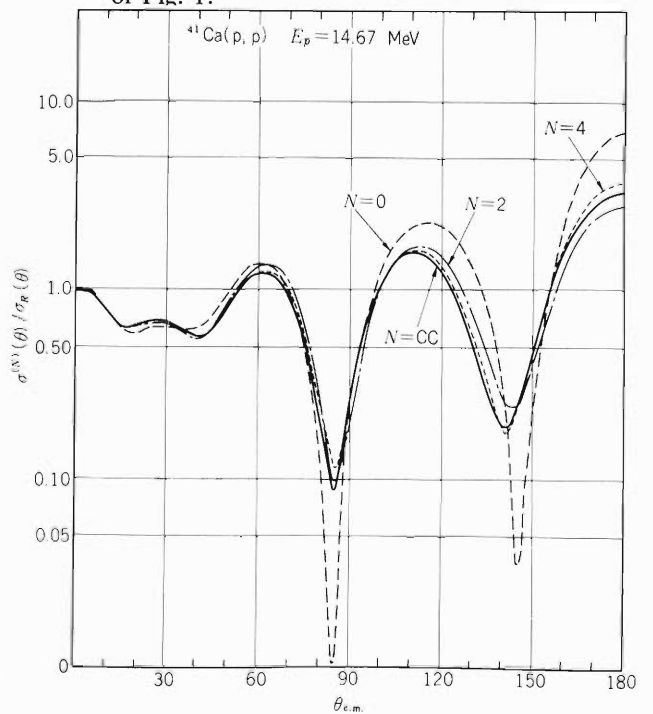


Fig. 6. Rutherford ratios of the scattering $^{41}Ca$ (p, p). For details, see the caption of Fig. 2.

Reference

1) T. Ohmura, B. Imanishi, M. Ichimura, and M. Kawai: Progr. Theor. Phys., 41, 391 (1969).

## 4-7. Quasimolecular Resonance by the $^{24}$Mg$(\alpha, {}^{12}$C$)^{16}$O Reaction

F. Soga, J. Schimizu, N. Takahashi, K. Takimoto,
R. Wada, T. Wada, T. Fujisawa, and H. Kamitsubo

Resonances in the $^{12}$C+$^{16}$O system were studied with the $^{24}$Mg($\alpha$, $^{12}$C)$^{16}$O reaction together with the elastic and inelastic scattering of alpha particles on $^{24}$Mg nuclei.

The alpha-beam accelerated by the cyclotron was used. The $^{12}$C ion was detected and identified with a $\Delta$E–E counter telescope of 6.8 $\mu$m and 30 $\mu$m Si detectors. The alpha particles were detected with four independent Si detectors at different scattering angles.

The measured excitation function of the $^{24}$Mg($\alpha$, $^{12}$C)$^{16}$O reaction is shown in Fig. 1, in which the open circles are the data obtained at IPCR and the closed circles are those obtained at INS. Data on the elastic and inelastic scattering of alpha particles from $^{24}$Mg nucleus are shown in Fig. 2. In Fig. 1, two peaks are seen at $E_\alpha$ = 22.77 MeV and $E_\alpha$ = 23.90 MeV, which correspond to 12.73 MeV and 13.7 MeV in the $^{12}$C+$^{16}$O system, respectively. The angular distribution of the $^{24}$Mg($\alpha$, $^{12}$C)$^{16}$O reaction at $E_\alpha$ = 22.77 MeV is shown in Fig. 3. The solid line is the result of Legendre polinomials fit, where the differential cross sections were fitted with the formula $\Sigma_L a_L P_L(\cos \theta)$. In this analysis $a_{L=14}$ has the maximum value. The dashed line is the curve of $| P_7(\cos \theta) |^2$ which shows good agreement with the experimental values with regard to the peaks and the dips. The dotted line is the result of Hauser-Feshbach calculation which can be considered as an estimation of the background reaction. Comparing these three calculated lines with the experimental values, the spin-parity of the resonance at $E_\alpha$ = 22.77 MeV can
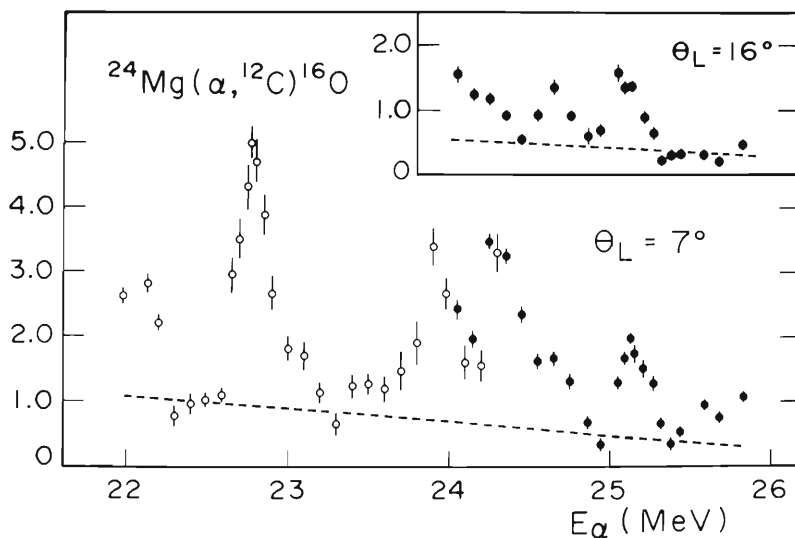


Fig. 1. Experimental excitation function for the reaction $^{24}$Mg ($\alpha$, $^{12}$C)$^{16}$O. Open circles are data obtained at IPCR and closed circles are those obtained at INS. Dotted curve is Hauser-Feshbach calculation using probable values for the parameters.
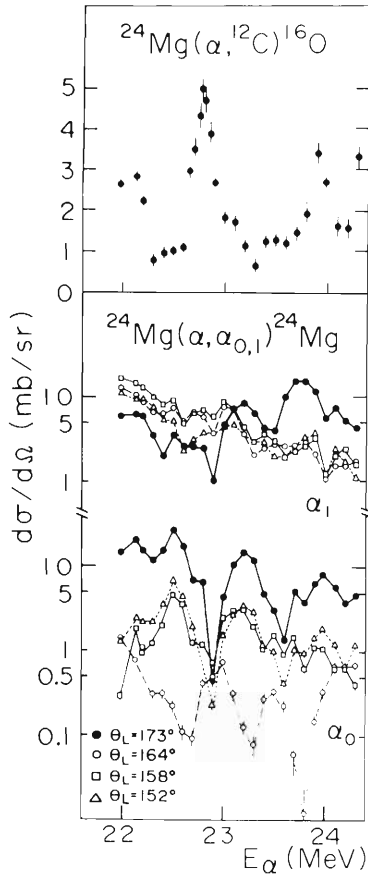
Fig. 2.    Experimental excitation functions for elastic and inelastic scattering of alpha particles from $^{24}$Mg at several backward angles. Lines are drawn only to guide the eye.
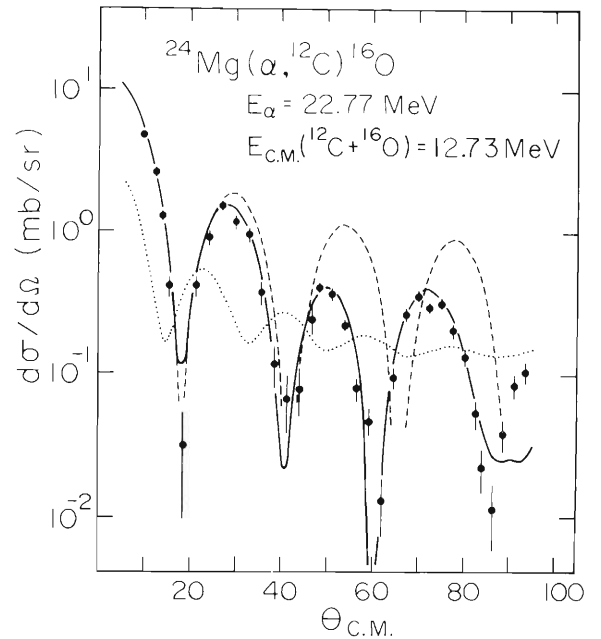
Fig. 3.    Angular distribution for $^{24}$Mg ($\alpha$, $^{12}$C)$^{16}$O at $E_\alpha$ = 22.77 MeV.   Solid curve is Legendre polinomial expansion fit; dashed curve is square of the Legendre polynomial of order 7 and dotted curve is Hauser-Feshbach calculation.

be clearly determined to be $7^-$.   The spin-parity of $E_\alpha$ = 23.90 MeV resonance was found to be $8^+$ by the members of our group.[1]

The correlation between the $\alpha + {}^{24}$Mg channel and the $^{12}$C $+ {}^{16}$O channel is clearly seen in the excitation function as is shown in Fig. 2.   At $E_\alpha$ = 22.77 MeV which corresponds to the peak of the $^{12}$C $+ {}^{16}$O channel, the $\alpha + {}^{24}$Mg elastic scattering shows deep minimum.   This fact suggests that there is a relation between the backward angle anomaly phenomena in the $\alpha + {}^{24}$Mg elastic scattering and the molecular resonance in the $^{12}$C $+ {}^{16}$O system.

# 4-8. Reformulation of DWBA Form Factor
# for Heavy Ion Transfer Reactions*

T. Tamura, T. Udagawa,** and H. Amakawa

A great number of exact finite range DWBA (EFR-DWBA) calculations have been made for transfer reactions induced by heavy ions. Most of these were based on the formulation of Austern et al.[1] This formulation becomes somewhat clumsy, however, when applied to transfer reactions with a large transferred angular momentum $l$. (Throughout the present article, we use the notation of Ref. 2.) The value of the factor $s_1^{\lambda_1} t_1^{\lambda_1} s_2^{\lambda_2} t_2^{\lambda_2}$, which appears in the summand in the expression for the finite-range form factor (Eqn. (4·10) of Ref. 2) gets very large and a drastic cancellation must follow.[3] This can result in serious numerical error, unless great care is exercised about the numerical calculations. However, EFR-DWBA calculations with large $l$ values are in fact needed, e.g., in the direct reaction approach to quasi- and deep-inelastic scattering[4] and in calculation of the dynamical polarization effect for transfer reactions.[5] Therefore, it is desirable to reformulate the calculation of the EFR-DWBA form factor so that the above difficulty is avoided. We do this reformulation in the following.

The definition of the form factor is

$$F^{l_1 n_1 l_2 n_2}_{l l_a l_b}(r_a r_b) = \frac{1}{2\ell+1} \times \sum_{m\ell} \int \int W_{l_1 n_1}(r_1) W_{l_2 n_2}(r_2)$$

$$\times [Y_{l_1}(\hat{r}_1) Y_{l_2}(\hat{r}_2)]_{\widetilde{lm}} \times [Y_{l_a}(\hat{r}_a) Y_{l_b}(\hat{r}_b)]_{\ell m\ell} d\hat{r}_a d\hat{r}_b \tag{1}$$

as given in Eqn. (4·5) of Ref. 2. We transform from the coordinate system of Ref. 2 in which $z /\!/ k_a$, to a new system in which $\hat{r}_b = \hat{z}'$ and all the vectors $r_a, r_b, r_1$, and $r_2$ lie in the $x$-$z$ plane. Then

$$[Y_{l_a}(\hat{r}_a) Y_{l_b}(\hat{r}_b)]_{\ell m\ell} = i^{l_b} \frac{\hat{\ell}_b}{\sqrt{4\pi}} \times \sum_{m'_{l_a} n_\ell'} Y_{l_a m'_{l_a}}(\theta, 0)(\ell_a m'_{l_a} \ell_b 0 | \ell n'_\ell) \times D^\ell_{m\ell n\ell'} \tag{2}$$

with $\theta = \hat{r}_a \wedge \hat{r}_b$ .

Similarly

$$[Y_{l_1}(\hat{r}_1) Y_{l_2}(\hat{r}_2)]_{\widetilde{lm}\ell} = \sum_{m_1' m_2' n_\ell''} Y_{l_1 m_1'}(\theta, 0) \times Y_{l_2 m_2'}(\theta 0)(\ell_1 m_1' \ell_2 m_2' | \ell n_\ell'')$$

$$\times (-)^{l+n_\ell''} D^{l*}_{m_\ell - n_\ell''} . \tag{3}$$

** Department of Physics, University of Texas at Austin.

This choice of the coordinate system is very similar to that adopted in Ref. 6, which described a DWBA calculation made in terms of the WKB approximation. Inserting (2) and (3) into (1), we obtain

$$F^{\ell_1 n_1 \ell_2 n_2}_{\ell\ell_a\ell_b}(r_a r_b) = \frac{\hat{\ell}_a \hat{\ell}_b \hat{\ell}_1 \hat{\ell}_2}{2(2\ell+1)} \times \sum_{m_\ell m_1' m_2'} (\ell_a m_\ell \ell_b 0 | \ell m_\ell)(\ell_1 m_1' \ell_2 m_2' | \ell \widetilde{m}_\ell) i^\ell b$$

$$\times \int W_{\ell_1 n_1}(r_1) W_{\ell_2 n_2}(r_2) \times \overline{P_{\ell_a m_\ell}}(\theta)\overline{P_{\ell_1 m_1'}}(\theta_1)\overline{P_{\ell_2 m_2'}}(\theta_2) d(\cos\theta), \qquad (4)$$

In Eqn. (4)     $\overline{P_{\ell m}}(\theta) = (\sqrt{4\pi}/\hat{\ell})Y_{\ell m}(\theta, 0)$

and     $\cos\theta_i = (t_i r_b + s_i r_a \cos\theta)/r_i.$     $(i = 1, 2)$

Equation (4) is free from the large factor $s_1{}^{\lambda_1} t_1{}^{\lambda_1} s_2{}^{\lambda_2} t_2{}^{\lambda_2}$ and thus from dangerous cancellations. An apparent disadvantage is the fact that summations over the magnetic quantum numbers $m_1$, $m_2$, and $m_\ell$ remain, making the evaluation of Eqn. (4) rather time consuming. Actually, however, the range of the integration over $\cos\theta$ in (4) is limited to the extreme near neighborhood of $\cos\theta = 1$.[2] This makes the factor $P_{\ell_a m_\ell}(\theta)$ very small unless $m_1 = 0$ (and possibly $m_\ell = 1$). Therefore, the summation over $m_\ell$ is in practice absent, and those over $m_1$ and $m_2$ are very much restricted.

In order to get some feeling for the merit of using the new algorithm of Eqn. (4) over the use of the old version of Eqn. (4·10) of Ref. 2, we performed calculations for the case of the $^{208}Pb(^{12}C, ^{13}C)^{207}Pb$ $(i_{13/2})$ reaction, which has $l = 7$. The FACOM 230-75 computer at IPCR was used, which had 36 bit words. It was found that with the old version (Eqn. (4·10)), double precision had to be used throughout: Calculation with single precision gave results which were meaninglessly poor. On the other hand, with the new version, calculations with single precision gave results which agreed with the double-precision results to within four significant figures. As for running time, it took 81 sec to perform a calculation (up to $l_a = 90$) with the old version and with double precision. The corresponding time was reduced to 12 sec when the new version was used with single precision and with $m_\ell = 0$ and 1. The merit of using the new version is evident.

Delic et al.[5] reported that they needed double precision on a CDC7600 computer which had 60 bit words. With our new version, single precision would have been sufficient. The computational time they needed ( $\approx$ 3 h ) would also have been reduced drastically.

Recently, several authors emphasized the merit of using a Gaussian expansion of various radial wave functions involved in DWBA and coupled-channel calculations.[7] This method might in general be more powerful than what has been in general use in the past,[1],[2] thus making even our new formulation given above unnecessary. However, it seems that the possibility of performing a Gaussian expansion of the distorted waves that appear in the case of heavy-ion reactions yet remains to be investigated carefully. We therefore feel it is worthwhile to report on the new formulation given here.

References

1) N. Austern, R. M. Drisco, E. C. Halbert, and G. R. Satchler: Phys. Rev., $\underline{133}$, B3 (1964).

2) T. Tamura: Phys. Reports, $\underline{14C,}$ 59 (1974).

3) K. S. Low and T. Tamura: Phys. Rev., $\underline{C11}$, 789 (1975).

4) T. Udagawa, B. T. Kim, and T. Tamura: Proc. IPCR Symp. on Macroscopic Features of Heavy-Ion Collisions and Pre-Equilibrium Process, Hakone, p. 3 (1977).

5) G. Delic, K. Pruess, L. A. Charlton, and N. K. Glendening: Phys. Letters, $\underline{69B,}$ 20 (1977).

6) S. Landowne, C. H. Dasso, B. S. Nilsson, R. A. Broglia, and Aa. Winther: Nucl. Phys., $\underline{A259}$, 99 (1976).

7) G. L. Payne and R. R. Carlson: Phys. Rev., $\underline{C12,}$ 1260 (1975);
M. Kawai, M. Kamimura, Y. Mito, and K. Takesako: Progr. Theor. Phys., $\underline{59,}$ 674, 676 (1978).

# 4-9. Calculation of Friction Force, Inertia Tensor and Potential Energy for the System $^{20}$Ne + $^{28}$Si Based on the Linear Response Theory

S. Yamaji, K. Sato, S. Yoshida,* and K. Harada**

We calculate the frictional coefficients, inertia tensors and potential for the system $^{20}$Ne + $^{28}$Si in the coupled equations of motion derived from the linear response theory.[1] We adopt a two-center harmonic oscillator Hamiltonian H in which the relative distance R and the deformations $\delta(\delta_1 = \delta_2)$ of two fragments appear as parameters.[2]

For the frictional coefficients $\gamma_{\mu\nu}$ ($\mu$ = R or $\delta$), the microscopic expressions were given in our previous work[3] in which, subtraction of a term arising due to a simple translation of two centers of the potential from the quantity $\partial H/\partial R$ was made in order to eliminate the spurious energy dissipation at sufficiently large distance.

In the present work, we propose tentatively another way to eliminate this spurious energy dissipation. We assume that the expression for the frictional coefficients $\gamma_{\mu\nu}$ given by the linear response theory[1] is available without any subtraction when two fragments overlap. Even when the fragments do not touch, there must be a tail region where the conservative forces are significant. The range of the tail region may be considered to be twice the diffuseness parameter and is taken to be 2 fm in the present calculation. When the two surfaces including the tail region overlap, we assume that frictions can still be obtained, modifying the expression for $\gamma_{\mu\nu}$[1] in the following way. In the calculation of matrix elements of $\partial H/\partial R$ with eigenfunctions of H, the system is described in cylindrical coordinates, where the z-axis is taken to be the symmetric axis of the system. The integration over the variable z is restricted within the two crossing points between the z-axis and the surface of the overlapping region. When there is no overlapping between the tail regions, the frictional coefficients $\gamma_{RR}$ and $\gamma_{R\delta}$ vanish. The typical contour maps on the R-$\delta$ plane are shown in Fig. 1.

For the inertias $m_{\mu\nu}$, the linear response theory gives the expression which corresponds to the cranking formula with finite temperature. The inertias thus calculated, however, change very rapidly with the change of variables R and $\delta$ due to their strong sensitivity to the single particle level structure. Therefore, we approximately replace those extended cranking inertias with hydrodynamical ones obtained by the use of the Werner-Wheeler method.[4] The results are shown in Fig. 2.

For the potential energy, we use the sum of the extended liquid-drop energy[5] and the shell correction energy which includes the dependence of the nuclear temperature.[6] The extended liquid-drop energy is the sum of the Coulomb energy and nuclear macroscopic energy which is given by

$$- a_s/(8\pi^2 a^4 r_0^2) \left\{ 1 - K_s(\frac{N-Z}{A})^2 \right\} \iint (\frac{|\vec{r}-\vec{r}'|}{a} - 2) \frac{e^{-|\vec{r}-\vec{r}'|/a}}{|\vec{r}-\vec{r}'|/a} d\vec{r} \, d\vec{r}',$$

---

* Tohoku University.

** Japan Atomic Energy Research Institute.
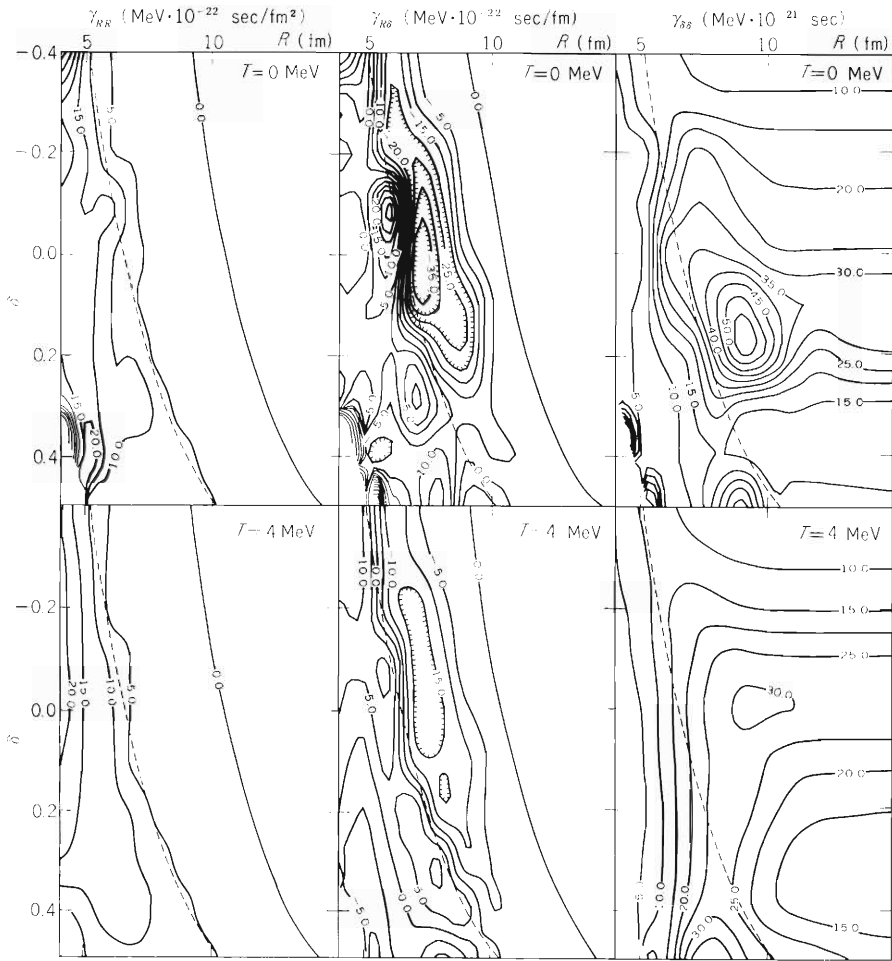
Fig. 1.   Contour maps of the frictional coefficients $\gamma_{RR}$, $\gamma_{R\delta}$, and $\gamma_{\delta\delta}$ for the temperature T=0 and 4 MeV as functions of the relative distance R and the deformation $\delta$.   The smearing width is taken to be 0.2 $h\omega_0$.   As the strength parameters of the terms ($\ell \cdot s$) and $\ell^2$ in the two center Hamiltonian, $\kappa$=0.08 and $\mu$=0.0 are used.   The formation of the neck during the collision is not taken into account.   The relative distance at which two deformed nuclei touch is shown by the dotted curves in all figures.
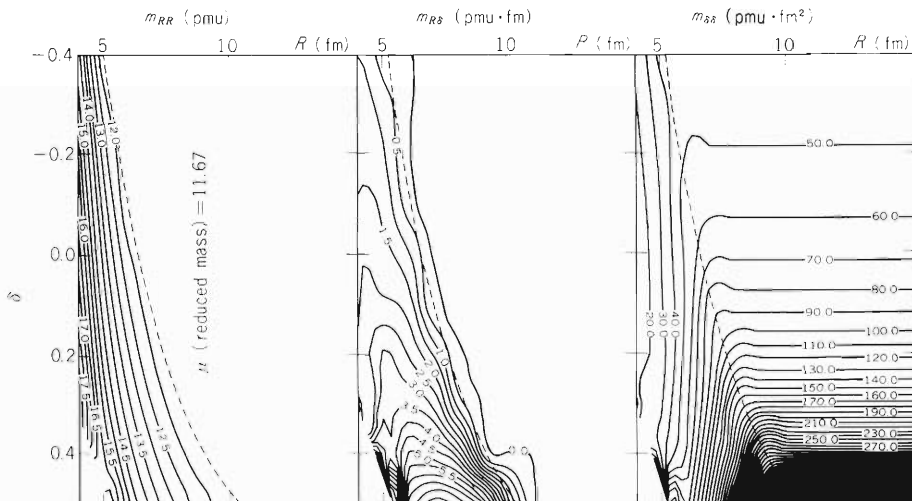


Fig. 2.   Contour maps of the inertias $m_{RR}$, $m_{R\delta}$, and $m_{\delta\delta}$ as functions of the relative distance R and the deformation $\delta$.
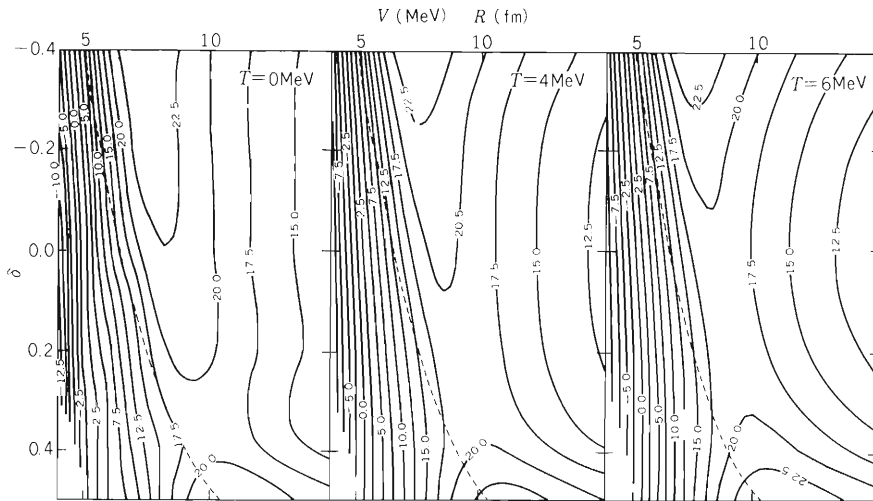
Fig. 3. Contour maps of the potential V for the temperature T=0, 4, and 6 MeV as functions of the relative distance R and the deformation δ. The order and smoothing range of the shell correction energy are taken to be 6 and 1.1 $\hbar\omega_0$, respectively.

where $r_0 = 1.18$ fm, a = 0.65 fm, $a_s = 21.7$ MeV, and $K_s = 3.0$. N, Z, and A are numbers of neutrons, protons, and nucleons, respectively. The potential energy is adjusted to vanish at sufficiently large distances (R → ∞) by adding a constant value. The contour maps of the potential for the temperature T = 0, 4, and 6 MeV are shown in Fig. 3. The map for T = 4 MeV has a structure similar to that for T = 6 MeV which is almost identical to that for the extended liquid-drop energy. Thus, the shell correction energy is considered to be negligible at T = 4 MeV.

References

1) H. Hofmann and P. J. Siemens: Nucl. Phys., A257, 165 (1976).
2) A. Iwamoto, S. Yamaji, S. Suekane, and K. Harada: Progr. Theor. Phys., 55, 115 (1976).
3) K. Sato, A. Iwamoto, K. Harada, S. Yamaji, and S. Yoshida: Z. Physik A , 288, 383 (1978).
4) K.T.R. Davies, A.J. Sierk, and J.R. Nix: Phys. Rev., C13, 2385 (1976).
5) H.J. Krappe, J.R. Nix, and A.J. Sierk: Preprint LA-UR-78-2289, submitted to Phys. Rev. Lett.
6) A.S. Jensen and J. Damgaard: Nucl. Phys., A203, 578 (1973).

# 4-10. Analysis of the Heavy Ion Reaction $^{20}$Ne + $^{28}$Si Based on the Linear Response Theory

S. Yamaji, K. Sato, S. Yoshida,* and K. Harada**

When classical approximation is introduced, the linear response theory[1] gives coupled dynamical equations of motion for the relative distance R and the deformations $\delta(\delta_1 = \delta_2)$ of two fragments as

$$\ddot{R} = \frac{1}{(m_{RR}m_{\delta\delta}-m_{R\delta}^2)}\Big[(\gamma_{R\delta}m_{R\delta}-\gamma_{RR}m_{\delta\delta})\dot{R} + (\gamma_{\delta\delta}m_{R\delta}-\gamma_{R\delta}m_{\delta\delta})\dot{\delta}$$
$$+ m_{R\delta}\frac{\partial V}{\partial\delta} - m_{\delta\delta}\frac{\partial}{\partial R}(V+V_\ell)\Big],$$

$$\ddot{\delta} = \frac{1}{(m_{RR}m_{\delta\delta}-m_{R\delta}^2)}\Big[(\gamma_{RR}m_{R\delta}-\gamma_{R\delta}m_{RR})\dot{R} + (\gamma_{R\delta}m_{R\delta}-\gamma_{\delta\delta}m_{RR})\dot{\delta}$$
$$+ m_{R\delta}\frac{\partial}{\partial R}(V+V_\ell) - m_{RR}\frac{\partial V}{\partial\delta}\Big].$$

The frictional coefficients $\gamma_{\mu\nu}$, inertias $m_{\mu\nu}$ and potential energy V are calculated in Ref. 2. We adopt the centrifugal potential $V_\ell = \hbar^2\ell^2/2\mu R^2$, where $\mu$ is the reduced mass.

In order to determine the time dependence of the nuclear temperature T(t) of the system, we assume that the following relation holds[3]

$$T(t) = \sqrt{E(t)^* / (A/20)} ,$$

where A is the number of nucleons of the system. The nuclear internal excitation energy E(t)* resulting from the friction is calculated by

$$E(t)^* = \int_{-\infty}^{t} [\gamma_{RR}\dot{R}(s)^2 + 2\gamma_{R\delta}\dot{R}(s)\dot{\delta}(s) + \gamma_{\delta\delta}\dot{\delta}(s)^2]ds .$$

For the relative distance R ≥ 15 fm, we use a pure Coulomb trajectory determined by the incident energy and the angular momentum $\ell$. The numerical integration of the coupled equations is started at the relative distance of R = 15 fm with the relative velocity $\dot{R}$ obtained by the pure Coulomb trajectory at the distance of R = 15 fm. The deformation $\delta$ and its velocity $\dot{\delta}$ are kept zero until two fragments come close to 15 fm.

We have performed a numerical calculation for the collision of 120 MeV $^{20}$Ne on $^{28}$Si. Several trajectories for various $\ell$ values on the R-$\delta$ plane are shown in Fig.1 to illustrate the development of the deformation. Collisions with small $\ell$ values lead to fusion. For all $\ell$ values large oblate deformation of both nuclei is seen in the early stage of the reaction. It occurs
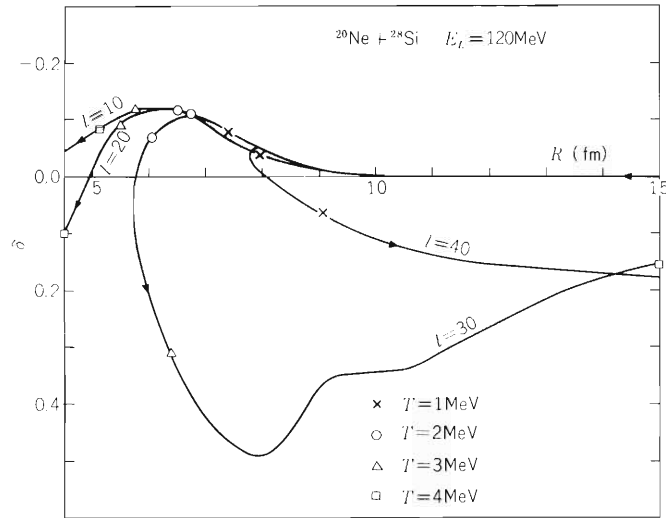
Fig. 1. Several trajectories for various relative angular momentum $\ell$ illustrated for the system $^{20}Ne + ^{28}Si$ at $E_L = 120$ MeV on the R-$\delta$ plane. The temperatures during the collision are 1 MeV($\times$), 2 MeV($\circ$), 3 MeV($\triangle$), and 4 MeV($\square$).

because the effect of the coupling term $\gamma_{R\delta}\dot{R}$ in the surface region dominates over that of the conservative force. As mentioned in Ref. 2, use of hydrodynamical inertias instead of extended cranking ones may be somewhat responsible for the behavior of the deforming motion obtained. If we have a large negative $m_{R\delta}$ in the surface region, the term $m_{R\delta}\gamma_{RR}\dot{R}$ in the coupled equations will prevent the development of the oblate deformation in the early stage of the collision.

Natowitz et al.[4] assumed in their analysis of the collision of 120 MeV $^{20}Ne$ on $^{27}Al$ that the system may be represented by a nuclear molecule in rigid rotation with the relative distance 10.2 fm which corresponds to the prolate deformation of $\delta\sim 0.45$. Our calculation gives the prolate deformation of $\delta\sim 0.35$ in the neighbourhood of the scission point. This is consistent with the above estimation.

The deflection function and energy loss versus angular momentum are shown in Fig. 2. We have found that the value of the critical angular momentum is smaller than the value of $\ell_{cr} = 34$ deduced from the experiment.[4] This discrepancy can be reduced by making the moment of inertia larger than $\mu R^2$. We define the heavily damped collision as the collision with the negative scattering angle. We obtain the energy dissipation of about $30\sim 40$ MeV which is in good agreement with the experimental result.[4]

The angular distribution is shown in Fig. 3. The calculated cross sections should be compared with the sum of various elements by eliminating the quasi-elastic component of the collision. The calculated angular distribution reproduces qualitatively the decreasing behavior of the experiment with the increasing angle. If the quasi-elastic component which is large in the forward angle [cf. Fig. 8 of Ref. 4] is subtracted from the experimental cross section in Fig. 3, the agreement between them becomes better. However, the calculated cross section is, at least, by one order of magnitude smaller than the experimental one.

In order to investigate an effect of the shell correction on the deflection function, energy loss and cross section, quantities obtained only by the liquid-drop model energy are shown by the
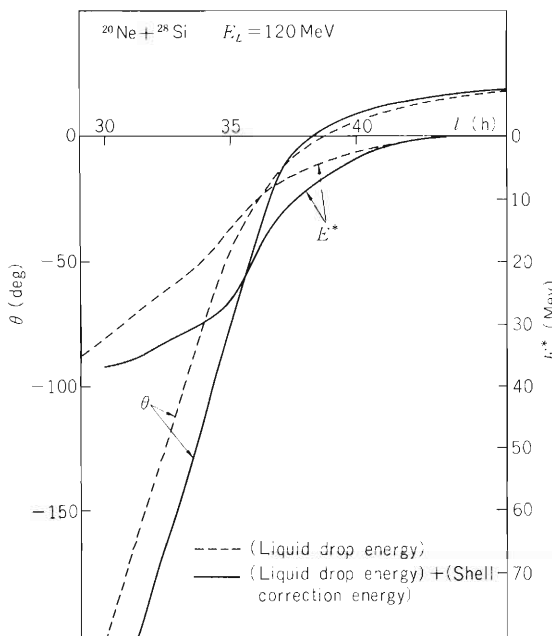
Fig. 2. The deflection function $\theta$ and the energy dissipation E* for the system $^{20}$Ne + $^{28}$Si at $E_L$ = 120 MeV plotted versus the relative angular momentum $\ell$. The dotted lines correspond to those of the liquid-drop energy.
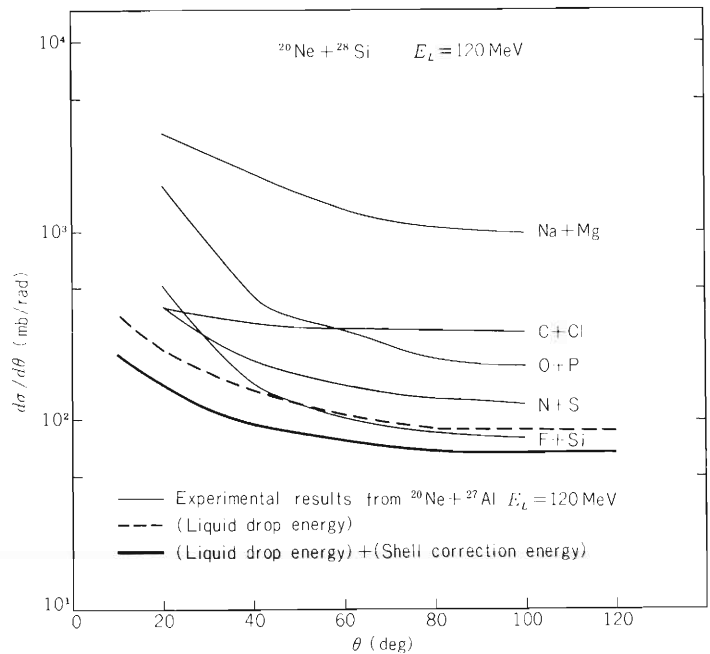
Fig. 3. The calculated cross sections $\frac{d\sigma}{d\theta}$ plotted for the system $^{20}$Ne + $^{28}$Si at $E_L$ = 120 MeV. The dotted line corresponds to that of the liquid-drop energy. The thin curves are taken from the experimental data.[4]

dotted curves in Figs. 2 and 3. Since in the early stage of the collision the temperature increases very rapidly up to the value at which the shell effect is negligible, neglecting the shell correction energy does not give an appreciable effect to the results as shown in Figs. 2 and 3.

The detail of this work is given elsewhere.[5]

## References

1) H. Hofmann and P. J. Siemens: Nucl. Physics, A257, 165 (1976).
2) S. Yamaji, K. Sato, S. Yoshida, and K. Harada: IPCR Cyclotron Progr. Rep., 12, 50 (1978).
3) P. Fong: Statistical theory of Nuclear fission, Gorden and Breach Press, p. 16 (1969).
4) J. B. Natowitz, M. N. Namboodiri, R. Eggers, P. Gonthier, K. Geoffroy, R. Hanus, C. Twosley, and K. Das: Nucl. Physics, A277, 477 (1977).
5) K. Sato, S. Yamaji, K. Harada, and S. Yoshida: Preprint of Tohoku University submitted to Z. Physik A.

### 4-11. Preequilibrium Emission of Light Particles in the
### $^{181}$Ta$+^{14}$N Reaction at 85 and 115 MeV

H. Utsunomiya, T. Nomura, T. Inamura,
T. Sugitate, and J. Schimizu

It is well known that in heavy-ion collisions at energies well above the Coulomb barrier, typically at $7 - 10$ MeV/amu, $\alpha$ particles are emitted predominantly in the forward direction with large probability.[1]   We have shown in the $^{209}$Bi + $^{14}$N reaction[2] that the same phenomenon is significant even at lower bombarding energies and that the projectile and target nuclei fuse together after emitting $\alpha$ particles.   Moreover, the energy spectra observed were shown to be well reproduced by the statistical formula of Ericson[3] with nuclear temperature decreasing monotonically with increasing emission angles.   Therefore, the above phenomenon can be interpreted as evaporation of $\alpha$ particles from a locally heated nuclear system (hot spot) proposed for preequilibrium phenomena by Weiner and Weström.[4]

If the hot-spot interpretation is valid for the above phenomena, the similar features should be expected in energy and angular distributions for other light particles like protons, for which the cross sections turned out to be too small to be clearly measured in the $^{209}$Bi + $^{14}$N reaction.   As the extension of the previous work we have studied the $^{181}$Ta + $^{14}$N reaction, in which efforts were made to measure protons, deuterons and tritons as well as $\alpha$ particles.   Light particles emitted from $^{14}$N-bombardment of a self-supporting $^{181}$Ta target of about 4 mg/cm$^2$ thickness were detected with Si $\Delta$E-E counter telescopes in a similar way as was described previously.[3]

Figures 1, 2 show the measured angular and energy distributions.   The angular distributions for $\alpha$ particles were strongly forward-peaked, while those for protons were less forward-peaked even
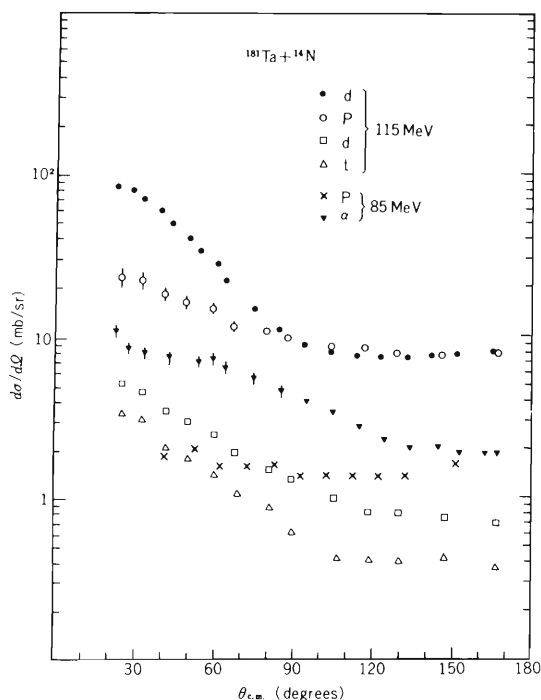


Fig. 1.   Angular distributions of protons, deuterons, tritons and $\alpha$ particles measured in the $^{181}$Ta + $^{14}$N reaction at $E_{lab}$ = 115 MeV and those of protons and $\alpha$ particles at $E_{lab}$ = 85 MeV.   (Deuterons and tritons could not be measured at 85 MeV due to their very small cross sections.)
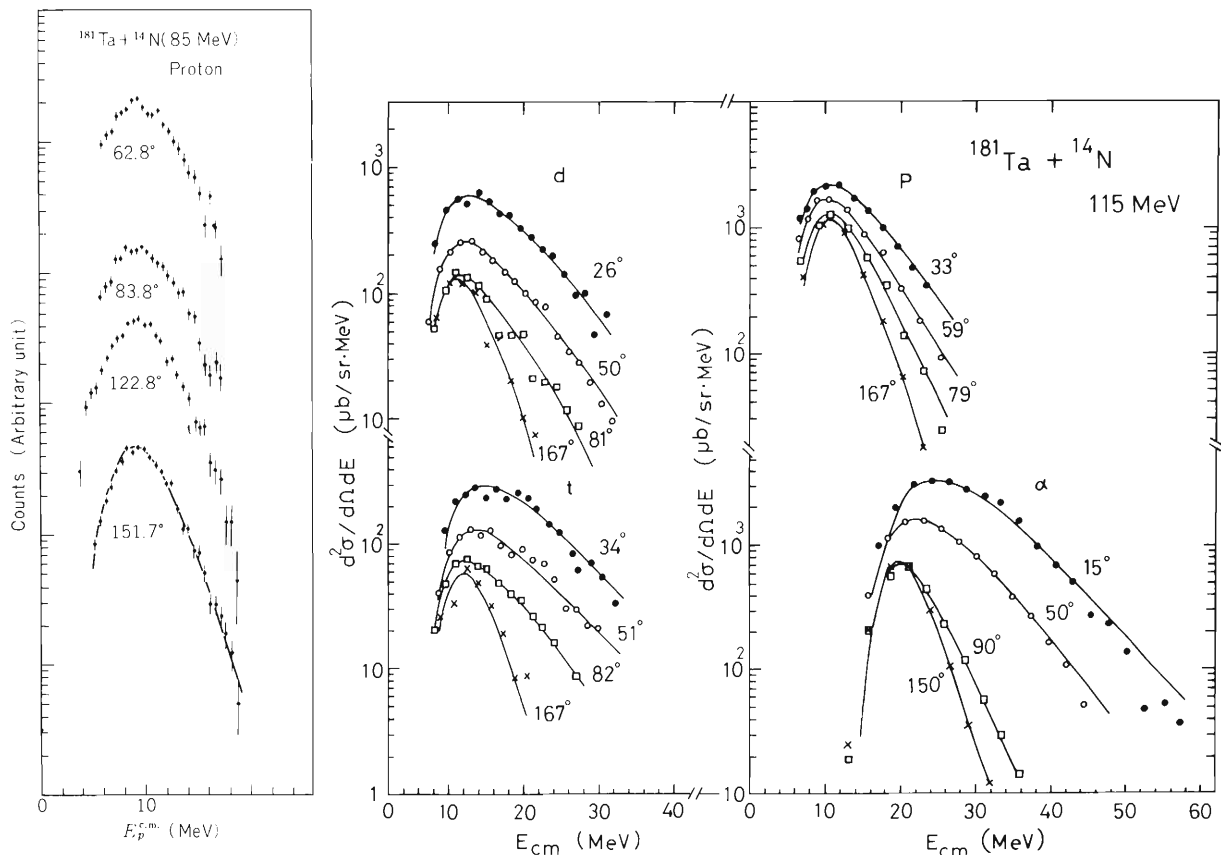
Fig. 2. Examples of the measured energy spectra of protons, deuterons, tritons and $\alpha$ particles observed in the $^{181}$Ta + $^{14}$N reaction at $E_{lab}$ = 115 MeV together with those of protons measured at $E_{lab}$ = 85 MeV. Solid curves for p, d, t, and $\alpha$ spectra show $\chi^2$-fit by the statistical formula given in Ref. 2, 3, where the inverse cross sections were calculated from optical potentials for corresponding particles.

at 115 MeV and almost flat at 85 MeV. These facts indicate that $\alpha$ particles are mainly emitted in the preequilibrium process, while the compound reaction is more responsible for the proton emission.

The energy spectra depend strongly, in general, on the observed angle as shown in Fig. 2, except for the case of protons at 85 MeV, being consistent with the above mentioned interpretation. A common feature of the energy spectra is a long exponential tail extending to high energies. This feature is characteristic of "evaporation spectrum" with high nuclear temperature. In fact, the statistical formula[3] yielded good fit to the observed spectra in all cases, when the nuclear temperature T was assumed to depend on the emission angle and was treated as a free parameter in a similar way as was described previously.[2]

Values of T obtained in the above fit are plotted versus the emission angle in Fig. 3. In the case of 115 MeV, the resultant T values for d, t, and $\alpha$ are nearly equal to each other when compared at the same angle, while the temperature for protons is slightly smaller at forward angles. This is made more evident by the data at 85 MeV, where the nuclear temperature for p is almost constant, indicating the dominant contribution of compound reaction to the proton emission as mentioned before.
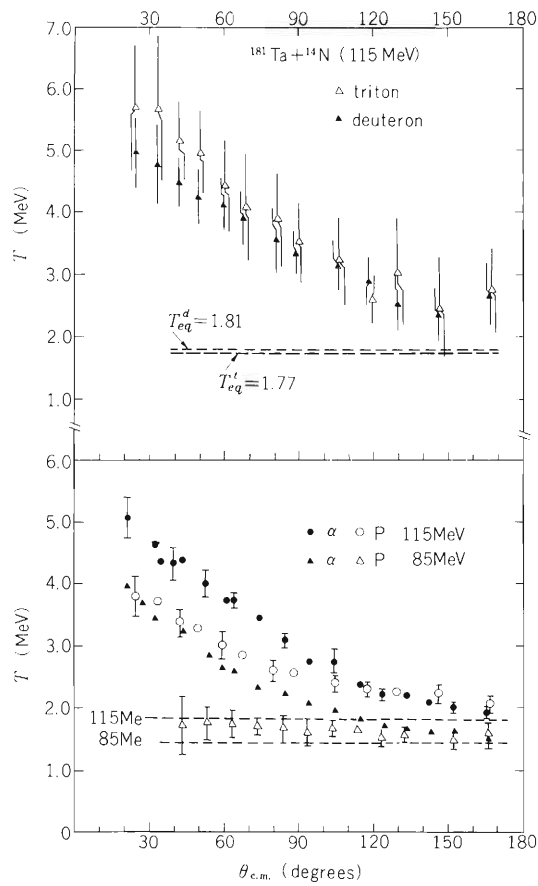
Fig. 3. Nuclear temperature obtained in the $\chi^2$-fit (see Fig. 2) versus the emission angle. Dashed lines show the equilibrium nuclear temperature of residual nuclei produced after emitting various light particles.

References

1) H.C. Britt and A.R. Quinton: Phys. Rev., 124, 877 (1961).

2) T. Nomura, H. Utsunomiya, T. Motobayashi, T. Inamura, and M. Yanokura: Phys. Rev. Lett., 40, 694 (1978).

3) T. Ericson: Advan. Phys., 9, 425 (1960).

4) R. Weiner and M. Weström: Nucl. Phys., A286, 282 (1977).

# 4-12. Preequilibrium $\alpha$ Emission in $^{14}$N-Induced Reactions

## The Most Probable Energies and Angular Distributions

H. Utsunomiya, T. Nomura, and T. Sugitate

It is well known that $\alpha$ particles are emitted with large probability in heavy-ion collisions at the bombarding energy well above the Coulomb barrier.   This phenomenon is often called "direct" or "fast" $\alpha$ emission since its angular distribution is strongly forward-peaked and its energy spectrum contains significant high-energy components.   However, the reaction mechanism involved is not well known although several authors have suggested possible origins for such $\alpha$ emission like projectile break-up, sequential decay from an exited projectile, effects of radial friction, massive transfer and preequilibrium decay.

We have studied the systematical trend of energy and angular distributions of "fast" $\alpha$ emission with a hope that these will give important information on the origin of the relevant phenomenon.   Self-supporting $^{209}$Bi, $^{197}$Au, $^{181}$Ta, $^{169}$Tm, and $^{159}$Tb targets of 2-3 mg/cm$^2$ thickness were bombarded with $^{14}$N beam at 85, 95, and 115 MeV from the cyclotron.   Charged particles with Z $\lesssim$ 8 were detected with conventional Si $\Delta$E-E counter telescopes and measured from 15° to 165° in step of 10° in most cases.

Characteristic features of the measured energy and angular distributions of "fast" $\alpha$ particles were the same as described in the preceeding report[1] in the case of $^{181}$Ta + $^{14}$N reaction.   Namely, the energy spectra were of evaporation type even at forward angles, being well reproduced by the statistical evaporation formula with high nuclear temperature;   the angular distributions turned out to be forward-peaked in all cases.

1)   The most probable energies

The present results on the energy spectra are consistent with the preequilibrium-decay interpretation for the relevant phenomenon.   In particular, we will describe the systematical trend of the most probable energies ($E_{mp}$).   The observed values of $E_{mp}$ in the $^{209}$Bi + $^{14}$N reaction at various incident energies are shown in Fig. 1.   The kinetic energy corresponding to the incident projectile velocity ($E_{inc}$) in also given by dashed lines.   The values of $E_{mp}$ are close to the Coulomb barrier in the exit channel at backward angles and increase monotonically with decreasing angles.   For the data at 85 MeV, the $E_{mp}$ values become larger than $E_{inc}$ at forward angles, but in the case of the 115 MeV data the $E_{mp}$ values are considerably smaller than the corresponding $E_{inc}$ even at forward angles.   $E_{mp}$ also turned out to be strongly target-dependent;   in the case of the $^{159}$Tb target the $E_{mp}$ values are by about 3 MeV smaller than those in the $^{209}$Bi + $^{14}$N reaction at the same angles as shown in Fig. 1.   This difference is roughly equal to the Coulomb barrier difference in the two exit channels.

These facts indicate that the Coulomb barrier in the exit channel is a dominant factor to determine the most probable energy.   The increase of $E_{mp}$ with decreasing angles can be well explained by angle-dependent nuclear temperature T($\theta$) (see Ref. 1) which was found to increase monotonically with decreasing angles in all cases.

The above fact is also consistent with the cases for other light particles.   Since angular

60
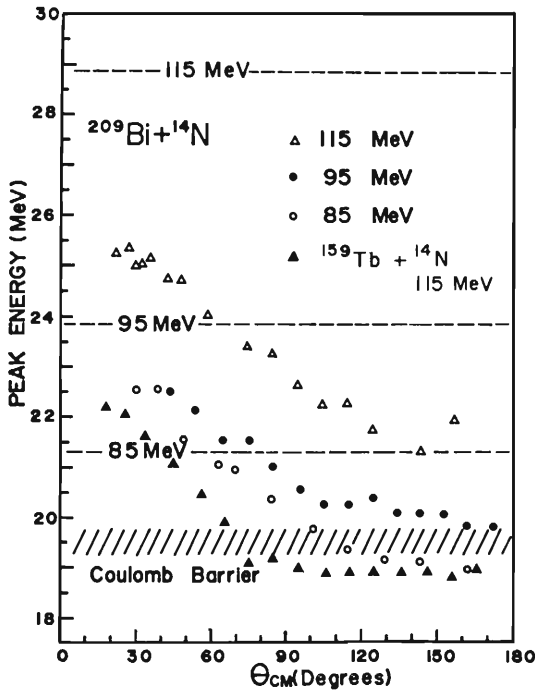


Fig. 1. The most probable energies ($E_{mp}$) of $\alpha$-particle spectra versus emission angles in the $^{209}$Bi + $^{14}$N reaction at 85, 95, and 115 MeV. The kinetic energy corresponding to the initial projectile velocity is shown by a dashed line for each incident energy. The $E_{mp}$ values in the $^{159}$Tb + $^{14}$N reaction at 115 MeV are also given for comparison.

distributions for protons, deuterons, tritons, and $\alpha$ particles turned out to be similar to each other as described in Ref. 1, it is natural to think that the same reaction mechanism is mainly responsible for the emission of these particles. If the $E_{mp}$ value is determined by the incident energy, then $E_{mp}$ should be roughly proportional to the mass of particle; for example, $E_{mp}$ for triton must be three times as large as that for proton. The observed values for p, d, and t are, however, roughly the same even at forward angles (see Ref. 1), being close to the Coulomb barrier in the exit channel.

2) Angular distributions

We shall show here that the forward-peaked angular distribution of "fast" $\alpha$ emission can also be expected from the preequilibrium-decay interpretation. For this purpose, we take a simple model in which the $\alpha$ emission of interest occurs from a "hot spot" sitting on the surface of the rotating target-nucleus (see Ref. 2).

The energy-integrated emission probability per unit time, $P_i$, of a particle i from a hot spot of temperature T is approximately given by

$$P_i(T) \propto g_i \mu_i R(T)^2 T^2 \exp\left(-(B_i + S_i)/T\right),$$

where $g_i$, $\mu_i$, $B_i$, and $S_i$ are the statistical spin factor, reduced mass, Coulomb barrier and separation energy of a particle i, respectively, and R is the "radius" of the hot spot. $P_i(T)$ clearly increases very rapidly with increasing T. This may explain the very forward-peaked angular distributions of the light-particle emission of interest since T increases monotonically with decreasing emission angles. When we take the model in Ref. 2, the time interval effective to the emission angle $\theta$ is independent of $\theta$, so that we can replace the angular distribution of a particle i with $P_i(T(\theta))$. Figure 2 shows $P_i(T(\theta))$ for protons and $\alpha$ particles versus $\theta$ together with the experimental angular distributions, where $T(\theta)$ is taken from the experimentally deduced values for each particle in the $^{181}$Ta + $^{14}$N reaction at 115 MeV. Although some ambiguity remains in subtracting the background the agreement between experiment and calculation is quite satisfactory in view of our very simple model.
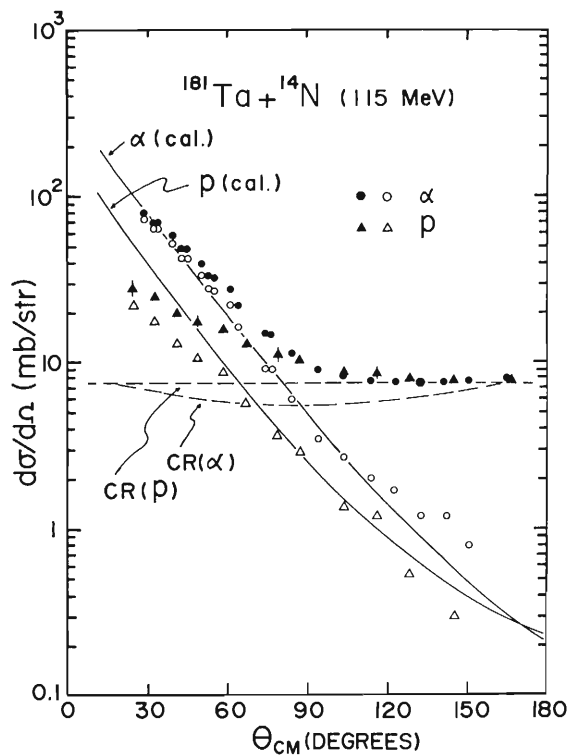
Fig. 2. The calculated (solid curves) and experimental (circles and triangles) angular distributions for protons and $\alpha$ particles in the $^{181}$Ta + $^{14}$N reaction at 115 MeV. Black circles and triangles are raw experimental data, while open ones indicate values after subtracting the compound-reaction contribution which has tentatively been estimated as shown by dashed curves. R(t) in Eqn. (2) is taken to be constant due to lack of the detailed knowledge and for simplicity, so that only relative values are given for the calculation.

## References

1) H. Utsunomiya, T. Nomura, T. Inamura, T. Sugitate, and J. Shimizu, IPCR Cyclotron Progr. Rep., 12, 56 (1978).

2) T. Nomura, H. Utsunomiya, T. Motobayashi, T. Inamura, and M. Yanokura: Phys. Rev. Lett., 40, 694 (1978);
T. Nomura, H. Utsunomiya, T. Inamura, T. Motobayashi, and T. Sugitate: J. Phys. Soc. Japan, 46, 335 (1979).

4-13.  Energy Relaxation during the Fusion Process

Probed by Preequilibrium $\alpha$ Emission

in Heavy Ion Reactions

T. Nomura, H. Utsunomiya, T. Inamura,

T. Motobayashi,* and T. Sugitate

As described in the preceeding reports,[1] $\alpha$ particles predominantly emitted in the forward direction in $^{14}$N-induced reactions on various heavy targets have energy spectra characteristic of evaporation from a locally heated nuclear system (hot spot) proposed for preequilibrium phenomena by Weiner and Weström.[2]   In fact, the observed spectra could be excellently fitted by the statistical evaporation formula when nuclear temperature was treated as a parameter depending on the emission angle $\theta$.   The resultant temperature $T(\theta)$ decreases monotonically with increasing angles, indicating the cooling-down process of the associated hot-spot.
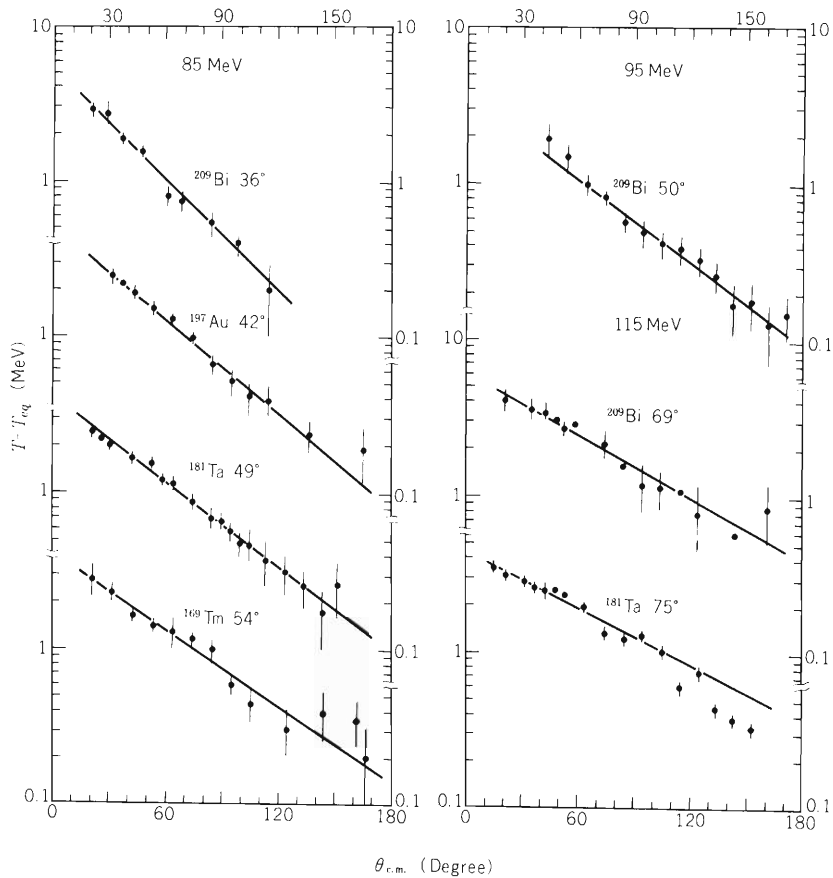


Fig. 1.   Difference between local temperature $T(\theta)$ and $T_{eq}$ versus the emission angles in various $^{14}$N-induced reactions.   The decay constant $\mu$ derived from the given straight line is given for each reaction, where the target nucleus used is also indicated.

Figure 1 shows the plot of $T(\theta)$ minus $T_{eq}$ versus emission angles in various reactions, where $T_{eq}$ is the equilibrium temperature expected in compound reactions and calculated by $T_{eq} \simeq (U_{av}/a)^{1/2}$ with $a = A/9$ MeV$^{-1}$ ($U_{av}$ is the averaged excitation energy of the residual nucleus with mass number A and a the usual level density parameter). A remarkable feature seen in Fig. 1 is that this difference falls almost exponentially with increasing angles; that is, the relation of $T(\theta) - T_{eq} \propto \exp(-\theta/\mu)$ roughly holds in all cases, where the "decay constant" $\mu$ depends on the target nuclei and bombarding energies.

Within the framework of the hot-spot model the above behaviour of $T(\theta)$ is considered to show the internal decay of the hot spot due to nucleon-nucleon multiple scatterings[2] provided the emission angle is somehow related to interaction time, for instance, in the similar way as is the case in deep inelastic phenomena.[3] In order to drive its decay time ($\tau_{hs}$), let us follow the conventional macroscopic picture of heavy-ion collisions. Consider projectile and target nuclei touching each other, which causes extreme local heating around the contact region (formation of the hot spot) mainly due to dissipation of radial kinetic energy. On the other hand, the initial orbital angular momenta are mainly transferred into the rotation of the target because of its large moment of inertia. We postulate that $\alpha$ particles of interest are emitted from this hot spot sitting on the rotating target nucleus. Then, the emission angle is simply related to the rotational motion of the target nucleus on the average.

We calculated the angular velocity ($\omega$) of the above rotational motion at the sticking condition[4] by assuming, for simplicity, the grazing angular momentum at the entrance channel. This seems reasonable since the relevant $\alpha$ emission has been suggested to originate from peripheral collisions. Using $\omega$ thus obtained we converted the decay constant $\mu$ into $\tau_{hs}$. The results are given in Table 1. It is remarkable that values of $\tau_{hs}$ obtained in various combinations of target and bombarding energy are nearly the same, being around $1.8 \times 10^{-21}$ sec. We believe that this lends strong support to the basis of the present model.

Table 1. Decay time of the hot spot obtained in various $^{14}$N-induced reactions.

| Target | Incident energy (MeV) | $\omega$[a] ($10^{20}$ rad·sec$^{-1}$) | $\mu$ (degrees) | $\tau_{hs}$ ($10^{-21}$ sec) |
|---|---|---|---|---|
| $^{209}$Bi | 85 | 3.6 | 36 | 1.8 |
| $^{209}$Bi | 95 | 4.6 | 50 | 1.9 |
| $^{209}$Bi | 115 | 6.2 | 69 | 1.9 |
| $^{197}$Au | 85 | 4.0 | 42 | 1.8 |
| $^{181}$Ta | 85 | 4.8 | 49 | 1.8 |
| $^{181}$Ta | 115 | 7.7 | 75 | 1.7 |
| $^{169}$Tm | 85 | 5.5 | 54 | 1.7 |

a) The angular velocity of the rotating target nucleus calculated at the sticking condition using the rigid-body moment of inertia with $r_0 = 1.25$ fm.

References

1) H. Utsunomiya, T. Nomura, T. Inamura, T. Sugitate, and J. Schimizu: IPCR Cyclotron Progr. Rep., 12, 56 (1978).

2) R. Weiner and M. Weström: Nucl. Phys., A286, 282 (1977).

3) J. Wilczynski: Phys. Lett., 47B, 484 (1973).

4) W.U. Schröder and J.R. Huizenga: Ann. Rev. Nucl. Sci., 27, 456 (1977).

## 4-14. Energy Distributions of $\alpha$-particles Emitted from the $^{14}N + ^{159}Tb$ Reaction

T. Inamura, T. Kojima, K. Hiruta, and T. Nomura

Energy distributions of $\alpha$-particles emitted forwards from the $^{14}N + ^{159}Tb$ reaction have been studied by specifing the outgoing channel. This would provide an additional information on the reaction leading to fast $\alpha$-particle emission.[1,2]

Alpha-particles were detected using a Si annular counter telescope (50 $\mu$m and 2000 $\mu$m). The solid angle subtended was 0.52 sr, the mean detection angle being 21.6° to the beam. Scattered beam was removed by an aluminium foil absorber placed in front of the counter telescope. To specify the outgoing reaction channel, a Ge(Li) counter was used, and coincidences were measured between the counter telescope and the Ge(Li) counter. The $^{159}Tb$ target was a self-supporting metallic foil 2.1 mg/cm$^2$ thick.

Figure 1 shows $\alpha$-energy distributions observed for $\alpha$3n, $\alpha$4n, and $\alpha$5n outgoing channels in



Fig. 1. $\alpha$-energy distributions for $\alpha$3n, $\alpha$4n, and $\alpha$5n outgoing channels in the $^{14}N + ^{159}Tb$ reaction at (a) $E_{^{14}N}$ = 95 MeV and (b) $E_{^{14}N}$ = 115 MeV, observed in the forward direction.

the $^{14}$N + $^{159}$Tb reaction at a) $E_{14_N}$ = 95 MeV and b) $E_{14_N}$ = 115 MeV.  The aluminium foil absorber used for 95 MeV $^{14}$N was 100 $\mu$m thick, and the one for 115 MeV $^{14}$N was 150 $\mu$m thick.  The $\alpha$-energies have been corrected for the effects of these absorbers.  It is seen that the $\alpha$-energy distribution for the $\alpha$3n channel possesses a double humped shape: the lower peak is at 18 MeV, about the Coulomb barrier for $\alpha$-emission, and the higher peak is at 29 MeV.  Here it should be reminded that $\gamma$-ray spectra observed in coincidence with fast $\alpha$-particles ($E_\alpha \geq 30$ MeV) are distinctly different from those of HI-induced compound nuclear reactions.[1], [2]  The high energy component with the peak at 29 MeV is naturally expected to relate to the above $\gamma$-ray observation.

It should also be noted that at $E_{14_N}$ = 115 MeV, possible peak position of high energy component is shifted towards higher energy by about 9 MeV compared with that at $E_{14_N}$ = 95 MeV.

The yield of high energy component at $E_{14_N}$ = 115 MeV is small compared with that at $E_{14_N}$ = 95 MeV.  This might be attributable to the difference in angular distributions for different incident energies provided the process leading to fast $\alpha$-particle emission is induced by a direct nuclear interaction between the projectile and the target nuclei: the maximum $\alpha$-yield for higher incident energies is expected to appear at smaller angles than that for lower incident energies.

Figure 2 shows energy distributions of $\alpha$-particles observed in the backward direction (the mean detection angle is 158.6° to the beam) for comparison.



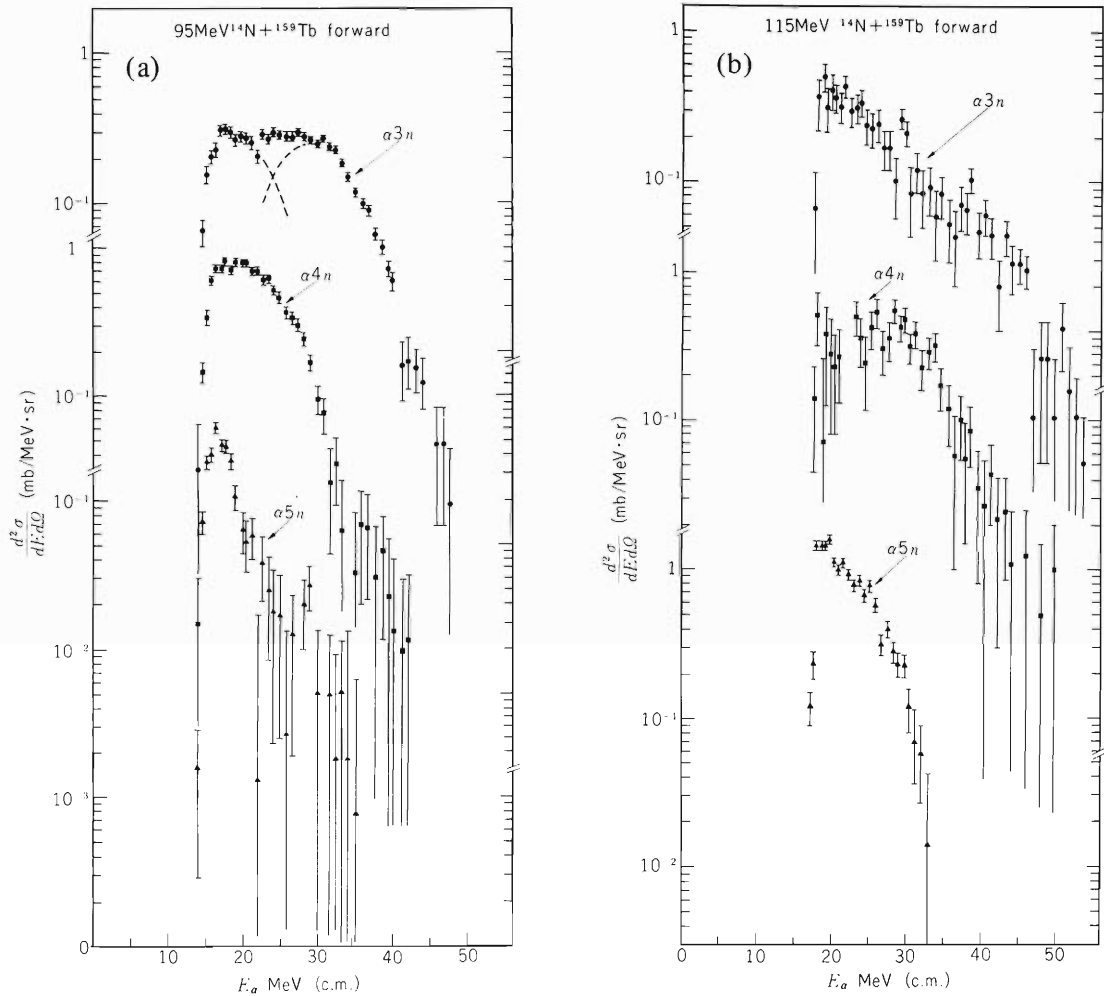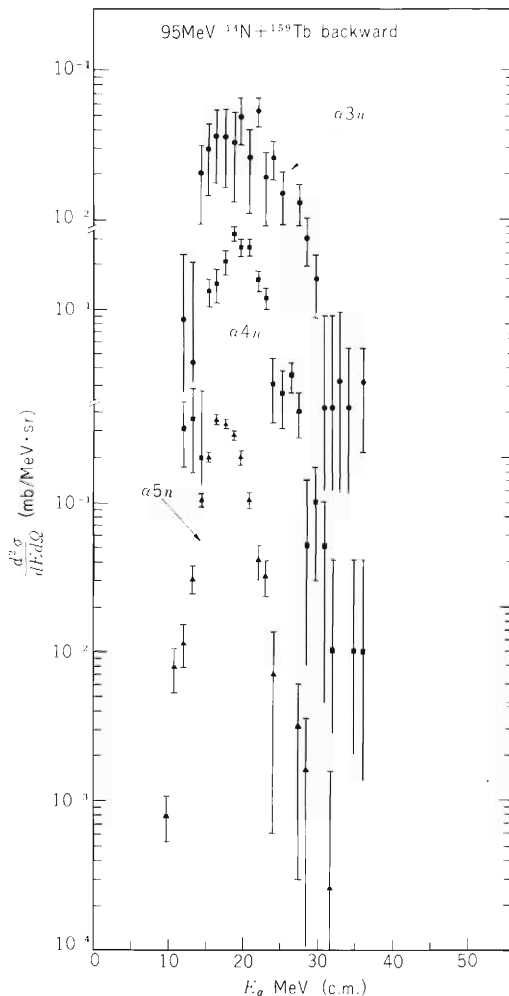Fig. 2.    $\alpha$-energy distributions for $\alpha$3n, $\alpha$4n, and $\alpha$5n outgoing channels in the $^{14}$N + $^{159}$Tb reaction at $E_{14_N}$ = 95 MeV, observed in the backward direction.

References

1) T. Inamura, M. Ishihara, T. Fukuda, T. Shimoda, and K. Hiruta: Phys. Lett., 68B, 51 (1977).
2) D. R. Zolnowski, H. Yamada, S. E. Cala, A. C. Kahler, and T. T. Sugihara: Phys. Rev. Lett., 41, 92 (1978).

# 5. NUCLEAR PHYSICS

## Nuclear Spectroscopy and Instrumentation

### 5-1. Recoil-distance Lifetime Measurements of States in $^{120}$Xe

T. Katou, H. Kumagai, Y. Tendow,
Y. Awaya, and A. Hashizume

Lifetimes of several levels in the ground state band of $^{120}$Xe were measured with a plunger apparatus reported before.[1]

A 60-MeV $^{14}$N beam from the cyclotron was used to populate the levels of interest by the $^{109}$Ag($^{14}$N, 3n) reaction. The target consisted of a 300 $\mu$g/cm$^2$ $^{109}$Ag layer evaporated onto a 1 mg/cm$^2$ thick gold foil. A thicker gold foil of 20 mg/cm$^2$ thickness was used to stop the recoil nuclei. The gamma-ray spectra were measured with a Ge(Li) detector placed at 0° to the beam axis at a distance of 5 cm from the stopper.

The gamma-ray spectra, gated by the beam bunch, corresponding to the transitions in the ground state band are shown in Fig. 1 for different target-stopper distance (D). The analysis of the gamma-ray spectra was carried out by means of least-squares fitting program in which some Gaussian peaks superimposed on a straight background were assumed. The peak areas $I_0$ and $I_s$ for the unshifted and shifted gamma-rays were obtained from the analysis. The areas of the
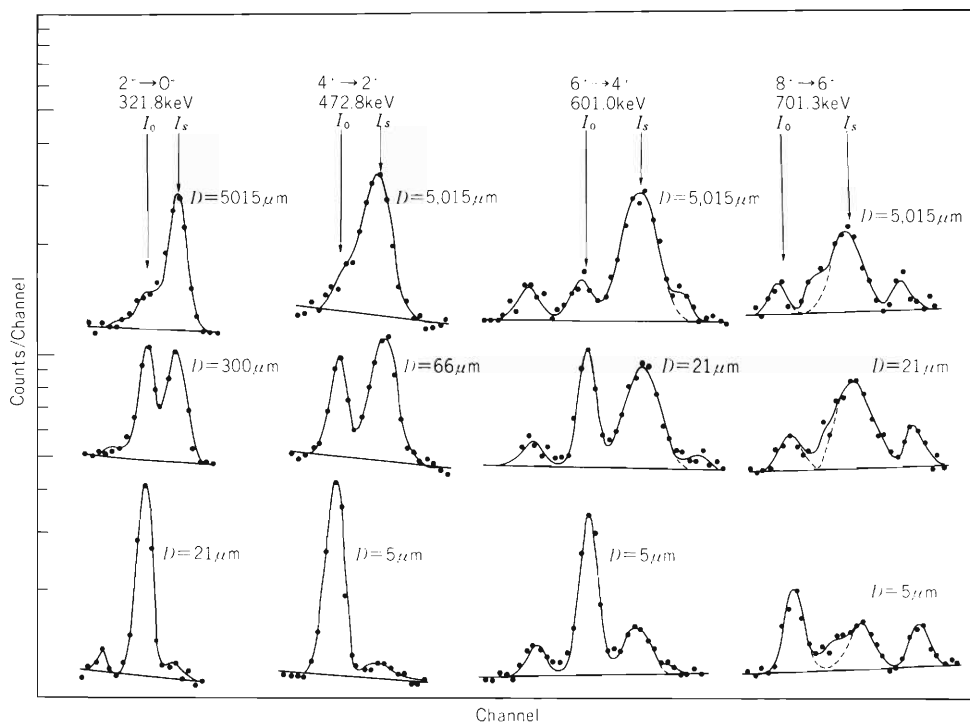


Fig. 1. Gamma-ray spectra for different target-stopper distances.
The solid lines are the results of the fitting procedure.

shifted components were corrected for the energy dependence of the Ge(Li) detector efficiency and for the large effective solid angle due to the nuclei's motion.  For each transition of interest the ratio $R = I_0/(I_0 + I_s)$ was plotted as a function of D.  The mean velocity of the recoil nuclei was determined to be 0.0080c from the difference in centroid energies of the two components.

Figure 2 shows the plot of R vs D for several states in $^{120}$Xe.  The constant background in the decay curves were observed and it may be due to the cascade transitions feeding from a long-lived isomer or from radioactive by-products.  Especially 601.0 keV (6+ → 4+) unshifted gamma-rays and gamma-rays from bombarded gold overlap each other.

In order to extract the lifetimes from the function R(D), we have followed the method of correction and the error analysis proposed by Kutschera et al.[2]

The lifetimes obtained in the present experiment are shown in Table 1 and are in good agreement with the values reported in Ref. 2.
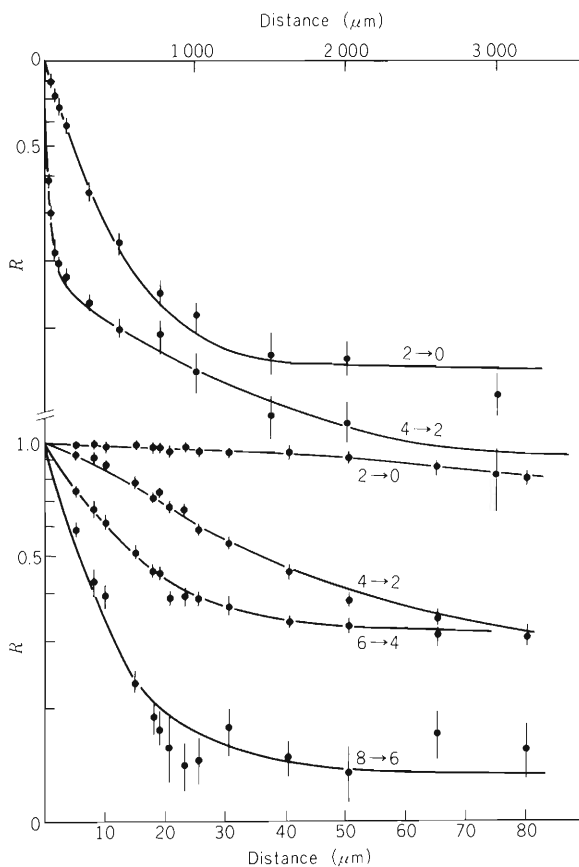


Fig. 2.　The ratio of the unshifted to total intensity for several transitions in $^{120}$Xe.  The solid lines are the results of the fitting procedure.

Table 1.　Lifetimes of levels in $^{120}$Xe.

| Transition | Energy (keV) | Lifetime (ps) present exp. | Ref. 2 |
|---|---|---|---|
| 2+ → 0+ | 321.8 | 122 ± 12 | 124 ± 15 |
| 4+ → 2+ | 472.8 | 11 ± 1.2 | 8.8 ± 1.8 |
| 6+ → 4+ | 601.0 | 3.0 ± 1.0 | (< 5.0) |
| 8+ → 6+ | 701.3 | (< 2.0) | |

70

References

1) T. Katou, H. Kumagai, Y. Tendow, Y. Awaya, and A. Hashizume: IPCR Cyclotron Progr. Rep., 11, 85 (1977).

2) W. Kutschera, W. Dehnhardt, O. C. Kistner, P. Kump, B. Povh, and H. J. Sann: Phys. Rev., C5, 1658 (1972).

## 5-2. Multiplicity of $\gamma$-Rays Following Fast $\alpha$-Particle Emission in the $^{159}$Tb + 95 MeV $^{14}$N Reaction

T. Kojima, T. Inamura, K. Hiruta, T. Nomura
T. Sugitate, and H. Utsunomiya

We have measured for the first time $\gamma$-multiplicity for fast $\alpha$-particle emission. A combination of $^{159}$Tb and 95 MeV $^{14}$N was chosen for the present study because it is one of typical reactions leading to fast $\alpha$-particle emission. A Si annular counter telescope (50 $\mu$m and 2000 $\mu$m) was used to detect $\alpha$-particles. The solid angle subtended was 0.52 sr ($\theta$ = 15.2° − 28.1° to the beam). Scattered beam was removed by a 100 $\mu$m thick Al absorber placed in front of the counter telescope. A NaI(Tl) detector (7.5 cm × 7.5 cm) was placed at 90° to the beam. The overall detection efficiency $\Omega$ of 1.02 % was realized with 10 % accuracy for any $\gamma$-rays of energy between 0.2 MeV and about 5 MeV by placing 4.6 mm thick Cu absorber in front of the detector and surrounding it with about 4 mm thick Cu and about 6 mm thick Pb. Low energy $\gamma$-rays, of energy below 170 keV, detected with NaI(Tl) were cut off by a discriminator. To specify the reaction channel, a 75 cm$^3$ Ge(Li) detector was placed at a distance of 4 cm from the target at 90° to the plane defined by the NaI(Tl) detector and the beam. Channel specifing $\gamma$-rays were as follows: for $\alpha$3n channel the 4 → 2 transition in $^{166}$Yb, for $\alpha$4n channel the 17/2 → 13/2 transition in $^{165}$Yb, for $\alpha$5n channel the 4 → 2 transition in $^{164}$Yb.

To extract the average $\gamma$-multiplicity $M_\gamma$, triple coincidences were demanded between the Si counter telescope, the Ge(Li) detector and the NaI(Tl) detector. $M_\gamma$ is given, to first order in $\Omega$, by $M_\gamma - 1 = N_{coin} / \Omega \cdot N_{singl}$, where $N_{singl}$ is the number of $\alpha$-particles recorded in coincidence with channel specifing $\gamma$-rays, and $N_{coin}$ is the number of triple coincidences for each reaction channel.

Table 1 presents the average $\gamma$-multiplicity measured for different kinetic energy ranges of $\alpha$-particles in c.m. Multiplicity of "Total Energy" was calculated from the integrated $\alpha$-spectrum. For comparison, $\gamma$-multiplicity following $\alpha$-particles emitted backwards is given in Table 2.

It is notable that for fast $\alpha$-particles ($E_\alpha \geq$ 26 MeV) the $\gamma$-multiplicity seems to decrease with increasing kinetic energy. For $\gamma$-rays in coincidence with $\alpha$-particles ($E_\alpha \geq$ 30 MeV), we have estimated the average angular momentum of entry state and obtained $I_m$ = 13 $\hbar$ in the $\alpha$3n channel from $\gamma$-intensities.[1] The average $\gamma$-multiplicity for $\alpha$-particles with energy $E_\alpha \geq$ 30 MeV is 9.3. If the average angular momentum removed by one $\gamma$ transition is assumed to be 1.5 $\hbar$, the value supposed to be reasonable in compound nucleus deexitation,[2] the value of $I_m$ becomes 16 $\hbar$. This value of $I_m$ is slightly larger than the value estimated from $\gamma$-intensity. Occurrence of such difference is, however, understandable because only statistical dipole transitions were assumed to feed the yrast band members in the latter estimation.

At present we do not make any correction for angular distribution effect, which is considered to be less than 20 %. Recently we have made a measurement at 125° to the beam. A detailed analysis is in progress.

Table 1. The average $\gamma$-multiplicity for $\alpha$-particles emitted in the forward direction in the $^{159}$Tb($^{14}$N, $\alpha$xn)$^{169-x}$Yb reaction.

| Reaction channel | $E_\alpha$ c.m. (MeV) | $M_\gamma$ |
|---|---|---|
| $\alpha$3n | (14.4 − 18.0 | 8.8 + 1.8) |
| | 16.0 − 20.0 | 12.8 + 2.2 |
| | 18.0 − 22.0 | 15.2 + 2.7 |
| | 22.0 − 26.0 | 15.9 + 2.5 |
| | 26.0 − 30.0 | 12.4 + 1.7 |
| | 30.0 − 34.0 | 9.8 + 1.4 |
| | 34.0 − | 8.3 + 1.5 |
| | Total energy | 12.2 + 1.6 |
| $\alpha$4n | (14.4 − 18.0 | 13.6 + 1.9) |
| | 18.0 − 22.0 | 12.5 + 1.6 |
| | 22.0 − 26.0 | 14.4 + 2.4 |
| | 26.0 − 30.0 | 7.2 + 2.1 |
| | 30.0 − | 5.9 + 2.3 |
| | Total energy | 12.3 + 1.3 |
| $\alpha$5n | (14.4 − 18.0 | 9.5 + 2.0) |
| | 18.0 − 22.0 | 11.8 + 3.7 |
| | 22.0 − | 13.8 + 8.8 |
| | Total energy | 10.8 + 2.1 |

Table 2. The average $\gamma$-multiplicity for $\alpha$-particles emitted in the backward direction in the $^{159}$Tb($^{14}$N, $\alpha$xn)$^{169-x}$Yb reaction.

| Reaction* channel | $E_\alpha$ c.m. (MeV) | $M_\gamma$ |
|---|---|---|
| | ( 0.0 − 14.4 | 7.6 + 0.8) |
| | 14.4 − 18.0 | 9.7 + 1.0 |
| $\alpha$3n | 18.0 − 22.0 | 9.7 + 1.0 |
| $\alpha$4n | 22.0 − 26.0 | 9.4 + 0.9 |
| $\alpha$5n | 26.0 − | 8.9 + 0.9 |
| | Total energy | 9.5 + 1.0 |

* Reaction channel are not specified.

References

1)  T. Inamura, M. Ishihara, T. Fukuda, T. Shimoda, and K. Hiruta: Phys. Lett., <u>68B</u>, 51 (1977).
2)  G. B. Hargeman, R. Broda, B. Herskind, M. Ishihara, S. Ogaza, and H. Ryde: Nucl. Phys., <u>A245</u>, 166 (1977).

A. Hashizume, T. Katou, Y. Tendow, and H. Kumagai

This study is one of the series of experiments on high spin states in Yb isotopes.[1]  Since $^{20}$Ne$^{6+}$ ions were accelerated successfully by pulsed operation of an ion source developed last year,[2] these ions were used to excite $^{160}$Yb by means of the $^{144}$Nd($^{20}$Ne, 4n) reaction.   A self-supporting and isotopically 97.8% enriched target of $^{144}$Nd was prepared by use of a vacuum evaporation where $^{144}$Nd$_2$O$_3$ was reduced by thorium.

Excitation functions in the incident energy range 100 - 150 MeV, $\gamma$-$\gamma$ coincidences and time spectra of $\gamma$-rays by using natural bunch of the cyclotron beam have been studied.   The $\gamma$-ray spectra of short life radioactivities were also examined by using the pulsed operation of the ion source.   The spectrum was observed about 3 ms after the activation of 1 ms for each modulation cycle of the ion source.

The high spin states in $^{160}$Yb have been studied by Ward et al.[3] and states up to 10$^+$ have been reported.   Figure 1 shows the sum of 5 coincidence spectra gated by the members of the ground state band from the 10$^+$ state.   Figure 2 shows excitation function for the $^{144}$Nd($^{20}$Ne, 4n) reaction taken by the 243.8 (2$^+$ → 0$^+$), 395.2 (4$^+$ → 2$^+$), 588.7 (8$^+$ → 6$^+$), and 636.0 (10$^+$ → 8$^+$) $\gamma$-rays.   The 508.8 keV (6$^+$ → 4$^+$) $\gamma$ rays reported by Ward could not be resolved from strong 511 keV annihilation $\gamma$-rays in singles spectra.   However, strong coincidences with 243 and 396 keV $\gamma$-rays were observed.   This proves that the 508 keV $\gamma$-transition is one of the members of ground state band.

Besides the transitions in the ground state band, 299.5, 404.0, 447.6, and 484.1 keV $\gamma$-rays were observed in the coincidence spectrum as shown in Fig. 1.   The excitation functions taken by these $\gamma$-rays show the same characteristics as those in the ground state band.   However, $\gamma$-$\gamma$ coincidence spectrum without gates shows the existence of unresolved peaks around the energy
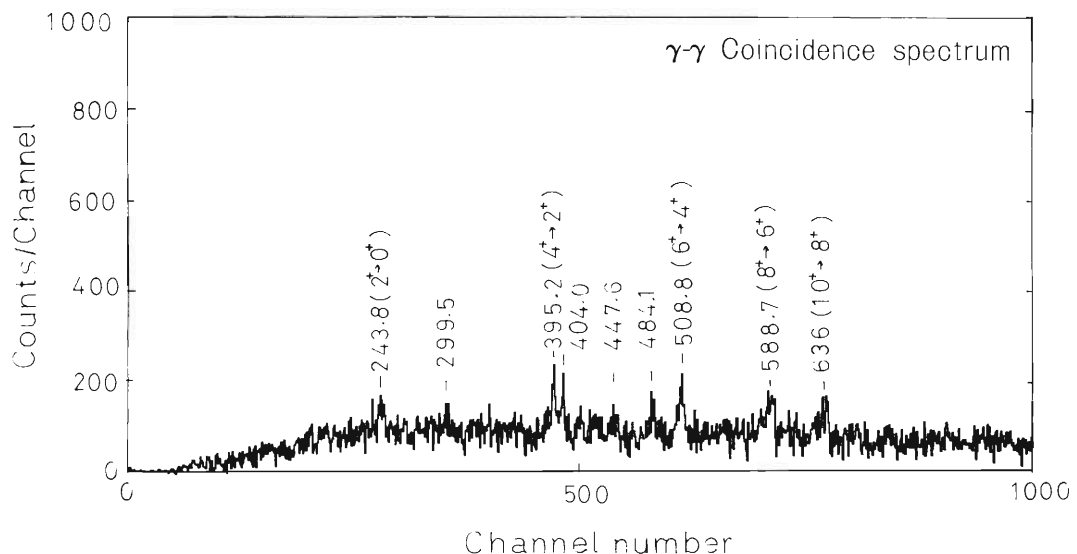


Fig. 1.   The sum of 5 spectra obtained by $\gamma - \gamma$ coincidences gated by the cascade transitions from 10$^+$ to the ground state.
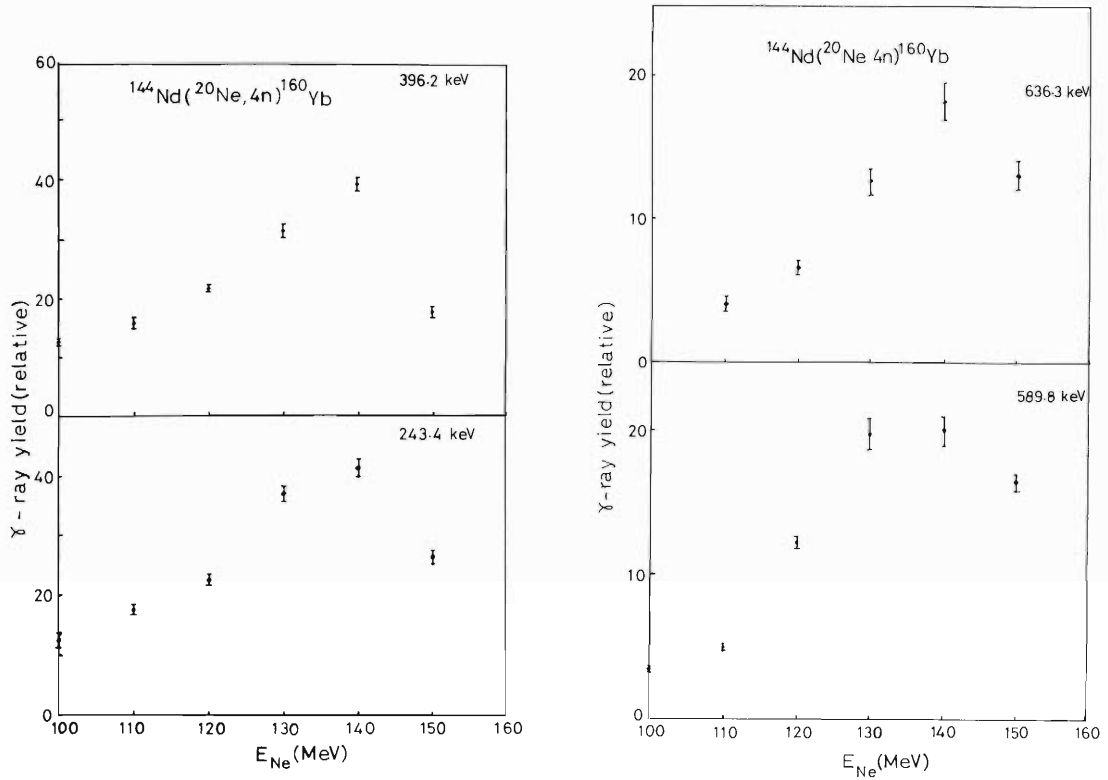
Fig. 2.    Excitation functions of levels of the ground state rotational band in $^{160}$Yb.

of $8^+ \rightarrow 6^+$ and $10^+ \rightarrow 8^+$ transitions.    As the above 4 $\gamma$ rays coincide in energy with that of $8^+ \rightarrow 6^+$ or $10^+ \rightarrow 8^+$ transition, more information is needed before concluding that they result from the transitions in $^{160}$Yb.    To elucidate this situation, more detailed study of coincidence spectra is in progress by choosing the gate position carefully for examining the data stored event by event in magnetic tapes.

The moments of inertia of the states up to $10^+$ in $^{160}$Yb change smoothly as a function of the square of rotational frequency.    However, from the systematic feature of the backbending curves of Yb isotopes and coincidence data, it is suggested that the backbending occurs from $12^+$ state in $^{160}$Yb.

## 5-4. Conversion Electrons in the Decay of $^{206}$Bi

A. Hashizume, T. Kimura, Y. Tendow,
and T. Hamada

$^{206}$Pb is a nucleus which has two neutron holes coupled with the closed shell core of $^{208}$Pb and the low-lying states are expected to be described by the shell-model.   Although the energy levels excited by the decay of $^{206}$Bi were established, the multipolarity mixing ratios of many transitions are not yet determined and their mixing ratios will be one of the sensitive tests of the theories.   Another point of interest in $^{206}$Bi is that it will be used for a conversion electron standard source for energy and efficiency calibration of solid state detectors, if the intensities of conversion electrons are well established.

The $^{206}$Bi(6.24 d) activity was prepared by bombarding natural lead (99.999 %) with 15 MeV protons for 5 to 20 h.   After removing most part of lead by precipitation, bismuth was separated from the target element by ion exchange method, and electro-deposited onto a 5 $\mu$m nickel foil to obtain a 1 $\times$ 15 mm$^2$ source.

The spectra of conversion electrons were taken by a double-focusing iron-free $\beta$-ray spectrometer with mean radius of 50 cm.   The typical spectra are shown in Figs. 1 and 2.   Preliminary results of some relative conversion electron intensities of 184 and 262 keV transitions are shown in Table 1.

The 2.384 MeV 6$^-$ state de-excites to 2.200 MeV 7$^-$ state by the 184.02 keV transition. The type of the transition is a nearly pure M1.   As the ratios of the internal conversion in L subshells are very sensitive to multipole orders, the L subshell-ratios are measured at resolution setting of 0.06 % of the spectrometer.   The results were $L_I/L_{II}$ = 9.06 $\pm$ 0.19, $L_I/L_{III}$ = 115.8 $\pm$ 19.7, and $L_{II}/L_{III}$ = 12.8 $\pm$ 2.2.   In view of the values of conversion coefficients calculated by Hager and Zeltzer, the mixing ratios determined by using these $L_I/L_{II}$, $L_I/L_{III}$, and $L_{II}/L_{III}$ were
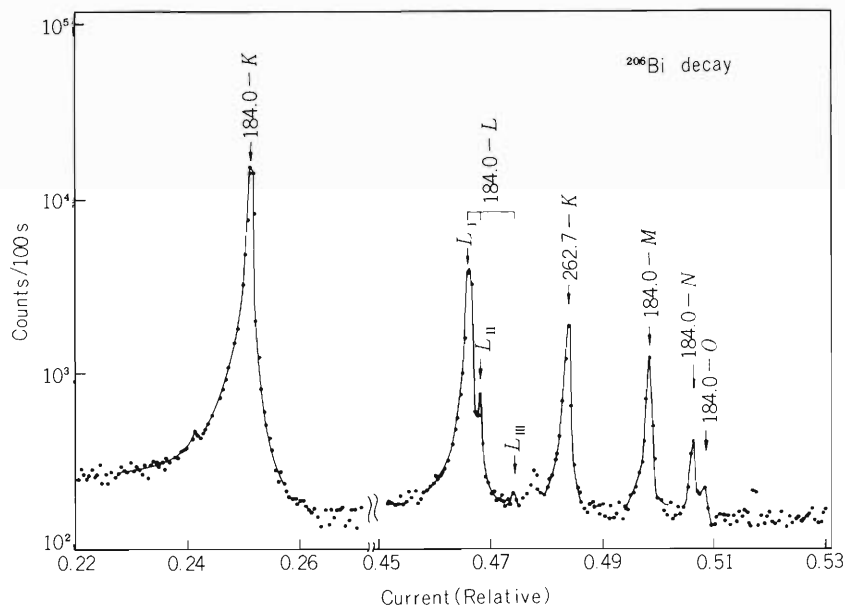


Fig. 1.   Conversion electron spectrum in $^{206}$Pb.
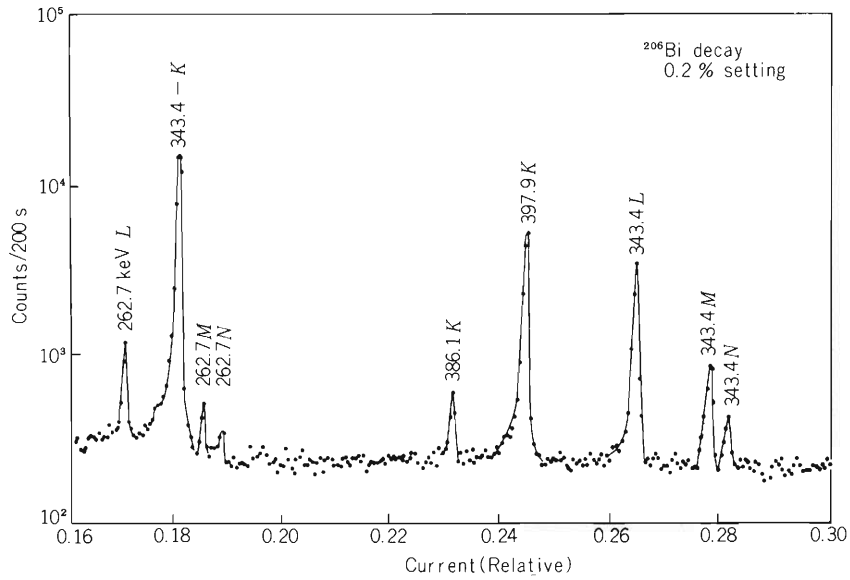
Fig. 2.   Conversion electron spectrum in $^{206}$Pb.

Table 1.   Conversion electron intensities of 184 and 263 keV
transitions in $^{206}$Pb for the decay of $^{206}$Bi.

| Transition energy | Shell | Electron energy | Intensity of CE |
|---|---|---|---|
| | K | 96.02 | 1000 |
| | L | 168.16 | 154.0 ± 2.1 |
| 184.02 ± 0.03 | M | 180.16 | 35.8 ± 1.1 |
| | N | 183.12 | 8.4 ± 0.7 |
| | O | 183.8 | 1.6 ± 0.4 |
| | K | 255.50 | 675.0 ± 5.0 |
| 262.70 ± 0.05 | L | 327.64 | 78.6 ± 1.7 |
| | M | 339.69 | 25.3 ± 1.2 |
| | N | 342.67 | 9.2 ± 0.9 |
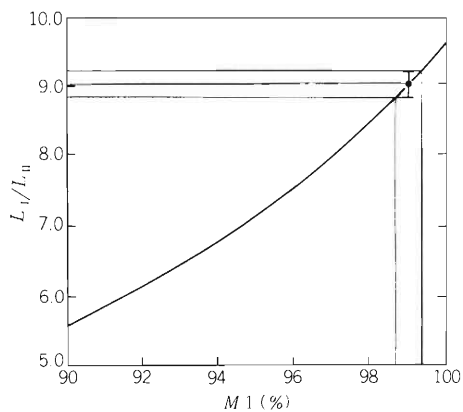


Fig. 3.   The M1-E2 mixing determined
by $L_I/L_{II}$ of the 184.02 keV transition.

1.0 ± 0.4 (Fig. 3), 0.2 ± 0.4, and 0.1 ± 0.5 %, respectively.   The errors cited are statistical ones. Due to the smallness of $L_{III}$ peak, the experimentally obtained values of $L_I/L_{III}$ and $L_{II}/L_{III}$ contain probably some systematic errors.   From the value of $L_I/L_{II}$, it can be concluded that the 184.02 keV transition has very small E2 admixture of (1.0 ± 0.4) % to M1.   The conversion electrons of higher energy are now under investigation.

# 6.  ATOMIC AND SOLID-STATE PHYSICS

## 6-1.  X-Rays Following Multiple Inner-Shell Ionization  (3)

Y. Awaya, T. Katou, H. Kumagai, T. Tonuma,
Y. Tendow, K. Izumo, T. Takahashi, A. Hashizume,
M. Okano, T. Hamada, and S. Özkök

The spectra of Y K and L X-rays excited by 6 MeV/amu N-ions and $\alpha$-particles were measured using a Bragg crystal spectrometer.[1]    A flat crystal of LiF(200) and a detection system of scintillation counter were used for K X-ray measurements.    By considering the energy values of K diagram line and $KL^n$ satellite lines extrapolated from the previous work,[2] the third reflection in the Bragg condition was adopted for $K\alpha$ X-ray measurement and the second reflection for $K\beta$ X-ray measurement.    The use of crystals of LiF(220) and LiF(420) was also tested and we found the LiF(200) crystal to be the best.    The L X-rays were measured by adopting a crystal of EDDT(020) and a detection system of proportional counter.    The Y target was a self-supporting metallic foil of $\sim$0.8 mg/cm$^2$ in thickness.

The $K\alpha$ and $K\beta$ spectra are shown in Figs. 1 and 2, respectively.    The $K\alpha$ spectrum obtained by N-ion bombardment was resolved by least square fitting of the multiple Gaussian curves and we found that the energy differences between the $K\alpha_1$ and $KL\alpha_1$ lines and between
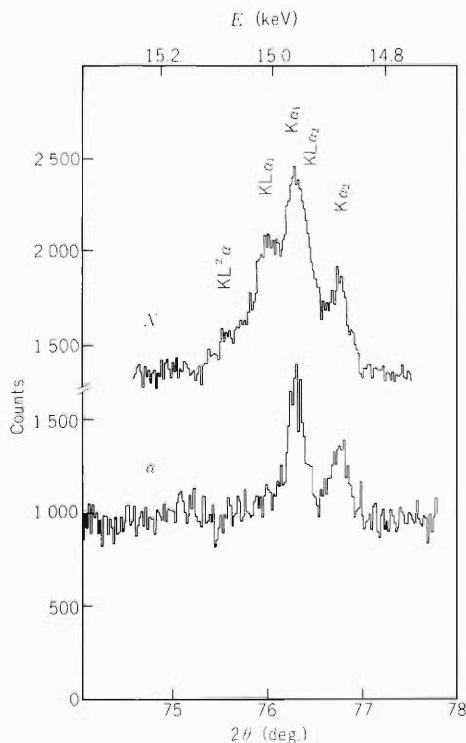


Fig. 1.    Y $K\alpha$ X-ray spectra induced by 6 MeV/amu N-ions and $\alpha$-particles.
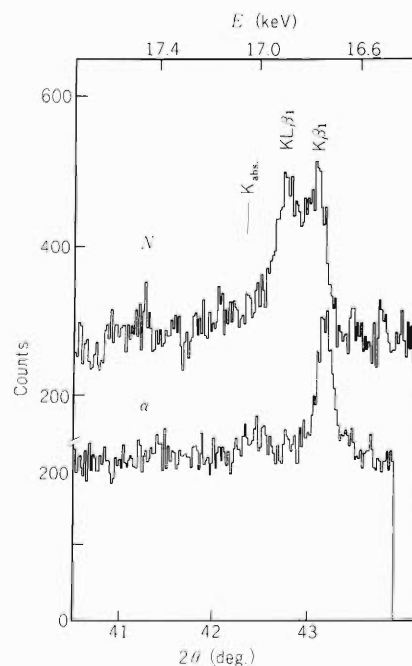


Fig. 2.    Y $K\beta$ X-ray spectra induced by 6 MeV/amu N-ions and $\alpha$-particles.

$K\alpha_2$ and $KL\alpha_2$ lines are $\sim 50$ eV and the relative intensity of the $KL\alpha_1$ to the $K\alpha_1$ line and that of the $KL\alpha_2$ line to the $K\alpha_2$ line take similar values. The energy values of $K\alpha_1$ and $K\alpha_2$ lines induced by N-ion bombardment agree with those induced by $\alpha$-particles within the limit of error, whereas the energy value of $K\beta_1$ line excited by N-ions is about 35 eV higher than that excited by $\alpha$-particles. This is due to the effect of the vacancies in the M-shell in addition to the K vacancy. The parameter $P_L(0)$[3] obtained for Y is shown in Fig. 3 in comparison with previous data.[3] The change of the fluorescence yield was not taken into account for the case of Y.

The spectra of L X-rays are shown in Fig. 4. The $LM^n$ lines whose origin is considered to be the single L plus n M vacancies are observed for $L\alpha$ and $L\beta_1$ X-rays. The arrows on the $L\alpha$ X-rays in Fig. 4 indicate the result of the Hartree-Fock-Slater calculation obtained by using the Herman-Skillman's program for single L and n M-shell vacancies and for double L-shell vacancies. The $L\ell$ X-rays could not be observed for the case of N-ion bombardment because of the high background (caused mainly by $\gamma$-rays following nuclear reactions and radioactivities) and multiple ionization.

A further analysis is in progress.
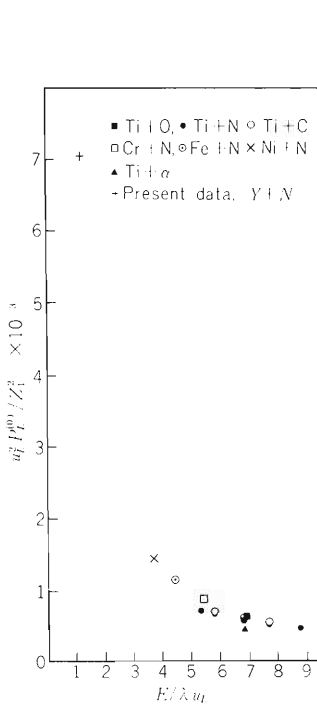


Fig. 3.   Plot of $P_L$ (0).
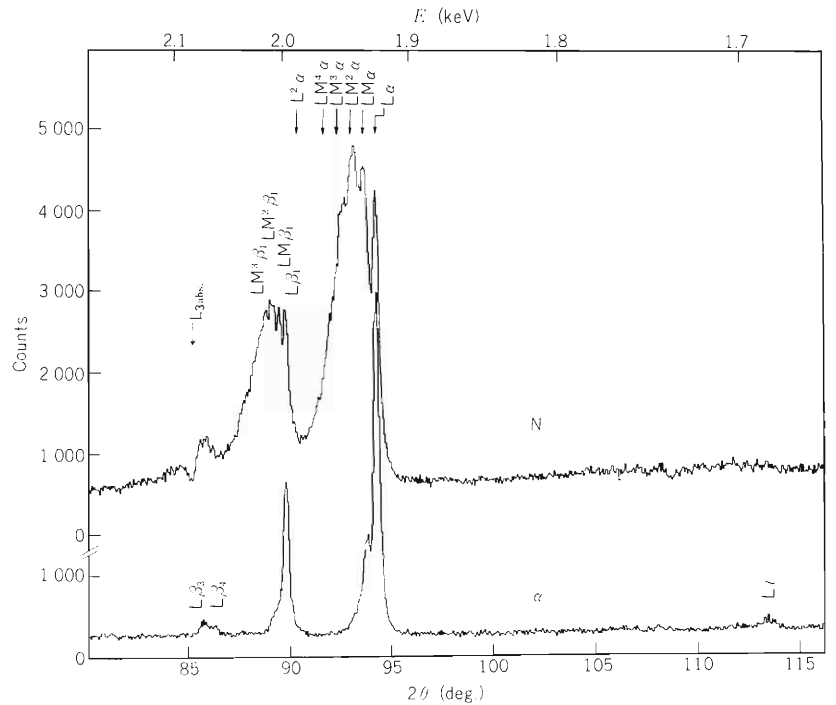


Fig. 4.   Y L X-ray spectra induced by 6 MeV/amu N-ions and $\alpha$-particles.

References

1)   Y. Awaya, Y. Tendow, H. Kumagai, M. Akiba, T. Katou, and T. Hamada: IPCR Cyclotron Progr. Rep., 9, 79 (1975); H. Kumagai, Y. Awaya, Y. Tendow, T. Katou, and M. Akiba: Reports I.P.C.R., (in Japanese), 53, 153 (1977).

2)   Y. Awaya, M. Akiba, T. Katou, H. Kumagai, Y. Tendow, K. Izumo, T. Takahashi, A. Hashizume, M. Okano, and T. Hamada: Phys. Letters, 61A, 111 (1977); IPCR Cyclotron Progr. Rep., 10, 78 (1976).

3)   Y. Awaya, K. Izumo, T. Hamada, M. Okano, A. Hashizume, T. Takahashi, Y. Tendow, H. Kumagai, T. Katou, and T. Tonuma: IPCR Cyclotron Progr. Rep., 11, 93 (1977).

# 6-2. Kα X-Ray Spectra of Ar Produced by Impact of N-Ions in the 66-110 MeV Energy Range

T. Tonuma, Y. Awaya, T. Kambara, H. Kumagai,
I. Kohno, and S. Özkök*

Change in the Kα X-ray spectra from argon is studied as a function of the argon target thickness and of the nitrogen ion energy in the 66 − 110 MeV range. The spectra were observed using a crystal spectrometer.[1] As the argon target a gas chamber of relatively high pressure was used.[2] The highest pressure used was 300 Torr. The mean charge state of nitrogen ions was 6.8 − 6.9 after passing through the entrance window and the argon target.[3]

In Fig. 1 are shown Ar K X-ray spectra induced by 86 MeV N-ions when the argon gas pressure is 300 Torr. The X-rays were detected by using a combination of a Ge(111) crystal and a side-window gas-flow proportional counter placed in the vacuum chamber. The energy resolution was 11 eV (full width at half-maximum) at 2.98 keV. The pressure of the argon target was monitored by an α-tron gauge throughout the experiment. The incident energy of 95 MeV N-ions reduced to 86 MeV at the center of the argon target owing to the energy loss of beams by an Al foil window and the argon gas. (The energy of N-ions described below is that at the center of the gas target). The peak in the figure is labelled by a symbol such as $K^m L^n$ which denotes the initial configuration having m K-shell and n L-shell vacancies. The K-shell absorption edge is denoted by $K_{abs}$ with an arrow. The values of energy differences between the $K\alpha_{1,2}$ diagram peaks and $KL^n\alpha$ satellite peaks, between $K^2\alpha$ and $K^2L^n\alpha$, and between the $K\alpha_{1,2}$ and $K^2\alpha$ are shown in Table 1. Those values agree with values obtained from X-ray energy difference data of the solid targets under the 84 MeV N-ion bombardment, by interpolating with respect to the target atomic number.[1] The energy difference between the $K\alpha_{1,2}$ and $K^2\alpha$ also agrees with that
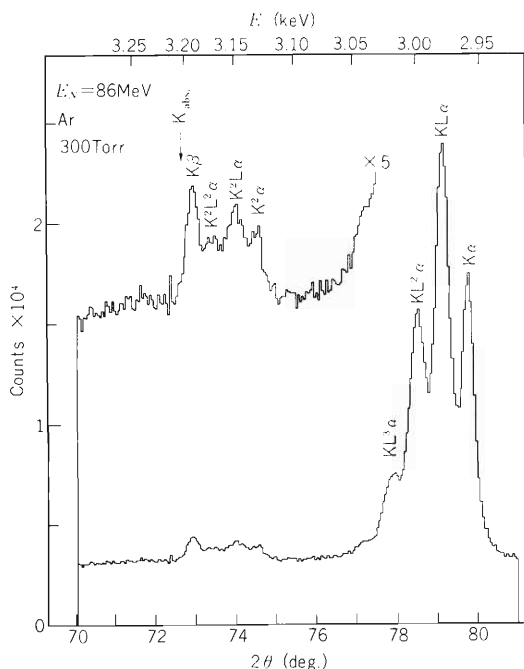


Fig. 1. Ar K X-rays spectra produced by 86 MeV N-ions impact. Ar gas pressure is 300 Torr.

* University of Istanbul Nuclear Physics Department, Istanbul, Turkey.

of Kelly and Palumbo who obtained by plasma excitation method.[4]

Kα X-ray spectra of argon were measured setting the gas pressure to 9.4, 110, and 290 Torr, respectively, to examine an influence of the target density. The energy of N-ions was adjusted to keep constant at 74 MeV at the center of the gas target even when the gas pressure was changed. In Table 2 are shown percentage of $KL^n\alpha$ in the Kα total intensity by fitting spectra by Gaussian form. Change of Ar Kα spectra due to change of gas pressure was not observed within experimental errors.

Table 1. Energy difference between $K\alpha_{1,2}$ and $KL^n\alpha$, between $K^2\alpha$ and $K^2L^n\alpha$, and between $K\alpha_{1,2}$ and $K^2\alpha$ of Ar target.

| $KL^n\alpha - K\alpha_{1,2}$ | $\Delta E(eV)$ |
|---|---|
| n = 1 | 21 |
| n = 2 | 40 |
| n = 3 | 61 |

| $K^2L^n\alpha - K^2\alpha$ | $\Delta E(eV)$ |
|---|---|
| n = 1 | 18 |
| n = 2 | 40 |

| $K^2\alpha - K\alpha_{1,2}$ | $179 \pm 2$ |
|---|---|

Table 2. Relative intensity of Ar $KL^n$ X-rays vs. Ar target pressure.

| $KL^n$ (%) | P (Torr) | | |
|---|---|---|---|
| | 9.4 | 110 | 290 |
| K | $19.5 \pm 1.0$ | $20.5 \pm 1.0$ | $21.0 \pm 0.5$ |
| KL | $37.5 \pm 1.0$ | $35.5 \pm 1.5$ | $35.3 \pm 0.5$ |
| $KL^2$ | $29.5 \pm 1.0$ | $30.5 \pm 1.5$ | $28.0 \pm 0.5$ |
| $KL^3$ | $11.5 \pm 1.0$ | $10.5 \pm 1.5$ | $10.5 \pm 1.0$ |
| $KL^4$ | $1.5 \pm 0.5$ | $3.0 \pm 1.0$ | $3.5 \pm 1.0$ |

Variation of the relative intensities of each peaks produced by bombardment of argon by N-ions having an energy between 66 and 110 MeV are shown in Fig. 2. The relative intensities of $KL^n$ X-rays are converted to the relative ionization cross sections by using the calculated fluorescence yield $\omega_{KL}n$.[5] $P_L$ (0), which is the probability of single ionization for L-shell with eight electrons, is determined by the least-squares fit, considering the relative ionization cross section for each $KL^n$ configuration to be a binomial distribution. In Fig. 3 is shown $P_L$ (0) as a function of N-ions energy. $P_L$ (0) decreases linearly with N-ion energy and may be approximated
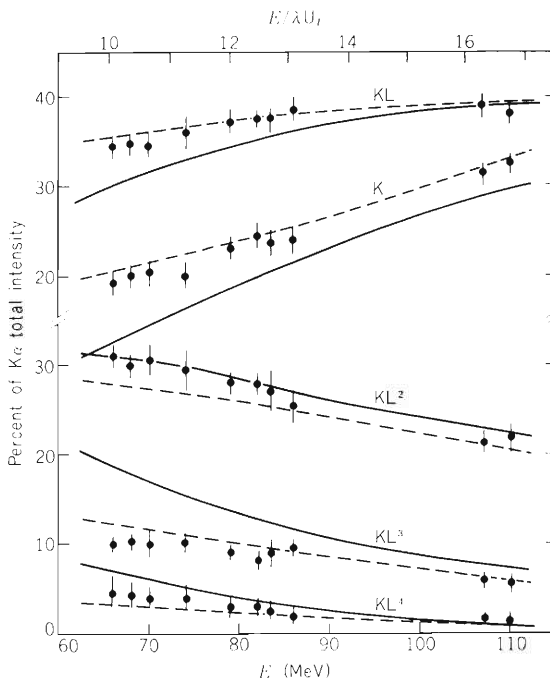


Fig. 2. Relative intensity of Ar K X-rays vs. N-ion energy and $E/\lambda U_L$, where $U_L$ is the binding energy of the Ar L electron and $\lambda$ is the mass of projectile in electron mass unit. Solid curves are calculated by BEA and dotted curves are estimated by using $P_L$ (0) shown in Fig. 3 with the dotted line.
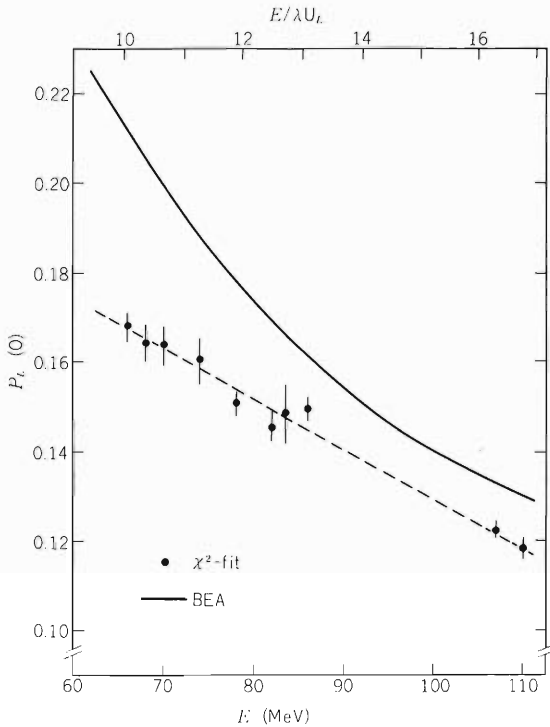
Fig. 3. $P_L(0)$ vs. N-ion energy and $E/\lambda U_L$. $P_L(0)$ shown with solid points are determined by the least squares fitting. Dotted line is drawn to guide the eye. Solid curve is calculated by BEA.

by a linear dotted line which is drawn to guide the eye in the figure. The $P_L(0)$ as given by the dotted line is converted to the relative intensity of $KL^n$ X-ray and is shown in Fig. 2 with dotted curves. Inner shell ionization cross section has been explained by the binary encounter approximation (BEA) under the condition of $Z_1 \ll Z_2$, where $Z_1$ and $Z_2$ are the atomic number of the projectile and the target element, respectively. The ionization probability $P_L(0)$ is computed by using the combination of BEA and the impact parameter formula.[6] The calculated $P_L(0)$ and the relative intensity $KL^n$ X-ray are shown by solid curves in Fig. 3 and Fig. 2, respectively, though the condition $Z_1 \ll Z_2$ is not satisfied in the present case.

In conclusion, the change of Ar $K\alpha$ X-ray spectra owing to the target thickness was not observed in the 10 − 300 Torr pressure region. The relative multiple ionization cross section fit a binomial distribution reasonably well in the high energy region of nitrogen ions of the present experiment. The ionization probability $P_L(0)$ decreases monotonically with the nitrogen energy and differs from 1/E dependence which the BEA theory predicts.

References

1) Y. Awaya, M. Akiba, T. Katou, H. Kumagai, Y. Tendow, K. Izumo, T. Takahashi, A. Hashizume, M. Okano, and T. Hamada: Phys. Lett., 61A, 111 (1972).

2) T. Tonuma, Y. Awaya, T. Kambara, H. Kumagai, and I. Kohno: IPCR Cyclotron Progr. Rep., 11, 16 (1977).

3) T. Tonuma, I. Kohno, Y. Miyazawa, F. Yoshida, T. Karasawa, T. Takahashi, and S. Konno: J. Phys. Soc. Japan, 34, 148 (1973).

4) R. L. Kelly and L. J. Palumbo: Naval Research Laboratory Report, p. 7559 (1974).

5) F. P. Larkins: J. Phys., B4, L29 (1971).

6) J. H. MaGuire and P. Richard: Phys. Rev., A8, 1374 (1973).

## 6-3.  Relative Intensity of Kr K$\beta$ X-Rays above Absorption Edge

T. Tonuma, Y. Awaya,

T. Kambara, H. Kumagai, and I. Kohno

K$\beta$ X-ray spectra induced by heavy ion bombardment have satellite KL$^n\beta$ similar to KL$^n\alpha$.   It is difficult, however, to detect some KL$^n\beta$ satellites of which energies are above the absorption edge, because of self-absorption and decrease of X-ray yields.   When $n \geq 2$, the KL$^n\beta$ energy of Kr target is expected to be above the absorption edge (14.323 keV) by the analogy with the K$\beta$ spectra of Y target observed with a crystal spectrometer (see 6-1 in this Report).   We estimated relative intensity of KL$^n\beta$ ($n \geq 2$) from Kr target by the following method, using a Si(Li) detector.

Expressing by "a" the ratio of intensity of K$\beta$ lines lying above the absorption edge to that of the total K$\beta$ lines when there is no self-absorption, the measured intensity ratio $I_{K\beta}/I_{K\alpha}$ of K$\beta$ and K$\alpha$ lines is given by

$$\frac{I_{K\beta}}{I_{K\alpha}} = \left(\frac{I_{K\beta}}{I_{K\alpha}}\right)_0 \cdot \frac{(1-a)e^{-\sigma_1 m} + a e^{-\sigma_2 m}}{e^{-\sigma m}} \quad ,$$

where $\sigma_1$ and $\sigma_2$ are cross sections of self-absorption below and above the absorption edge of K$\beta$ spectra, respectively, and $\sigma$ is that for K$\alpha$ spectra region.   m is the thickness the photons have to
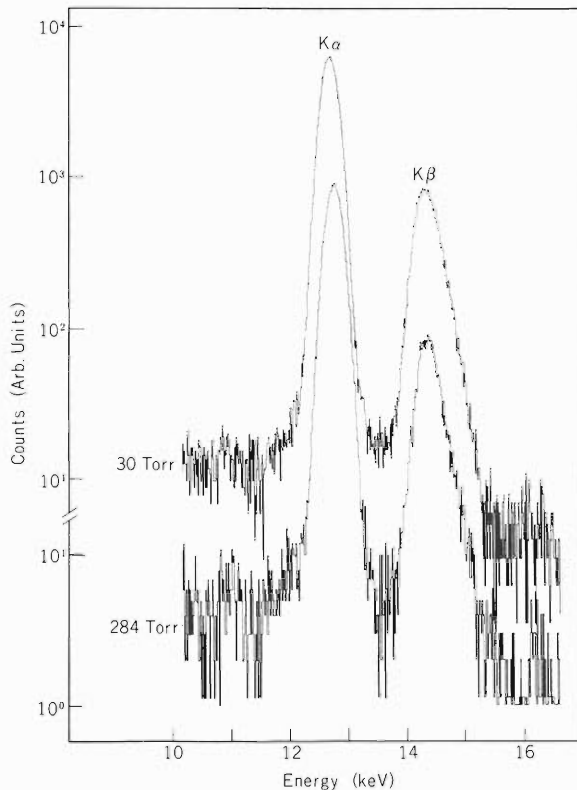


Fig. 1.   K$\alpha$ and K$\beta$ spectra of Kr target induced by 6 MeV/amu Ne ions.   Kr gas pressures were 30 and 284 Torr.   Spectra were observed with a Si(Li) detector.
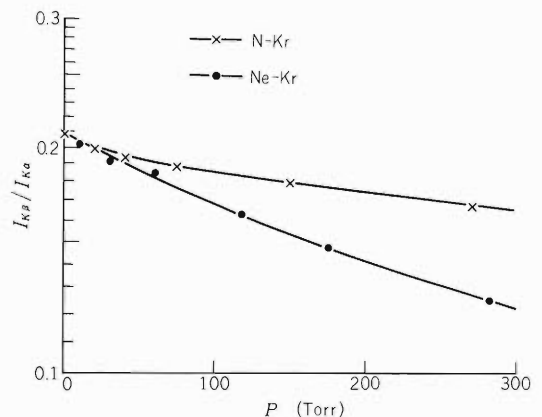
Fig. 2.   $I_{K\beta}/I_{K\alpha}$ ratios of Kr X-rays induced by 6 MeV/amu N and Ne ions as a function of Kr target pressure. Solid lines are drawn to guide the eye.

go through in the Kr gas target to reach the detector. $(I_{K\beta}/I_{K\alpha})_0$ is the $I_{K\beta}/I_{K\alpha}$ ratio without self-absorption, that is, when gas pressure approaches zero. The measurement of $I_{K\beta}/I_{K\alpha}$ varying Kr gas pressure can give the relative intensity "a".

A gas chamber with windows for beam entrance and exit was used to measured $K\alpha$ and $K\beta$ X-ray yields from Kr target.[1] Self-absorption of K X-rays occurs between the center of the target and the Be window, the distance of which was 77 mm, in the chamber. The attenuation of K X-rays by the Be window and by air between the chamber and the Si(Li) detector was negligible. The size of the heavy ion beam spot was less than 5 mm in diameter. Figure 1 shows $K\alpha$ and $K\beta$ spectra of Kr target obtained by the bombardment of 6 MeV/amu Ne ions. The pressures of the target gas were 30 and 284 Torr, respectively. The energy resolution of the Si(Li) detector was 280 eV (full width at half-maximum) for 14.39 keV $\gamma$-rays emitted by a $^{57}$Co source. The gas pressure was measured with an $\alpha$-tron gauge the accuracy of which was 10 percent. Figure 2 shows intensity ratios $I_{K\beta}/I_{K\alpha}$ of K X-rays from Kr gas target induced by 6 MeV/amu N and Ne ions as a function of Kr gas pressure. Table 1 shows the estimated "a" and $(I_{K\beta}/I_{K\alpha})_0$ using values of $\sigma_1$, $\sigma_2$, and $\sigma$ in Ref. 2.

Table 1. Ratio of $K\beta$ intensity "a" above the absorption edge to that of the total $K\beta$ of Kr target X-rays induced by bombardment of 6 MeV/amu N and Ne ions. $(I_{K\beta}/I_{K\alpha})_0$ is the intensity ratio of $K\alpha$ and $K\beta$ when there is no self-absorption at nearly zero pressure.

|  | a | $(I_{K\beta}/I_{K\alpha})_0$ |
| --- | --- | --- |
| N ion | 0.35 ± 0.03 | 0.205 ± 0.002 |
| Ne ion | 0.61 ± 0.05 | 0.207 ± 0.002 |

In conclusion, we see that it is found the ratio of $K\beta$ intensity "a" above the absorption edge to that of the total $K\beta$ lines increases with the atomic number $Z_1$ of the incident particle. The increase of "a" means that intensity of higher order satellites of Kr $KL^n\beta$ produced by heavy ion bombardment increases with $Z_1$. The ratios $(I_{K\beta}/I_{K\alpha})_0$ obtained for two different kinds of ions, N and Ne ions, but of the same velocity are almost the same.

References

1) T. Tonuma, Y. Awaya, T. Kambara, H. Kumagai, and I. Kohno: IPCR Cyclotron Progr. Rep., 11, 96 (1977).

2) Wm. J. Veigele: Atomic Data, 5, No. 1, 64 (1973).

# 6-4. REC X-Rays by 120 MeV Ne-Gases Collisions

T. Tonuma, Y. Awaya, T. Kambara,

H. Kumagai, and I. Kohno

Highly stripped heavy ion can capture a free or weakly bound target electron directly into the K-shell vacancy with subsequent emission of an X-ray photon. This process is known as radiative electron capture (REC).[1] The energy of the photon is given approximately by the sum of the binding energy of a K electron in a hydrogen-like or helium-like ion and the kinetic energy of an electron which is at rest in the target, relative to the moving ion.

About 20 % of 120 MeV $Ne^{6+}$ accelerated by the cyclotron change to $Ne^{9+}$ and 80 % to $Ne^{10+}$ when the ions reach the center of the gas chamber after passing through the foil at the entrance of the chamber. Therefore, the REC X-rays are mostly those of $Ne^{10+}$ and the energy lies in the neighbourhood of 4 keV. Figure 1 shows REC X-ray spectra from 120 MeV Ne ions colliding with gaseous targets of $H_2$, $N_2$, Ne and Kr. Spectra were detected by a Si(Li) X-ray detector which was placed perpendicular to the beam direction. The energy resolution of the detector was 230 eV (full width at half-maximum) at 6.4 keV. The gas pressures of $H_2$, $N_2$, Ne, and Kr targets were measured with an α-tron gauge and were 180, 200, 300, and 13 Torr, respectively. Energy shifts of REC X-ray peaks in the spectra shown with arrows come mainly from different kinetic energies of Ne ions at the center of the target gas since the ions experience different energy losses in different kinds of gases and gas pressures in traversing the distance of 70 mm between the entrance window and the center of the chamber.
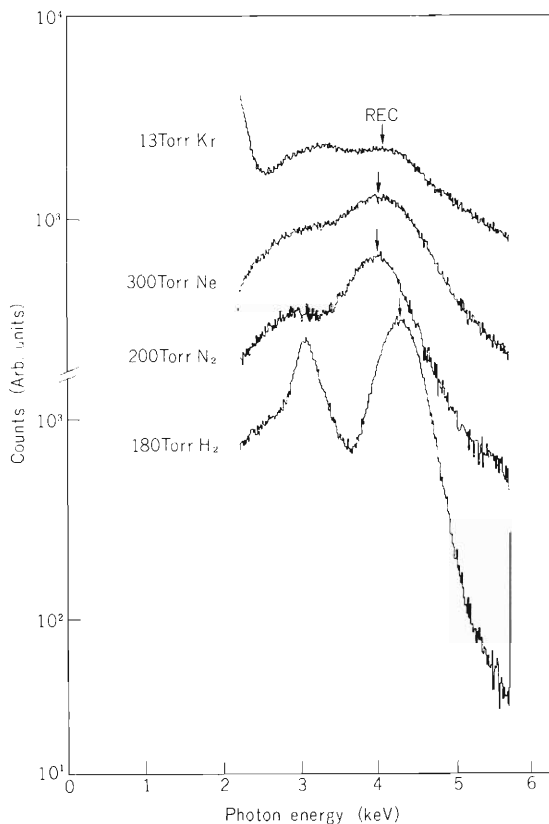


Fig. 1. REC Spectra observed in 120 MeV Ne ions-$H_2$, $N_2$, Ne, Kr collisions. The arrows indicate Ne REC peak energy in gases.

Figure 2 shows the relation between the energy width (FWHM) of REC X-ray spectra and the atomic number $Z_T$ of target. It has been found that the width is approximately proportional to $(Z_T)^{1/2}$. Further study of REC is in progress.
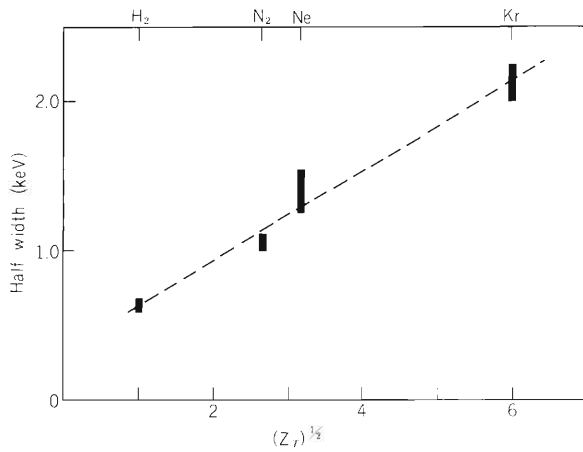


Fig. 2. Half width of Ne REC spectra vs. atomic number $Z_T$ of targets. The dotted line is drawn to guide the eye.

References

1) H. W. Schnopper, Hans D. Betz, J. P. Delvaille, K. Kalata, and A. R. Sohval: Phys. Rev. Letters, 29, 898 (1972).

2) J. B. Marion and F. C. Young: "Nuclear Reaction Analysis Graphs and Tables", North-Holland, p. 45 (1968).

3) T. Tonuma, Y. Awaya, T. Kambara, H. Kumagai, and I. Kohno: IPCR Cyclotron Progr. Rep., 11, 96 (1977).

# 6-5.  Dependence of F Kα Satellite Intensities Produced

## by Fast Ions on Chemical Environment

M. Uda, H. Endo, K. Maeda,

M. Kobayashi, and Y. Sasa

Chemical effect reflected in characteristic X-rays with satellite structure has received much attention in recent years.   X-ray spectra produced by fast ion impact have shown dramatic change in intensity distributions from one compound to another, and some attempts have been made to explain the distributions.   However, discussion in this field is still a matter of conjecture.[1] – [3]

A quantitative analysis of the satellite intensity distributions has been performed on F Kα spectra of several fluorides induced by p, $\alpha$, $C^{4+}$, and $N^{4+}$ (6 MeV/amu), and is still in progress with success.   In such experiments an attention has been payed on the following points.   1) An incident energy of the projectiles is high enough to adopt the direct Coulomb ionization process in which L shell vacancy distributions produced at the time of collision are independent of chemical environment of the compounds used.   2) The ionization cross section varies with the energy of the ions slowing down in the solid.   3) The valence band of compounds used is composed of L shell electrons of target element.   In such a condition direct information of chemical bonding is given through change in relative intensities of the X-ray satellites because a refilling of the vacancies by ligand valence electrons prior to X-ray emission is expected.   4) Bonding nature of the compounds should vary to a large extent from one compound to another.   5) Decomposition or contamination of target materials should be avoided during ion bombardment.

Thin targets of a series of fluorides; NaF, $Na_3AlF_6$, $AlF_3$, $NiF_2$, $CuF_2$, and $(CF_2)_n$ bombarded with ions with 6 MeV/amu were selected for our analysis.   Change in the intensity distribution of the F Kα X-ray spectra from these compounds related to the Pauling bond
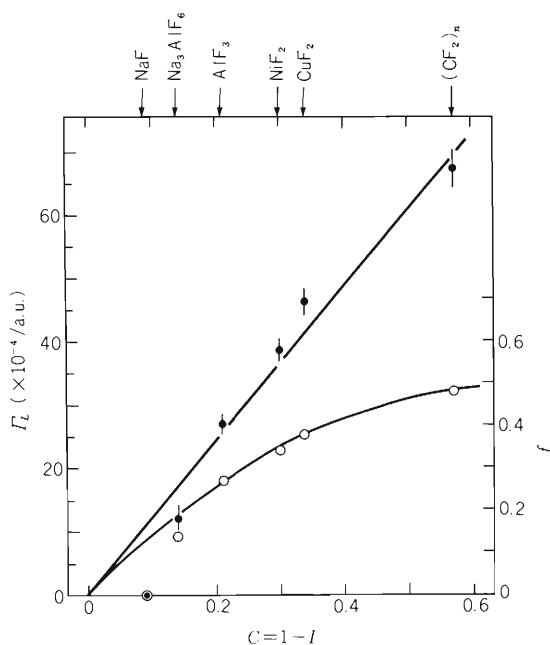


Fig. 1.   Variation of L shell width $\Gamma_L$ (closed circles) and L shell vacancy refilling probability $f$ (open circles) with the covalency C.

ionicity or covalency. The ionicity I is defined by Pauling[4] to be $I = 1.0 - \exp[-0.25(x_A - x_B)^2]$ where $x_A$ or $x_B$ is the electronegativity of element A or B. If we define the L shell width $\Gamma_L$ as $\Gamma_L = f \cdot \Gamma_K/(1 - f)$ where $\Gamma_K$ and $f$ are K shell width and refilling probability of L shell vacancies respectively, we get linear relationship between $\Gamma_L$ and the covalency C $( = 1.0 - I)$.[5] An example for 84 MeV $N^{4+}$ impact is shown in Fig. 1. This indicates that F L shell vacancies produced at the moment of collision transfer only through the covalent character of molecular orbitals made of the F L shell and the outer shells of the neighboring atoms. The ion-induced X-ray spectroscopy offers promise for determining the ionicity or covalency of chemical compounds without thermal and dielectric measurements of the compounds.

References

1) P. G. Burkhalter, A. R. Knudson, D. J. Nagel, and K. L. Dunning: Phys. Rev., A6, 2093 (1972).

2) J. McGuire, D. K. Olsen, H. H. Wolter, and C. F. Moore: ibid., A10, 200 (1974).

3) J. A. Demarest and R. L. Watson: ibid., A17, 1302 (1978).

4) L. Pauling: The Nature of the Chemical Bond, third edition, Cornell U. P., Ithaca, N. Y. (1960).

5) M. Uda, H. Endo, K. Maeda, Y. Awaya, M. Kobayashi, Y. Sasa, H. Kumagai, and T. Tonuma: to be published elsewhere.

## 6-6. $Z_2$ Dependence of L Shell Vacancy Rearrangement Process in $K\alpha$ X-Ray Satellites

H. Endo, M. Uda, K. Maeda,
M. Kobayashi, and Y. Sasa

Large difference between observed intensity distribution of $K\alpha$ X-ray satellite and expected intensity distribution from L shell vacancy distribution generated at heavy ion impact has been pointed out. Recently L shell vacancy rearrangement process via inter- or intra-atomic transition prior to the $K\alpha$ X-ray emission has been proposed[1)-3)] to explain the difference. The $K\alpha$ satellite structure is expected to give information on a structure of the valence or conduction band in solids through L vacancy relaxation process. The quantitative and detailed understanding of the L shell vacancy rearrangement process for wide range of a target atomic number $Z_2$ is indispensable for the study of chemical effect as well as of the inner shell ionization mechanism.

We have investigated the L shell vacancy rearrangement process in $K\alpha$ satellites produced by 84 MeV $N^{4+}$ impact. Chemical compounds composed of $Z_2 = 9 - 28$ are used for the comparison of their $K\alpha$ X-ray spectra which are expected to show chemical effect in their intensity distributions.

Assuming one-by-one cascading process of vacancy configurations and neglecting simultaneous multi-electron transfer to the L shell holes, the relaxed $n^{th}$ satellite intensity $y_n^X$ of the $K\alpha$ X-rays can be expressed by simultaneous equations as follows:

$$y_n^X = \frac{\omega_n}{\tilde{\omega}}( 1 - f_{n,n-1}) ( y_n + f_{n+1,n} \cdot y_{n+1} + f_{n+2,n+1} \cdot f_{n+1,n} \cdot y_{n+2}$$

$$+ \cdots + f_{8,7} \cdot f_{7,6} \cdot \cdots \cdot f_{1,0} \cdot y_8 ) \quad , \tag{1}$$

where $\tilde{\omega}$, $y_n$, and $f_{n,n-1}$ are the average fluorescence yield, the initial L shell vacancy distribution produced at the time of collision, and the probability that $K^1 L^n$ configuration is transferred to $K^1 L^{n-1}$ through L shell refilling, prior to the K shell vacancy refilling. In such a simple relaxation scheme, the reaction mechanism of the multi-ionization is responsible only for the satellite structure determined by the quantity $y_n$. If the velocity of incident ions is much higher than that of K and L orbital electrons, the initial vacancy distribution is expected to be almost independent of the outer shell electron configurations. In such a case we can solve the simultaneous equations (1) to get $f_{n,n-1}$ which is an atomic structural quantity. The L vacancy rearrangement probability $f_{n,n-1}$ is connected with $\Gamma_K(K^1 L^n)$ and $\Gamma_L(K^1 L^n)$ which are the K and L shell widths for the $K^1 L^n$ vacancy configuration state and is written as

$$f_{n,n-1} = \frac{\Gamma_L ( K^1 L^n )}{\Gamma_K ( K^1 L^n ) + \Gamma_L ( K^1 L^n )} \quad . \tag{2}$$

In the special case of small L shell ionization probability, the quantities $f_{n,n-1}$, $\Gamma_K(K^1 L^n)$ and $\Gamma_L(K^1 L^n)$ can now be replaced by $\tilde{f}$, $\tilde{\Gamma}_K$ and $\tilde{\Gamma}_L$, independent of the L shell vacancy configurations, respectively.

We deduced $\widetilde{f}$ from the observed $K\alpha$ satellite intensities of $F(NaF, Na_3AlF_6, AlF_3, NiF_2,$
$CuF_2, (CF_2)_n)$, $Na(NaF, Na_3AlF_6, Na_2SO_4, NaSCN, Na_2S_2O_6)$, $Mg(MgO)$, $Al(Al, Al_2O_3)$,
$S(Cu_2S, Na_2SO_4)$, $Cl(KCl, NaCl)$, $K(KCl)$, $Ca(CaF_2)$, $Fe(Fe, FeO, Fe_2O_3)$, and $Ni(Ni, NiO)$, as
shown in Fig. 1. Two important features of $\widetilde{f}$ are found. First is the dramatic change in $\widetilde{f}$
for the fluorides. The large "chemical effect" is caused by the fact that the L shell of $F^-$ in
the fluorides constitutes the valence band, and hence the L vacancy rearrangement is directly
reflected in $K\alpha$ satellite structure. We have discussed the chemical effect elsewhere.[4] Second is
a monotonic increase of $\widetilde{f}$ with $Z_2$ in the region where the valence or conduction band is composed
of its M shell. Although no calculations or observed data were reported on the L shell widths for
multiple L and K vacancy configuration states, $\widetilde{\Gamma}_L$ can be replaced by $\Gamma_L(K^0L^1M^m)$ which should
be smaller than $\Gamma_L(K^0L^1M^0)$ in our experimental condition. Assuming $\widetilde{\Gamma}_K = \Gamma_K(K^1L^0)$, $\widetilde{f}$ is then
expressed as

$$\widetilde{f} = \frac{\beta\Gamma_L(K^0L^1M^0)}{\Gamma_K(K^1L^0) + \beta\Gamma_L(K^0L^1M^0)} , \qquad (3)$$

where the quantity $\beta$ is a constant smaller than unity. Using the calculated values of $\Gamma_K(K^1L^0)$
and $\Gamma_L(K^0L^1M^0)$[5,6], the $Z_2$ dependence of $\widetilde{f}$ is now well reproduced by the theoretical estimation
obtained from equation (3) with $\beta = 1/3$ (the dashed line in Fig. 1).

The investigation of $\widetilde{f}$ for wide range of $Z_2$ than that adopted here is in progress.
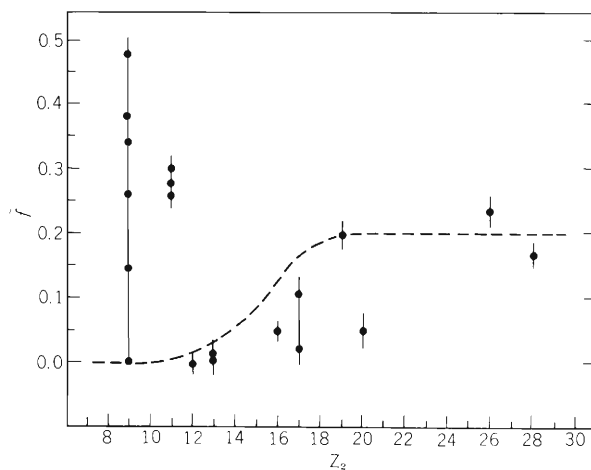


Fig. 1. Variation of the L shell
vacancy rearrangement probability
$\widetilde{f}$ with the atomic number $Z_2$ and
chemical compounds. Dashed
line denotes the theoretical value
of $\widetilde{f}$.

References

1) R. L. Watson, A. K. Leeper, B. I. Sonobe, T. Chiao, and F. E. Jenson: Phys. Rev., A15, 914 (1977).

2) J. A. Demarest and R. L. Watson: ibid., A17, 1302 (1978).

3) R. L. Kauffman, K. A. Jamison, T. J. Gray, and P. Richard: Phys. Rev. Lett., 36, 1074 (1978).

4) M. Uda, H. Endo, K. Maeda, M. Kobayashi, and Y. Sasa: IPCR Cyclotron Progr. Rep., 12, 88 (1978).

5) J. H. Scofield: Phys. Rev. 179, 9 (1969).

6) E. J. McGuire: ibid., A3, 587 (1971).

## 6-7. Energy Straggling of C and He Ions in Metal Foils

T. Takahashi, Y. Awaya, A. Hashizume, K. Izumo,

H. Kumagai, T. Tonuma, and S. Uchiyama

The energy loss straggling of C and He ions in foils of aluminum, silver, gold, and lead has been studied using $5 - 7$ MeV/nucleon cyclotron beams and results were compared with Bohr's theory. According to Bohr's theory, the full width at half maximum is given by

$$\eta_{Bohr} = 2 \, (2 \ln 2)^{1/2} \, (4 \, \pi \, e^4 Z_1^2 N Z_2 \Delta x)^{1/2} \, ,$$

where $Z_1 e$ is the charge of the incident particle, N is the number of atoms per $cm^3$ of the stopping material with atomic number $Z_2$ and thickness $\Delta x$. The foil thickness ($\Delta x$), mean energy in the foil ($\overline{E}$/nucleon), the full width at half maximum obtained from our experiment ($\eta_{exp}$), the full width at half maximum calculated from Bohr's theory ($\eta_{Bohr}$), the ratio $\eta_{exp}/\eta_{Bohr} = R$ and $R^C/R^{He}$ are shown in Table 1. Here, $R^C$ is the ratio $\eta_{exp}^C/\eta_{Bohr}^C$ for C ion and $R^{He}$ is that for He ion. The ratio $R^C/R^{He}$ is given by $\eta_{exp}^C/(3\eta_{exp}^{He})$, where numerical factor 3 comes from $Z_1$ in Bohr's theory. $\eta_{exp}^C$ and $\eta_{exp}^{He}$ were compared with each other for the same foil to avoid the effect of foil inhomogeneity. In Fig. 1, the ratio $R^C/R^{He}$ is shown. If Bohr's theory is applicable, $R^C/R^{He}$ should be unity, but the ratio is larger than unity for all foils investigated. If $R^{He}$ is $1.1 - 1.2$, the foil can be regarded homogeneous, according to Strittmatter and Wehring.[1] $R^{He}$ value for each foil is indicated in Fig. 1. Homogeneity of lead and gold

Table 1. Energy straggling of C and He ions in metal foils.

| | $\Delta x$ (mg/cm$^2$) | $\overline{E}$/n (MeV) | $\eta_{exp}$ (keV) | $\eta_{Bohr}$ (keV) | R | $R^C/R^{He}$ |
|---|---|---|---|---|---|---|
| He in Al | 3.195 | 6.931 | 81 ± 7 | 73.1 | 1.11 | |
| C in Al | 3.195 | 5.392 | 372 ± 24 | 220 | 1.69 | 1.53 ± 0.16 |
| C in Al | 3.195 | 4.834 | 377 ± 17 | 220 | 1.71 | 1.55 ± 0.15 |
| He in Ag | 5.196 | 6.927 | 98 ± 7 | 88.6 | 1.11 | |
| C in Ag | 5.196 | 7.095 | 470 ± 23 | 267 | 1.76 | 1.59 ± 0.14 |
| C in Ag | 5.196 | 5.379 | 517 ± 24 | 267 | 1.94 | 1.75 ± 0.15 |
| He in Au | 12.03 | 6.856 | 211 ± 7 | 129 | 1.63 | |
| C in Au | 12.03 | 6.910 | 1570 ± 116 | 389 | 4.04 | 2.47 ± 0.20 |
| C in Au | 12.03 | 5.171 | 1910 ± 118 | 389 | 4.91 | 3.00 ± 0.21 |
| C in Au | 12.03 | 4.586 | 2060 ± 85 | 389 | 5.30 | 3.24 ± 0.17 |
| He in Pb | 5.334 | 6.941 | 148 ± 7 | 85.6 | 1.73 | |
| C in Pb | 5.334 | 7.150 | 1200 ± 69 | 257 | 4.67 | 2.70 ± 0.20 |
| C in Pb | 5.334 | 5.436 | 1290 ± 72 | 257 | 5.02 | 2.90 ± 0.21 |
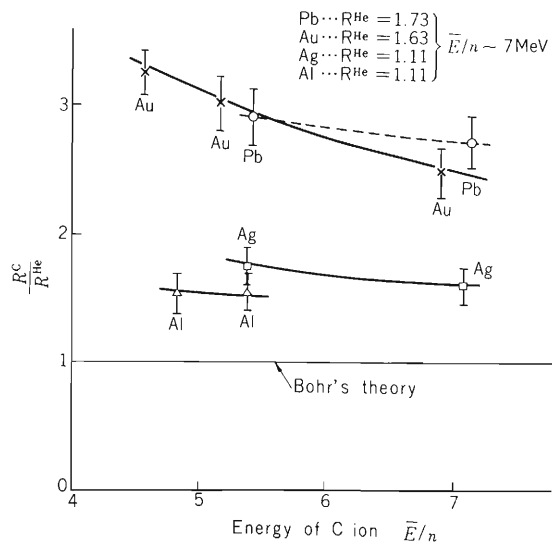
Fig. 1. $R^C/R^{He}$ versus energy of C ions. $R^{He}$ was obtained at $E/n \approx 7$ MeV (see Table 1).

foils seems unsatisfactory, but that of silver and aluminum foils seems to be good. The disagreement between the theory and experiment (even for foils of satisfactory homogeneity) is apparent, but no explanation for it is given yet.

Reference

1) R. B. Strittmatter and B. W. Wehring: Nucl. Instr. Meth., 135, 173 (1976).

# 6-8. Secondary Electron Emission from Metal Surface by High Speed Ion Bombardment

A. Koyama, T. Shikata, and H. Sakairi

In the phenomenological theory of the secondary electron emission from metal surface by high speed ion bombardment, the emission ratio was given semi-empirically on an assumption that the number of excited electrons inside the solid is in proportion to the stopping power for an incident ion.[1,2]   One of the present authors (A.K.) made, without the above assumption, a calculation for the total backward secondary electron emission yield from Al by high speed proton bombardment.[3]   In the calculation the number of inner excited secondaries was calculated by the Born approximation, and the transport and the emission process of them were expressed by the Boltzmann equation.   The calculated value of the emission yield was about one fourth of the experimental value reported by Aarset et al.   The addition of the contribution from $L_{2,3}$·VV Auger electrons can only make it increase to a half of the experimental one.   The origin of this discrepancy must be investigated from both theoretical and experimental sides.

The study on the total backward secondary electron emission ratio has started this year with the vacuum evaporated metal target which is expected to have cleaner surface than that used in the previous experiment.[4]   It is planned to investigate the incident ion energy dependence of the emission yield and the dependence of it on incident ion charge number, and the variation of these dependences with the target materials by bombardments of proton, $\alpha$-particle and heavier ions such as $C^{4+}$, $N^{4+}$, and $O^{5+}$.

Figure 1 shows the schematic diagram of the measuring system.   The target (T) is a vacuum evaporated thick film on an iron substrate.   After evaporation, the target can be set perpendicular to the incident beam direction by turning the target holder without being exposed to the air. The vacuum is about $1 \times 10^{-7}$ torr and about $1 \times 10^{-8}$ torr during evaporation and during measurement, respectively.   The collimator is composed of slits $S_1$ and $S_2$, apertures of which are 1 mm and 3 mm in diameter, respectively.   The collector (C) has a cover outside of it so as not to catch stray electrons in the scattering chamber.   The deflector (D) prevents the electrons
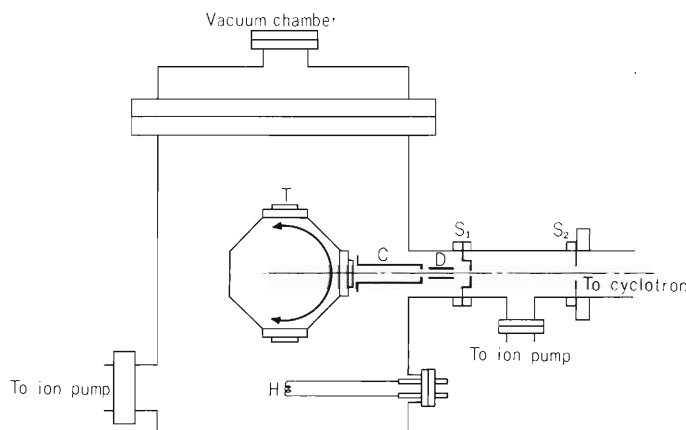


Fig. 1.   Schematic diagram of the measuring system.   T: rotatable target holder and targets.   C: collector.   D: deflector to prevent secondary electrons emitted from the edge of the slit $S_1$ from reaching the target and the collector.   $S_1$ and $S_2$: slit system which has two apertures of 1 and 3 mm diameter, respectively.   H: heater for vacuum evaporation.

emitted by incident ions at the edge of the slits $S_1$ from reaching the collector and the target. A preliminary measurement is now in progress on Al target.


References

1)  E. L. Sternglass: Phys. Rev.. <u>100,</u> 1 (1957).

2)  K. Kanaya and S. Ono: Japan. J. appl. Phys., <u>13,</u> 944 (1974).

3)  A. Koyama: ibid., <u>16,</u> 431 (1977); A. Koyama: Ionizing Radiation, (in Japanese), <u>5,</u> 17 (1978).

4)  B. Aarset, R. W. Cloud, and J. G. Trump: J. appl. Phys., <u>25,</u> 1365 (1951).

## 6-9. Helium Embrittlement of the First Wall Materials for Fusion Reactor

H. Shiraishi, H. Shinno, R. Watanabe,*
H. Kamitsubo, I. Kohno, and T. Shikata

The degradation of mechanical properties by neutron irradiation is a serious problem in nuclear reactor design.   Stainless steels belonging to type 300 series (especially SUS 316) are supposed to be the most promising materials for use in proto-type reactors, but it was widely recognized recently that they have disadvantages of large void swelling and severe embrittlement. High nickel austenitic alloys are well known to be highly resistive to the void swelling, therefore, these materials are expected to be very promising as structural materials in fast breeder reactors and fusion reactors.   Other hopeful materials are molybdenum and its alloys because of their attractive physical properties and large mechanical strength at high temperatures.   Effect of helium on the high temperature embrittlement is yet little known for the latter two kinds of materials. The present work intends to clarify this point.

The details of the experimental procedures were reported previously.[1,3]   Here, only main features will be given.   The tensile test specimen was plate-like in shape and had a cross-section of 0.2 × 4 mm with a gauge length of 10 mm.   The cold work was done by cold rolling.   Helium injection was performed by the cyclotron.   An Instron type machine was used for the tensile test in the vacuum of $2 \times 10^{-6}$ Torr.   The strain rate was $5 \times 10^{-4}$/sec.   Test temperatures were 650 °C and 750 °C.

Table 1 shows the chemical composition of the high nickel austenitic alloys examined. Sample 7502 is a solution hardened alloy.   Sample 7510 is strengthened by a $\gamma'$ – intermetallic compound precipitation.   The pre-injection conditions, the injection temperature, and the tensile test results are given in Table 2.   Pre-injection treatment by 5 % straining was very effective to suppress the helium embrittlement in SUS 316 stainless steel.[2,3]   Two kinds of treatments were given to the precipitation strengthened alloy.   The sample given the 20 % cold work before aging had a lower strength but a higher ductility compared with the sample treated in the reversed sequence.

The helium embrittlement was clearly observed in every helium injected specimen.   Higher the test temperature was, larger reduction of the ductility occurred.   The embrittlement of the solution hardened alloy was found to be severer than that in the similarly treated SUS 316 stainless steel, the result of which was already reported elsewhere.[2,3]   It is noteworthy that there was no effect of 5 % prestrain.   This point made a clear contrast to SUS 316 stainless steel.[2,3]   The largest embrittlement occurred in the $\gamma'$ – precipitation hardened alloy.   The material which had the largest strength undergone the severest helium embrittlement.   The helium effect to these two types of materials (SUS 316 stainless steel and high nickel austenitic alloys) was considerably different, but the fundamental mechanism of the embrittlement in the high

* National Research Institute for Metals.

Table 1. Chemical composition of the high nickel
austenitic alloys (wt. %).

| Sample | C | Ni | Cr | Si | Mn | Mo | Ti | Al | B |
|---|---|---|---|---|---|---|---|---|---|
| 7502 | 0.057 | 35.12 | 14.72 | 0.45 | 1.41 | 1.59 | – | – | <0.0002 |
| 7510 | 0.063 | 35.60 | 14.86 | 0.51 | 0.94 | 1.71 | 1.79 | 0.24 | <0.0002 |

Table 2. Experimental conditions and tensile test results of the helium injected
high nickel austenitic alloys.

| Sample No. | Pre-irr. treat. | He cont. (at. ppm) | Irrad. temp. (°C) | Test temp. (°C) | 0.2% proof stress (kg/mm$^2$) | Tensile strength (kg/mm$^2$) | Uniform elonga. (%) | Total elonga. (%) |
|---|---|---|---|---|---|---|---|---|
| 7502 |  | 6.3 | 800 | 650 | 15.3 | 32.0 | 19.7 | 21.4 |
| 7502 | ST[*] | 0 | 750 | 650 | 16.2 | 33.2 | 32.3 | 62.4 |
| 7502 | 1050°C | 6.3 | 800 | 750 | 14.1 | 18.8 | 6.6 | 7.6 |
| 7502 | 30 min | 0 | 750 | 750 | 14.1 | 21.1 | 16.5 | 62.3 |
| 7502 |  | 6.3 | 800 | 650 | 20.4 | 32.3 | 15.0 | 18.3 |
| 7502 | 5% | 0 | 750 | 650 | 26.5 | 35.6 | 26.2 | 50.6 |
| 7502 | prestrain | 6.3 | 800 | 750 | 16.5 | 19.4 | 4.6 | 8.9 |
| 7502 |  | 0 | 750 | 750 | 19.6 | 21.8 | 9.8 | 49.1 |
| 7510 |  | 5.0 | 650 | 650 | 31.6 | 44.0 | 8.0 | 12.8 |
| 7510 | 20% CR[**] | 0 | 500 | 650 | 28.9 | 46.6 | 15.7 | 50.3 |
| 7510 | + 650°C, 10$^3$h | 5.0 | 650 | 750 | 22.1 | 26.0 | 3.3 | 4.7 |
| 7510 |  | 0 | 500 | 750 | 22.0 | 27.7 | 9.6 | 58.4 |
| 7510 |  | 5.0 | 650 | 650 | 63.6 | 67.6 | 1.7 | 2.2 |
| 7510 | 650°C, 10$^3$h | 0 | 500 | 650 | 73.2 | 78.5 | 2.3 | 14.4 |
| 7510 | + 20% CR[**] | 5.0 | 650 | 750 | 26.7[***] | – | 0 | 0 |
| 7510 |  | 0 | 500 | 750 | 43.4 | 50.4 | 2.3 | 13.5 |

[*]   Solution treatment

[**]   Cold rolling

[***]   No plastic strain

Tensile test strain rate:   $5 \times 10^{-4}$/sec

nickel austenitic alloys was not established. A transmission electron microscopic study may clarify this problem in the near future.

A molybdenum sample was helium injected at 1000°C. The injected helium concentration was 10 atomic ppm. The main impurity contents were as follows: C 50, O 4, N 8, and Zr 30 (ppm in weight). The sample was annealed at 1300°C for 1 h before the helium injection. The tensile test at 1000°C and at the strain rate of $5 \times 10^{-4}$/sec showed no loss of ductility.

98

References

1) R. Watanabe, H. Shiraishi, H. Shinno, H. Kamitsubo, I. Kohno, and T. Shikata: IPCR Cyclotron Progrs. Rep., 10, 104 (1976).

2) H. Shinno, H. Shiraishi, R. Watanabe, H. Kamitsubo, I. Kohno, and T. Shikata: ibid., 11, 114 (1977).

3) H. Shinno, H. Shiraishi, R. Watanabe, H. Kamitsubo, I. Kohno, and T. Shikata: IPCR Cyclotron Progr. Rep., Suppl. 7, to be published.

## 6-10. Lattice Location of Ni Atoms Implanted in Al

E. Yagi, A. Koyama, H. Sakairi, and R. R. Hasiguti*

The atomic configuration of interstitials in f.c.c. metals is one of the fundamental problems in the field of crystal lattice defects. With respect to the determination of the magnitude of atomic displacement of interstitials, the channeling method is the most effective one among several experimental methods applied to the investigation of interstitial configuration. There have been no channeling investigation on the self-interstitials in f.c.c. metals. But, on mixed interstitials composed of Al and impurity atoms in Al solid solution, several investigations have been performed by Swanson et al.[1] In the present work, the location of Ni atoms implanted in Al was investigated by means of proton backscattering. As Ni has very small solubility in Al it is expected that the implanted Ni atoms occupy interstitial sites. If it is the case, the information on the interstitial site will be obtained from the determination of Ni atom location.

Preliminary experimental results and a qualitative explanation of them were given in the last volume.[2] Results of advanced experiments and a quantitative explanation are presented here.

In order to investigate the location of the implanted Ni atoms, an angular scan was performed through $<100>$, $<110>$, and $<111>$ axes. Figure 1 shows the normalized backscattering yields $\chi$ from Ni and Al atoms as a function of the angle $\theta$ between the incident beam direction and the $<100>$ axial direction. Figures 2 and 3 show the results for the $<110>$ axis and the $<111>$ axis, respectively.



Fig. 1. Normalized backscattering yields from Ni and Al atoms as a function of the angle $\theta$ between the incident beam direction and the $<100>$ axial direction. Incident proton energy is 5.8 MeV.

* Faculty of Science and Technology, Science University of Tokyo.
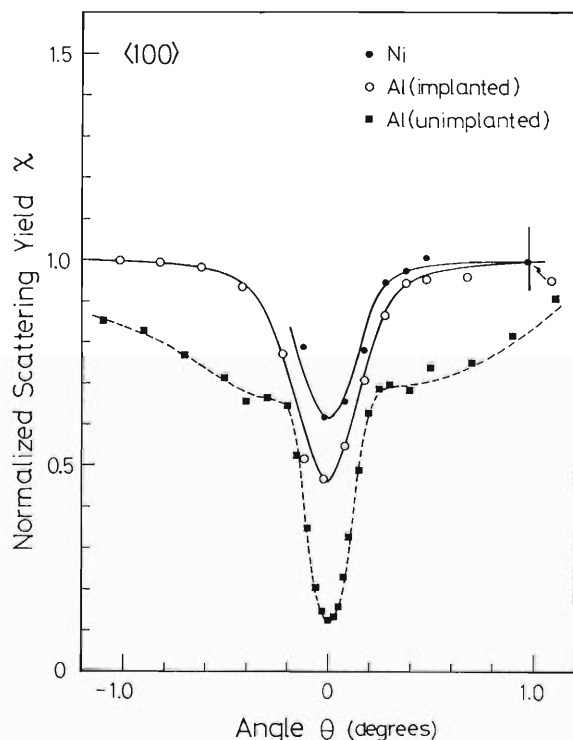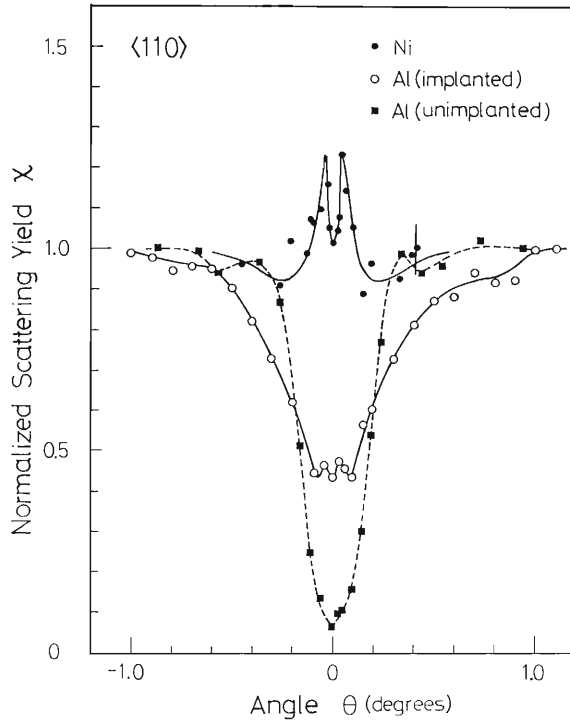
Fig. 2.   Normalized backscattering yields from Ni and Al atom as a function of the angle $\theta$ between the incident beam direction and the <110> axial direction.   Incident proton energies are 4.8 MeV and 5.8 MeV for an implanted specimen and an unimplanted one, respectively.



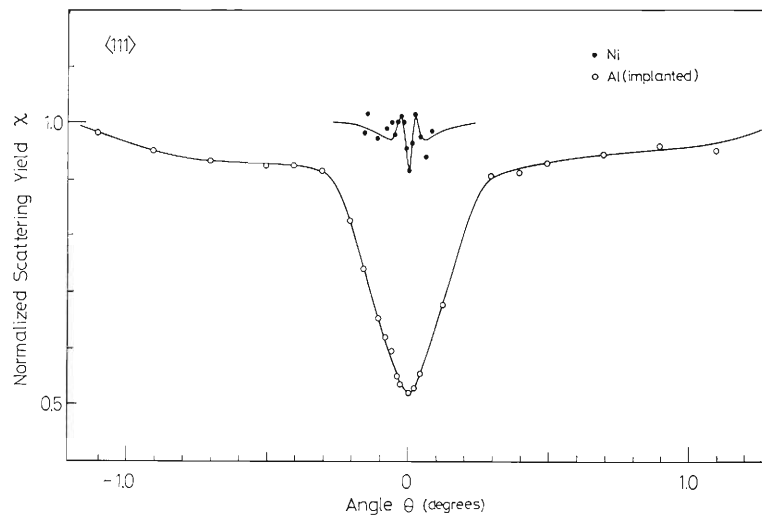Fig. 3.   Normalized backscattering yields from Ni and Al atom as a function of the angle $\theta$ between the incident beam direction and the <111> axial direction.   Incident proton energy is 4.8 MeV.

The angular scan of the backscattering yield from Ni atoms shows a dip with minimum yield $\chi_{min}$ of about 0.65 for the <100> axis, while a double peak is obtained for both <110> and <111> axes.   The angle $\theta_p$ giving rise to the peaks are ±0.04° and ±0.03° for <110> and <111> axes.   The peak height of the <111> double peak is smaller than that of the <110> double peak.   The <100> Ni-dip has the same half-width at half-minimum as that of Al-dip. The double peak results from the flux-peaking effect and indicates that Ni atoms are located at interstitial sites.   These experimental results suggest that the Ni atom occupies the interstitial site displaced from the normal lattice site in the Al crystal in the <100> direction.   In the <110> angular scan, the Al-dip has fine structure consisting of a small double peak around the

center of the dip, i.e., $\theta_p = \pm 0.03°$. As in the case of Ni atoms, this result suggests the presence of interstitial Al atoms displaced from normal lattice sites by nearly the same amount in the $<100>$ direction. Such displacement of Al atoms is considered to be induced by Ni atoms occupying the adjacent interstitial sites. Thus a split type interstitial consisting of an Al and a Ni atoms is produced.

The first order expression to relate the angular position of the peak $\theta_p$ to the displacement position from the center of the channel $r_j$ is given by

$$E\theta_p^2 = U(r_j), \tag{1}$$

where E is the incident ion energy and U(r) is the continuum potential of the atomic row, normalized to value of zero at the potential minimum. Using the continuum potential given by Erginsoy for U(r),[3] the magnitude of the displacement of Ni atoms from normal lattice sites in the $<100>$ direction was estimated to be about $1.3(\alpha/4)$ and $1.2(\alpha/4)$ from the data of $<110>$ and $<111>$ angular scans, respectively, where $\alpha$ represents the lattice constant of the Al crystal. These two values are in fairly good agreement. For interstitial Al atoms the displacement was a little larger than that of Ni atoms, i.e., $1.4(\alpha/4)$. The channeling experiments made by Swanson et al. on Al-Mn alloys irradiated and annealed at low temperatures indicate the presence of $<100>$ mixed split type interstitials.[1] A Mn atom has the atomic size close to that of a Ni atom, and the displacement of Mn atoms in the $<100>$ direction was estimated to be about $1.3(\alpha/4)$. As to such displacement no calculation has been made for Al crystal, but for a split type self-interstitials in Cu crystal Gibson et al. obtained about $1.2(\alpha/4)$ by the calculation using the Born-Mayer potential.[4] The experimental results by Swanson et al. and by the present authors are in good agreement with the calculated one.

References

1) M. L. Swanson, F. Maury, and A. F. Quenneville: Application of ion beams to Materials, Plenum Press, New York, p. 393 (1974).

2) E. Yagi, A. Koyama, H. Sakairi, and R. R. Hasiguti: IPCR Cyclotron Progr. Rep., 11, 102 (1977).

3) C. Erginsoy: Phys. Rev. Lett., 15, 360 (1965).

4) J. B. Gibson, A. N. Goland, M. Milgram, and G. H. Vineyard: Phys. Rev., 120, 1229 (1960).

# 6-11. Hyperfine Interactions of $^{119}$Sn in Magnetic Chalcogen Spinels

T. Okada, H. Sekizawa, and T. Yamadaya

Recently, much interest has been aroused by the discovery of large hyperfine magnetic fields induced at the diamagnetic-atom nuclei in various magnetic materials. These magnetic fields are induced by the supertransferred hyperfine interactions. The purpose of the present work is to investigate the supertransferred hyperfine field (STHF) at diamagnetic ions such as tin ions in magnetic materials by means of Mössbauer spectroscopy. Ions of stable isotope $^{119}$Sn is used in our investigation. Investigations on hyperfine interactions of diamagnetic Sn ions in ferromagnetic chalcogenide spinel system $CuCr_{2-x}Sn_xS_4$ $(0 \leq x \leq 1)$ have previously been carried out.[1, 2] The present investigation is an extension of the work to a series of similar magnetic Cr chalcogenide spinels to elucidate the mechanisms giving rise to the hyperfine interactions in these systems.

Samples used are tin doped spinels with formula $ACr_{1.9}Sn_{0.1}X_4$, where A denotes various divalent metal ions occupying tetrahedral sites and X denotes S, Se or Te. The Cr ions occupy the octahedral sites, and a small amount of Sn ions doped into these crystals are known to occupy the same sites replacing Cr ions. All the samples were prepared by procedures similar to those described before.[1] The observed Mössbauer line widths were generally much broader than the natural width. The electric quadrupole splittings were negligibly small for all the samples. For some of the samples, the sign of the hyperfine magnetic field was determined by applying an external longitudinal magnetic field of 35kOe. The values of the isomer shifts (IS) at room temperature, the hyperfine magnetic field ($H_{hf}$) at 5K and the magnetic properties are listed in Table 1. In Fig. 1 the IS of various samples are plotted against the lattice constant. As can

Table 1. $H_{hf}$ at 5K, IS at room temperature, magnetic ordering temperature and magnetic properties of various Cr chalcogen.

| | $H_{hf}$ (kOe) | IS (mm/s) | $T_c$ or $T_n$ (K) | Mag. |
|---|---|---|---|---|
| $CuCr_{1.9}Sn_{0.1}S_4$ | +600 | +1.50 | 395 | ferro |
| $CuCr_{1.9}Sn_{0.1}Se_4$ | +570 | +1.70 | 418 | ferro |
| $CuCr_{1.9}Sn_{0.1}Te_4$ | +280 | +2.10 | 343 | ferro |
| $FeCr_{1.9}Sn_{0.1}S_4$ | +600 | +1.25 | 186 | ferri |
| $CoCr_{1.9}Sn_{0.1}S_4$ | +580 | +1.35 | 212 | ferri |
| $MnCr_{1.9}Sn_{0.1}S_4$ | 220 | +1.20 | 90 | ferri |
| $CdCr_{1.9}Sn_{0.1}S_4$ | +220 | +1.15 | 82 | ferro |
| $HgCr_{1.9}Sn_{0.1}S_4$ | 140 | +1.15 | 31 | meta |
| $CdCr_{1.9}Sn_{0.1}Se_4$ | +270 | +1.50 | 125 | ferro |
| $HgCr_{1.9}Sn_{0.1}Se_4$ | 160 | +1.50 | 101 | ferro |
| $ZnCr_{1.9}Sn_{0.1}S_4$ | 120 | +1.20 | 16 | antiferro |
| $ZnCr_{1.9}Sn_{0.1}Se_4$ | 130 | +1.55 | 18 | antiferro |
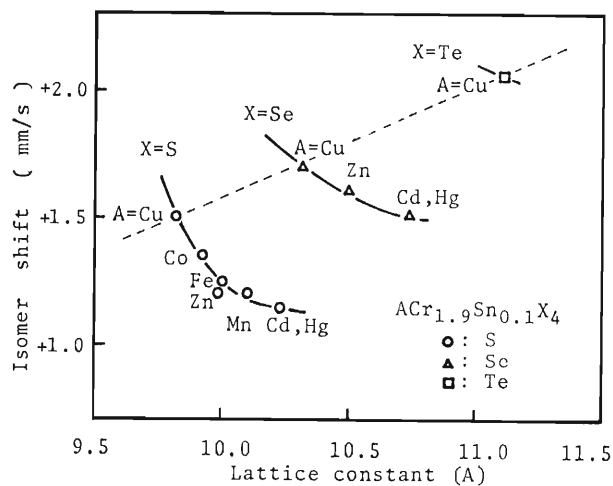
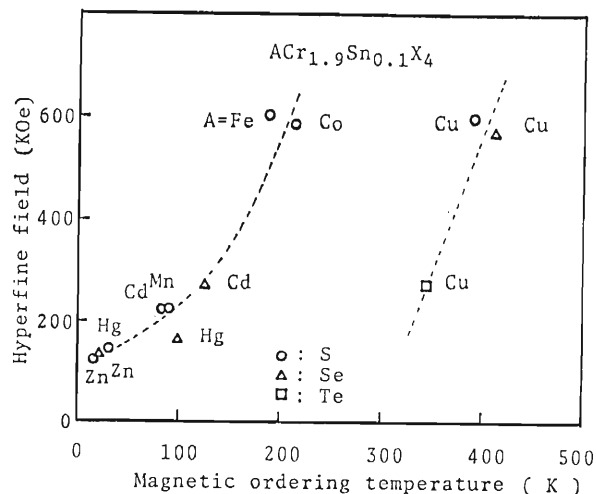Fig. 1. Isomer shifts at room temperature relative to $BaSnO_3$ versus lattice constants for $ACr_{1.9}Sn_{0.1}X_4$. ○: sulfide, △: selenide, □: telluride.

Fig. 2 Hyperfine fields at 5K versus magnetic ordering temperatures for $ACr_{1.9}Sn_{0.1}X_4$. ○: sulfide, △: selenide, □: telluride.

be seen, the IS varies systematically. These results can be interpreted as fair reflection of the degree of covalency between Sn and chalcogen ions in these compounds: for a fixed chalcogen ion, the increase in the lattice constant makes the distance between Sn and chalcogen ions larger resulting in a decrease in covalency; for a fixed divalent metal ion, the covalency increases on going from sulfide to selenide and then to telluride.

In Fig. 2, $H_{hf}$ at 5K are plotted against the ordering temperature, $T_c$ or $T_n$. Apparently, the compounds can be classified into two groups: the one comprizing $CuCr_2X_4$'s, and the other comprizing all the others which show some tendency of rough proportionality between $H_{hf}$ and $T_c$ (or $T_n$). In the Cr chalcogen spinels, the Cr-Cr (or B-B) interaction is considered to be the dominant one in determing the ordering temperatures. This, along with the tendency seen in Fig. 2, suggests that polarized spins coming (directly or indirectly) from Cr ions to Sn ions play an important role in giving rise to the STHF at Sn ions. A noticeable feature of the STHF in the Cr chalcogen spinels is that they are positive in sign without exception so far as we have determined. Our investigations will be extended to radioactive isotope $^{119}Sb$ or $^{119m}Te$ ions which are prepared by the Cyclotron.

References

1) H. Sekizawa, T. Okada, and F. Ambe: Proc. Intern. Conf. of Magnetism, ICM-73, 2, 152 (1974).

2) I. S. Lyubutin and T.V. Dmitrieva: JETP Lett., 21, 59 (1975).

## 6-12. Positron Lifetime Study on Annealing Behavior
## of Irradiated or Quenched Platinum

K. Hinode, S. Tanigawa, H. Kumakura,

M. Doyama, and N. Shiotani

Annealing behavior of $^3$He ion- or neutron-irradiated platinum, and quenched platinum was studied by means of positron lifetime measurements. After the Stage III annealing, the positron mean lifetimes ($\tau_M$) of neutron-irradiated specimens and quenched specimens recovered nearly completely. However, $\tau_M$ of $^3$He ion irradiated specimens showed only a partial recovery in this temperature range.

Experimental conditions are as follows:

$^3$He ion irradiation: dose = $1.3 \times 10^{17}$ /cm$^2$ at a temperature below 100°C,

Neutron irradiation: dose = $3.8 \times 10^{16}$ /cm$^2$ at 4.2 K,

Quenching: from 1500°C (in air) to 0°C (water).

Isochronal annealing for 20 min was carried out for each specimen, and Fig. 1 represents the results of mean lifetime ($\tau_M$) analyses.

The decrease of $\tau_M$ in quenched specimen has indicated a simple annealing process with the activation energy of 1.4 eV between 250°C and 450°C. Here the second order reaction was assumed. This value agrees well with that evaluated for vacancy migration process from electrical resistivity measurements.[1] In neutron-irradiated specimen, $\tau_M$ increased in the temperature range between 100°C and 200°C and decreased at around 250°C and 400°C. In such case of neutron irradiation, the short-range defect migration stages often appear at lower temperature than the typical temperature of the long-range migration stages because of the structure of the damage. It is plausible that the short-range vacancy migration to so-called 'stabilized depleted zones' causes the
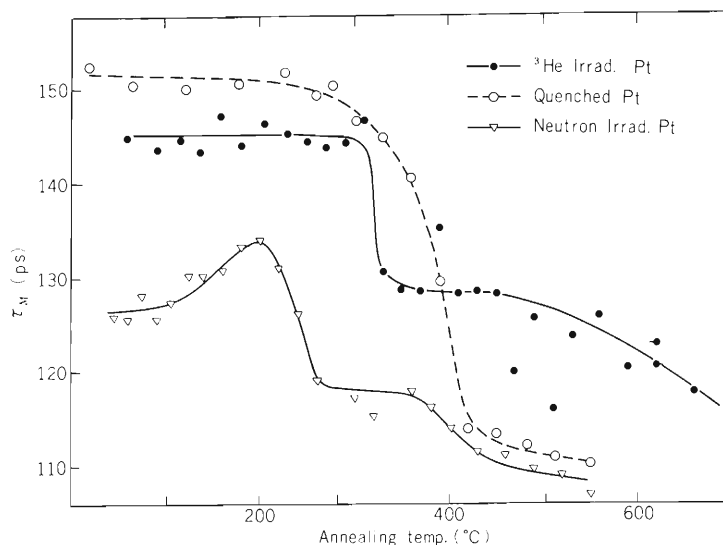


Fig. 1. Positron mean lifetimes of the three types of the platinum specimens measured after each isochronal annealing treatments.

growth of the zone resulting in the increase of $\tau_M$. Successive decrease of $\tau_M$ (at about 250°C) may be attributed to the long-range migration and annihilation of the vacancies. The highest stage of decrease at around 400°C may be attributable to the annealing of the vacancy clusters. For the above mentioned two specimens, $\tau_M$ have reached the value of that of the specimen annealed well at 500°C.

In $^3$He ion-irradiated specimens, $\tau_M$ showed a stepwise decrease around 320°C, and thereafter the gradual decrease continued up to the temperature above 600°C. The type of the residual defects could be an association of single vacancy or di-vacancy with a He atom.

Reference

1)   J. J. Jackson: "Lattice Defects in Quenched Metals", Academic Press Inc., New York, p. 467 (1965).

# 7. RADIOCHEMISTRY AND NUCLEAR CHEMISTRY

## 7-1. Measurement of Excitation Function for the $^{14}$N (p, n)$^{14}$O Reaction

T. Nozaki, T. Karasawa, M. Iwamoto,
Y. Terai, and M. Okano

Reliable thick target yield for the $^{14}$N(p, n)$^{14}$O reaction is needed for the estimation of the following two quantities in the production of $^{11}$C by the $^{14}$N(p, $\alpha$)$^{11}$C reaction: (1) required thickness of neutron shields in the use of the 'Self-shielding Baby Cyclotron', and (2) activity of $^{14}$O formed simultaneously with $^{11}$C in the on-line diagnostic use of $^{11}$CO$_2$ and $^{11}$CO. We measured the excitation function for the $^{14}$N(p, n)$^{14}$O reaction up to proton energy of 15 MeV.

Nitrogen gas was used as the target of the measurement. It was contained in cylinders (25.0 mm in height and 60 mm in inner diameter) made of metal pipes and aluminium foils of known thicknesses. A suitable number of the cylinders were closely lined up on an electrical insulator and bombarded with protons (15 or 8 MeV, 1 $\mu$A, 1.2 min). The cylinders were then transferred as quickly as possible to a counting room. The 2.31 MeV $\gamma$-ray activity of $^{14}$O was measured by a Ge(Li) detector connected to two analyzers, one being operated in multi-scaler mode and the other for taking the entire $\gamma$-ray spectrum for each 5 seconds. Since annihilation radiations from the coexisting $^{11}$C were so strong as to badly disturb the measurement, lead plates with 25 mm total thickness were inserted between the source and the detector to attenuate them.

The excitation function thus obtained is shown in Fig. 1. Although we are confident in its shape, there still remains up to 30 % uncertainty in the absolute cross section. Marked differences are found between the present result and the same excitation function reported by Kuan and Risser.[1] The cross section in their report is higher than our value by almost one order
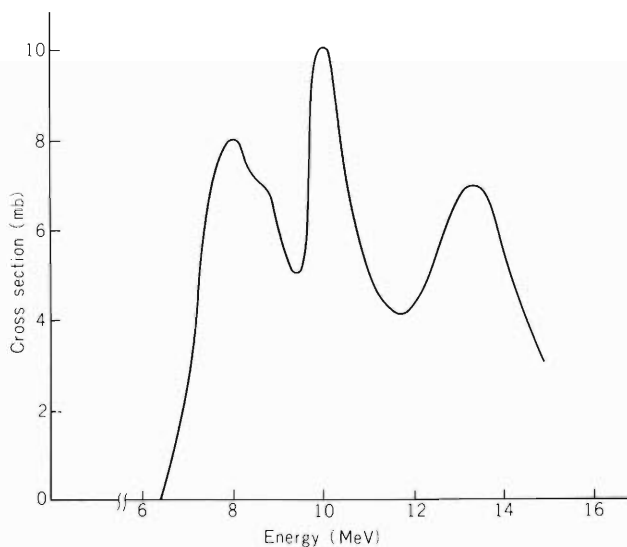


Fig. 1. Excitation function for the $^{14}$N(p, n)$^{14}$O reaction.

of magnitude.   In our experiment, the excitation function for the simultaneous formation of $^{11}$C was also measured;  the cross section obtained agreed fairly well with the generally accepted value.[2]   The $^{14}$N(p, n)$^{14}$O reaction has thus been found to be of such a small cross section that neither the neutron generation by this reaction nor the $^{14}$O contamination in the $^{11}$CO$_2$ and $^{11}$CO production requires any serious consideration.

References

1)   H. M. Kuan and J. R. Risser:  Nucl. Phys., <u>51</u>, 518 (1963).
2)   E.g., B. W. Wieland and R. S. Howell:  Proc. 2nd Intern. Symp. Radiopharm. Chem., July, Oxford (1978).

## 7-2. Chemical Separation for Charged Particle Activation Analysis of Trace Oxygen in Various Metals

T. Nozaki and Y. Terai

Although oxygen in metals has been analysed by various methods, there have been some problems of sensitivity and interference of surface oxygen.  Charged particle activation analysis by the reaction of $^{16}O(^{3}He, p)^{18}F$ is useful for the determination of trace oxygen.[1]  In this analysis, however, gamma emitters formed from the metal matrices themselves usually interfere with the measurement of the $^{18}F$ positron annihilation.  Hence, chemical separation with consideration of $^{18}F$ life time (110 min. half life) is needed.  We have investigated rapid chemical separation procedures for $^{18}F$ from various metal plate samples (iron, copper, zinc, germanium, tin, lead, silver, titanium, aluminum, molybdenum, and stainless steel) of high purity (99.9 – 99.9999 %).

The sample was bombarded with $^{3}He$ particles (1 – 3 $\mu A$, 16 MeV at metal plate surface) for 10 or 30 min.  The surface was chemically etched to remove the effect of surface oxygen (Table 1).  The plate was then dissolved in a selected reagent (Table 1) containing KF (5 mmol) or HF (larger amount) and the $^{18}F$ was separated by the chemical procedure shown in Fig. 1.



Fe, Cu, Sn, Ge, Pb,
Ag, Al, Ti, Mo,
Stainless steel(Sus)

Zn
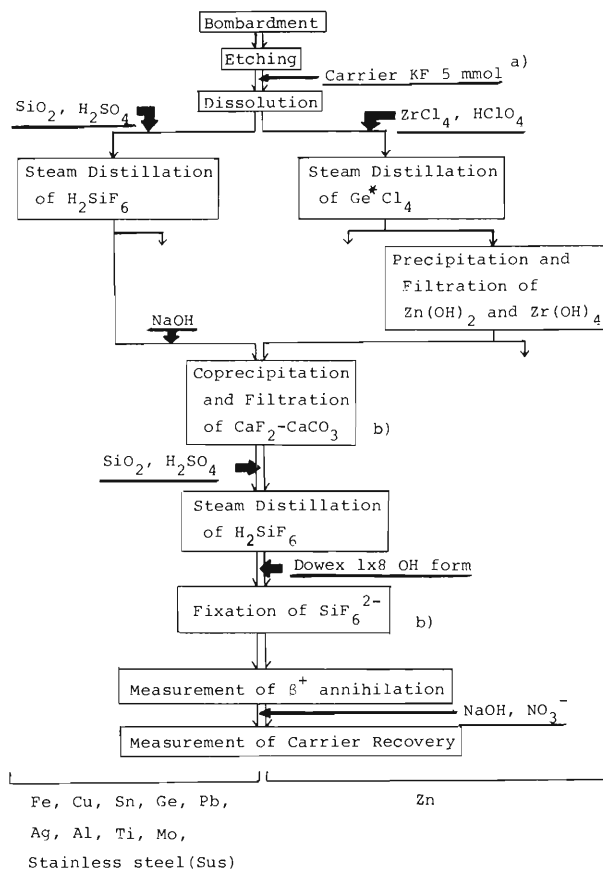
a) Carrier HF for Ti
b) LiF is used for Ti

Fig. 1.   Chemical separation procedure.

Table 1.    Etching reagents and dissolution reagents.

| | Fe | Cu | Zn | Sn | Ge | Pb | Ag | Al | Ti | Mo | Sus |
|---|---|---|---|---|---|---|---|---|---|---|---|
| Etching reagent | $Br_2$ AcOH | $Br_2$ AcOH | $Br_2$ AcOH | $Br_2$ AcOH | HF $HNO_3$ | AcOH $H_2O_2$ | $HNO_3$ | NaOH | HF | $HNO_3$ | $HNO_3$ |
| Dissolution reagent | $HNO_3$ | $HNO_3$ | HCl | $HNO_3$ HCl $Cu(NO_3)_2$ | $H_2O_2$ NaOH | AcOH $H_2O_2$ | $HNO_3$ | HCl | HF $HNO_3$ | $HNO_3$ HCl | $HNO_3$ HCl |

Table 2.    Oxygen contents (ppm) and carrier recoveries (%) in various metals.

| Exp. Date | Fe | Cu | Zn | Ge | Sn | Pb |
|---|---|---|---|---|---|---|
| 2/8 | 160 (13%) | 1.9 (38%) | | | | |
| 3/29 | | 2.1 (36%) | | | | |
| | | 2.1 (13%) | | | | |
| 4/6 | 184 (59%) | <4 (14%) | | | | |
| | 200 (4%) | | | | | |
| 5/29 | 184 (14%) | 2.5 (42%) | 20 (21%) | 0.4 (10%) | | |
| 6/14 | 183 (44%) | 2.4 (56%) | 30 (63%) | 0.47 (74%) | 6.2 (59%) | 1.8 (47%) |
| | | 3.2 (33%) | 32 (51%) | | | |
| 11/1 | | | | | 4.3 (72%) | 13 (53%) |

| Exp. Date | Ag | Ti | Al | Mo | Sus |
|---|---|---|---|---|---|
| 9/26 | 8.7 (58%) | 1030 (43%) | 0.24 (31%) | 5.8 (68%) | 29 (53%) |
| | 8.3 (66%) | | 0.16 (31%) | 6.0 (31%) | 30 (57%) |
| 11/1 | 9.4 (65%) | 980 (47%) | 0.18 (66%) | 9.9 (14%) | 31 (53%) |
| | | 1070 (59%) | 0.25 (34%) | | |
| 11/15 | | | 0.29 (64%) | | |

Radiochemical purity of the separated ^{18}F was checked by the gamma-ray spectra and the decay curve.

No gamma-rays except annihilation radiation were found, and the decay curve agreed well with the decay of ^{18}F even for germanium samples with low oxygen contents (0.5 ppm).    The

carrier recovery was measured by titration with the help of a fluoride electrode. Quartz plates were used as the activation standard. The separation time was always 60 to 90 min., which was shorter than the half life of $^{18}$F. The oxygen contents and the carrier recoveries are given in Table 2. The first column in this table shows the experimental date. The present methods have been shown to give fairly good reproducibility.

Reference

1)  T. Nozaki, Y. Yatsurugi, N. Akiyama, Y. Endo, and Y. Makide: J. Radioanal. Chem., 19, 109 (1974).

## 7-3. Charged Particle Activation Analysis of Oxygen in Silicon Nitride Film on Silicon Wafer

T. Nozaki, M. Iwamoto, K. Usami,
I. Mukai, and A. Hiraiwa

Charged particle activation analysis by the $^{16}O(^3He, p)^{18}F$ reaction was applied to the determination of oxygen in silicon nitride films on semiconductor silicon wafers, which are often used as protective film and diffusion mask in the production of integrated circuits. The sample film was prepared by epitaxial deposition from a gas mixture of $SiH_4$-$NH_3$-$N_2$ under a glow discharge in the Central Research Laboratory of the Hitachi Electric Company. Thicknesses of the wafer and film were about 500 $\mu$m and 30 to 500 $\mu g/cm^2$, respectively.

We used the same bombardment apparatus and similar experimental procedures as were described in our previous report.[1] Two identical samples were placed, with the film sides face to face in good contact, on a water-cooled target holder and set in the bombardment apparatus. The sample disposition is illustrated in Fig. 1 together with the classification of the oxygen position in the sample. After evacuation, the samples were bombarded with $^3He$ particles (0.5 to 0.8 $\mu$A, 5 to 20 min) of 32.5 MeV initial energy, which was degraded by the beam window foils and the wafer to about 7.5 MeV at the films. The silicon nitride film with some part of the wafer (about 5 $mg/cm^2$ thickness) was then removed from the main part of the wafer by mechanical grinding and was collected in a counting tube. This process was carried out separately for each of the two samples bombarded in contact.
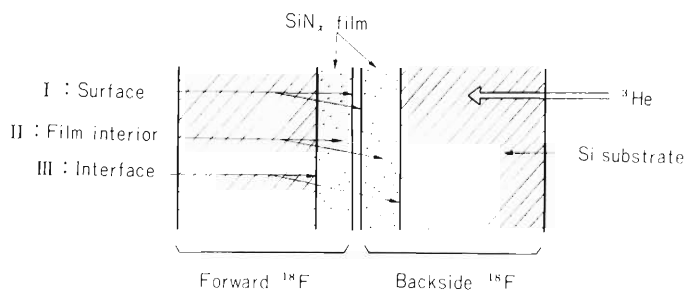


Fig. 1. Sample arrangement.

The annihilation radiation from the tube was measured by a scintillation counter with a well-type crystal and a single channel analyzer. The decay curve thus obtained agreed completely with the decay of $^{18}F$ after more than 2 h from the bombardment.

As for the activation standard, a stack of Mylar foils (about 3 $mg/cm^2$ thickness) was bombarded at an almost identical position with the silicon nitride films under bombardment to give an apparent excitation curve for the $^{18}F$ formation in a $^3He$ energy range about 7.5 MeV. The effect of a small variation of the wafer and film thicknesses on the result of the analysis was corrected by the use of this curve.

The oxygen quantities thus determined are shown in Fig. 2 vs. film thickness for samples of different thicknesses and various preparation conditions. Type A samples and Type B samples were prepared from the gases in different cylinders and on different days. The temperature in Fig. 2 is the temperature of the silicon wafer at the epitaxial deposition of the nitride film.
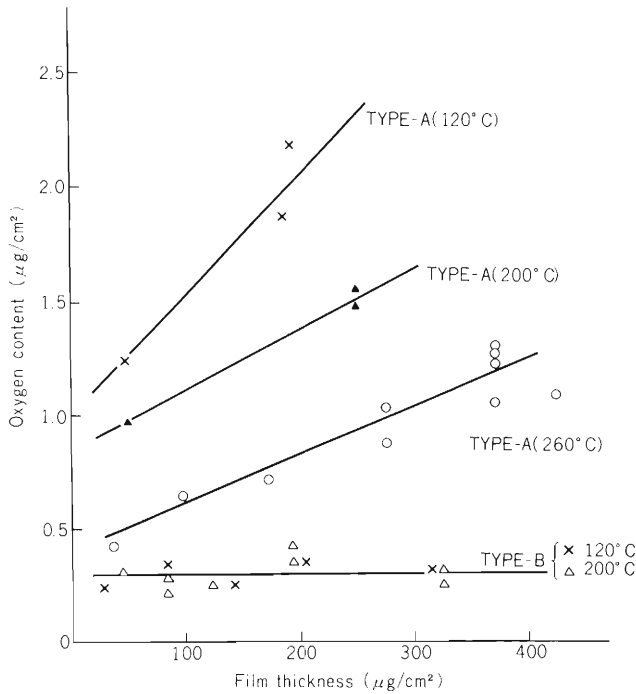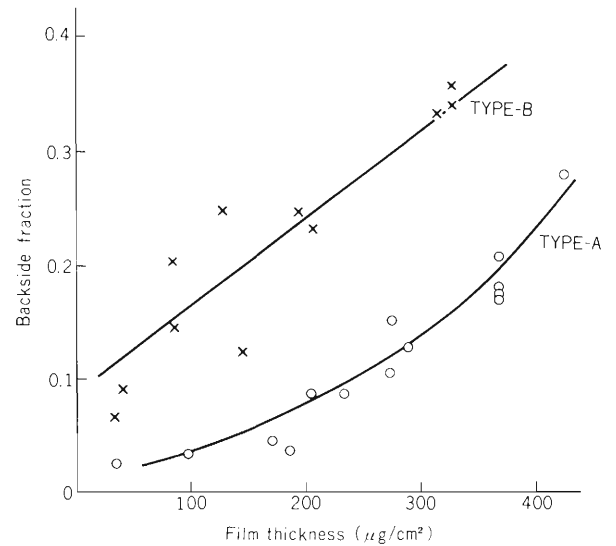
Fig. 2.  Oxygen  quantity  vs  film thickness.



Fig. 3.  Backside $^{18}$F  fraction  vs film  thickness.

In Fig. 3 is shown the film thickness dependence of the backside $^{18}$F fraction, which is the fraction of $^{18}$F in the backside sample to the sum of $^{18}$F in both samples (see Fig. 1). From Figs 2 and 3, the position of the main part of oxygen in the sample can be known for each type of the sample by deduction based on the ralationships in Table 1.   These relationships can be easily understood from the nuclear recoil effect of the $^{18}$F at its formation.   A summary of the results is shown in Table 2.   In order to get some more quantitative information about the oxygen position, the spectrum for the forward recoil range of the $^{18}$F is necessary.   We are going to measure it for various $^3$He energies and in different materials.

The oxygen was also measured by ESCA, which is sensitive only to a surface layer of about 5 nm thickness.   Actually, the results of ESCA were found to be higher usually by about one order than those of the activation analysis for Type A samples.

Table 1.  Oxygen position vs. observation quantities.

| Oxygen position | Film-thickness dependence of total oxygen | Backside $^{18}$F fraction | Film-thickness dependence of the fraction |
|---|---|---|---|
| (I)   Surface | Independent | Small | Independent |
| (II)   Film interior | Proportional to thickness | Larger than I | Increase with thickness |
| (III) Interface | Independent | Larger than II | Steeper increase than II |

Table 2. Quantity and position of oxygen (Summary of results).

| Sample type | | A | B |
|---|---|---|---|
| Oxygen quantity | Total quantity | Large ($0.4 - 2\ \mu g/cm^2$) | Small ($0.2 - 0.3\ \mu g/cm^2$) |
| | Film-thickness dependence | Linear increase with thickness | Independent of thickness |
| Film-thickness dependence of backside F-18 fraction | | Slight increase with thickness | Pronounced increase with thickness |
| Main oxygen position | | Film interior ($0.2 - 0.6\ \%$) + Surface ($0.4 - 1.0\ \mu g/cm^2$) | Interface ($0.2 - 0.3\ \mu g/cm^2$) |

Reference

1) T. Nozaki and M. Iwamoto: IPCR Cyclotron Progr. Rep., 11, 116 (1977).

## 7-4. Production of Radioisotopes and Labelled Compounds

T. Nozaki, S. Ambe, Y. Terai,
M. Iwamoto, K. Fukushi, and T. Irie

Following radioisotopes were produced for their carrier- and salt-free separation study, labelling experiment or tracer use: $^{18}$F, $^{43}$K, $^{73,74}$As, $^{73}$Se, and $^{77}$Br.[1]–[3]

Use of KF-crown ether (18-crown-6) system proved to be effective for fluorination with $^{18}$F produced by $^3$He- or $\alpha$-particle bombardment of water.[1] The $^{18}$F-labelling yield was examined for various conditions of the fluorination experiment, such as the reaction medium and quantity of the crown ether and of the added carrier. Carrier-free 21-fluoro-progesterone-$^{18}$F has been obtained by the reaction of 21-mesylprogesterone with the carrier-free $K^{18}$F-crown ether in chloroform followed by chromatography of the product. It was found that the presence of a trace amount of foreign metal ions which form complex with fluoride ion would noticeably lower the $^{18}$F-labelling yield.

By bombardment of germanium with protons (15 MeV) $^{73,74}$As was produced. The metallic germanium target was dissolved in $HF-HNO_3$, the solution evaporated, and the residue dissolved in 10 N HCl. From the solution, Ge(IV) was removed first by $CCl_4$ extraction and then by anion exchange. The $^{73,74}$As was reduced to As(III), extracted into $C_6H_6$, and back-extracted into water to give an almost neutral salt-free solution of carrier-free $^{73,74}$As. By colorimetry with phenylfluorone, no Ge(IV) was detected in this solution (less than 1 $\mu$g in 10 ml). This product was offered to Kitazato University to be used as an $^{74}$As ($T_{1/2}$ = 17.9 d) tracer. As for $^{73}$As, the count rates of its K$\alpha$ X-rays, K$\beta$ X-rays and 13.3 keV $\gamma$-rays were found to be in the ratio of 1500 : 300 : 1 when measured by a 16$\phi \times$ 5 mm Si(Li) detector. Possibility of using $^{73}$As as a Mössbauer source of $^{73}$Ge is now under consideration.

Carrier- and salt-free separation of $^{73}$Se from arsenic targets was studied by various methods.[2] Volatilization of $^{73}$Se oxide from condensed polyphosphoric acid added with a small amount of $H_2O_2$ was found to be the most suitable for this purpose, because the arsenic proved to be retained in the glassy polyphosphoric acid. Our study of $^{73}$Se-labelling is reported separately in this volume.

Agricultural use of $^{77}$Br and $^{43}$K has been continued. Uptake of $^{43}$K by rice plants under various conditions was studied in order to get information about the most effective use of potassium fertilizers.

Carrier-free 21-bromoprogesterone-$^{77}$Br was successfully synthesized from the corresponding mesylate, similarly with 21-fluoroprogesterone-$^{18}$F. Synthesis of radio-halogen derivatives of cholesterol has been continued, and their adrenal affinity and lipoprotein binding were measured and discussed.[3] Also, radio-halogen labelling of tyrosine and phenylalanine is under way for the study of their mis-incorporation in protein molecules caused by aging of protein-synthesizing enzymes.

References

1) T. Irie, K. Fukushi, T. Ido, and T. Nozaki: Proc. 2nd Intern. Symp. Radiopharm. Chem., p. 17 (1978), (Printed in Hammersmith Hospital, London).
2) T. Nozaki, Y. Itoh, M. Iwamoto, and K. Ogawa: ibid., p. 223.
3) K. Fukushi, T. Irie, T. Nozaki, T. Ido, and Y. Kasida: ibid., p. 49.

### 7-5. Preparation of $^{73}$Se-2-Selenouracil

K. Ogawa,* K. Taki, and T. Nozaki

For the purpose of the medical use of selenium-73 ($T_{1/2}$ = 7.1 h) instead of selenium-75 ($T_{1/2}$ = 120 d), synthesis of $^{73}$Se-labeled compounds has been studied.[1]   It is well known that sulfur atoms in some thio-compounds such as 2-thiouracil and 6-mercaptopurine can be labeled by isotopic exchange with elemental $^{35}$S-sulfur.   From the similarity of sulfur and selenium in chemical properties, such an isotopic exchange can be expected to take place also between some selenium compounds and elemental selenium.

Actually, 2-selenouracil was found to be labeled by isotopic exchange with red $^{75}$Se-selenium in a mixture of pyridine and carbon disulfide (1:1) at 110 °C.   The occurrence of exchange was confirmed by paper chromatography using a mixture of n-butanol, acetic acid and water (2:1:1) and also by repetition of reprecipitation and activity measurement.   The result of the latter is shown in Fig. 1.

Figure 2 shows the activity of $^{75}$Se-2-selenouracil in the reaction of 2-selenouracil (1 mg) with red $^{75}$Se-selenium (4.9 $\mu$g) in 2 ml of the above solvent at 110 °C, as a function of the heating time.   When $^{73}$Se is used instead of $^{75}$Se, the radioactivity of $^{73}$Se-2-selenouracil gives a maximum at a reaction time of 5 to 7 h because of the short life of $^{73}$Se.

$^{75}$Se-2-selenouracil formed as above was leached from the reaction mixture into an aqueous solution after the addition of hold-back carriers of red selenium (10 ml of $CS_2$ solution) and metallic selenium (10 mg) followed by evaporation of the solvent.   The radioactivity of elemental selenium remaining in this solution as a contaminant was found to be less than 0.5 % of the product activity.
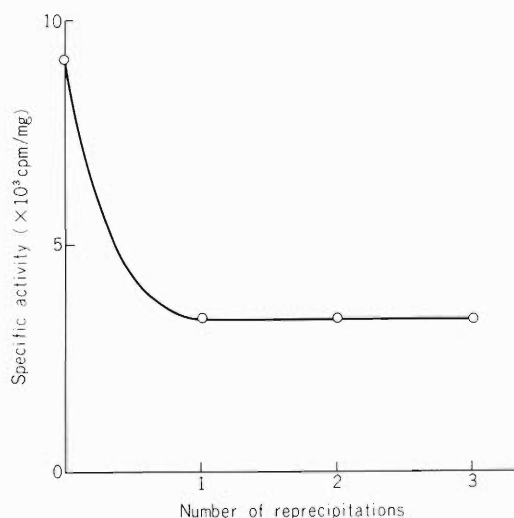


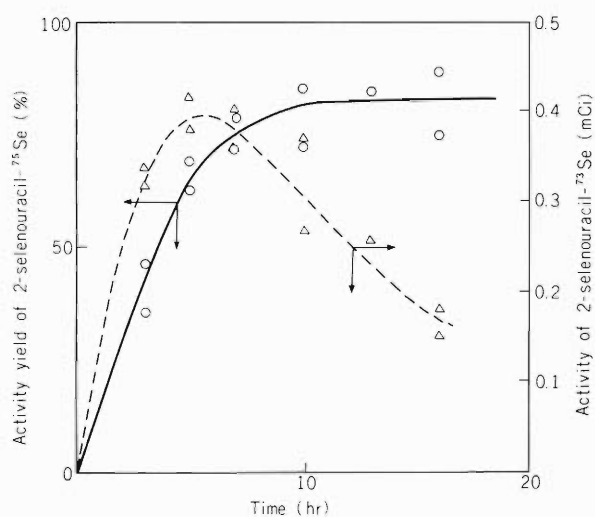Fig. 1.   Specific activity of $^{75}$Se-2-selenouracil after repeated reprecipitations.

Fig. 2.   Activity yield of $^{75}$Se-2-selenouracil ( ——o—— ) and activity of $^{73}$Se-2-selenouracil ( -----△----- ) as a function of reaction time (h).

*  Faculty of Hygenic Science, Kitasato University.

As reported previously,[2] the selenium-73 was produced by the nuclear reaction $^{75}$As(p, 3n)$^{73}$Se induced by bombardment with protons from the FM cyclotron. After the target (As$_2$O$_3$) was dissolved into the mixture of conc. HNO$_3$ and conc. HCl (3:1) containing 5 $\mu$g of H$_2$SeO$_3$ as carrier, the selenium was reduced to red selenium with hydrazine and extracted into carbon disulfide. In order to examine the contamination by arsenic, carrier-free $^{74}$As-arsenous acid was added to the target solution and its behavior was followed. No activity of the $^{74}$As was detected in the final carbon disulfide extract.

Thus 600 $\mu$Ci of $^{73}$Se-2-selenouracil was obtained by the reaction of 5 mCi of $^{73}$Se with 1 mg of 2-selenouracil in the above solvent (2 ml) at 110 °C for 7 h.

References

1)  K. Ogawa, K. Taki, T. Nozaki, and M. Okano: IPCR Cyclotron Progr. Rep., 11, 137 (1977).
2)  T. Nozaki, Y. Itoh, M. Iwamoto, T. Karasawa, K. Fukushi, T. Irie, and T. Hara: ibid., p. 134.

# 8. RADIATION CHEMISTRY AND RADIATION BIOLOGY

### 8-1. Measurement of Fast Emission Decay of Heavy Ion-Irradiated Single Crystals; Nanosecond Time-Resolved $\sigma$-Emission Spectra of KBr

K. Kimura and M. Imamura

We have made measurement of the emission spectra for heavy-ion irradiated single crystals to elucidate the nature and behavior of the electronic excited states, and compared with the results for X-ray or electron irradiation. In fact, an extraordinarily large intensity-ratio of $\sigma$-emission to $\pi$-emission has been found with a KBr single crystal irradiated with C-ions at 4.2 K;[1] the ratio is about 5 times larger than that for X-ray or electron irradiation. We have intended, for better understanding of the primary processes in the heavy-ion irradiated systems, to measure the time-dependent emission spectra with a resolution of nano-subnanosecond. There are many difficulties, however, for accomplishing such a resolution because of low and unstable beam current and inherent widths of beam pulses as well as the requisition of a highly sensitive detection technique. These difficulties have ultimately been overcome by developing the assembly of equipments described below, and the measurement of decay curves was successfully made with KBr at 4.2 K.

The decay processes of emissions were studied under the conditions of single-ion irradiation and single photon counting using a TAC (time-to-amplitude converter). Experimental setup is shown in Fig. 1. A thin plastic scintillator about $10\mu$m thick placed on the way of heavy ion-beams emits several tens photons per an ion having passed through, which were detected with a Hamamatsu R647 photomultiplier (dark counts: about 20 cps) to generate "stop pulses". As the present beam current is less than the rate of an ion per a beam bunch, the width of the beam bunch is negligibly small. 'Start pulses" were generated by the output from the photomultiplier
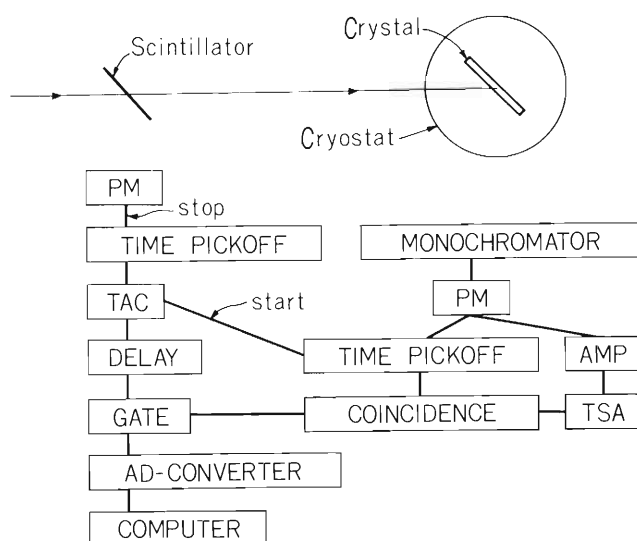


Fig. 1. Setup for measurement of time-dependent emission spectra.

which detects emission from a target cooled at 4.2 K. Since the frequency of the stop pulses was conditioned to be much higher than that of the start pulses, exact measurement of the lifetimes of excited states could be performed. Periods between the stop and start pulses were measured with a TAC in the setup shown in Fig. 1. The counts of output pulses from the TAC were accumulated using an online computer; the resulting plot of the counts vs. the pulse heights gives the decay curve of the excited states at a given wavelength. The time scale was calibrated using a RF frequency of the cyclotron or delay lines. Figure 2 shows such a decay curve obtained at 280 nm for the $\sigma$-exciton created in a KBr single crystal irradiated with 85MeV C-ions at 4.2 K. Apparently the decay curve consists of two components as shown in Fig. 3, where logarithm of photon counts is plotted as a function of time. The half-lives of the intense and short-lived component and the weak and long-lived one were found to be 2 and 7 ns, respectively; the corresponding values reported for electron or proton irradiation are 3.3 and 17 ns, respectively.[2] Very close half-lives of the fast-decay components for heavy-ion and electron or
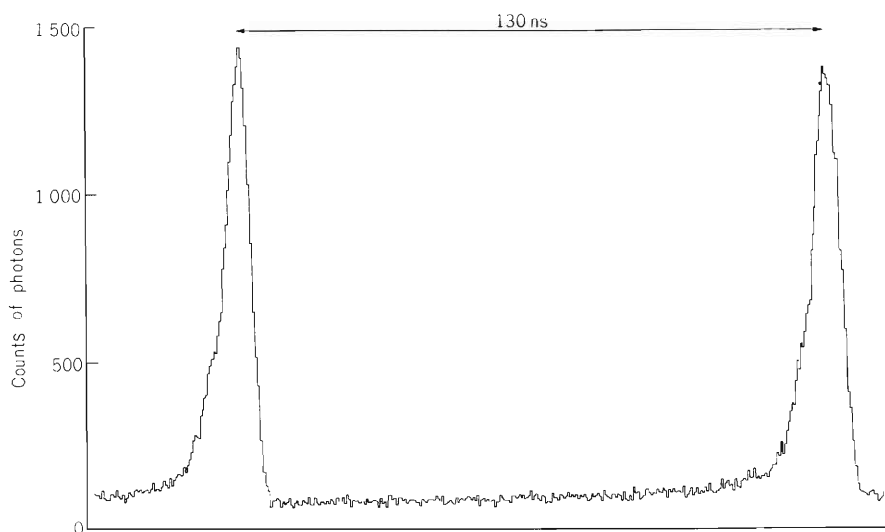


Fig. 2. A plot of photon counts vs. pulse heights for KBr irradiated at 4.2 K. $C^{6+}$-beam currents were about 10 pA. Separation of beam bunches was 130 ns.
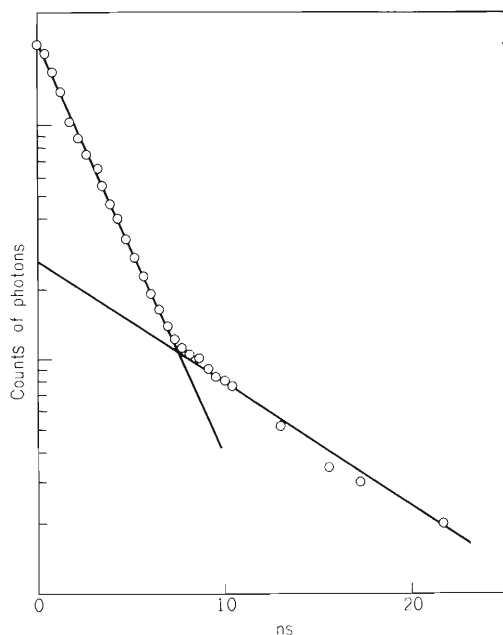


Fig. 3. Exponential plot of the data in Fig. 2.

proton irradiation as well as a good straight line in Fig. 3 indicate that neither interaction of the $\sigma$-excitons with color centers nor interaction between $\sigma$-excitons takes place in these irradiated crystals.   This conclusion supports the previous suggestion[3] that the extraordinarily large intensity ratio of the $\sigma$-emission to $\pi$-emission is due to interaction of free excitons at the higher excited states.   In conclusion, we can say the yield of the $\sigma$-exciton is 5 times higher than that of the $\pi$-exciton in the heavy-ion irradiated KBr single crystal.

Our technique is useful for elucidating dynamic processes in the primary stages of heavy-ion irradiation which have been little known.   Furthermore, this technique may be useful in the cases of irradiation experiments under sparse beam currents, e.g., when using radioisotopes.

The authors are indebted to T. Fujisawa for helpful advice and support to the coincidence technique.

References

1)   K. Kimura and M. Imamura: Phys. Lett., 67A, 159 (1978).
2)   I. M. Blair, D. Pooley, and D. Smith: AERE-R6906 (1971).

# 8-2. Effects of $\alpha$-Particles on Mammalian Cells

M. Sasaki, S. Sawada, F. Yatagai,
I. Kaneko, and A. Matsuyama

Experimental studies are in progress on the action of high LET particles on mammalian cells since 1976.  Following works were done in 1978:

1.  Relative effectiveness of $\alpha$-particles and $\gamma$-rays in the formation of chromosome aberration in human blood lymphocytes.

Peripheral blood lymphocytes obtained from healthy person were irradiated with 4.8 MeV/amu $\alpha$-particles accelerated by the cyclotron and the frequencies of chromosome aberrations were measured with the cells at the first mitosis after irradiation.   Chromosome aberrations were efficiently produced and a linear dose-response relation of $1 \times 10^{-2}$/cell/rad was obtained for the induction of dicentrics and rings.   The distribution of chromosome aberrations among cells deviated from the Poisson distribution.   This fact indicates that $\alpha$-particles do not give the uniform effect on the cell, especially in the low dose range differing from that X- or $\gamma$-rays.   This feature could be reasonably explained by the track model in which the dose is not given in rad but by the number of particles which penetrated a cell.   The track model when applied to the distribution of chromosome aberrations indicates that a single passage of a 4.8 MeV/amu $\alpha$-particle, corresponding to the average dose of 27 rads, leads to the interphase death of the cell and/or the inactivation of phytohemagglutinin activity to give survival level of approximately 37%.

2.  Comparison between the effect of $\gamma$-rays and that of $\alpha$ particles in the production of double-strand cuts and their rejoing in DNA of mouse leukemic L5178Y cells by DNA fiber autoradiography.

Mouse leukemic L5178Y cells labeled with $^3$H-thymidine were irradiated with Co 60 $\gamma$-rays and $\alpha$-particles acceralated in the cyclotron (4.8 MeV/amu at sample).   Immediately after irradiation, cells were collected to prepare for molecular autoradiograms of DNA to estimate the number of double-strand cuts.   At various times (up to 120 min.) of post-irradiation incubation at 37°C, the number of rejoined broken DNA strand was determined.   Cells collected in these determinations were treated as described previously for the case of DNA fiber autoradiography.[1]

Preliminary results showed that the length of DNA becomes shorter with the increase of irradiation dose up to 20 krads but no further change occurs up to 50 krads in both $\gamma$- and $\alpha$-ray irradiation.   It appears that Co 60 $\gamma$-irradiation might be more effective for the production of the double-strand cuts of DNA than $\alpha$-irradiation, although the temperature effects during the irradiation remains to be investigated.   The length of the irradiated DNA increased in proportion to the time of incubation at 37°C after the irradiation and returned to the length of the unirradiated DNA by 120 min incubation at 37°C.   These facts indicated that DNA damages by $\alpha$-particles were repairable as well as those by Co 60 $\gamma$-rays.   The rate of the repair in the case of $\gamma$-ray irradiation was higher than that of $\alpha$-particle irradiation.

3. Storage of cultured mammalian cells

To meet the need of constant supply of cells for further investigations concerning the effect of high LET radiations on the mammalian cells, Chinese hamster V79 BIM, mouse L-929, mouse Lp3$^{COR}$, and HeLa S3 cells have been stored in liquid nitrogen.

Reference

1) S. Sawada, M. Sasaki, S. Okada, F. Yatagai, I. Kaneko, and A. Matsuyama: IPCR Cyclotron Progr. Rep., 11, 42 (1977).

## 8-3. Studies on Molecular Damages Induced by High-LET Particles

F. Yatagai, S. Kitayama, Y. Hattori, and A. Matsuyama

1. Inactivation of ribonuclease A in solution by α-particles

Effect of α-particles with energy of about 4.6 MeV/amu on the inactivation of bovine pancreatic ribonuclease (RNase) A (EC 2.7.7.16) in solution was studied with particular attention to the influence of co-existing substances. The apparatus and system were essentially the same as described previously.[1] Sample solutions were as follows: (1) $5 \times 10^{-6}$ M aqueous solution of RNase A; (2) $5 \times 10^{-6}$ M RNase A plus salmon sperm deoxyribonucleic acid (DNA) (10μg/ml) — RNase-DNA complex; (3) $5 \times 10^{-6}$ M RNase A in 0.1M $NaClO_4$ plus DNA (10μg/ml) — dissociated complex; (4) $5 \times 10^{-6}$ M RNase A in 0.1M $NaClO_4$. Experimental results obtained so far showed some protective effects on the inactivation of RNase A in the above-mentioned three types of mixed solutions: (2), (3), and (4).

According to Lynn,[2] DNA protects RNase A against inactivation by γ-rays when it forms complex with RNase A, but DNA does not show such action when the complex is dissociated by the presence of 0.1M $NaClO_4$. Since $ClO_4^-$ has an extremely low affinity to OH radical and hydrated electron as well,[3] it seems improbable that $ClO_4^-$ acts as a scavenger for those species. Thus the protective activity of the solutions containing $NaClO_4$ in case of α-irradiation suggests that the mechanism of enzyme inactivation by α-particles may differ from that by γ-rays.

In the course of study in this period it was found that the improvement of the cell for irradiation is necessary in order to increase the reproducibility of data.

2. Induced mutagenesis in phage φX174 irradiated with α-particles and N-ions

An amber 3 mutant of phage φX174 was irradiated with α-particles and N-ions having energy of about 4.6 MeV/amu to determine the efficiency of reverse mutation to (pseudo) wild-type. In the cases of both ion beams, the efficiency did not increase with increasing dose to the phage when host cells (E. coli HF47043 (uvrA)) had not been irradiated. On the other hand, mutation induction was observed with UV-irradiated host cells. The induced mutagenesis observed can be explained by the error-prone DNA repair (sos repair) in the UV-irradiated host cells.

Molecular mechanism of induced mutagenesis has been studied by analysis of the first round DNA replication on UV-irradiated φX174 DNA.[4] UV-induced photolesions in viral DNA are considered to cause a permanent blockage of DNA replication in intact host cells, while a significant fraction of irradiated φX174 DNA molecules seems to be fully replicated due to the sos repair in UV-irradiated host cells. Similar analysis was made on α-particle irradiated φX174 DNA, but there was no increase in the relative amount of double-stranded DNA which was estimated from equilibrium $Cs_2SO_4$-Hg density-gradient analysis. The relative amount of double-stranded DNA was also found to be much higher than that predicted from the surviving fraction of irradiated φX174. These preliminary results suggest the possibility that some components other than replicative form (RFI) may be included in the double-stranded DNA fractions obtained.

124

3. Enhanced priming activity of DNA in M. radiodurans by N-ions

Irradiation of cells or DNA at low LET range induces single strand breaks in duplex DNA and some of them are priming sites for DNA polymerase. This is the reason why $\gamma$-ray irradiation stimulates DNA synthesis in living cells or permeable cells as previously reported.[5)-8)] After improvement of irradiation apparatus to keep the temperature near $0°C$, permeable cells of M. radiodurans were irradiated with $\alpha$-particles (4.78 MeV/amu). It was concluded that biochemical lesions similar to those induced by $\gamma$-rays were brought about along the track of $\alpha$-particles.[8)] This conclusion was supported by "42°C effect" on M. radiodurans, i.e. loss of extreme radioresistance of this bacterium by brief postincubation at $42°C$ following the irradiation with $\gamma$-rays, $\alpha$-particles or treatment with chemicals which induce single strand breakage in DNA.[9)]

Permeable cells of M. radiodurans covered with a thin filter were irradiated with N-ions (4.5 MeV/amu) to compare the changes in template/primer activity of endogenous DNA. DNA synthetic rate was increased up to 2 fold by increasing the dose of N-ions as was the case in $\gamma$-ray irradiation. This result implies that N-ions induce the same biochemical lesions in DNA as irradiation with low LET radiation along its track where many secondary electrons are ejected. This supports the conclusion that biochemical lesions induced by high LET particle irradiation is accompanied by many lesions similar to those induced by $\gamma$-rays of $^{60}$Co even if characteristic biochemical lesions are induced by such particles.

References

1) Y. Hattori, F. Yatagai, and A. Matsuyama: IPCR Cyclotron Progr. Rep., 11, 130 (1977).

2) K. R. Lynn: Radiat. Res., 66, 644 (1976).

3) M. Anbar and P. Nete: Int. J. Appl. Radiat. and Isotopes, 18, 493 (1967).

4) P. Caillet-Fauguet, M. Details, and M. Radman: J. Mol. Biol., 117, 95 (1977).

5) P. T. Emmerson and M. Kohiyama: Nature, New Biol., 233, 214 (1971).

6) D. Billen and G. R. Hellerman: Biochim. Biophys. Acta, 361, 166 (1974).

7) S. Kitayama and A. Matsuyama: ibid, 418, 321 (1976).

8) S. Kitayama, F. Yatagai, and A. Matsuyama: IPCR Cyclotron Progr. Rep., 11, 126 (1977).

9) S. Kitayama, K. Siratori, F. Yatagai, and A. Matsuyama: Agr. Biol. Chem., 41, 2297 (1977).

# 9. RADIATION MONITORING

9-1. Routine Monitoring

K. Igarashi, I. Sakamoto, and I. Usuba

Results of routine radiation monitoring carried out on the cyclotron from April 1977 to March 1978 are described.

No remarkable change in leakage radiation and residual activities was observed during this period. Some aspects of the leakage radiation are described in the following report.

(1) Surface and air contamination

The surface contamination has been kept below $10^{-6}$ $\mu$Ci/cm$^2$ on the floor of cyclotron room and the underground passage, and below $10^{-7}$ $\mu$Ci/cm$^2$ in the experimental areas, hot laboratory and chemical laboratories. The contamination was wiped off twice a year, and by this decontamination, the contamination on the floor of cyclotron room and the underground passage could be reduced to a value below $10^{-7}$ $\mu$Ci/cm$^2$.

When the accelerating chamber was opened, slight contamination of the air in the cyclotron room was observed. The value of radioactivity concentration (beta-gamma) was $10^{-13}$ $\mu$Ci/cm$^3$.

(2) Drainage

The radioactive concentration of the drain water from the cyclotron building was found to be

Table 1. Annual exposure dose received by the cyclotron workers from April 1977 to March 1978.

| Workers | Number of persons | | | | Collective dose (man-mrem) |
|---|---|---|---|---|---|
| | Dose undetectable | 10–100 (mrem) | 101–300 (mrem) | >300 (mrem) | |
| Operators | | 1 | 5 | 1 | 1740 |
| Nuclear physicists | 11 | 9 | 2 | | 460 |
| Accelerator physicists | 5 | 1 | 1 | | 200 |
| Physicists in other fields | 12 | 8 | | | 170 |
| Nuclear chemists | 1 | 7 | 4 | | 940 |
| Radiation chemists | 7 | | | | |
| Biological chemists | 8 | | | | |
| Health physicist | | 1 | | | 10 |
| | | | | Total | 3520 |

Average annual dose per person: 41.9 mrem

Maximum individual annual dose: 540 mrem

of the order of $10^{-7}$ $\mu Ci/cm^3$. The total quantity of activities in the aqueous release in this period was about 3.4 $\mu Ci$, which is about 13 % larger than that of the last year.

(3) Personnel monitoring

The external exposure dose to personnel was measured with gamma-ray and neutron film badges. The dose received during the present period by all the cyclotron workers is shown in Table 1. The collective gamma-ray dose to all workers was 3520 man-mrem, while those owing to thermal and fast neutron exposures were too small to be detected.

The dose to the cyclotron workers increased by about 61 % compared with that of the last year. In this period the dose to the cyclotron operators was 1740 man-mrem, which was 49.4 % of the dose of cyclotron workers, and the maximum individual annual dose was 540 mrem.

## 9-2. Leakage Radiation Measurement at the Underground Passage

I. Sakamoto

Leakage radiation during operation of the cyclotron at the underground passage of the cyclotron building was measured. Leakage dose received during the present period by the gamma-neutron film badges which were left at the underground passage, is shown in Table 1. The ratio of neutron dose to total dose was about 0.3.

Among the dose values at the point No. 1 measured every month, the maximum dose of 2770 mrem was observed in October. In this case, the values of gamma dose, thermal neutron dose and fast neutron dose were 1680 mrem, 860 mrem and 230 mrem, respectively.

The machine time for deuteron acceleration was allotted in May, July and October. The total dose at the point No. 1 measured in the three months was 4990 mrem, which was 78.7 % of the total dose in this period.

Table 1. Leakage radiation dose (in mrem) at the underground passage from April 1977 to March 1978.

| Radiation \ Point of observation* | 1 | 2 |
|---|---|---|
| gamma ray (mrem) | 4390 | 430 |
| thermal neutron (mrem) | 1670 | 110 |
| fast neutron (mrem) | 280 | 40 |
| Total (mrem) | 6340 | 580 |

\* See the figure shown below.



Cross section          Ground plan          Basement
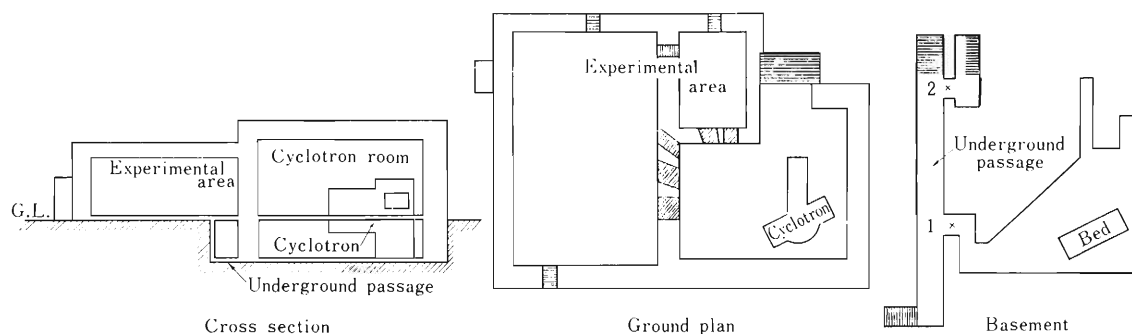
# 10. HEAVY ION LINEAR ACCELERATOR PROJECT

## 10-1. Status of the Constructional Work

M. Odera

All resonators, except the first one which was installed at the end of 1976 were installed this year without any significant change in their design from that of the first one. The first cavity was tested for a year and only some minor modifications such as increase of capacity of motor for shorting plane drive and change of material of the cooling water line inside of vacuum chamber were found necessary. The second cavity arrived at the laboratory on Jan. 7th from the factory and then at intervals of about ten days, other cavities were successively carried in. The installation and alignment work was completed by the end of March. Figure 1 shows the array of six cavities
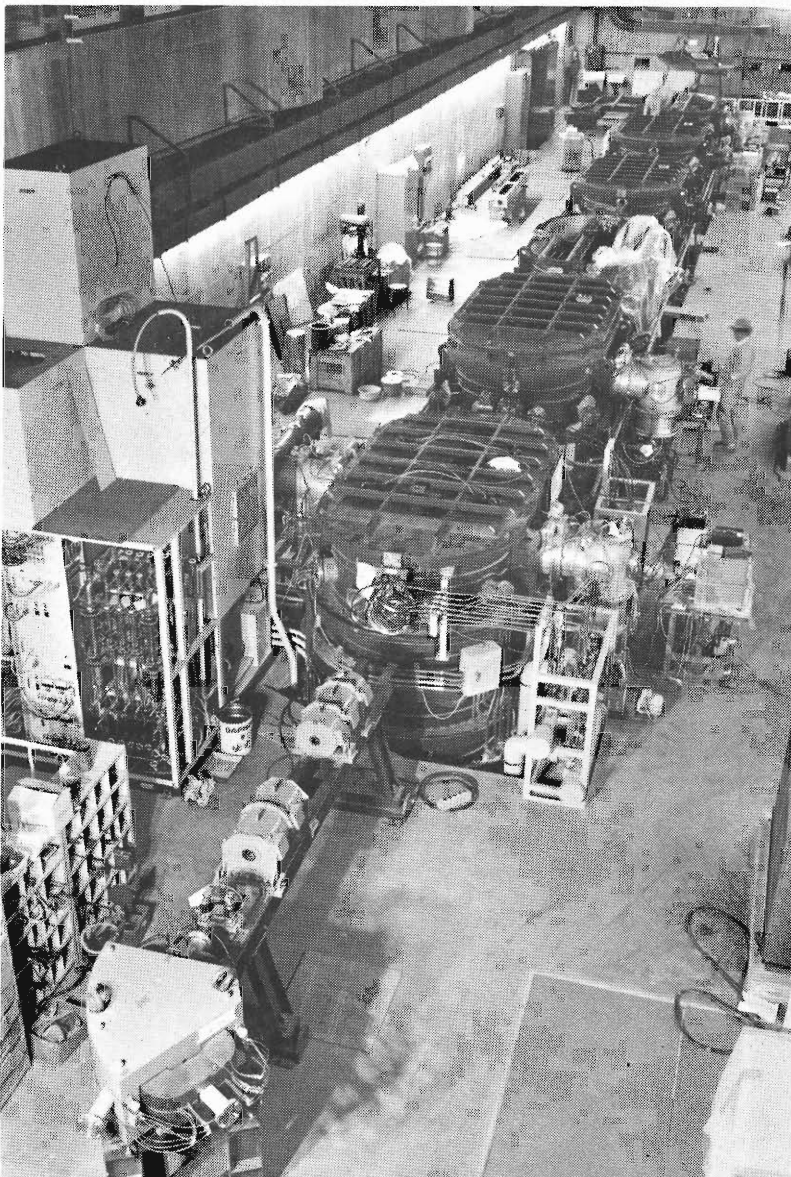


Fig. 1. Resonators in the accelerator vault.

installed in the accelerator vault.

Orders for the magnets of the beam transport line and their power supplies were given to the factories in May and September respectively. Those will be installed before the end of Apr. 1979.

The radiation monitoring system is being manufactured. It will begin operation from Jan. 1979 to record background radiation before completion of the linac.

For the beam line, the ISO-type vacuum flanges and components have been adopted. Those were developed from the European PNEUROP standard and can be easily mated with the Japanese Industrial Standard components with the minimum number of converters. It is planned to distribute the relatively small turbo-molecular pumps and getter ion pumps along the beam line and to get high vacuum free of oil or other contamination.

Installation of the accelerator control system begins in Nov. and will be completed before Aug. next year.

Construction of the remaining parts of the building such as the target areas, remote control and measurement room, electronic shop, vacuum equipment testing room, ion source preparation room etc. began in Feb. and finished at the end of November.

## 10-2. Installation and Alignment of the Resonators and the Drift Tubes

M. Odera, Y. Miyazawa, and M. Hemmi

It took nearly three months to install the five resonators and to align them to the first one. Some parts were rechecked for vacuum tightness before assembling, though they were tested already at the factory. Some small leaks were found and stopped. Alignment of the drift tubes in each tank was checked in the accelerator vault by the hot-wire method described in Ref. (1). The optical axis of the drift tube quadrupole magnets was found within ± 0.1 mm of the beam axis.

Relative positions of the six resonators were adjusted by use of the wedge and screw device with the precision of ± 0.2 mm. The value is satisfactory since a couple of steering magnets can easily correct beam trajectory for such small deviation if necessary.

Reference

1) I. Takeshita, I. Yokoyama, T. Kambara, and M. Odera: IPCR Cyclotron Progr. Rep., 10, 140 (1976); I. Takeshita, T. Kambara, and I. Yokoyama: Reports I.P.C.R., (in Japanese), 53, 44 (1977).

## 10-3. Control System

T. Kambara, M. Odera, and S. Takeda

Parameters of many devices and power supplies of the linac should be set to different combination of values corresponding to each energy-ion combination. In order to help operators monitor and control the parameters, we introduce a control system using a minicomputer HP2171A.

The computer plays the following functions: (1) a digital signal communication center connecting the control room and the devices, (2) a signal conversion and display apparatus in direct contact with operators, and (3) an auxiliary data keeper with which operators can talk and interact. For the convenience of the software design, the IEC bus[1] is used as the standard data-way.

The interlock and sequence logic of the vacuum- and cooling-systems are hard-wired and self-contained locally. Informations on their status are transmitted to the control room and fed to the computer but no control commands are given from the computer.

Devices such as the magnet power supplies, the RF devices and the high-voltage power supply of the injector can be controlled by the computer system. Protection, sequence and feedback systems of each individual device are hard-wired locally. Every device sends its status informations (on/off and interlock status, analog values) to the computer and when the device is not in local control mode it receives commands (on/off, analog setpoints) from the computer.

As the interface between the computer system and the devices, four data stations are installed in the accelerator vault and one in the control room. Those in the accelerator vault are connected to the computer by a serial data link and the IEC bus. The data station has an intelligent interface (a standard product of the Hewlett-Packard Company) and signal conditioner modules. The intelligent interface has a control board with a microprocessor which talks with the computer, and several function boards which provide analog-to-digital conversion and digital input/output under the control of the microprocessor. The signal conditioner modules are installed between the function boards and accelerator devices for electric isolation and signal conversion. The data station can provide the following input/output functions; (1) analog input by voltage signals with full scale of 1V or 10V, (2) analog output by voltage signal with full scale of 10V and resolution of 10bit or 14bit, (3) digital input by floating contacts for status monitoring, (4) digital output by relay contacts for status control.

A control console is installed in the control room which provides the interface between operators and the computer. The data (status and numerals) gathered by the computer are displayed on each of two CRT's (one character display and one graphic/character display) in the most convenient format. Operators can change the status and setpoints using a cursor and a keyboard, and they can also command calculations or data-loggings by calling adequate programs. The graphic/character display is used to show the results in diagrams or graphs.

The device hierarchy is shown in Fig. 1. The computer uses a real time operating system RTE IV which provides foreground and background capability.
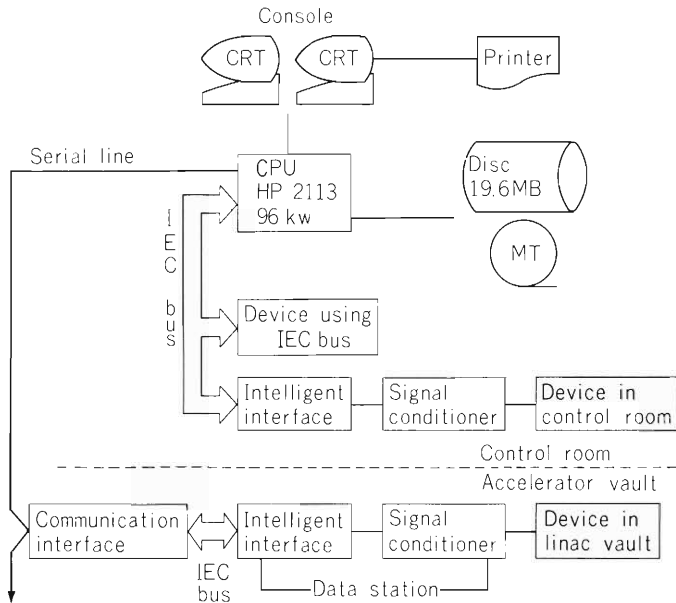
Fig. 1. Hardware hierarchy of the computer system.

Video and other fast signals are transmitted to the control room via coaxial cables individually. A TV display panel and an oscilloscope panel are set in the control room. There are also monitoring panels for cooling, vacuum, and radiation leakage watching systems. The display circuits of them are hard-wired independent of the computer system.

The hardwares such as the signal conditioner modules are being manufactured and tested in the factory of the contractor. The whole system will be installed in spring 1979.

Table 1. Hardware components of the computer system. They are the standard products of the Hewlett-Packard Company.

| | |
|---|---|
| Computer | |
| CPU HP2113 | 1 |
| Main memory 16 bit 96 kW | 1 |
| Disc 20 MB | 1 |
| Magnetic tape 9 track 800 bpi | 1 |
| Console | |
| 24 × 80 character display | 1 |
| 24 × 80 graphic/character display | 1 |
| Serial printer | 1 |
| I/O devices | |
| HP2240A/2241A intelligent interface | 5 |
| IEC bus | 1 |
| Serial link compatible to the IEC bus | 1 |

Reference

1) Dale Horelick: IEEE Trans. Nucl. Sci., NS-22, No. 1, p. 488 (1975).

# 10-4.  Design of a Beam-Emittance Measuring Device

J. Schimizu and M. Odera

Besides beam intensity one of the most important properties of an injector system is the beam quality as measured by emittance.   A detailed knowledge of the beam-emittance behavior as a function of particle mass to charge ratio, injector voltage and transport parameters is needed to match the injector system to the later section of the accelerator.   A device to measure simply and quickly the emittance of an ion beam is therefore a valuable diagnostic tool for injector system and for ion source development and test work.   In this report a simple beam-emittance measuring device is described.

Figure 1 shows the principle of the emittance-measuring device.   The beam of the injector impinges upon the aperture plate; that part of the beam which passes each slit is analyzed by a scanning probe after traversing the drift length L of 15 cm.   The current collected by the scanning probe is fed into x-y recorder.   The position of a particular slit gives the transverse coordinate on the emittance diagram ($x_1$ or $y_1$) and the corresponding image is converted into a measure of the divergence ($x'$ or $y'$) by means of the following formulae:[1]
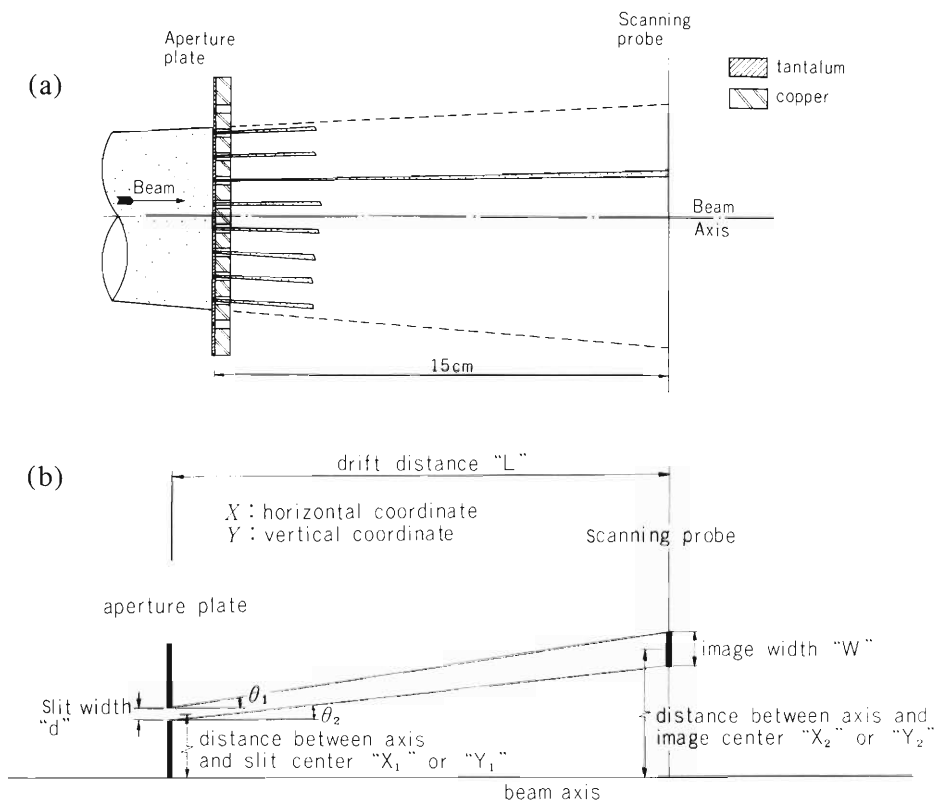


Fig. 1.    Principle of beam-emittance measurement.    (a) Schema of emittance measuring apparatus.    (b) Illustrating method of calculating angular limits of beam.

134

$$\theta_1 = \arctan\left[\{(x_2 + w/2) - (x_1 + d/2)\}/L\right],$$
$$\theta_2 = \arctan\left[\{(x_2 - w/2) - (x_1 - d/2)\}/L\right].$$

The meaning of various symbols is given in Fig. 1(b).   The normalized emittance N is calculated from following formulae:

$$N = \epsilon\beta\gamma \text{ (mm mrad)},$$

where $\epsilon$ is the emittance given by

$$\epsilon = A/\pi \text{ (mm mrad)},$$
$$A = \text{area of emittance diagram},$$
$$\beta = \text{ion velocity}/c,$$
$$\gamma = (1 - \beta^2)^{-1/2}.$$

Values of the main parameters of this device are as follows:

Ten slits of size 0.2 × 50 × 0.5t (Ta), each being separated by 6 mm, a probe of 0.3$\phi$ × 50 (W) which is driven by a pulse motor with speed of 2 mm/sec and stroke of 75 mm,

drift distance 150 mm.

The beam-emittance measuring device described above does not work quickly but is very simple.   To study the quality of the beam from the injector system this emittance device is used until a computer controllable quick device becomes available.


Reference

1)   H. Wroe: Nucl. Instr. and Meth., 52, 67 (1967).

# 10-5. Studies on a PIG Source in the Test Facility

I. Kohno, A. Shimamura, and T. Tonuma

In the test facility[1] we studied production of metal and non-metal ions and formation of ion beam at the position 1.4 m downstream from the source magnet.

For production of metal and non-metal ions a PIG source shown in Fig. 1 which has a sputtering electrode was fabricated. The anode of this source consists of three parts. Upper and lower parts are made of copper cooled by water and the part at the center is made of stainless steel. A sputtering electrode is made of a charge material and insulated from the anode. When
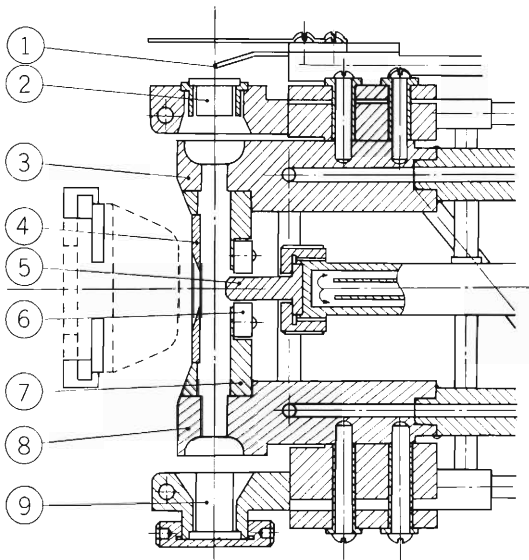


Fig. 1. Hot cathode PIG source with a sputtering electrode.
① Filament, ② Cathode, ③⑧ Cold anode (Cu),
④ Slit, ⑤ Sputtering electrode,
⑥ Insulator, ⑦ Anode (SUS),
⑨ Anti-cathode.
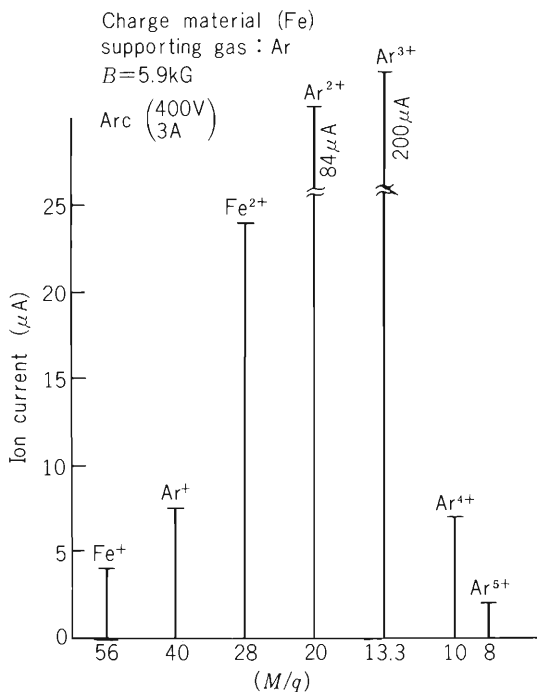


Fig. 2. The m/q spectrum of the ion beam measured in the test facility under the source condition of Varc=440V, Iarc=3A, supporting gas Ar, sputtering electrode Fe.

an electrical potential of about $-500$ V relative to the anode potential is applied to the sputtering electrode the charge material is sputtered by bombardment of ions from the arc plasma. Then sputtered material is ionized and extracted from the ion source. Figure 2 shows a m/q spectrum measured in the test facility when the ion source was operated under the following condition: arc voltage 440 V, arc current 3 A, supporting gas Ar and sputtering electrode Fe. In this figure we can recognize the existence of $Fe^+$ and $Fe^{2+}$ ions together with several Ar multiply charged ions. Although $Fe^{3+}$, $Fe^{4+}$, and $Fe^{5+}$ ions could not be found in the spectrum because of poor resolution, it is supposed that they are produced in the ion source, because $Ar^{3+}$, $Ar^{4+}$, and $Ar^{5+}$ ions are produced with enough quantities. Figure 3 shows the eroded sputtering electrodes after two hours operation and seven hours operation of the ion source, respectively.
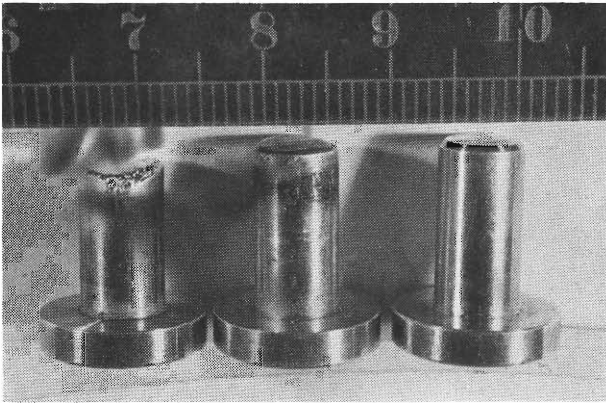


Fig. 3. Three sputtering electrodes: from right to left not eroded, eroded after two hours' operation and seven hours' operation, respectively.
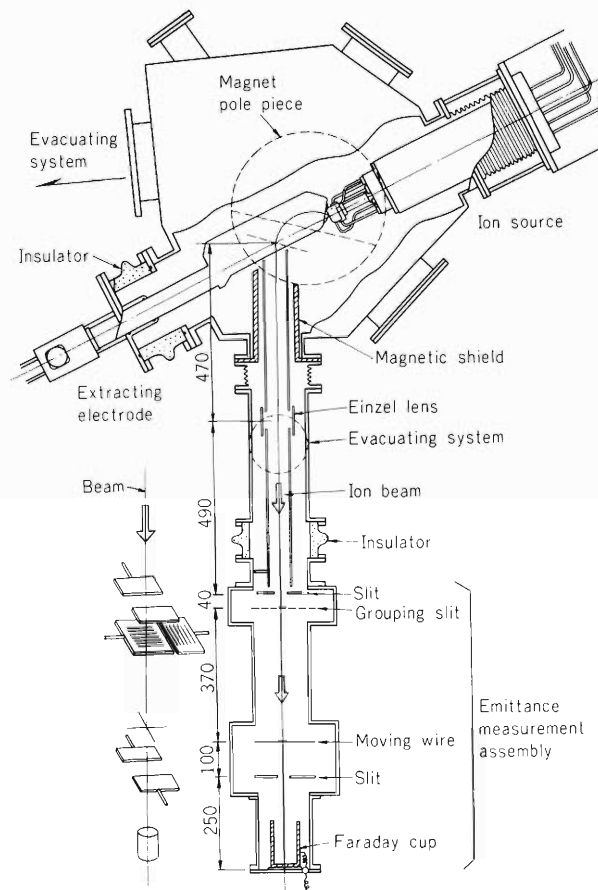


Fig. 4. Cross sectional view of the test facility.

We have studied the formation of the ion beams extracted from the ion source using $Ar^{2+}$ ions. Figure 4 shows a cross sectional view of the test facility. We could obtain a beam of good emittance at the position of moving wire, 1.4 m from the source magnet by reducing the effect of the magnetic fringing field by a magnetic sield and using an einzel lens system as is shown in Figs. 5 and 6.
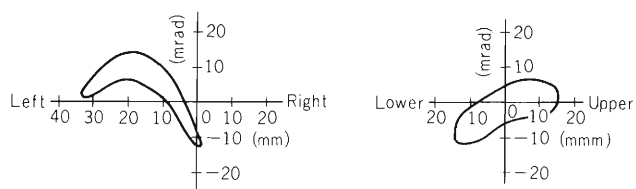
Fig. 5. Beam emittance measured for $Ar^{2+}$.
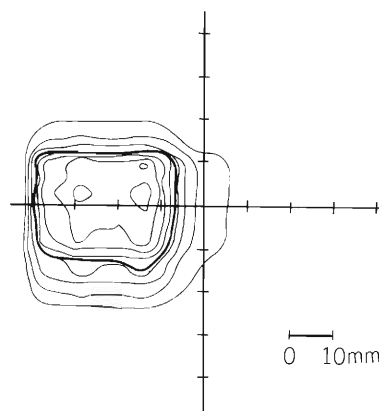
Fig. 6. Beam profile measured by moving wires.

Reference

1) I. Kohno, A. Shimamura, and T. Tonuma: IPCR Cyclotron Progr. Rep., 11, 149 (1977).

M. Hemmi, Y. Miyazawa, M. Odera, and T. Tonuma

Figure 1 shows the layout of the beam distributing, focusing and analysing system.   At present, there are nine pipe-end stations and two mid-line stations for experiments.   To guide and focus the beam into those stations, one switching magnet, two analysing, one small angle deflecting, one vertically deflecting magnets and ten quadrupole-doublet  magnets are necessary. All these magnets use so-called tape-coils[1) to make power dissipation small.
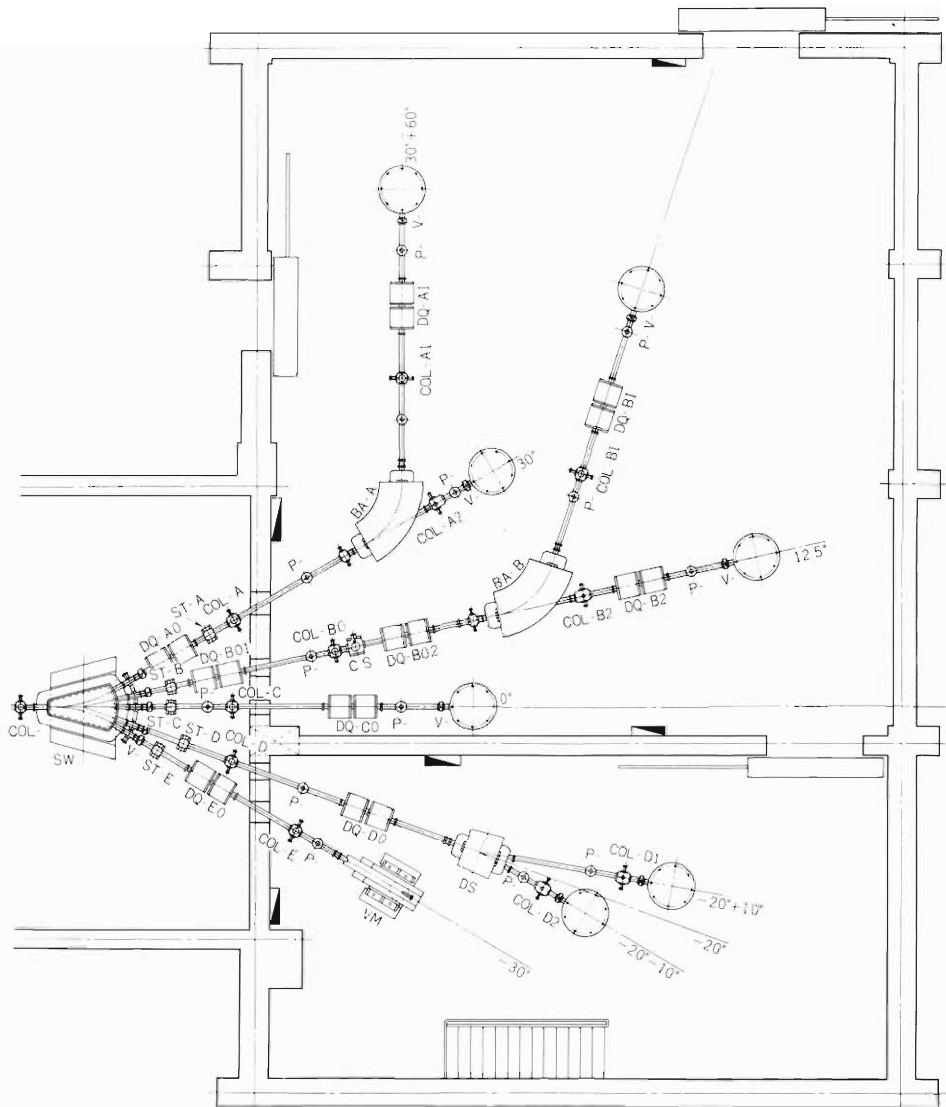


Fig. 1.    Layout of the beam transport system.
SW: Switching mag., BA: Analysing mag., VM: Vertically
bending mag., DQ: Quadrupole doublet mag.,
ST: Steering mag., P: Pump, V: Valve, COL: Slits and Beam stopper,
CS: Charge stripper.

Figure 2 shows dimensions of the switching magnet capable to deflect all kinds of particles accelerated by the linac. Its special mechanical structure to be mentioned is construction of its vacuum chamber. A thin stainless steel plate 1.5 mm thick forms the side wall of the chamber and is welded to the sides of the upper and lower pole tips which function as the lids of the chamber. The stainless steel spacers determine pole gap. Parts of the pole tips in the vacuum is plated· with nickel.

The analysing magnet is shown in Fig. 3. It can analyse particles having magnetic rigidity less than 1800 kG-cm. Some ions have rigidity larger than this value and need to be charge-stripped in order to be accepted by this analysing magnet. Since experiments expected to use analysed beam do not require beams of high intensity, the need of charge stripping and subsequent decrease of the beam intensity for some ions will not make difficulty. Its vacuum chamber is made of flattened non-magnetic stainless tube of circular cross section. Its wall thickness is only 1.5 mm and is easily flattened when pressed between pole tips. Those two types of the vacuum chambers, i.e. those for the switching and the analysing magnets have been suggested by R.M. Main of the LBL, University of California, when he visited this laboratory in 1977.

The vertically deflecting magnet (VM) has a similar construction to the analysing magnet
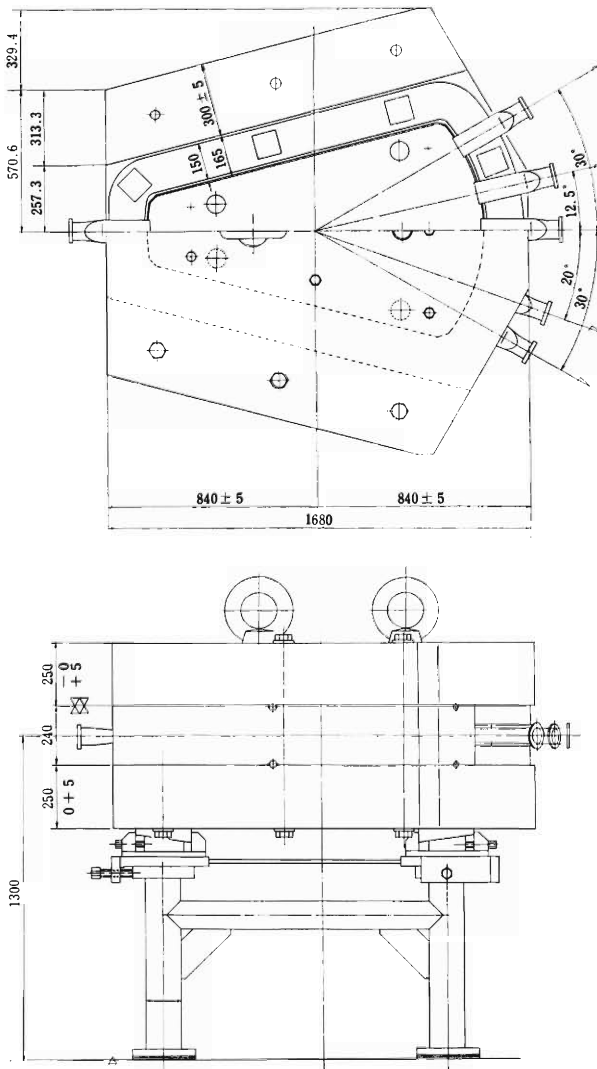


Fig. 2.　Beam switching magnet.
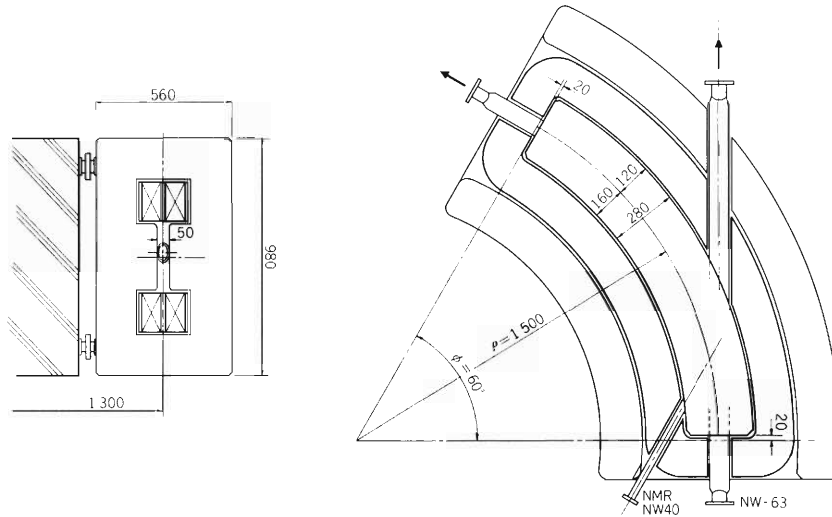
Fig. 3.   Beam analysing magnet.

except it has pole boundary with its normal making angle of 26.5 degree between beam trajectory at the beam entrance and exit in stead of the normal incidence of beam with the boundary in the case of the analysing magnets.

Figure 4 shows the quadrupole doublet.   The method of fabrication and characteristics of its coils were described elsewhere.[2]

The ISO NW-63 size has been adopted for the beam pipes.   The turbomolecular pumps of 120 l/s and the getter ion pumps of the same pumping speed are used to evacuate the beam lines.   Beam diagnostic elements such as the beam profile, bunch and emittance probes in addition to the slit box or Faraday chamber are distributed at suitable positions of the beam lines.
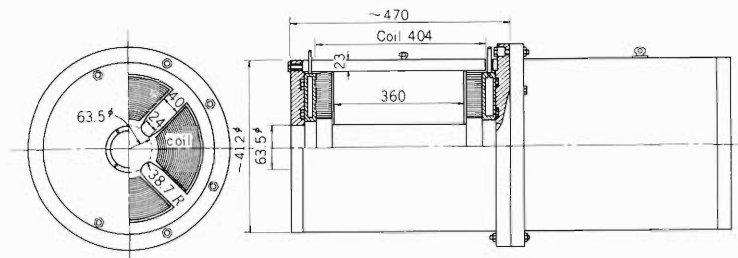


Fig. 4.   Quadrupole doublet magnet.

References

1)   R. M. Main and R. Yourd: Proc. 4th Intern. Conf. on Magnet Technology, p. 349 (1972).
2)   M. Hemmi and F. Yoshida: IPCR Cyclotron Progr. Rep., 10, 145 (1976).

# 10-7. Performance of an Axial Extraction PIG Ion Source

S. Nakajima

An ion source commercially available for ion implantation processing of semiconductors has been purchased for preliminary testing of the 500 kV accelerating column of the injector. Operating characteristics of the ion source was measured to obtain parameter values suitable for the intended use.

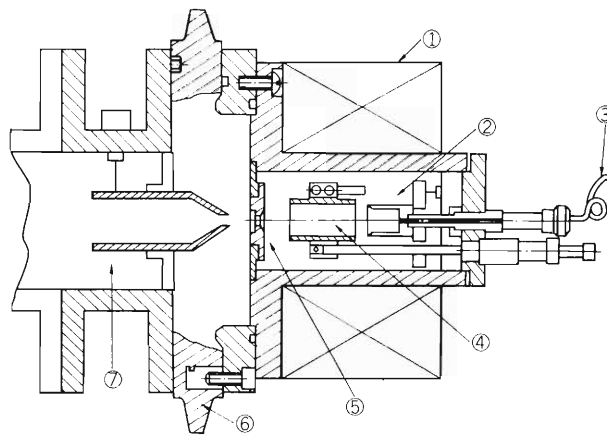Figure 1 shows the cross section of the cold cathode PIG source of axial extraction type.



Fig. 1.  Axial extraction PIG ion source.
①  Solenoid coil    ②  Cathode
③  Gas inlet         ④  Anode
⑤  Cathode aperture  ⑥  Insulator
⑦  Extracting electrode

Change of arc currents as a function of arc voltage is shown in Fig. 2.   Rate of gas supply is taken as the parameter in (a) and the current in the coil which produces magnetic field at the position of discharge in (b).   Field strength is 150 Gauss for coil current of 1 A.   In Fig. 3, extracted currents are given as functions of the gas supply rate and coil current.   The extracted current is not necessarily proportional to the rate of gas supply, while increase of coil current is clearly effective to obtain high current.   Variation of the extracted intensity as a function of extracted voltage is shown in Fig. 4.   For our purpose of the column test, 10 $\mu$A is sufficient and the gas load to the vacuum pump is quite small.   Divergence of the beam is 0.05 rad. at full width for extraction voltage of 6 kV and 0.04 rad. for 8 kV at this small current.

The ion source works stably with the following parameter values: gas supply between 0.05 cc/min. and 0.5 cc/min., magnetic field between 200 and 500 Gauss and arc voltage between 1 and 3 kV.

a) Effect of gas feed rate with
N$_2$ (upper) and air (lower)

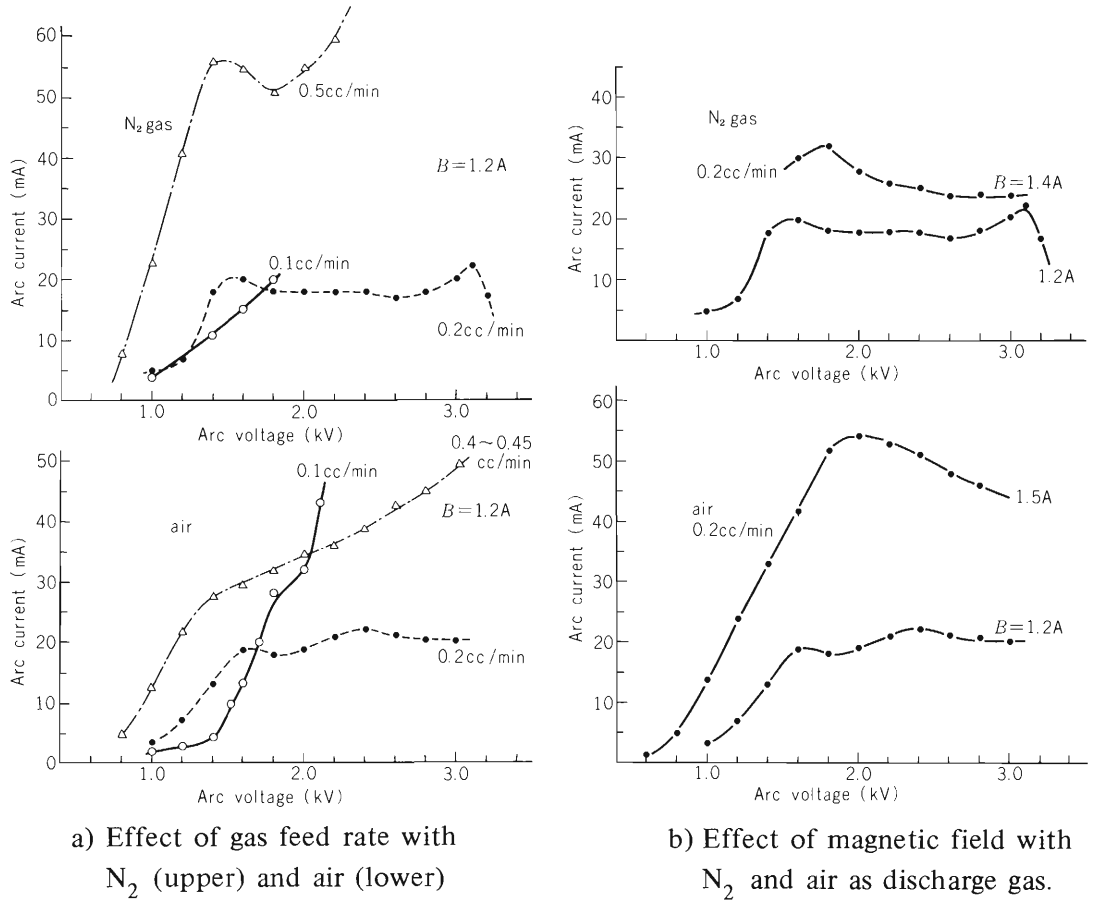b) Effect of magnetic field with
N$_2$ and air as discharge gas.

Fig. 2.  Arc current characteristics as functions of arc voltage.
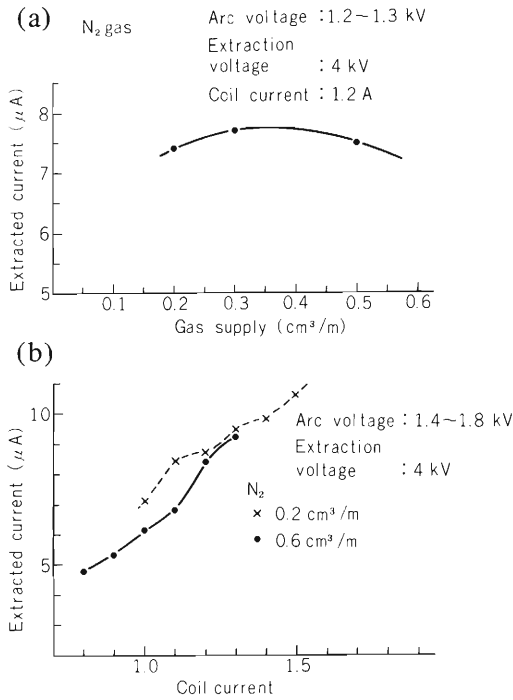


Fig. 3.  Extracted current as function
of (a) gas feed rate and (b) coil current.
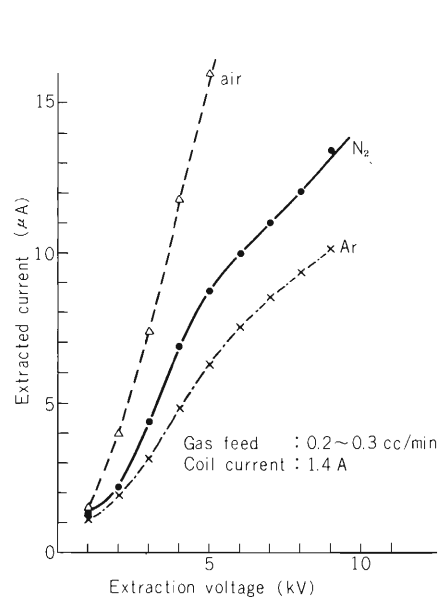Current was measured at 100 cm from
the anode.

Fig. 4.  Effect of extraction voltage
on the beam intensity.

# 11. LIST OF PUBLICATIONS

1. Machine development and accelerator physics

   1) H. Takebe, K. Ogiwara, and I. Kohno: "Measurements of the Turn-Separation and $\nu_z$ of the Ion Beam in the IPCR 160 cm Cyclotron", Reports I.P.C.R., (in Japanese), <u>54</u>, 77 (1978).

   2) A. Shimamura, T. Tonuma, and I. Kohno: " On the Multiply-charged Metal Ion Source", Reports I.P.C.R., (in Japanese), <u>54</u>, 116 (1978).

2. Nuclear physics and nuclear instrumentation

   1) T. Nomura: "Evidence for a Pure Prolate-to-Oblate Transition between $^{56}$Fe and $^{58}$Fe", Genshikaku-kenkyu, (in Japanese), <u>22</u>, 104 (1977).

   2) T. Kammuri, T. Motobayashi, I. Kohno, S. Nakajima, M. Yoshie, K. Katori, T. Mikumo, and H. Kamitsubo: "Effects of Recoil and Sequential Transfer on the $^{12}$C ($^{14}$N, $^{12}$C)$^{14}$N Reaction," J. Phys. G.: Nucl. Phys., <u>4</u>, L94 (1978).

   3) F. Soga, J. Schimizu, N. Takahashi, K. Takimoto, R. Wada, T. Fujisawa, T. Wada, and H. Kamitsubo: "Study of the Quasimolecular Resonance by the $^{24}$Mg $(\alpha, \gamma)^{12}$C, $^{16}$O Reactions", J. Phys. Soc. Japan, <u>44</u>, Suppl., 644 (1978).

   4) Y. Toba, H. Sakaguchi, A. Goto, F. Ohtani, N. Nakanishi, N. Kishida, M. Yasue, and T. Hasegawa: "Proton Inelastic Scattering on $^{28,29,30}$Si and Blocking Effect in the Core-Excitation of $^{29}$Si", J. Phys. Soc. Japan, <u>45</u>, 367 (1978).

   5) T. Nomura, J. Delaunay, C. Tosello, and N. Bendjaballah: "Partial Breakdown of the Evaporation Model and Possible Preequilibrium $\alpha$-Particle Emission in Heavy Ion Fusion Reactions", Nucl. Phys., <u>A305</u>, 262 (1978).

   6) H. Amakawa, S. Yamaji, A. Mori, and K. Yazaki: "Two-Step Process in Proton Inelastic Scattering", Phys. Lett., <u>76B</u>, 157 (1978).

   7) K. I. Kubo and H. Amakawa: "Energy Dependence of Two-Step (p, t) Cross Sections", Phys. Rev., <u>C17</u>, 1271 (1978).

   8) F. Soga, J. Schimizu, H. Kamitsubo, N. Takahashi, K. Takimoto, R. Wada, T. Fujisawa, and T. Wada: "Intermediate Structures in $^{12}$C + $^{16}$O System through $\alpha$-induced Reactions on $^{24}$Mg", Phys. Rev., <u>C18</u>, 2457 (1978).

   9) T. Nomura, H. Utsunomiya, T. Motobayashi, T. Inamura, and M. Yanokura: "Statistical Analysis of Preequilibrium $\alpha$-Particle Spectra and Possible Local Heating", Phys. Rev. Lett., <u>40</u>, 694 (1978).

   10) T. Fujisawa, M. Nakamura, M. Yasue, N. Ueda, T. Hasegawa, H. Kamitsubo, K. Hatanaka, T. Tanaka, M. Sekiguchi, T. Wada, Y. Toba, and F. Soga: "Spin Flip Asymmetry in the Inelastic Scattering of Protons on $^{12}$C at 28 MeV", Proc. of INS Intern. Symp. on Nucl. Direct Reaction Mechanism, Fukuoka (1978)

   11) T. Tamura, T. Udagawa, and H. Amakawa: "Reformulation of DWBA Form Factor for Heavy Ion Transfer Reactions", Prog. Theor. Phys., <u>60</u>, 1238 (1978).

   12) K. Sato, A. Iwamoto, K. Harada, S. Yamaji, and S. Yoshida: "Microscopic Calculation of Friction in Heavy Ion Reaction Using Linear Response Theory", Z. Physik A, <u>288</u>, 383 (1978).

3. Atomic and solid-state physics

   1) Y. Itikawa, Y. Awaya, and H. Suzuki: "Reports on the 10th Intern. Conf. on

the Physics of Electronic and Atomic Physics, The 5th Intern. Seminar on Ion-Atom Collisions, and the Satellite Meeting of Electronic Collisions", Butsuri (Phys. Soc. Japan) (in Japanese), 33, 157 (1978).

2) A. Koyama: "Secondary Electron Emission from Al by High Speed Proton or $\alpha$-Particle Bombardment (Calculation)", Ionizing Radiation, (in Japanese), 5, 17 (1978).

3) Y. Awaya and H. Kumagai: "An on-line X-ray Crystal Spectrometer of IPCR", Ionizing Radiation, (in Japanese), 5, 74 (1978).

4. Radiochemistry, radiation chemistry and radiation biology

1) F. Ambe and S. Ambe: "Defect $^{119}$Sn Atoms after Nuclear Decays and Reaction in SnSb and SnTe", J. Physique, 37, C6-923 (1976).

2) M. Matsui and M. Imamura: "The Radiolysis of Binary Mixtures of Tetrahydrofuran with Benzene, Thiophene, Pyridine, and Nitrobenzene", Bull. Chem. Soc. Japan, 51, 2191 (1978).

3) K. Kimura and M. Imamura: "Emission Spectra of Excitons Created in a Single Crystal of KBr by Irradiation of Heavy Ions at 4.2 K", Phys. Lett., 67A, 159 (1978).

5. Heavy ion linear accelerator

1) M. Odera: "Linear Accelerators of the Heavy Elements", J. Atomic Energy Japan, (in Japanese), 20, 553 (1978).

(Papers presented at meetings)

1. Machine development and accelerator physics

1) H. Kamitsubo, S. Motonaga, T. Nomura, N. Nakanishi, T. Wada, I. Kohno, J. Fujita, H. Nakajima, K. Ogiwara, H. Takebe, F. Yoshida, T. Fujisawa, T. Inamura, M. Ishihara, S. Nakajima, S. Fujita, T. Kageyama, S. Kohara, T. Karasawa, M. Hemmi, Y. Miyazawa, T. Kambara, I. Yokoyama, and I. Takeshita: "A Proposed Multipurpose Separated-Sector Cyclotron at IPCR", (IPCR Internal Report SSC-1) 2nd Symp. on Accelerator Science and Technology, Tokyo, March (1978).

2) N. Ueda, T. Hattori, T. Fujino, Y. Ohshiro, Y. Sakurada, and J. Schimizu: "Development of Heavy Ion Source I", Ann. Meeting of Phys. Soc. of Japan, Sendai, Apr. (1978).

3) N. Kumagai, S. Motonaga, H. Kamitsubo, T. Wada, F. Yoshida, K. Ogiwara, N. Nakanishi, and J. Fujita: "Model Magnet of the Separated Sector Cyclotron Proposed at IPCR", Autumn Divisional Meeting of Phys. Soc. of Japan, Matsumoto, Sept. (1978).

4) H. Kamitsubo, S. Motonaga, N. Kumagai, T. Nomura, N. Nakanishi, T. Wada, I. Kohno, J. Fujita, H. Nakajima, K. Ogiwara, H. Takebe, and F. Yoshida: "A Proposed Multi-Purpose Separated Sector Cyclotron at IPCR", 8th Intern. Conf. on Cyclotrons and their Applications, Indiana, Sept. (1978); Autumn Divisional Meeting of Phys. Soc. of Japan, Matsumoto, Sept. (1978).

5) T. Wada, N. Kumagai, H. Kamitsubo, S. Motonaga, T. Nomura, N. Nakanishi, I. Kohno, J. Fujita, H. Nakajima, K. Ogiwara, H. Takebe, and F. Yoshida: "The Injection in IPCR Separated Sector Cyclotron", 8th Intern. Conf. on Cyclotrons and their Applications", Indiana, Sept. (1978).

2. Nuclear physics and nuclear instrumentation

1) F. Soga, J. Schimizu, N. Takahashi, K. Takimoto, R. Wada, T. Fujisawa, T. Wada, and H. Kamitsubo: "Quasimolecular Resonance by $^{24}$Mg ($\alpha$, $^{12}$C)$^{16}$O Reaction", Ann. Meeting of Phys. Soc. of Japan, Sendai, Apr. (1978).

2) T. Tanabe, K. Sato, M. Yasue, J. Schimizu, K. Ogino, Y. Kadota, and F. Shimokoshi: "Experimental Study of the Heavy Ion Reaction Induced by 116 MeV $^{20}$Ne", Ann. Meeting of Phys. Soc. of Japan, Sendai, Apr. (1978).

3) A. Hashizume, T. Katou, H. Kumagai, and Y. Tendow: "High Spin States in $^{164}$Yb", Ann. Meeting of Phys. Soc. of Japan, Sendai, Apr. (1978).

4) S. Ise, T. Inamura, K. Hiruta, T. Shimoda, T. Nomura, and M. Ishihara: "Coincidence Measurements of Forward-peaked $\alpha$-Particles and $\gamma$-Rays in the $^{159}$Tb+$^{14}$N Reaction", Ann. Meeting of Phys. Soc. of Japan, Sendai, Apr. (1978).

5) K. Hiruta, T. Inamura, S. Ise, T. Shimoda, and M. Ishihara: "Angular Distributions of 'Direct' $\alpha$-Particles Emitted from the $^{159}$Tb+$^{14}$N Reaction and Rainbow Angle", Ann. Meeting of Phys. Soc. of Japan, Sendai, Apr. (1978).

6) T. Inamura, K. Hiruta, S. Ise, T. Shimoda, and M. Ishihara: "Kinematics of 'Direct' $\alpha$-Particles Emitted from the $^{159}$Tb+$^{14}$N Reaction", Ann. Meeting of Phys. Soc. of Japan, Sendai, Apr. (1978).

7) H. Utsunomiya, T. Nomura, T. Motobayashi, T. Inamura, and M. Yanokura: "Preequilibrium $\alpha$-Particle Emission in $^{14}$N-induced Reactions and Possible Local Heating I", Ann. Meeting of Phys. Soc. of Japan, Sendai, Apr. (1978).

8) K. Sato, K. Harada, S. Yamaji, and S. Yoshida: "The Calculation of the Frictional Coefficients on the Basis of the Linear Response Theory", Ann. Meeting of Phys. Soc. of Japan, Sendai, Apr. (1978).

9) H. Amakawa, A. Mori, and K. Yazaki: "Core Polarization Effects on Inelastic Proton-$^{13}$C Scattering", Ann. Meeting of Phys. Soc. of Japan, Sendai, Apr. (1978).

10) K. Takimoto, R. Wada, E. Takada, M. Fukuda, T. Yamaya, H. Endo, K. Umeda, T. Suehiro, J. Schimizu, and Y. Ohkuma: "The (d, $^6$Li) Reaction on Light Nuclei at 54.25 MeV", 3rd Intern. Conf. on Clustering Aspects of Nuclear Structure and Nuclear Reactions, Manitoba, June (1978).

11) A. Hashizume, T. Kimura, and T. Hamada: "The Decay of $^{206}$Bi and Measurement of Internal Conversion Electrons", The 15th Ann. Meeting on Radioisotopes in Physical Sciences and Industry, Tokyo, June (1978).

12) T. Inamura, K. Hiruta, S. Ise, M. Ishihara, T. Nomura, and T. Shimoda: "Angular-momentum Distributions of Residual Nuclei after Fast $\alpha$-Particle Emission in Heavy-ion Reactions", Intern. Conf. on Nuclear Interactions, Canberra, Aug. (1978).

13) K. Hiruta, T. Inamura, S. Ise, M. Ishihara, and T. Shimoda: "Angular Distributions of Fast $\alpha$-Particles Emitted from the $^{159}$Tb+$^{14}$N Reaction", Intern. Conf. on Nuclear Interactions, Canberra, Aug. (1978).

14) K. Ogino, Y. Kadota, M. Yasue, J. Schimizu, Y. Nishiwaki, and K. Ohori: "$^{12}$C, $^{20}$Ne ($\alpha$,d) Reaction at $E_\alpha$ = 65 MeV", Autumn Divisional Meeting of Phys. Soc. of Japan, Matsumoto, Sept. (1978).

15) K. Umeda, T. Yamaya, T. Suehiro, K. Takimoto, R. Wada, E. Takada, M. Fukuda, J. Schimizu, and Y. Ohkuma: " $^{16}$O, $^{40}$Ca, $^{58}$Ni(d, $^6$Li) Reaction", Autumn Divisional Meeting of Phys. Soc. of Japan, Matsumoto, Sept. (1978).

16) T. Kojima, T. Inamura, K. Hiruta, T. Nomura, and T. Sugitate: "Multiplicity of $\gamma$-Rays Following Fast $\alpha$-Particle Emission in the $^{159}$Tb + 95 MeV $^{14}$N Reaction", Autumn Divisional Meeting of Phys. Soc. of Japan, Matsumoto, Sept. (1978).

17) K. Hiruta, T. Inamura, T. Kojima, and T. Nomura: "Energy Distributions of Channel-specified $\alpha$-Particles in the $^{159}$Tb + 95 MeV $^{14}$N Reaction", Autumn Divisional Meeting of Phys. Soc. of Japan, Matsumoto, Sept. (1978).

18) H. Utsunomiya, T. Nomura, T. Sugitate, T. Inamura, and T. Motobayashi: "Preequilibrium $\alpha$-Particle Emission in $^{14}$N-induced Reactions and Possible Local Heating II", Autumn Divisional Meeting of Phys. Soc. of Japan, Matsumoto, Sept. (1978).

19) T. Nomura, H. Utsunomiya, T. Motobayashi, T. Inamura, and T. Sugitate: "Energy Relaxation during Fusion Processes Probed by Preequilibrium $\alpha$ Emission", Autumn Divisional Meeting of Phys. Soc. of Japan, Matsumoto, Sept. (1978).

20) M. Ichimura, B. Imanishi, and M. Kawai: "Study of (d, p) Reaction by Coupled Method", Autumn Divisional Meeting of Phys. Soc. of Japan, Matsumoto, Sept. (1978).

21) T. Fujisawa, M. Nakamura, M. Yasue, N. Ueda, T. Hasegawa, H. Kamitsubo, K. Hatanaka, T. Tanaka, M. Sekiguchi, T. Wada, Y. Toba, and F. Soga: "Spin Flip Asymmetry in the Inelastic Scattering of Protons on $^{12}$C at 28 MeV", Autumn Divisional Meeting of Phys. Soc. of Japan, Matsumoto, Sept. (1978).

22) T. Hoshino: "On the Adiabatic Approximation of TDHF", Autumn Divisional Meeting of Phys. Soc. of Japan, Matsumoto, Sept. (1978).

23) K. Sato, S. Yamaji, K. Harada, and S. Yoshida: "Analysis of the Collision $^{20}$Ne + $^{28}$Si by Solving the Coupled Dynamical Equations of Motion", Autumn Divisional Meeting of Phys. Soc. of Japan, Matsumoto, Oct. (1978).

24) M. Ichimura: "How Many Steps Should be Taken into Account in (d, p) Reactions", INS Intern. Symp. on Nuclear Direct Reaction Mechanism, Fukuoka, Oct. (1978).

25) H. Amakawa, S. Yamaji, A. Mori, and K. Yazaki: "Adiabatic Treatment of Deuteron-Nucleus Scattering", INS Intern. Symp. on Nuclear Direct Reaction Mechanism, Fukuoka, Oct. (1978).

26) N. Kishida and H. Ohnuma: "The Variations of (d, p) j-Dependence with Energy and its EFR-DWBA Analyses Including the Deuteron D-state", INS Intern. Symp. on Nuclear Direct Reaction Mechanism, Fukuoka, Oct. (1978).

27) T. Fujisawa, M. Nakamura, M. Yasue, N. Ueda, T. Hasegawa, H. Kamitsubo, K. Hatanaka, T. Tanaka, M. Sekiguchi, T. Wada, Y. Toba, and F. Soga: "Spin Flip Asymmetry in the Inelastic Scattering of Protons on $^{12}$C at 28 MeV", INS Intern. Symp. on Nuclear Direct Reaction Mechanism, Fukuoka, Oct. (1978).

28) T. Nomura: "Preequilibrium $\alpha$-Particle Emission in Low-Energy Heavy Ion Reactions and Local Heating", Intern. Workshop on Reaction Models for Continuous Spectra of Light Particles, Bad Honnef, Nov. (1978).

3. Atomic and solid-state physics

1) Y. Awaya and T. Tonuma: "X-Rays Induced by Heavy Ions", Symp. on Atomic Process by Heavy Ions, Tokyo, Jan. (1978).

2) T. Takahashi, F. Yatagai, and A. Matsuyama: "Application of Katz's Theory to Radiation Biology", Ann. Meeting of Japan Soc. of Appl. Phys., Tokyo, March (1978).

3) T. Takahashi, S. Uchiyama, Y. Awaya, A. Hashizume, H. Kumagai, T. Tonuma, and

T. Doke: "Electronic Stopping Power of Several MeV/amu C and He Ions", Ann. Meeting of Phys. Soc. of Japan, Sendai, March (1978).

4) A. Koyama: "Secondary Electron Emission from Al by High Speed Proton Bombardment", IPCR Symp. on Excitation of Secondary Electron and Auger Electron by Heavy Ions, Wako, March (1978).

5) T. Tonuma, Y. Awaya, T. Kambara, H. Kumagai, and I. Kohno: "K X-rays of Gas Target Elements Induced by Heavy Ions", Ann. Meeting of Phys. Soc. of Japan, Sendai, Apr. (1978).

6) T. Tonuma, Y. Awaya, T. Kambara, H. Kumagai, and I. Kohno: "Ar K X-Rays Induced by N-Ion Bombardment", Spring Divisional Meeting of Phys. Soc. of Japan, Sendai, Apr. (1978).

7) E. Yagi, A. Koyama, H. Sakairi, and R. R. Hasiguti: "Lattice Location of Ni Atoms Implanted into Al", U.S.-Japan Seminar on Fundamental and Application of Particle Channeling, Tokai, May (1978).

8) H. Sakairi: "Displacement and Replacement of Atoms in Irradiated Metals", IPCR Symp. on Application of Ion Beams to Material Science, Wako, May (1978).

9) E. Yagi: "Interstitials in Reduced Rutile and in Ni–Implanted Al", IPCR Symp. on Application of Ion Beams to Material Science, Wako, May (1978).

10) T. Takahashi: "Spatial Distribution of Ionization Energy Deposited about the Path of a Heavy Ion", Symp. on the Heavy Ion Irrad. Effect on Biological Material, Oiso, June (1978).

11) T. Okada, H. Sekizawa, and T. Yamadaya: "Hyperfine Interactions of $^{119}$Sn in Magnetic Chalcogen Spinels", Intern. Conf. on the Applications of the Mössbauer Effect, Kyoto, Aug. (1978).

12) Y. Awaya, T. Katou, H. Kumagai, T. Tonuma, Y. Tendow, K. Izumo, T. Takahashi, M. Okano, T. Hamada, and S. Özkök: "K and L X-Rays of Yttrium Induced by Heavy Ion Bombardment", Autumn Divisional Meeting of Phys. Soc. of Japan, Shizuoka, Oct. (1978).

13) S. Uchiyama, T. Takahashi, Y. Awaya, H. Kumagai, T. Tonuma, A. Hitachi, and T. Doke: "Energy Loss and Straggling of Several MeV/amu C and He Ions", Autumn Divisional Meeting of Phys. Soc. of Japan, Shizuoka, Oct. (1978).

14) H. Shinno, H. Shiraishi, R. Watanabe, H. Kamitsubo, I. Kohno, and T. Shikata: "Effect of Post Irradiation Aging Treatment on the Helium Embrittlement of SUS 316 stainless steel", 83rd Ann. Meeting of The Japan Institute of Metals, Toyama, Oct. (1978).

15) Y. Awaya: "X-Rays Following Multiple Inner-Shell Ionization", Symp. on Atomic Collisions, Tokyo, Dec. (1978).

16) T. Tonuma, Y. Awaya, T. Kambara, H. Kumagai, and I. Kohno: "Ar K X-Ray Spectra Induced by 66-110 MeV N-Ion Bombardment", Symp. on Atomic Collisions, Tokyo, Dec. (1978).

4. Radiochemistry, radiation chemistry and radiation biology

1) K. Kimura and M. Imamura: "Emission Spectra of Single Crystals Irradiated with Heavy Ions at 4.2 K", Symp. on Solid State Physics Using Heavy Ion Beams, Tokai, Dec. (1977).

2) K. Kimura and M. Imamura: "Emission Spectra of Excitons Created in a KBr Single Crystal Irradiated with Heavy Ions at 4.2 K", 2nd Symp. on Accelerator Science and Technology, Tokyo, March (1978).

3) T. Nozaki, Y. Itoh, M. Iwamoto, and K. Ogawa: "Yield of $^{73}$Se and $^{77}$Br for Various Reactions and Their Carrier- and/or Salt-free Separation", 2nd Intern. Symp. on Radiopharm. Chem., Oxford, July (1978).

4) T. Irie, K. Fukushi, T. Ido, T. Nozaki, and Y. Kasida: "$^{18}$F-fluorination by K$^{18}$F-crown Ether System", 2nd Intern. Symp. on Radiopharm. Chem., Oxford, July (1978).

5) K. Fukushi, T. Irie, T. Nozaki, T. Ido, and Y. Kasida: "Adrenal Affinity and Plasma Lipoprotein Binding of Radiohalogeno Derivatives of Cholesterol", 2nd Intern. Symp. on Radiopharm. Chem., Oxford, July (1978).

6) K. Kimura: "Emission Spectra of Single Crystals Under Heavy Ion Irradiation", Symp. on the Boundary Region between Physics and Radiation Chemistry, Osaka, Sept. (1978).

7) K. Kimura and M. Imamura: "Measurements of Subnanosecond Time-Dependent Emission Spectra of KBr Single Crystals Irradiated with Heavy Ions at 4.2 K", 21st Conf. on Radiation Chemistry, Tokyo, Sept. (1978).

8) A. Kira, M. Matsui, and M. Imamura: "Yields of Trapped Electron in Ethanol Glass Irradiated with Heavy Ions", 21st Conf. on Radiation Chemistry, Tokyo, Sept. (1978).

9) T. Nozaki, M. Iwamoto, K. Usami, K. Mukai, and A. Hiraiwa: "Activation Analysis of Oxygen in Thin Silicon Nitride Films on Silicon Substrates", Discussion Meeting on Radiochem., Tokyo, Oct. (1978).

10) T. Nozaki and Y. Terai: "Chemical Separation of $^{18}$F in Charged Particle Activation Analysis of Oxygen in High-purity Metals", Discussion Meeting on Radiochem., Tokyo, Oct. (1978).

11) T. Nozaki, T. Karasawa, M. Iwamoto, Y. Terai, and M. Okano: "Excitation Function for the $^{14}$N (p, n)$^{14}$O Reaction", Discussion Meeting on Radiochem., Tokyo, Oct. (1978).

5. Heavy ion linear accelerator

1) I. Kohno, A. Shimamura, T. Tonuma, and I. Takeshita: "A Penning Multiply-Charged Ion Source for the IPCR Linac", 2nd Symp. on Ion Source and Application Technology, Tokyo, Feb. (1978).

2) A. Shimamura, T. Tonuma, and I. Kohno: "PIG Heavy Ion Source for the IPCR Linac II (Experimental Results with the Test Facility)", Ann. Meeting of Phys. Soc. of Japan, Sendai, Apr. (1978).

# 12. LIST OF PERSONNEL

## Members of the Board

DOTE Toshihiko　土 手 敏 彦 (Chairman)　　HAMADA Tatsuji　浜 田 達 二
KAMITSUBO Hiromichi　上 坪 宏 道　　KOHNO Isao　河 野 功
NAKANE Ryohei　中 根 良 平　　NOZAKI Tadashi　野 崎 正
ODERA Masatoshi　小 寺 正 俊

## Users Committee

HAMADA Tatsuji　浜 田 達 二(Chairman)　　IMAMURA Masashi　今 村 昌
KAMITSUBO Hiromichi　上 坪 宏 道　　KOHNO Isao　河 野 功
MATSUYAMA Akira　松 山 晃　　NOZAKI Tadashi　野 崎 正
ODERA Masatoshi　小 寺 正 俊　　SAKAIRI Hideo　坂 入 英 雄
SEKIZAWA Hisashi　関 沢 尚

## Operation and Machine Maintenance Group

FUJITA Shin　藤 田 新　　IKEGAMI Kumio　池 上 九 三 男
KAGEYAMA Tadashi　影 山 正　　KOHARA Shigeo　小 原 重 夫
KOHNO Isao　河 野 功　　NAKAJIMA Hisao　中 嶋 尚 雄
OGIWARA Kiyoshi　荻 原 清　　TAKEBE Hideki　武 部 英 樹

## Scientific and Engineering Personnel
### Cyclotron Laboratory

AMAKAWA Hirotaka　天 川 博 隆　　FUJISAWA Takashi　藤 沢 高 志
FUJITA Jiro　藤 田 二 郎　　INAMURA Takashi　稲 村 卓
*ISHIHARA Masayasu　石 原 正 泰　　KAMITSUBO Hiromichi　上 坪 宏 道
KARASAWA Takashi　唐 沢 孝　　KOHNO Isao　河 野 功
KUMAGAI Noritaka　熊 谷 教 孝　　MOTOBAYASHI Tohru　本 林 透
MOTONAGA Shoshichi　元 永 昭 七　　NAKAJIMA Shunji　中 島 諄 二
NAKANISHI Noriyoshi　中 西 紀 喜　　NOMURA Toru　野 村 亨
SHIKATA Takashi　四 方 隆 史　　WADA Takeshi　和 田 雄
YAMAJI Shuhei　山 路 修 平

### (Visitors)

HATTORI Toshiaki　服 部 俊 章　(Inst. Nucl. Study, Univ. of Tokyo)
HAYAKAWA Shunichiro　早 川 俊 一 郎　(Dept. Phys., Waseda Univ.)
HIRUTA Kotaro　蛭 田 幸 太 郎　(Dept. Phys., Tokyo Gakugei Univ.)
ICHIMURA Munetake　市 村 宗 武　(Inst. Phys., College General Education, Univ. of Tokyo)
IGARASHI Masamichi　五 十 嵐 正 道　(Tokyo Medical College)
IMANISHI Bunryu　今 西 文 竜　(Inst. Nucl. Study, Univ. of Tokyo)
KAMMURI Tetsuo　冠 哲 夫　(Dept. Phys., Osaka Univ.)
LEE S. M.　李 相 茂　(Centrum de Recherche Nucl. Strasbourg)
MIKUMO Takashi　三 雲 昂　(Inst. Phys., Tsukuba Univ.)
NAKAHARA Hiromichi　中 原 弘 道　(Dept. Chem., Tokyo Metropolitan Univ.)

* On leave to Cyclotron Inst., Texas A & M University untill Jan. 1979

NODA Akira　　野田　章　(Inst. Nucl. Study, Univ. of Tokyo)
OHNUMA Hajime　　大沼　甫　(Dept. Phys., Tokyo Inst. Technol.)
ÖZKÖK S.　(Dept. Phys., Istanbul Univ.)
SHINNO Hitoshi　　新野　仁　(Nat. Res. Inst. for Metals)
SHIRAISHI Haruki　　白石春樹　(Nat. Res. Inst. for Metals)
SOGA Fuminori　　曾我文宣　(Inst. Nucl. Study, Univ. of Tokyo)
TAKAHASHI Noriyuki　　高橋令幸　(Dept. Phys., Univ. of Tokyo)
TAKIMOTO Kiyohiko　　滝本清彦　(Dept. Phys., Kyoto Univ.)
TAMURA Taro　　田村太郎　(Dept. Phys., Texas Univ.)
UDAGAWA Takeshi　　宇田川猛　(Dept. Phys., Texas Univ.)
WADA Ryoichi　　和田良一　(Dept. Phys., Kyoto Univ.)

(Students)

HASHIMOTO Naoki　　橋本直樹　(Dept. Phys., Tokyo Inst. Technol.)
ISE Sugao　　伊勢須賀雄　(Dept. Phys., Tokyo Gakugei Univ.)
KISHIDA Norio　　岸田則生　(Dept. Phys., Tokyo Inst. Technol.)
KOJIMA Toshiyuki　　小島敏行　(Dept. Phys., Rikkyo Univ.)
MIAKE Yasuo　　三明康郎　(Lab. Nucl. Study, Osaka Univ.)
NORO Tetsuo　　野呂哲夫　(Dept. Phys., Kyoto Univ.)
SATO Kenichi　　佐藤憲一　(Dept. Phys., Tohoku Univ.)
SHIMODA Tadashi　　下田　正　(Dept. Phys., Kyoto Univ.)
SUGITATE Toru　　杉立　徹　(Dept. Phys., Tokyo Inst. Technol.)
TOBA Yoshiyuki　　外羽吉幸　(Dept. Phys., Kyoto Univ.)
UTSUNOMIYA Hiroaki　　宇都宮弘章　(Dept. Phys., Kyoto Univ.)
YANOKURA Minoru　　矢野倉実　(Dept. Chem., Tokyo Metropolitan Univ.)

## Linac Laboratory

CHIBA Yoshiaki　　千葉好明
HOSHINO Tohru　　星野　亨
KAMBARA Tadashi　　神原　正
ODERA Masatoshi　　小寺正俊
SHIMAMURA Akira　　島村　旻
TONUMA Tadao　　戸沼正雄
YOSHIDA Fusako　　吉田房子

HEMMI Masatake　　逸見政武
INOUE Toshihiko　　井上敏彦
MIYAZAWA Yoshitoshi　　宮沢佳敏
SCHIMIZU Jun　　清水　純
TAKESHITA Isao　　竹下勇夫
YOKOYAMA Ichiro　　横山一郎

(Visotor)

TAKEDA Shigeru　　竹田　繁　(Nat. Lab. High Energy Phys.)

## Radiation Laboratory

AWAYA Yohko　　粟屋容子
HASHIZUME Akira　　橋爪　朗
KATOU Takeo　　加藤武雄
KUMAGAI Hidekazu　　熊谷秀和
TAKAHASHI Tan　　高橋　旦

HAMADA Tatsuji　　浜田達二
IZUMO Koichi　　出雲光一
KONNO Satoshi　　金野　智
OKANO Masaharu　　岡野真治
TENDOW Yoshihiko　　天道芳彦

(Visitors)

DOKE Tadayoshi　　道家忠義　(Sci. and Eng. Res. Lab., Waseda Univ.)
FUJIOKA Manabu　　藤岡　学　(Dept. Phys., Tohoku Univ.)
HAYASHIBE Shogo　　林部昭吾　(Dept. Phys., Tohoku Univ.)

ISHII Keizo　　石井慶造　(Cyclotron, Tohoku Univ.)
MORITA Susumu　　森田　右　(Dept. Phys., Tohoku Univ.)
NAGAHARA Teruaki　　永原照明　(Inst. Atomic Energy, Rikkyo Univ.)
TAWARA Hiroyuki　　俵　博之　(Dept. Nucl. Eng., Kyushu Univ.)
UCHIYAMA Sadayuki　　内山貞幸　(Clear Pulse Co. Ltd.)

Metal Physics Laboratory

KOYAMA Akio　　小山昭雄　　　　SAKAIRI Hideo　　坂入英雄
SHIOTANI Nobuhiro　　塩谷亘弘　　　YAGI Eiichi　　八木栄一

(Visitor)

TANIGAWA Shoichiro　　谷川庄一郎　(Dept. Metallurgy and Materials Sci. Faculty Eng.,
　　　　　　Univ. of Tokyo)

(Students)

HINODE Kenji　　日野出憲治　(Dept. Metallurgy and Materials Sci. Faculty Eng., Univ.
　　　　　　of Tokyo)
KUMAKURA Hiroaki　　熊倉浩明　(Dept. Metallurgy and Materials Sci., Faculty Eng.,
　　　　　　Univ. of Tokyo)

Magnetic Materials Laboratory

ASAI Kichizo　　浅井吉蔵　　　　OKADA Takuya　　岡田卓也
SAKAI Nobuhiko　　坂井信彦　　　SEKIZAWA Hisashi　　関沢　尚

(Visitors)

MIZOGUCHI Tadashi　　溝口　正　(Dept. Phys., Gakushuin Univ.)
YAMADAYA Tokio　　山田谷時夫　(Matsushita Res. Inst. Tokyo, Inc.)

Solid State Chemistry Laboratory

ENDO Hiroshi　　遠藤　寛　　　　KOBAYASHI Masayoshi　　小林雅義
MAEDA Kuniko　　前田邦子　　　SASA Yoshihiko　　佐々嘉彦
UDA Masayuki　　宇田応之

Radiochemistry Laboratory

AMBE Fumitoshi　　安部文敏　　　AMBE Shizuko　　安部静子
ARATANI Michi　　荒谷美智　　　ITO Yoshiko　　伊東芳子
IWAMOTO Masako　　岩本正子　　NOZAKI Tadashi　　野崎　正
TERAI Yoshiro　　寺井善郎

(Visitors)

FUKUSHI Kiyoshi　　福士　清　(Nat. Inst. of Radiological Sci.)
HIRAIWA Atsushi　　平岩　篤　(Central Res. Lab., Hitachi Electric Co.)
IRIE Toshiaki　　入江俊章　(Nat. Inst. of Radiological Sci.)
KASIDA Yoshihiko　　樫田義彦　(Nat. Inst. of Radiological Sci.)
MUKAI Kiichiro　　向　喜一郎　(Central Res. Lab., Hitachi Electric Co.)
TAKI Ko　　滝　幸　(Dept. of Hygen., Kitazato Univ.)
USAMI Katsuhisa　　宇佐美勝久　(Central Res. Lab., Hitachi Electric Co.)

## Radiation Chemistry Laboratory

IMAMURA Masashi 　今 村　　昌　　　　　　　KIMURA Kazuie 　木 村 一 宇

(Visitor)

MATSUI Masao 　松 井 正 大　　(Dept. of Pharmacy, Hokuriku Univ.)

(Student)

MOCHIZUKI Kiyoshi 　望 月　　清　　(Dept. Phys., Chuo Univ.)

## Radiobiology Laboratory

HATTORI Yukihiko 　服 部 行 彦　　　　　　　　KANEKO Ichiro 　金 子 一 郎
KITAYAMA Shigeru 　北 山　　滋　　　　　　　　MATSUYAMA Akira 　松 山　　晃
YATAGAI Fumio 　谷 田 貝 文 夫

(Visitors)

OKADA Shigefumi 　岡 田 重 文　　(Faculty of Medicine, Univ. of Tokyo)
SASAKI Masao 　佐々木 正 大　　(Dept. Cytogenetic, Medical Res. Inst., Tokyo Medical
　　　　　　　　　　　　　　　　　and Dental Univ.)
SAWADA Shozo 　沢 田 昭 三　　(Res. Inst. Nucl. Medicine and Biology, Hiroshima Univ.)

## Safety Control Affairs Office

HAMADA Tatsuji 　浜 田 達 二　　　　　　　　　IGARASHI Kazui 　五 十 嵐 一 戍
SAKAMOTO Ichiro 　坂 本 一 郎　　　　　　　　　USUBA Isao 　薄 葉　　勲

# 13. LIST OF OUTSIDE USERS AND THEIR THEMES

(Jan. – Dec. 1978)

1) M. Nakahara, M. Watanabe, Y. Nakamura,      Faculty of Science, Tokyo
   H. Kudo, K. Muramatsu, Y. Nagame, T. Ishii,      Metropolitan Univ.
   K. Horiuchi, and Y. Murakami
   "Production of $^{57,58}$Co"

2) A. Hishinuma, T. Furuta, H. Kamizuka,      Japan Atomic Energy Research Inst.
   K. Fukai, and T. Otomo
   "Simulation Test on Neutron Irradiation
   Damage of Stainless Steel for Fast Breeder
   Reactors by $\alpha$-Bombardment"

3) Y. Wada, K. Senno, K. Fukuda, M. Suzuki,      Musashino Electrical Communication Lab.,
   K. Suzuki, and H. Sakamoto      Nippon Telegraph and Telephone
   "Study of Irradiation Damage of      Public Corporation
   Transistors by Proton Bombardment"

4) N. Nagashima, M. Tamura, and T. Suzuki      Semiconductor Dept., Hitachi Ltd.
   "Determination of C in Si by Activation
   Analysis"

5) Y. Honma      Kyoritsu College of Pharmacy
   "Production of $^{48}$V, $^{48}$Cr, $^{77}$Br and $^{81}$Rb"

6) K. Usami and K. Mukai      Hitachi R & D Center
   "Surface Analysis by Charged Particle
   Activation"

7) M. Shimada, K. Kohashi, M. Terasawa,      Toshiba R & D Center
   and M. Iimura
   "Cyclotron Irradiation for Study of
   FBR Material Embrittlement"

8) K. Yuita      National Inst. of Agricultural Sciences
   "Production of $^{43}$K"

154

9) S. Hayashi, S. Iwata, M. Yanokura,* and
   A. Murakami**
   "Calibration of Solid Track Detectors
   with Heavy Ions"

Research Reactor Inst.,
Kyoto Univ.
* Faculty of Science, Tokyo
  Metropolitan Univ.
**Faculty of Science and Engineering,
  Saga Univ.

10) A. Furusawa
    "Production of $^{152,154}$Eu"

Faculty of Science, Niigata Univ.

# AUTHOR INDEX

理化学研究所

埼玉県　和光市　広沢

理化学研究所

埼玉県　和光市　広沢